MODELLING OF CONVENTIONAL AND MICROCHANNEL DELUGEABLE TUBE BUNDLE FOR A DIRECT AIR-COOLED STEAM CONDENSER

ESTER ANGULA

OCTOBER 2023

MODELLING OF CONVENTIONAL AND MICROCHANNEL DELUGEABLE TUBE BUNDLE FOR A DIRECT AIR-COOLED STEAM CONDENSER

A DISSERTATION REPORT SUBMITTED IN FULFILMENT OF THE REQUIREMENTS FOR THE DEGREE OF DOCTOR OF PHILOSOPHY IN MECHANICAL ENGINEERING

OF

THE UNIVERSITY OF NAMIBIA

BY

ESTER ANGULA

218178755

OCTOBER 2023

MAIN SUPERVISOR: PROF. PAUL CHISALE (THE COPPERBELT UNIVERSITY, ZAMBIA)

CO-SUPERVISOR: DR. FILLEMON N. NANGOLO (NAMIBIA UNIVERSITY OF SCIENCE AND TECHNOLOGY)

Abstract

This study presents the thermal performance modelling of conventional and microchannel delugeable tube bundle which incorporated into a second stage of the induced Hybrid (Dry/Wet)) Dephlegmator (HDWD). Hybrid dry/wet dephlegmator was proposed to replace a Conventional Dephlegmator (CD) of a direct Air-Cooled Condenser (ACC) system, coupled to 30 MW steam turbine of a generating unit. The Conventional Delugeable Tube Bundle (CDTB) thermal performance was modelled and configured using one- and two - dimensional models by employing heat and mass transfer approach. The geometric parameters for both first and second stages tube bundles of HDWD were derived from that of CD of ACC system of the considered generation unit. Therefore, the thermal performance of CDTB was optimised to ensure highest performance, and appropriate geometric parameters that are corresponding to that of CD and available space for installation. The best CDTB configuration's performance was compared to similar existing Delugeable Round Tube Bundle (DRTB) in literatures. When the tube pitch varied from 25 mm to 38 mm, the DRTB's heat transfer rate and air-side pressure drop were found to be in the range of 1.4 to 2 times and 1.3 to 2.2 times that of CDTB, respectively. The Microchannel Delugeable Tube Bundle (MDTB) thermal performance was analysed using semi-empirical model, which comprises of microchannel heat transfer and flow correlations. The size and geometric parameters of MDTB was equivalent to that of CDTB, and the only difference was that, the MDTB has microchannel/ ports on the steam-side. The MDTB thermal performance was found to increase as the hydraulic diameter of the channels decreased. The thermal performance comparison of the CDTB and MDTB at bundle, component and system levels was carried out. At all the levels, the MDTB performance was higher than that of CDTB. However, this higher performance came at expense of higher steam-side pressure drop. As the ambient air temperature increased from 32 ℃ to 44 ℃, the MDTB's heat transfer rate for 140 μm hydraulic diameter was found to be 9 to 6 % higher than that of CDTB. The air-side pressure drop variations between the two bundles were insignificant. Furthermore, the thermal performance of HDWD incorporated with either CDTB or MDTB was compared to that of CD at component and system levels. At system level, and as the ambient air temperature increased from 32 ℃ to 44 ℃, the heat transfer rate of the CD was found to be 27 % to 31 % less than that of HDWD incorporated with either CDTB or MDTB. The Air-side pressure drop for HDWD was found to be about 41 % higher than that of CD. Additionally, the steam turbine output and net powers were found to be higher when the ACC was incorporated with HDWD than when CD was incorporated into ACC.

List of Publication(s)/Conference(s) proceedings

Peer Reviewed Conference Publications

1. Ester Angula, Paul Chisale, Fillemon N Nangolo, Analysis of microchannel delugeable tube bundle thermal performance, *17th International Heat Transfer Conference (IHTC),* 14 - 18 August 2023, Cape Town. https://ihtc17.org/wp-content/uploads/2023/08/IHTC-17-Programme-07.08.2023.pdf
2. Ester Angula, Paul Chisale, Fillemon N Nangolo, Modelling of Cold-end System for a Direct Air-Cooling Generating Unit, *Proceedings 16th International Conference on Heat Transfer, Fluid Mechanics and Thermodynamics (HEFAT)*, 2022, pp 663-669, Virtual conference. https://hefat2022.org/
3. Ester Angula, Paul Chisale, Fillemon N Nangolo, Optimization of Hybrid (Dry/Wet) Dephlegmator Delugeable Second stage Tube Bundle Thermal Performance, *7th International Conference on Mechanical, Manufacturing and Plant Engineering*, 29 November 2021, Kuala Lumpur, Malaysia, Virtual conference.
4. Ester Angula, Paul Chisale, Fillemon N Nangolo, An improved discretized two-dimensional numerical thermal model for flat bare tube condensers application, *Proceedings, 15th International Conference on Heat Transfer, Fluid Mechanics and Thermodynamics (HEFAT),* 2021, pp 241-250, Virtual conference. https://hefat2021.org/
5. Ester Angula, Paul Chisale, Fillemon Nangolo, One-dimensional model for predicting flat bare tube bundle's thermal performance under deluging cooling, *6th International*

Conference on Mechanical, Manufacturing and Plant Engineering, 25 - 26 November 2020. Kuala Lumpur, Malaysia.

Peer Reviewed Journal Publications

1. Ester Angula, Paul Chisale, Fillemon N Nangolo, Optimization of delugeable tube bundle thermal performance for a hybrid dry/wet dephlegmator second stage, *Material Science and Engineering Technology Journal*, 2022 **(Under review)**

Peer Reviewed Book Chapter

1. Ester Angula, Paul Chisale, Fillemon N Nangolo, Thermal performance modelling of a flat bare tube bundle under deluging cooling conditions, *Advances in Science Engineering, Lecture Note in Mechanical Engineering, Springer, Scopus*, 2021, pp102-110. https://www.springerprofessional.de/en/thermal-performance-modelling-of-a-flat-bare-tube-bundle-under-d/19334052

Table of Contents

List of Tables

List of Figures

List of Abbreviations and/or Acronyms

Nomenclature

A	Area	m^2
$\mathbf{c_p}$	Specific heat at constant pressure	$[J/kg\ K]$
$\boldsymbol{C}$	Friction coefficient	[-]
$\boldsymbol{d}$	Diameter of duct	[m]
$\boldsymbol{D}$	Hydraulic Diameter	[m]
$\boldsymbol{e}$	Heat Transfer Effectiveness	[-]
$\boldsymbol{f}$	Friction factor	[-]
$\boldsymbol{G}$	Mass velocity	$[kg/m^2\ s]$
g	Gravitation acceleration	$[m/s^2]$
H	Height	[m]
h	Heat transfer coefficient	$[W/m\ K]$
$\boldsymbol{h_d}$	Mass transfer coefficient	$[kg/m^2\ s]$
$\boldsymbol{i}$	Enthalpy	$[J/kg]$
$\boldsymbol{i_{fg}}$	Latent heat	$[J/kg]$
j	Colburn Factor	[-]
$\boldsymbol{k}$	Thermal conductivity	$[W/mK]$
$\boldsymbol{L}$	Length	[m]
$\boldsymbol{m}$	Mass flow rate	$[kg/s]$
$\boldsymbol{N\ or\ n}$	Number	[-]
$\boldsymbol{P}$	Pitch	[m]
$\boldsymbol{p}$	pressure	$[p_a]$
$\boldsymbol{Q}$	Heat transfer rate	[W]
$\boldsymbol{R}$	Gas constant or resistance	$[J/kgK]$
$\boldsymbol{r_1, r_2, r_3, y_4, r_5}$	Distance	[m]
$\boldsymbol{r}$	Radius	[m]

$\boldsymbol{RH}$	Relative humidity	[%]
$\boldsymbol{t}$	Thickness	[m]
$\boldsymbol{T}$	Temperature	[℃]
$\boldsymbol{U}$	Overall heat transfer coefficient	$[\mathrm{W/m^2K}]$
$\boldsymbol{v}$	Velocity	$[\mathrm{m/s}]$
$\boldsymbol{W}$	Width	[m]
$\boldsymbol{w}$	Humidity ratio	$[\mathrm{kg\ (H_2O)/}$ kg dry air]
$\boldsymbol{x}$	Co-ordinate or distance	[m]
$\boldsymbol{y}$	Co-ordinate or distance	[m]
$\boldsymbol{y_1, y_2, y_3, y_4, y_5}$	Distance	[m]
$\boldsymbol{z}$	Co-ordinate or distance	[m]

Greeks symbols

Δ	Differential	
$\boldsymbol{\delta}$	Distance or thickness	[m]
$\boldsymbol{\mu}$	Dynamic viscosity	[kg/ms]
$\boldsymbol{\rho}$	Density	$[\mathrm{kg/m^3}]$
$\boldsymbol{\phi}$	Relative humidity	[%]
$\boldsymbol{\nu}$	Kinematic viscosity	$[\mathrm{kg/ms}]$
$\boldsymbol{\tau}$	Tangential	
$\boldsymbol{\theta}$	Angle	Degree

Dimensionless groups

$\boldsymbol{Le_f}$	Lewis factor, $h_a/c_{pam}h_d$
$\boldsymbol{NTU}$	Number of transfer units
$\boldsymbol{Nu}$	Nusselt number, hL/k
$\boldsymbol{Pr}$	Prandtl number, $\mu c_p/k$

$\boldsymbol{Re}$	Reynolds number, $\rho v L/\mu$
$\boldsymbol{Sc}$	Schmidt number, ν/D_{AB}
$\boldsymbol{Sh}$	Sherwood number, $h_d L/D_{AB}$
$\boldsymbol{Po}$	Poiseuille Number fRe

Abbreviations

ACC	Air-Cooled Condenser
AR	Aspect Ratio
CD	Conventional Dephlegmator
CDTB	Conventional Delugeable Tube Bundle
CFD	Computational Fluid Dynamics
CHX	Conventional Heat Exchanger
DRTB	Delugeable Round Tube Bundle
HEFAT	Heat Transfer, Fluid Mechanics and Thermodynamics
HDWD	Hybrid (Dry/Wet) Dephlegmator
HDWCS	Hybrid (Dry/Wet) Cooling System
HP	High Pressure
LMTD	Log Mean Temperature Difference
LP	Low Pressure
MDTB	Microchannel Delugeable Tube Bundle
MHX	Microchannel Heat Exchanger
NTU	Number of Transfer Units
TPI	Thermal Performance Index
AMTD	Arithmetic Mean Temperature Difference

Subscripts

$\boldsymbol{a}$	Air
$\boldsymbol{av}$	Air and water mixture
$\boldsymbol{ac}$	Convection heat transfer
$\boldsymbol{am}$	Mass transfer

$\boldsymbol{b}$	Bundle
$\boldsymbol{B}$	Buoyancy or Boiler
$\boldsymbol{BL}$	Boundary Layer
$\boldsymbol{cr}$	Critical
$\boldsymbol{c}$	Condensate or channel
$\boldsymbol{cm}$	Condensate mean
$\boldsymbol{cs}$	Condensate surface
$\boldsymbol{cw}$	Condensate water
$\boldsymbol{d}$	Drainage
$\boldsymbol{w}$	deluge water
$\boldsymbol{wm}$	Deluge water mean
$\boldsymbol{ws}$	Deluge water surface
$\boldsymbol{e}$	Entry or extraction
$\boldsymbol{F}$	Fan
$\boldsymbol{f}$	Flat
$\boldsymbol{fg}$	Fluid gas
$\boldsymbol{fr}$	Frontal
$\boldsymbol{fw}$	Feed water
$\boldsymbol{g}$	Gravity
$\boldsymbol{GN}$	Gnielinski
$\boldsymbol{HP}$	High pressure
$\boldsymbol{h}$	Hydraulic
$\boldsymbol{i}$	Inlet
$\boldsymbol{i,j}$	Grind point index
$\boldsymbol{LP}$	Low pressure
$\boldsymbol{m}$	Mean
$\boldsymbol{ma}$	Air-water vapour mixture
$\boldsymbol{masw}$	Saturated air
$\boldsymbol{mc}$	Microchannel

$\boldsymbol{mw}$	Deluge water mass flow rate
$\boldsymbol{n}$	Normal
$\boldsymbol{o}$	outlet
$\boldsymbol{r}$	Rows or intervals or round
$\boldsymbol{ref}$	Reference
$\boldsymbol{r_1, r_2, r_3, y_4, r_5}$	Location or position
$\boldsymbol{s}$	Surface or steam or static
$\boldsymbol{st}$	Steam
$\boldsymbol{sw}$	Saturated water
$\boldsymbol{T}$	Turbine
$\boldsymbol{t}$	Tube
$\boldsymbol{tr}$	Tube row
$\boldsymbol{y_1, y_2, y_3, y_4, y_5}$	Location or position
$\boldsymbol{va}$	Air velocity
$\boldsymbol{w}$	Wet
$\boldsymbol{wb}$	Wet-bulb
$\boldsymbol{x}$	Co-ordinate
$\boldsymbol{y}$	Co-ordinate
$\boldsymbol{z}$	Co-ordinate

Acknowledgements

I would like to acknowledge the following people for their valuable contributions:

- My God for his wisdom, protection, strength and guidance.
- Prof. Paul Chisale for his guidance and support throughout the study.
- Dr Fillemon N Nangolo for his guidance and support throughout the study.
- University of Namibia, School of Engineering and the Built Environment for funding my study.
- My Husband Mr Festus Fericky Petrus and the entire family for their support.

Dedication

This work is dedicated to the memory of my parents, who couldn’t see its completion.

Declarations

I, Ester Angula, hereby declare that this study is my own work and is a true reflection of my research, and that this work, or any part thereof has not been submitted for a degree at any other institution. No part of this dissertation may be reproduced, stored in any retrieval system, or transmitted in any form, or by means (e.g. electronic, mechanical, photocopying, recording or otherwise) without the prior permission of the author, or The University of Namibia in that behalf. I, Ester Angula, grant The University of Namibia the right to reproduce this thesis in whole or in part, in any manner or format, which The University of Namibia may deem fit.

Ester Angula	___________________	October 2023
Name of Student	**Signature**	**Date**

Chapter 1: Introduction

1.1. Orientation of the study

Despite, rapid growth of the renewable energy resources in power generation industry, the coal-fired power plants still topping in power generation industry. The coal-fired power plants produce 40 % of world's electricity, and South Africa and China generate 94 % and 70 % - 75 %, respectively of their electricity using these plants (Ritchie and Roser, 2020). As indicated in Figure 1.1, the coal-fired power plants operate based on the Rankine Cycle. The heat produced by heat sources (burning fuel) in the boiler is used to generate high-pressure steam at constant rate. This steam, is then expanded in the steam turbine where some of heat energy are extracted by the turbine to produce power. The low-pressure steam leaves the turbine exhaust to a cooling system where the remaining heat energy is rejected to the cooling medium, in order to complete the cycle.

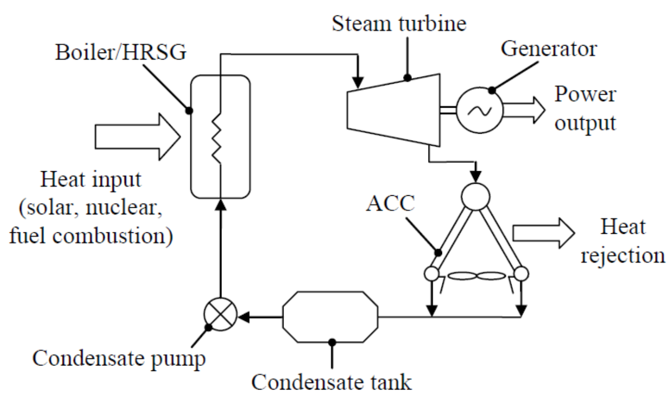

Figure 1. 1: Schematic diagram of a direct air-cooled power plant, source: (Owen, 2013)

In power generation, direct air-cooling system (air-cooled condenser) is considered as an economical and promising technique, because of its water-saving advantages, since the ambient air is used as a cooling medium to condense the exhaust steam (Zhang *et al.*, 2021). Furthermore, due to water usage restrictions and water shortage in arid regions, as well as the limitation of water-cooled condensers usage (Walsh *et al*., 2011), the Air-Cooled Condensers (ACC) applications became extensive. The application of air-cooling systems eliminates more than 90% of a plant's water requirements (Donovan et al, 2012). However, ACCs performance is sensitive to meteorological and ambient air conditions. In addition to that, air has poor heat transfer characteristics and thermodynamic properties. This leads to higher backpressure for generating unit with direct air-cooling system compared to generating unit with water-cooling system (Zhang *et al.,* 2019). Furthermore, ACCs' sensitivity to ambient air conditions, imposed a higher requirement on the control system to attain steady and economic operation of direct air-cooling condenser (Zhang *et al.*, 2021).

Gadhamshetty *et al.* (2006) reported a 10 % reduction in power plant output at high ambient temperatures for plants with ACC. This is due to the fact that, the coal fired power plant energy efficiency mainly depends on the performance of its turbine-condenser system (Laković *et al.*, 2010). In a worse scenario, poor ACC performance can have consequences on emergency shutdowns of the turbine (Owen, 2013). Therefore, during hot periods, a large amount of air is required to be circulated in order for the ACC to provide enough cooling. However, the air-side pressure drop should be minimised, in order to reduce the fan power consumption (Hassani *et al.,* 2005). Additionally, the dephlegmators units at different power plants have shown that, over the range of operating conditions, the dephlegmator units poorly transfer heat. This is mainly due to flooding in the finned tubes (Smit, 2000). Therefore, the demand to increase the ACC performance and their applications flexibility is high (Plessis and Owen, 2020b).

In the attempt to improve the ACC performance, the Hybrid (Dry/Wet) Dephlegmator (HDWD) was found to be one of the reasonable and economically viable performance enhancement measurements of an ACC (Heyns and Kröger, 2012). The HDWD can improve the performance and availability of the ACC during the high ambient temperature, as well as level the power generation rate by lowering fluctuations caused by the ambient conditions, and minimise the water usage. The HDWD is proposed to replace a dry Convectional Dephlegmator (CD) in each “street” of an ACC. The HDWD has two stages connected in series and combined in one condenser unit. The first stage has inclined finned tubes and second stage with a bundle of horizontal bare tubes. The second stage operates in the dry mode, during cold or off-peak periods, and in the wet mode during hot and peak periods.

During the wet operating mode, the most commonly used and economically viable evaporative cooling systems, which can be employed in thermal performance enhancement of ACCs, are deluge and adiabatic cooling systems. During deluge cooling systems, the recirculating deluge water are sprayed over the heat exchangers surface area. Some of the deluge water evaporates in the air stream. This enables both sensible and latent heat transfer from the heat exchanger’s surface. While, during adiabatic cooling systems the fine water droplets are sprayed into the inlet ambient air before it enters the heat exchanger. The evaporation of water results in cooling of the inlet air closer to its wet-bulb temperature. Due to the fact that, in the deluge cooling systems evaporation takes place directly on the tubes surface rather than in the air, the deluge cooling systems was found to have high performance than precooling systems (Charles and David, 2002).

Therefore, the deluge cooling system was considered in this study, for the evaluation of HDWD's second stage tube bundle, when operating in the wet mode.

The HDWD thermal performance is mainly dependent on its second stage tube bundle performance. Therefore, the best tube configuration, as well as the tube's geometric parameters, shape and structure of the second stage should be properly selected and sized. In this study, two bundles comprise of conventional and microchannel bare flat tubes as shown in Figure 1.2 (a, b) were considered, and were incorporated into the second stage of an induced HDWD. Hence, the HDWD's thermal performance was carried out through the performance modelling, optimization, and comparison of Convectional and Microchannel Delugeable Tube Bundles (CDTB and MDTB). Since, the HDWD was proposed to replace the dry CD of an ACC system coupled to a 30 MW steam turbine of a local generating unit, its performance was compared to that of CD.

a) Conventional tube **b) Microchannel tube**

Figure 1. 2: The conventional and microchannel tubes

1.2. Dephlegmator Role in ACC

The ACC of the power plant consists of several "streets", which are made up of primary condenser and dephlegmator units, and which are connected in series, as shown in Figure 1.3. For easier condensate drainage, the units are installed in A or V-frame arrangement. The initial condensation of the steam occurs in the primary condenser units, whereby the axial fans force the ambient air through the finned tube bundles. The uncondensed steam from primary condenser units is further condensed in the dephlegmator units.

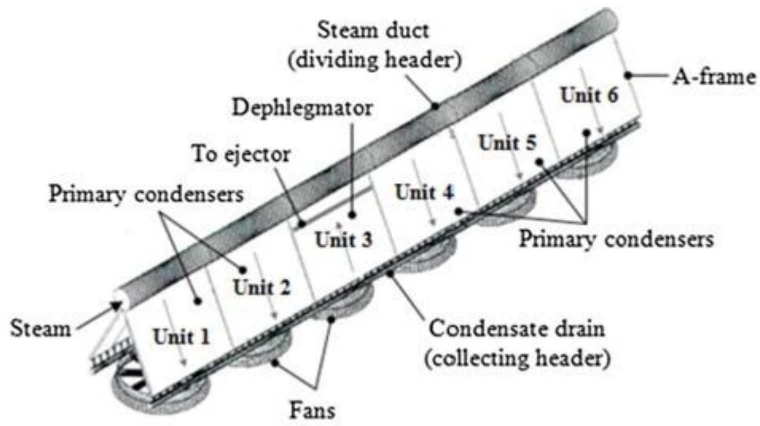

Figure 1. 3: Direct ACSC Street, source: (Owen, 2013)

The condensate is collected in the collecting header to the condensate sump, before it pumped to the boiler drum. The steam flow in the ACC "street" with five primary condenser units and one dephlegmator unit is depicted in Figure 1.4.

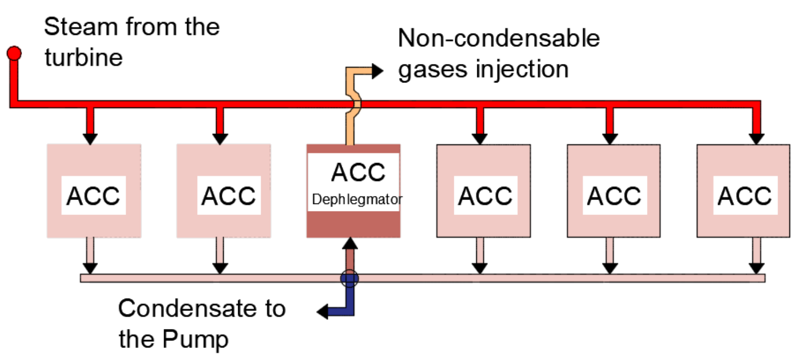

Figure 1. 4: Steam flow in the ACC "street" incorporated with CD

The ACC operates below atmospheric pressure. Therefore, the non-condensable gases leak into the system, and can form dead zone, which results in reduction of tube's heat transfer surface area, and worsens the ACC performance during high ambient air temperatures. Therefore, to avoid this from happening, dephlegmator is essential to eject the non-condensable gases, draw and condensed more steam in order to steady and accelerate the steam flow in the primary condenser units. Thus, performance improvement of the dephlegmator is meaningful, since it will directly lead to the ACC performance enhancement, and sequential of the generating unit.

1.3. The Concept of HDWD

The HDWD can be forced or induced draft as shown in Figure 1.5. The HDWD has two stages connected in series and combined in one condenser unit. To accommodate the second stage tube bundle, the first stage inclined finned tubes are shorter compared to that of CD tubes. The recirculated deluge water sprayed on the surface of the second stage tube bundle, during the wet operating mode is collected in troughs under the tube bundle. The drift eliminator above the tube bundle, traps the water droplets blown up by the air. The tubes of second stage bundle are bare, in order to avoid corrosion and fouling risk during the wet operating mode.

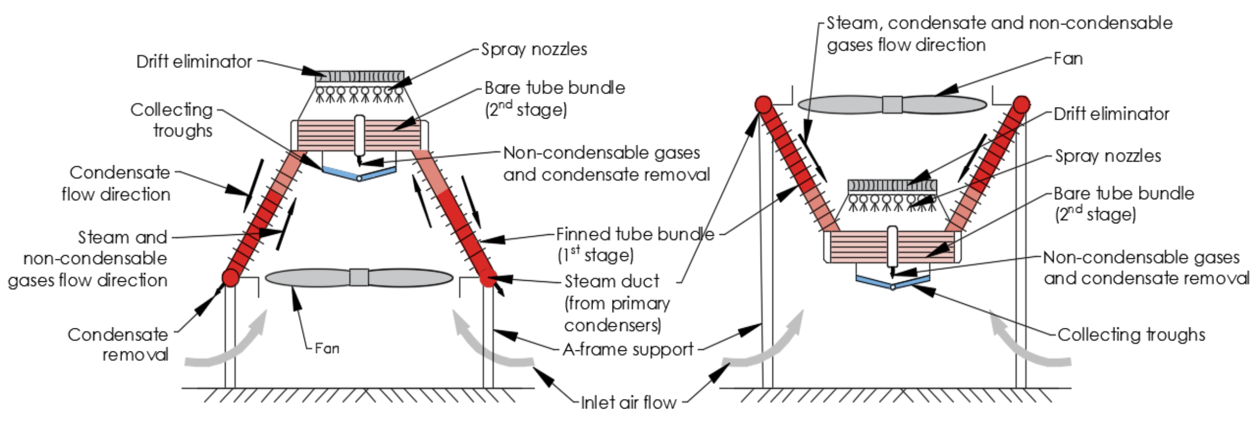

Figure 1. 5: Schematic diagram of the HDWD

The risk of flooding has been reported in the forced HDWD, and therefore its application is limited (Owen, 2013). However, these limitations have been addressed by changing the configuration of the HDWD to induced draft. In the induced draft HDWD the risk of flooding is minimised by co-current flow of condensate and vapour. The steam flow in the ACC ”street” with five primary condenser units and one the HDWD is shown in Figure 1.6.

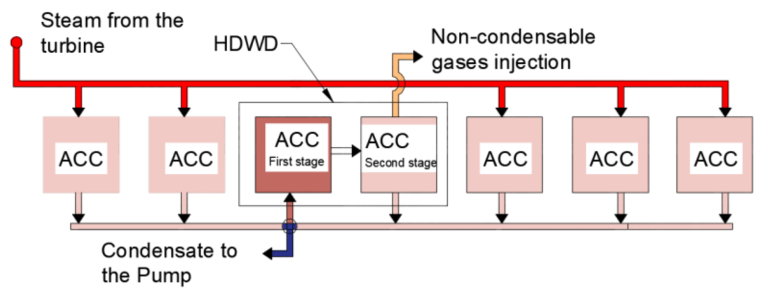

Figure 1. 6: Steam flow in the ACC “street”, incorporated with the HDWD

1.4. Microchannel Fluid Flow and Heat Transfer

The Microchannel Heat Exchanger’s (MHX) development and applications have advanced rapidly in recent years. As the technology is improving, the conventional macro-scale heat exchangers sizes are turned into micro-scale heat exchangers. Experimental results showed that the capacity of conventional macro-scale heat exchangers can be increased by 4% by using MHXs (Zhou *et al.*, 2017).

In addition to that, the MHXs (condensers and evaporators) have been found to yield promising performance (Al-Zaidi *et al.*, 2018). The MHXs consist of microchannel tube bundles which can be finned or unfinned, and can operate under both wet and dry conditions (Xu *et al.*, 2015). Therefore, in MHXs the heat is transferred through multiple tubes which contain small channels with the widths in the range of 10 to 1000 µm (Cheng and Xia, 2017). MHXs have the same working principles as Conventional Heat Exchangers (CHXs), however, the heat transfer processes and fluid flow in macroscale thermal systems, are described using convectional theories which were established based on the study of heat transfer processes and fluid flow macroscopic view. These convectional theories do not take into account most of the micro phenomena that were reported to have impacts on the microchannel heat transfer. Therefore, the study and analysis of the microscale thermal systems are totally different from that of macroscale thermal systems (Lui *et al.*, 2009).

The performance of the MHXs is highly dependent on the geometrical dimensions and choice of working fluid (Ghajar and Darabi, 2014). For the same heat transfer rate and pressure drops, MHX is about one-fifth the size of CHX (Lydia, 2008). The basic factor that drives the applications of MHXs lies in the Nusselt number ($Nu = hD_h/k$), where h is the convective heat transfer coefficient, D_h is the hydraulic diameter of the microchannels, and k is the thermal conductivity of the fluid. Since, the Nusselt number is a function of the convective heat transfer coefficient and channel/duct diameter, it is expected that in order to maintain the Nusselt number value constant, as the channel size decreases, the convective heat transfer coefficient value should increase extremely, leading to the increase of heat transfer.

The heat transfer in microchannel can be either two-phase flow boiling or single-phase heat transfer. The two-phase flow boiling heat transfer in microchannel is one of the most effective resolutions for cooling devices, as well as for other thermal systems (Lui *et al.*, 2009); (Kim and Mudawar, 2012); (Fayyadh, *et al.*, 2015). However, it was reported that the two-phase flow boiling phenomena in microscale channels is not yet well outlined. Furthermore, two-phase flow boiling is not a consistent technique due to back flow and instabilities in the flow (Cheng and Xia, 2017). Moreover, most of the accessible two-phase flow boiling heat transfer phenomena researches in microscale channels are showing inconsistent and conflicting results regardless thousands of theory and experimental studies that have been carried out in last decades (Cheng and Xia, 2017). Therefore, in this study, the single-phase heat transfer in microchannel was considered.

1.5. Statement of the Problem

Due to the scarcity of water in arid regions, and high energy demand, the ACCs became more popular, and the main means of rejecting heat into atmosphere in steam turbine power plants. However, the ACCs experience performance reduction, during hot periods, which affects the overall performance of the steam turbine power plants, and imposed a higher requirement on the control system to attain a steady and economic operation of direct ACC. Since, the energy demand is ever increasing, in order to meet the power demand during the high ambient temperature; the power plants should operate more often than during cold period. This leads to an increase of the labour and operating costs of the plants, burning of fossil fuels and emission of greenhouse gasses.

The replacement of CD with HDWD was found to be an appropriate performance enhancement technique which is cost effective and uses less water during the wet operating mode. However, the HDWD second stage delugeable tube bundle configuration that yields the best thermal performance should be configured. In addition to that, the MHXs or microchannel tube bundles were reported to have higher thermal performance compare to CHXs. However, the literatures lack evidence of modelling of MHXs or microchannel tube bundles, as well as the comparison of the CHXs and MHXs or tube bundles operating under deluging conditions, and with steam as a working fluid. Furthermore, the incorporation of MDTB into the second stage of induced HDWD of ACC is also poorly presented in the literatures.

1.6. Aim of the Research

1.6.1. Main Objective of the Research

The aim of the study was to develop the models that can be employed for predicting the thermal performance of an induced draft HDWD and CD for ACC system coupled to a steam turbine in terms of heat transfer rate and air-side pressure drop.

1.6.2. Specific Objectives of the Research

The objectives were to:

1. Develop a one- and two- dimensional models based on three methods of analysis: Poppe, Merkel and heat and mass transfer analogy to study the thermal performance of CDTB.
2. Identify the best CDTB configuration through optimization and geometric parameter's adjustment.
3. Analyse the thermal performance of HDWD incorporated with CDTB.
4. Investigate the CD thermal performance.
5. Compare the thermal performances of CD and HDWD incorporated with CDTB.
6. Evaluate the MDTB thermal performance.
7. Compare the CDTB and MDTB thermal performances.
8. Carry out the statistical analysis on the tube bundles performance data.

1.7. Hypotheses of the Research

The hypotheses of the study were as follows:

- H_{01} - The thermal performance of HDWD at component, and system levels is not higher than that of CD, with a level of significance of 0.05.
- H_{02} - The thermal performance of MDTB at bundle, component, and system levels is not higher than that of CDTB, with a level of significance of 0.05.
- H_{11} - The thermal performance of HDWD at component, and system levels is higher than that of CD, with a level of significance of 0.05.
- H_{12} - The thermal performance of MDTB at bundle, component, and system levels is higher than that of CDTB, with a level of significance of 0.05.

1.8. Delimitations of the Research

The delimitations of this study were:

1) This research focused on the thermal performance evaluation of induced draft HDWD, and CD of ACC system coupled to 30 MW steam turbine of the generating unit. The induced HDWD thermal performance was investigated, since the forced draft HDWD application is limited due to the possible occurrence of flooding of primary condenser tubes.
2) The input data used in this study were limited to that of the considered generation unit.
3) The deluge cooling system was considered over precooling, since it uses less water and has a higher performance.

4) The delugeable tube bundles consist of flat bare tubes, since the literatures lack the evidence of the thermal performance analysis of the flat tubes under deluging conditions.

1.9. Limitations of the Research

There are several softwares that can be used to model thermal performance of the fluid flow and heat transfer in the tubes, however in this study MathCAD was used to conduct the analysis, since it is available. Only the operating data from 30 MW steam turbine local generating unit, were used in this study, therefore all the findings were based on the operating data for this generating unit.

1.10. Significance of the Research

Literatures in the subject of HDWD have limited data on the accurate way of modelling thermal performance of a CDTB that can be incorporated into the HDWD of ACC system. Moreover, the incorporation of MDTB into the induced HDWD of ACC system, as well as the modelling of MDTB under deluging conditions, and with steam as a working fluid is barely indicated in the accessible literatures. Therefore, this study is expected to have the following contributions to engineering knowledge:

1. The improved modelling of CDTB and MDTB thermal performance under deluging conditions, and with steam as a working fluid.
2. The incorporation of the MDTB into the induced HDWD of ACC system coupled to the steam turbine.
3. The single-outed thermal performance analysis of CD of ACC system coupled to the steam turbine, which is not a case in most available literatures.

1.11. Thesis organization

CHAPTER 1. Introduction: provides the overview of ACC, HDWD as well as MHXs, and highlights the main role of dephlegmator. The problem statement, objectives, hypotheses and significance of the study are also presented in this Chapter.

CHAPTER 2. Literature Review: presents the literature reviews on the thermal performance analysis of the CHXs and tube bundles operating under wet, air-side and working fluid-side characteristics of the MHXs, as well as the ACC thermal performance evaluation. The research gaps are also presented in this Chapter.

CHAPTER 3. Models Development for Conventional Delugeable Tube Bundle Thermal Performance Analysis: presents the development of a one- and two-dimensional models, the solution methods employed in the evaluation and validation of the models.

CHAPTER 4. Design Optimization of Conventional Delugeable Tube Bundle Thermal Performance: details the design optimization and geometric parameters adjustment of the CDTB.

CHAPTER 5. Analysis of Conventional Dephlegmator Thermal Performance: provides the development and validation of a mathematical model of a direct air-cooling generating unit's cold-end system coupled to 30 MW steam turbine. The sensitivity of the ACC performance to the high ambient air temperature, and the fan rotational speed, as well as the outlining of the CD thermal performance are also presented in this Chapter.

CHAPTER 6. Analysis of Thermal Performance for HDWD incorporated with Conventional Delugeable Tube Bundle: provides the thermal performance analysis of the CDTB, as well as of the HDWD incorporated with CDTB into its second stage. The Chapter also offers the comparison of thermal performance of the CD and HDWD incorporated with CDTB.

CHAPTER 7. Analysis of Microchannel Delugeable Tube Bundle Thermal Performance: presents the performance analysis of the MDTB, as well as of the HDWD incorporated with MDTB into its second stage. The Chapter also offers the comparison of thermal performances of the CDTB and MDTB.

CHAPTER 8. Results and discussions: presents the results for the thermal performance evaluations of CD, HDWD, CDTB and MDTB at all levels, as well as their performance comparisons. In addition to that, the analyses, scrutinization, and discussions of the results are also included in this Chapter.

CHAPTER 9. Statistical Analysis of Performance Data: offers the statistical analysis of the performance data of CDTB and MDTB at all levels, and testing of hypotheses.

CHAPTER 10. Conclusion and Recommendations: provides the conclusions and recommendations of the study.

Chapter 2: Literature Review

This chapter provides the summary of the literature reviews on the thermal performance analysis of both CHXs and MHXs or tube bundles operating under wet conditions. In addition to that, the literatures on the working fluid-side performance characteristics of the MHXs, are also included in the Chapter. Furthermore, the literatures on the ACC thermal performance, in which the CD is incorporated are also outlined in this Chapter.

2.1. Conventional Heat Exchangers/Tube Bundles Operating Under Wet Mode

2.1.1. HDWD Thermal Performance Evaluation

Several studies have been carried out in an attempt to identify a configuration of the HDWD second stage's tube bundle that provides higher performance.

Heyns (2008) analytically modelled one-dimensional flow delugeable round bare tube bundle for a forced HDWD second stage, based on simplified Merkel analysis. The model was validated by experiment results, and a good correlation was found between the analytical model and experimental results.

Heyns and Kröger (2012) incorporated Heyns (2008)'s tube bundle in their study in which the output power of the steam turbine cooled by ACC incorporating the HDWD, ACC with pre-cooling of inlet air, and over-sized ACC by 33% were compared. Authors reported that during the hot ambient conditions, all considered ACCs performed the same. However, the water consumption of the HDWD was around 20% less water than for the pre-cooling technology, and the cost difference between the HDWD and the convectional dephlegmator is small. Therefore, it is reasonable to employ the HDWD as a performance enhancement measurement of an ACC.

Owen (2013) investigated the steam-side operation of an air-cooled steam condenser using a combination of Computational Fluid Dynamics (CFD), numerical, analytical and experimental methods. Furthermore, Owen (2013) compared the HDWD and CD performance, on a component level (for the whole dephlegmator) and on a system level (for the whole ACC). On a component level, the performance of HDWD was found to be two to three times that of the CD when operated in wet mode, while on a system level, the ACC's heat transfer rate with five primary condensers and one HDWD was 15 % -30 % higher than for a similar ACC with CD.

Angula (2015) investigated the performance a delugeable flat bare tube bundle for the induced draft HDWD. Both one-dimensional analytical and two-dimensional numerical models were employed in the analysis. The analytical model was based on Merkel, Poppe, and heat and mass transfer analogy, while the numerical model was based on heat and mass transfer method of analysis only. However, the modelling was performed under an assumption that the tube has a flat end not round. The tube bundle was found to deliver higher performance during wet operating conditions than during dry operating conditions.

Reuter and Anderson (2016) employed Anderson (2014)'s experimental data for induced draft HDWD performance of dry ACC systems. Based on those experimental data, Authors derived the correlations of mass transfer, heat transfer and air-side pressure loss coefficient for the round bare tube bundle under wet and dry operation conditions.

All correlations were functions of the air mass velocity, the deluge water flow rate and mean deluge water temperature.

Graaff (2017) investigated the performance of a Hybrid (Dry/Wet) Cooling System (HDWCS) by using the correlations of Anderson (2014) and Mizushina *et al.,* (1967). At different air relative humidity and an ambient dry bulb temperature of 32 ºC, the HDWCS' performance was found to be between 35 % and 140 % relative to a conventional cooling system.

Plessis and Owen (2020a) experimentally measured the partial and full condensation steam pressure drop inside a circular horizontal tubes of a single-stage HDWD for ACC system. During the test, the horizontal primary condenser units, with tube length of 2.5 m and an inside tube diameter of 19.3 mm, and similar to the proposed single-stage HDWD was used. The steam flow and steam pressure drop were measured, and compared to existing correlations for pressure drop. A mean error of ±15.6% was found between the experimental results and Lockhart and Martinelli correlation.

Plessis and Owen (2020b) experimentally investigated steady-state air-side pressure drop of a delugeable bare round tube bundle of 19 mm and 25 mm diameters of a single-stage HDWD for ACC system. The experiment was carried out for both dry and wet operating modes. The empirical correlations for both dry and wet operating modes were developed using experiment results. The absolute average error between the measured and predicted values for the dry and wet correlations were found to be of 3.2 % and 4.5 %, respectively. These empirical correlations were used to study the under- and overprediction effects of air-side pressure drops on the two small evaporative coolers thermal case study which correspond to fan power consumptions of 1.1 kW and 5.5 kW.

Plessis (2021) developed and validated a discretised model of a single-stage HDWD to be incorporated into a model of a hybrid ACC coupled to a 238 MW steam turbine. During the study the steam-side and air-side pressure drops were experimentally investigated , and the findings achieved were reported in Plessis and Owen (2020a) and Plessis and Owen (2020b), respectively.

2.1.2. Evaporative Heat Exchangers Thermal Performance

The HDWD operates as an evaporatively cooled condenser during the wet operating mode. The tube bundle's surfaces are deluged with water, and the axial fan drawn the air through the bundle, which results on steam condensation inside the tubes. Therefore, the knowledge of the studies in which the analysis of thermal performance of evaporatively cooled condensers/coolers were carried out is worthwhile.

Jahangeer *et al.* (2011) numerically analysed the effect of deluge water film thickness and air velocity on the tube-side, water and overall heat transfer coefficient in the cross-flow plain round tube evaporative-cooled condenser performance for air-conditioning applications. As the film thickness increased from 0.075 to 0.15 mm, the heat transfer coefficients were found to decrease as the air velocity increased from 1 to 4 *m/s*, tube-side and the overall heat transfer coefficient increased from 29000 to 33000 W/m^2K and 330 to 800 W/m^2K, respectively.

Zhang *et al.* (2014 a) experimentally and numerically studied the thermal performance evaluation of cross-flow evaporative mist precooling; deluging cooling and the combination of the two cooling systems on the louver fin flat tube heat exchanger. The deluge water mass flow rate and air velocity effects on the heat exchanger capacity, water drainage behaviour and air-side pressure drop were examined. As the water mass flow rate and air velocity increased, both heat exchanger capacity and air-side pressure drop increased. At 0.2 $g/s\ m^2$ and 1 $g/s\ m^2$ water mass flux, 70 % and 30 % of the water, respectively evaporated

Fiorentino and Starace (2017a) presented an evaporative condensers performance analysis test rig. The experiments were carried out to investigate the dry bulb temperature and relative humidity effects on the system performance. As both the relative humidity and the dry bulb temperature increased, the heat transfer rate was found to decrease. This is due to fact that, the evaporative condenser capacity was found to be proportional to the temperature difference between condensing and wet bulb temperatures.

Fiorentino and Starace (2017b) experimentally analysed the overall performance of the counter current evaporative condensers. During the tests, the air temperature and relative humidity were controlled and set at different values, and a relationship between air dry bulb temperature and relative humidity at the exit of the condenser was established. Furthermore, the water flow rate effect on the cooling capacity was assessed. A maximum deviation lower than 2.5 % and 4 % between the experimental and predicted data of air temperature and relative humidity, respectively were achieved. An increase of 50 % of the sprayed water resulted in an increase of 14 % of the performance.

Jaafarian and Kazemian (2017) mathematically modelled the two-stage evaporative cooling system. The model was validated against the experimental data from the literatures. The effects of air temperature and humidity on the system performance were assessed using the validated model. At different inlet air relative humidity, the outlet air temperature was found to significantly increase with inlet air temperature. At different inlet air temperatures, as the outlet air temperature decreased, the evaporative pad efficiency and overall heat transfer coefficient of heat exchanger increased.

Yang *et al.* (2020) experimentally investigated a refrigeration unit performance by incorporating a spray evaporative cooling system to an air-cooled unit. Without including the spray cooling system energy consumption, the average coefficient of performance of the unit was increased by 3.78 % – 8.33 %.

2.2. Microchannel Heat Exchangers

2.2.1. Air-side Performance Characteristics Analysis Under Wet Operating Mode

Kim and Bullard (2000) performed an experimental study for the brazed aluminium louvered fin cross-flow MHX air-side thermal-hydraulic under dehumidified conditions, and for residential air conditioning systems. The heat transfer and pressure drop characteristics for wet surface were analysed, and water was used as a working fluid. The test was performed for air-side Reynolds number, tube-side water flow rate, dry-bulb temperature, wet-bulb temperature and inlet water temperature of 80 - 300, 320 kg/h, 27 °C, 19 °C and 6 °C, respectively. The analysis was conducted employing effectiveness-NTU method, and the j- and friction factors for wet surface heat exchanger were compared to the dry one. At low Reynolds number, the sensible heat transfer coefficient and pressure drops for the wet surface were found to be smaller and larger, respectively than that of the same dry heat exchanger surface. This is due to the fact that, condensation of water on surface built a film that acts as thermal resistance, and decrease the air flow path between the fins. Furthermore, at smaller louver angles, the pressure drops were found to be higher.

Chen *et al.* (2013) conducted an experimental analysis on the heat transfer performance of a finned flat aluminium tube MHX with spray cooling. The water spraying conditions, air flow rate, and relative humidity effects on the heat transfer were investigated. Authors found that at lower water spraying rate the heat transfer performance increased. However, at high spraying rate the part of the non-evaporated drops attached to the fin surface form a liquid film, which blocks the flow passage. Nevertheless, in general the water spray can improve the air-side heat transfer performance significantly.

Huang *et al.* (2015) developed finite-volume for an air-to- fin heat and mass transfer model with heat conduction of tube-to-tube, for a variable geometry MHX operating under dry, wet (dehumidified), and partially wet conditions using the fin analysis method. The model was developed for evaporators and condensers, and was verified by using the results from CFD package simulation and validated against the experiment data. Authors reported that, the predicted capacity deviated from measured values by 2.44 % and 2.92 % for condensers and evaporators, respectively.

Xu *et al.* (2015) carried out the experimental study of the finned horizontal flat tube MHX with rectangular ports for refrigeration system applications, under wet (dehumidified) and frosting conditions. Three samples with louver fins, wavy fin and wavy fin with drainage design were considered. It was found that, when the air velocity is 1 m/s the capacities of samples with wavy fin and wavy fin with drainage design were 25.8 % and 56.7 %, respectively higher than that of sample with louver fins, while the air-side pressure drops were 35 % and 63 % lower than that of sample with louver fins. Authors concluded that, these results were due to the factor that, some the droplets remained in the fins trough obstructed air flow and increased heat transfer resistance. Similar conclusion was made by Kim and Bullard (2000) and Korte and Jacobi (2001) that under wet conditions, as fin pitch decreases, the retention of condensate increases, and as a result the heat transfer performance decreases and friction increases.

Zou *et al.* (2016) modelled the thermal performance of A-shaped round tube plate fin evaporator and louver finned flat tube microchannel evaporator with 26 rectangular ports under wet (dehumidified) air conditions for residential air-conditioning system. A refrigerant was used as a working fluid. Both uniform and maldistribution of refrigerant among parallel microchannel tubes were investigated and dehumidified air condition was simulated based on the total enthalpy and heat and mass transfer method. The simulated results of these two methods were close and within ±10 % of the measured capacity, and the heat and mass transfer method were found to be easier to use. The refrigerant maldistribution was found to reduce the capacity by 5 % compared to uniform distribution.

Srisomba *et al.* (2017) conducted an experimental research on the effects of inlet relative humidity, air frontal velocity, air inlet temperature, and refrigerant (R134a) temperature on air-side performance of multi-louvered finned flat tube aluminium MHX with 14 channels under the wet conditions (dehumidified). The relative air humidity, air inlet temperature, refrigerant-saturated temperatures and Reynolds numbers in the ranges of 45 % to 80 %, 27 to 33 ℃, 18 to 22 ℃ and 128 to 166, respectively were considered. It was reported that, as the inlet relative humidity, air frontal velocity, air inlet temperature increased, the average heat transfer rate and air-side pressure drop increases too. However, at constant air frontal velocity, the effect of the air temperature on air-side pressure drop was insignificant.

2.2.2. Working fluid-side Performance Characteristics Analysis

The analysis of the working fluid-side performance characteristics of the MHXs have been performed by several researchers. This includes, the condensation flow and heat transfer modelling, and geometry effects of the microchannel.

The hydraulic diameter and aspect ratio have a significant effect on the fluid flow and heat transfer characteristics in a microchannel. Several researches investigated the effect of geometrical parameters of the channel; however most of them achieved contradictory conclusions. This is due to the fact, that they have been varying the height of the channel for a constant channel width or the other way around, which means that the hydraulic diameter and Aspect Ratio (AR) are changing at same time (Sahar *et al.*, 2017). As a result, the importance of the hydraulic diameter and aspect ratio were not outlined clearly. The substantial laminar to turbulent flow transition were also reported in numerous studies, in which single phase flow and heat transfer in microchannels were analysed.

Peng and Peterson (1996) investigated the rectangular microchannel (hydraulic diameter in the range of 0.155 mm - 0.747 mm) size effect on single phase flow and heat transfer characteristics using water and methanol as working fluids. Authors reported that, laminar to turbulent flow transition starts at Reynolds number (Re) = 300, and fully developed turbulent flow regime starts at Re = 1000.

Pfund *et al.* (2000) experimentally studied the pressure drop across a microchannel with hydraulic diameter in the range of 0.025 mm - 0.19 mm, using water as a working fluid. The laminar to turbulent flow transition was reported to start at Re in the range of 1500 – 2200.

Xu *et al.* (2000) investigated a single-phase pressure drop in silicon and aluminium microchannels (hydraulic diameter in the range of 0.03 mm - 0.344 mm) using water as a working fluid. The laminar to turbulent flow transition was reported to start at Re = 1500.

Gao *et al.* (2002) experimentally studied a single-phase flow of water in rectangular silicon wafer microchannels heat sink with a channel height range, a fixed width, aspect ratio range and hydraulic diameter range of 0.1 mm - 1 mm, 25 mm, 0.003 mm - 0.04 mm and 0.008 mm - 0.077 mm, respectively. It was found that, for a channel height less than 0.4 mm, the decreasing of channel height resulted in decreasing of Nusselt number. However, the plotted results of heat transfer coefficient vs channel height showed that as the channel height decreased, the heat transfer coefficient increased. Furthermore, the laminar to turbulent flow transition was reported to start at Re in the range of 3500 – 4000.

Gunnasegaran *et al.* (2010) conducted a numerical study on the effect of shape of the channel on water flow and heat transfer in multi-microchannel heat sink for the Reynolds number in the range of 100 -1000. The geometrical shapes considered in the study were rectangular, trapezoidal and triangular, and hydraulic diameter and aspect ratio range of 0.259 mm - 0.385 mm and 1.03-2.56, respectively were considered. Authors found that, the rectangular channel with the smallest hydraulic diameter has the highest heat transfer coefficient and Poiseuille number compared to the other geometries.

El Mghaira *et al.* (2014) conducted a steam condensation numerical investigation in a non-circular microchannel. The investigation was carried out for both single- and two-phases, and for several microchannel hydraulic diameters, microchannels shapes, aspect ratios, inlet vapor mass fluxes and contact angles. Furthermore, different correlations well-known for determining the condensation flow heat transfer were analysed. It was found that, for constant mass flux, as the hydraulic diameter of microchannel decreased from 250 mm to 80 mm, the condensate film thickness reduced and the average heat transfer coefficient increases up to 39%. For rectangular microchannels, the condensation average heat transfer was found to increase with aspect ratio. For the square microchannel, the average Nusselt numbers was lower than that for triangular and rectangular microchannels. Additionally, Shah and London (1978) correlation was recommended to be used to evaluate condensate heat transfer coefficient in microchannels.

Zhang *et al.* (2014 b) experimentally investigated the hydraulic diameter and aspect ratio effects on fluid flow and heat transfer of water in aluminium multiport microchannel flat tubes. The hydraulic diameter was varied in the range of 0.48 mm to 0.84 mm for nearly constant aspect ratio (AR = 0.83 - 0.88), and the aspect ratio was varied in the range of 0.45 to 0.88 for nearly constant hydraulic diameter (D_h = 0.6 mm - 0.63 mm). The range of relative roughness and Reynolds number considered was from 0.29 % to 1.06 % and from 120 to 3750, respectively. The aspect ratio was reported to have an insignificant effect on heat transfer rate; however, the effect of surface roughness and the entry region have substantial effect on the heat transfer enhancements. Furthermore, the laminar to turbulent flow transition was reported to start at Re range of 1200 –1600.

Moharana and Khandekar (2015) carried out a numerical study of axial wall heat conduction in rectangular microchannels for developing flow using water at Re = 100. The aspect ratio and hydraulic diameter of the channel were varied from 0.45 to 4.0 and 0.16 mm to 0.203 mm, respectively, with a boundary condition of constant heat flux. Up to AR = 2, the average Nusselt number was found to decrease with increase of aspect ratio, then for constant cross-sectional area and heating perimeter of the channel, the Nusselt number began to increase with aspect ratio.

Wang *et al.* (2016) conducted similar study as that of Zhang *et al.* (2014 b) however, the hydraulic diameter and aspect ratio were in the range of 0.172 mm to 0.406 mm and 1.03 to 20.33, respectively. They concluded that the rectangular geometry attained the best performance, as well as a lowest thermal resistance compared to the other geometries. Furthermore, authors found that as Reynolds number and aspect ratio increased the pressure drop increased too, which results in high pumping power consumption. Therefore, authors suggested that to improve performance, a smaller hydraulic diameter should be combined with a larger wetted perimeter and convective heat exchange area.

Doan *et al.* (2017) conducted a 3D numerical simulation on phase change of steam and effect of gravity on condensation profile in a microchannel counter flow surface condenser with water as a coolant. The $k - \omega$ SST (Shear Stress Transport) turbulence model was used to account for the turbulence effects on the fluid flow and heat transfer in a condenser. The microchannel condenser consists of 10 square channels with hydraulic diameter of 500 μm. It was found that, the temperature of condensed water is a function of the steam mass flow rate as it was varied from 0.01 *g/s* to 0.1 *g/s*, and the gravitational force has insignificant effect on the condensation profile.

Sahar *et al.* (2017) performed a numerical study on hydraulic diameter and aspect ratio effect on water single-phase steady flow and heat transfer in a rectangular microchannel heat sink. For constant aspect ratio at 1, the hydraulic diameter was varied from 0.1 mm to 1 mm, while for constant hydraulic diameter at 0.56 mm, the aspect ratio was varied from 0.39 to 10. Authors used Ahmad and Hassan (2010), and Galvis *et al.* (2012) correlations to validated their model. They found that, up to AR = 2, the friction factor decreased with increasing of aspect ratio, then after that it started increasing with aspect ratio. However, no significant effect of aspect ratio on the heat transfer was found. Furthermore, it was concluded that, as the hydraulic diameter increased the friction factor and average Nusselt number increased too. Moreover, the laminar to turbulent flow transition was reported to start at Re = 2000, and the numerical results were in good agreement with both Ahmad and Hassan (2010), and Galvis *et al.* (2012) correlations.

Wang *et al.* (2018) developed the theoretical film, annular flow regime, condensation heat transfer model for the refrigerant flows inside the oval-shaped microchannels. The surface tension, disjoining pressure, interfacial shear stress and inter- facial thermal resistance effects were considered during modelling. The study was carried out for two refrigerants, R134a and R1234ze(E), and for the range of 300–1500 kg/(m^2 s) of mass fluxes. The model was validated against the correlations in the literatures. Due to higher liquid conductivity of R134a, the circumferential mean heat transfer coefficient for R134a was found to be slightly higher than that of R1234ze(E).

Ali *et al.* (2019) numerically investigated the surface roughness effect on the counter flow MHX performance for hydraulic diameters value of 20 μm, 50 μm, 110 μm, 150 μm and using water as a working fluid. The findings showed that, as the surface roughness increased, the pressure drop increased, and as the hydraulic diameter increased, the pressure drop decreased.

Fung and Majnis (2019) used Computational Fluid Dynamics simulation to analyse the microchannel geometry effects on the heat transfer between refrigerant flow and air flow in segmental rectangular and circular MHX (R134a condenser). The rectangular and circular MHX performance were compared in terms of effectiveness, pressure drop and performance index. The heat exchanger effectiveness, pressure drops and performance index were found to be higher for circular than that of rectangular.

Li *et al.* (2020) experimentally and numerically analysed the condensation flow and heat transfer performance of the R22 in a mini-channels of Printed Circuit Heat Exchanger hot side. The experimental analysis was conducted for inlet pressures, mass flux, and inlet temperatures ranges of 0.5 MPa to 0.65 MPa, 10.52 kg m^{-2} s^{-1} to 109.42 kg m^{-2} s^{-1}, and 273 K to 289 K, respectively. The numerical model was validated against the experiment. The results showed that, as the mass flux increased the pressure drop, heat transfer coefficient and Nusselt number increased. Furthermore, the Nusselt numbers were found high at lower pressure values.

Abdel-Baky *et al.* (2020) investigated the use of microchannel condenser as a performance improvement measurement of an air conditioning unit. Two R-22 air conditioning units with cooling capacities of 3516 W and 5274 W were used during the study. It was found that, the energy efficiency ratio of the microchannel condenser increased by 4.3:11.3 % and 9.5:29 % for the first and second units, respectively, when compared to traditional round finned tube condenser unit. This was reflected on the device total efficiency and energy cost reduction. Furthermore, the convective heat transfer coefficient was enhanced by 61.6:84.1 %.

Başaran and Yurddaş (2021) modelled and designed the thermal performance microchannel condenser for refrigeration applications with isobutane (refrigerant R600a) as a working fluid. The model makes used of the existing correlations in the literatures for predicting refrigerant heat transfer and pressure drop flow inside the microchannel. The numerical model was validated using the experimental results. Furthermore, the model was used to investigate the hydraulic diameter of microchannels and pass arrangement effects on heat transfer performance. Both heat transfer coefficient and pressure drops were found to increase as the hydraulic diameter decreased.

2.2.3. Hydrodynamic entry length correlations

The entry length is defined as the length from the channel entrance to the position at which the velocity achieves 99% of its fully developed value (Sahar *et al.*, 2017). Several studies, in which the entry length in the microchannel was determined, have been conducted. However, the correlations, for defining the hydrodynamic entry length in microchannels, are limited in the literatures. Some of the available correlations are from Ahmad and Hassan (2010) and Galvis *et al.* (2012).

Ahmad and Hassan (2010) experimentally investigated the hydrodynamics in the entrance region of square microchannels with hydraulic diameter of 0.5 mm, 0.2 mm and 0.1 mm, using microparticle image velocimetry. They proposed the correlation in Eq. (2.1) and concluded that, for Re > 10, the channel size effect on the entrance length was insignificant, and therefore, the dimensionless entry length (L_e/D_h) depends only on Reynold number (Re).

$$\frac{L_e}{D_h} = \frac{0.60}{0.14Re + 1} + 0.0752\mathrm{Re} \tag{2.1}$$

Galvis *et al.* (2012) numerically investigated the aspect ratio and hydraulic diameter effects on the hydrodynamic entrance length in rectangular microchannels of hydraulic diameter between 0.1 mm and 0.5 mm, and aspect ratio between 1 and 5. They found that, for *Re* > 50 the effect of channel aspect ratio on the dimensionless entrance length is insignificant. Furthermore, they proposed correlations for rectangular microchannels with 1 < *AR* < 5 and for *Re* < 50, as presented in Eq. (2.2) to (2.5).

$$\frac{L_e}{D_h} = \frac{0.740}{0.09Re + 1} + 0.0889\mathrm{Re}; \qquad \mathrm{AR} = 1.0 \tag{2.2}$$

$$\frac{L_e}{D_h} = \frac{0.715}{0.115Re + 1} + 0.0825\mathrm{Re}; \qquad \mathrm{AR} = 1.25 \tag{2.3}$$

$$\frac{L_e}{D_h} = \frac{1}{0.098Re + 1} + 0.989\mathrm{Re}; \quad \mathrm{AR} = 2.50 \tag{2.4}$$

$$\frac{L_e}{D_h} = \frac{1.1471}{0.034Re + 1} + 0.081\mathrm{Re}; \quad \mathrm{AR} = 5.0 \tag{2.5}$$

2.2.4. Heat Transfer and Friction Factor Correlations for Single-Phase Flow Heat Transfer

Due to wide practical applications in highly specialized fields of heat transfer and fluid flow in microchannels, several studies have been conducted in single-phase flows. The correlations developed for single-phase steam flow inside microchannel are relatively limited in the literatures. Thus, the well-known heat transfer correlations of Dittus and Boelter (1930) and Gnielinski (1976) for macrochannel/ conventional tubes/ mini-channel were used in Ducoulombier *et al.* (2011); Sahar *et al.* (2016); and Başaran and Yurddaş (2021) studies. However, Gnielinski (1976)'s correlation (Eq. (2.6) establishes good agreements with experimental data for the microchannel (Ducoulombier *et al.*, 2011); (Derby *et al.*, 2012); and (Sahar *et al.*, 2016).

$$Nu_{GN} = \frac{\left(\frac{f}{8}\right)(Re - 1000)Pr}{1 + 12.7\left(\frac{f}{8}\right)^{\frac{1}{2}}\left(Pr^{\frac{2}{3}} - 1\right)} \qquad \text{for } (2300 < \mathrm{Re} < 10^6) \tag{2.6}$$

$$\mathrm{Nu_{GN}} = 4.36 \quad \text{for } (\mathrm{Re} < 2300)$$

where *f* is a friction factor that can be evaluated using (Filonenko, 1954) correlation as:

$$f = (1.82\log(Re) - 1.64)^{-2} \tag{2.7}$$

Another correlation that is closer to that of Gnielinski (1976) is Adams *et al.* (1997). This correlation was proposed based on experimental data, and for Nusselt number for small diameter tubes.

$$\mathrm{Nu_{GN}} = \mathrm{Nu_{GN}}(1 + \varphi)$$

$$\varphi = 7.6 \times 10^{-5}\mathrm{Re}\left(1 - \left(\frac{D_h}{1.164 \times 10^{-3}}\right)^2\right) \tag{2.8}$$

Derby *et al.* (2012) conducted a comparison study of single-phase heat transfer coefficients of R134a in square, triangular, and semi-circular channel geometries with constant hydraulic diameter of 1 mm. The Nusselt numbers attained by experiments and Gnielinski (1976) correlation for different cross-sectional microchannels showed a good agreement.

Martı’nez-Ballester *et al.* (2013) developed a model for air-to-refrigerant microchannel condensers and gas coolers, which was validated using experimental data. On the refrigerant-side, they employed Gnielinski (1976) and Churchill (1977) correlation (Eq. (2.9)) to predict heat transfer coefficient and friction factor respectively for single-phase flow. For the condenser, the model results concur well with experimental, and errors were within an error band of +-5 %.

$$f = 8\left(\left(\frac{8}{Re}\right)^{12} + \left(\left(2.457ln\left(\frac{1}{\left(\frac{7}{Re}\right)^{0.9} + 0.27e}\right)\right)^{16} + \left(\frac{37530}{Re}\right)^{16}\right)^{-3/2}\right)^{1/12} \quad (2.9)$$

Xing *et al.* (2013) proposed a simplified and an approximate correlation for Poiseuille number (P_o) which expressed as:

$$Po = fRe = \frac{24}{(1+\alpha)^2(1-0.6274\alpha)} \quad (2.10)$$

where α is aspect ratio.

Yin *et al.* (2015) used both Gnielinski (1976) and Churchill (1977) correlations in their work, in which the finite-volume-based numerical condenser model was developed and validated experimentally. They reported that, Churchill (1977) correlation was verified to be able to determine the single-phase friction pressure drop, for the flow from laminar to turbulent regimes.

Sahar *et al.* (2017) validated the friction factor and Nusselt number results obtained from the numerical model, against the experimental data of Ozdemir *et al.*, (2015) as well as against Shah and London (1978) for fully developed, Eq. (2.11) and developing flow, Eq. (2.12), and Bejan (2004), Eq. (2.13) for developing laminar flow correlation's data. They reported that, the numerical results concur very well with the experimental and correlations data. However, the results by Bejan (2004) were higher.

$$Nu = 1.953\left(\frac{RePrD_h}{L}\right); \qquad for\ \left(\frac{RePrD_h}{L}\right) \geq 33.3 \quad (2.11)$$

$$Nu = 4.364 + 0.0722\left(\frac{RePrD_h}{L}\right); \qquad for\ \left(\frac{RePrD_h}{L}\right) \leq 33.3 \tag{2.12}$$

$$Nu = 1.5\left(\frac{L}{RePrD_h}\right)^{-0.5} \tag{2.13}$$

Al-Zaidi *et al.* (2018) experimentally studied the refrigerant mass flux, local vapor quality, coolant flow rate and inlet coolant temperature effects on the local condensation heat transfer coefficient. For single-phase analysis, they compared the friction factor and Nusselt number to that of Shah and London (1978), Eq. (2.14); Peng and Peterson (1996), Eq. (2.15); and Bejan (2004), Eq. (2.13), and reported a good agreement between experimental results and correlation data.

$$f = \frac{24(1 - 1.355\alpha + 1.946\beta^2 - 1.7012\beta^3 + 0.9564\beta^4 - 0.2537\beta^5)}{Re} \tag{2.14}$$

$$Nu = 0.1165\left(\frac{D_h}{W_c}\right)\left(\frac{H_c}{W_c}\right)Re^{0.62}Pr^{1/3} \tag{2.15}$$

Ren *et al.* (2020) also employed Shah and London (1978) correlation, Eq. (2.14) in their study, in which the counter-flow MHX performance was analysed. In this study, the log mean temperature difference method in conjunction with iteration process were adopted to define the heat transfer rate from both fluids, as well as the outlet temperatures for both considered fluids. In comparison to conventional heat exchanger, the overall heat transfer coefficient of the considered MHX, was found to be much higher. The pressure drops of 0.202 kPa and 1.884 kPa were obtained for liquid water and air, respectively.

Hsieh *et al.* (2021) experimentally investigated the convective heat transfer coefficient and friction factor for single phase roughened rectangular microchannels. The friction factor results were compared to that of Shah and London (1978), Eq. (2.14), and good agreement was achieved.

2.3. ACCs performance

Smit (2000) experimentally investigated the factors that affect the effective operation of the dephlegmator units of ACC in different power plants. Furthermore, they proposed the dephlegmator with a horizontal arrangement. The main factor that leads to ineffective performance of the dephlegmator was found to be flooding in the finned tubes. Moreover, for the proposed horizontal arranged dephlegmator, no flooding was found during the experiment at both zero and some angles to horizontal.

Putman and Harpster (2000) scrutinized how the costs of the chemicals used for the dissolved oxygen concentration in both the condensate and feedwater can be evaluated. Furthermore, they proposed some approaches that can control the backpressure of the condenser, which can affect the economic operation of a turbo-generator unit. The fluctuations of the condenser backpressure were found to affect both Rankine Cycle thermodynamics relationships and dissolved oxygen level in the condensate. As a result, to compensate the dissolved oxygen level, the chemicals (such as hydrazine) were added into the condensate returned to the boiler. However, proper measurements to control the condenser back pressure can offset the cost of the chemicals used for the dissolved oxygen concentration.

Honing (2009) examined the effect of steam-side and air-side characteristics on the performance of the ACC, distribution of steam and critical length of the dephlegmator in power plants. The investigation was conducted for both single and two-row condensers.

For both row condenser, the tube inlet loss coefficient was found to have the major effect on the critical length of the dephlegmator tubes. Furthermore, performance of the ACC, distribution of steam and critical length of the dephlegmator were affected by ambient conditions.

Laković *et al.* (2010) analysed the impact of the cooling water temperature and flow rate on the performance of the surface condenser, specific heat rate and energy efficiency of the coal fired turbine-follow mode plant using thermodynamic theory. It was found that, increasing of cooling water temperature decreased both heat transfer rate and energy efficiency, while increasing of cooling water flow rate increased both heat transfer rate and energy efficiency.

O'Donovan *et al.* (2012) measured and assessed the steam-side characteristics of the modular ACC for a concentrated solar power under certain vacuum conditions. Furthermore, the relationship between fan speed and condenser pressure was determined. Furthermore, the steam-side pressure drop through the condenser tubes was also measured. For a given steam mass flow rate, the condenser pressure was found to decrease as the fan rotational speed increased. The frictional pressure drops obtained from the experiment were comparable and in agreement Lockhart & Martinelli (1949) correlation.

Moore *et al.* (2014) design the modular ACC for concentrated solar power, which uses smaller speed-controlled fans that incorporated into each module, and this allows the operating point of the condenser to change in order to maximise plant efficiency at all times. Furthermore, they stated that, at a particular condition, by varying fan speed by 10 % of the full speed, the plant output can be increased by over 10 %. However, this is applicable only below the optimum operating condition. Furthermore, they indicated that, the fan power consumption increases with fan speed. Consequently, the net plant output decreases.

O'Donovan *et al.* (2014) presented a modular ACC design in attempt to minimise the weather effect on the A-frame ACC. Similar measurements as that was conducted in Donovan *et al.* (2012) were used to analyse a 50 MW steam turbine gross output. The plant output was found to increase with fan speed until a point, at which larger power consumption rates of the fan offset further increases in plant output power. Furthermore, the plant output was found to decrease as the ambient air temperatures increased.

O'Donovan and Grimes (2015) experimentally studied the steam-side pressure losses in a circular tube bundle ACCs with a bank of axial fans that provides a cross flow of cooling air. The experiments were performed over the range of 0.05 bar to 0.14 bar absolute and 33 ℃ to 55 ℃ of steam pressure and temperature, respectively. During the experiment, the mass fluxes, per individual tube was varied from 0.7 kg/m^2 s to 2 kg/m^2 s, and steam-side pressure losses were evaluated over a vapour and liquid Reynolds numbers in the range of 1890 to 5150 and 25 to 95, respectively. Due to momentum recovery as the condensate formed, the measured pressure drop through the tube bundle was found quite small. The magnitude of momentum recovery was closer to that of the frictional losses, therefore, momentum recovery offset the frictional losses.

Zhang *et al.* (2019) dynamically modelled the cold-end system for the direct air-cooling generating unit. The exhaust steam condensation dynamic process in the condenser was captured by employing the modified moving boundary method. The developed model was validated against the operating data. Based on the developed model, the model predictive controller with feedforward compensation strategy was projected to maintain unit backpressure stable at the optimum set-point while overpowering the ambient temperature disturbances by controlling the fan rotation speed. The model was found to attain both acceptable regulation of backpressure and disturbance rejection performance.

Huang *et al.* (2020) employed the computational fluid dynamics methods to analyse the effect of the rotational speed of the windward fans with constant power consumption for a 2 × 660 MW power plant. As the windward fans rotational speed increased, the inlet air temperature and fan mass flow rates were found to decrease and increase, respectively. As a result, the ACCs heat rejections were improved even at high wind speeds.

Zhang *et al.* (2021) developed a model for a direct air- cooling condenser pressure by taking into account the condenser dynamics and couplings with adjacent systems. Furthermore, the model predictive control and zone economic model predictive control were applied to the developed model. The model was used to analyse the impact of a condenser pressure of a direct air-cooling on the turbine bleed flow and generation unit economy. The results illustrated that, the proposed zone economic model predictive controller offers a possible way of concurrently deal with the changes of ambient temperature and economic optimization issues. The condenser pressure was found to decrease as the rotation speed of the fan increased, and as a result, all the extraction steam flow as well as unit power output and fan power consumption increased.

2.4. Research Study Gap

In most of the reviewed literatures on HDWD performance evaluations, the thermal performance of delugeable round bare tube bundle for HDWD were analysed, except in Angula (2015), were delugeable flat bare tube bundle thermal performance was evaluated. However, in Angula (2015) there were some assumptions considered during modelling that may affect bundle performance. Therefore, in this study the improved modelling of delugeable flat bare tube bundle thermal performance for induced draft HDWD was conducted.

The reviewed literatures on the MHX performance analysis for both dry and wet operating conditions focused on air-conditioning applications, where the working fluid is refrigerant except in Doan *et al.* (2017), where the thermal performance of the surface condenser with steam as a working fluid operates under dry mode was reported. In addition to that, the wet operating mode analyses for MHX performance in literatures, were mainly performed under dehumidification conditions, not deluging/spraying conditions, except in Chen, Yang and Hu (2013), where experimental study of air-cooled finned flat aluminium tube MHX performance with spray cooling was conducted.

Furthermore, in most MHX's literatures, the considered tubes were finned on the air-side. The trapping of the water by fins of finned tubes, which increases heat transfer resistance and air-side pressure drop have been reported by Qureshi and Zubair (2005); Xu *et al.* (2015); Chen *et al.*, (2013), and Korte and Jacobi (2001). Additionally, the evidence of incorporation of the MDTB into a second stage of induced draft HDWD, as well as the investigation of performance of MDTB operating under deluging conditions is not well reported in most of the accessible literatures. Hence, beside the CDTB performance evaluation, the MDTB with bare tubes operating under deluging conditions, and with steam as a working fluid, as well as incorporation of the MDTB into second stage of HDWD was considered in this study.

For the ACC literatures, in most of the them, the CD performance analysis was not single-outed, except in Smit (2000), where the experimental investigation of the factors that affect the effective operation of the dephlegmator units of ACC in different power plants, and therefore, coupled to different steam turbine was performed. Therefore, in this study, the CD unit's thermal performance was evaluated and single-outed, through the mathematical modelling of a direct air-cooling generating unit's cold-end system coupled to 30 MW steam turbine.

Chapter 3: Models Development for Conventional Delugeable Tube Bundle Thermal Performance Analysis

This chapter focuses on the development of models to be employed in thermal performance evaluation of a CDTB. The thermal performance of CDTB was modelled by means of a combination of one-dimensional analytical and two-dimensional numerical models. In addition to that, the solution methods of the governing equations, and validation of models are also presented in this Chapter.

3.1. Physical Models

A single-row CDTB was considered in this study. CDTB consists of the flat bare tubes, which have a vertical flat section and two round-ends as shown in Figure 3.1.

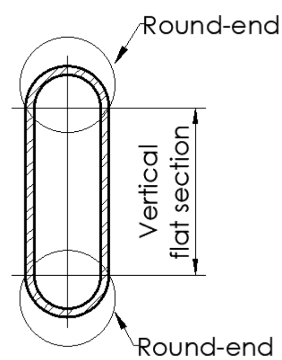

Figure 3.1: Bare flat tube for CDTB

The modelling of the CDTB was conducted in the such a way that, vertical flat section and round-ends are modelled separately. Whereby, the heat transfer analysis for the round sections of the tube, was carried out using round control volume, for which the cylindrical coordinates were employed to derive the governing differential equations. While, for vertical flat section of the tube, the flat control volume was used for heat transfer analysis, and the governing differential equations were derived using Cartesian coordinates. Both control volumes are shown in Figure 3.2. The flat control volume was drawn from the centerline of the tube to the symmetry line between the two adjacent tubes, while the round control volume was taken from the center of round-end, at angle (θ), to the symmetry line between the two adjacent tubes.

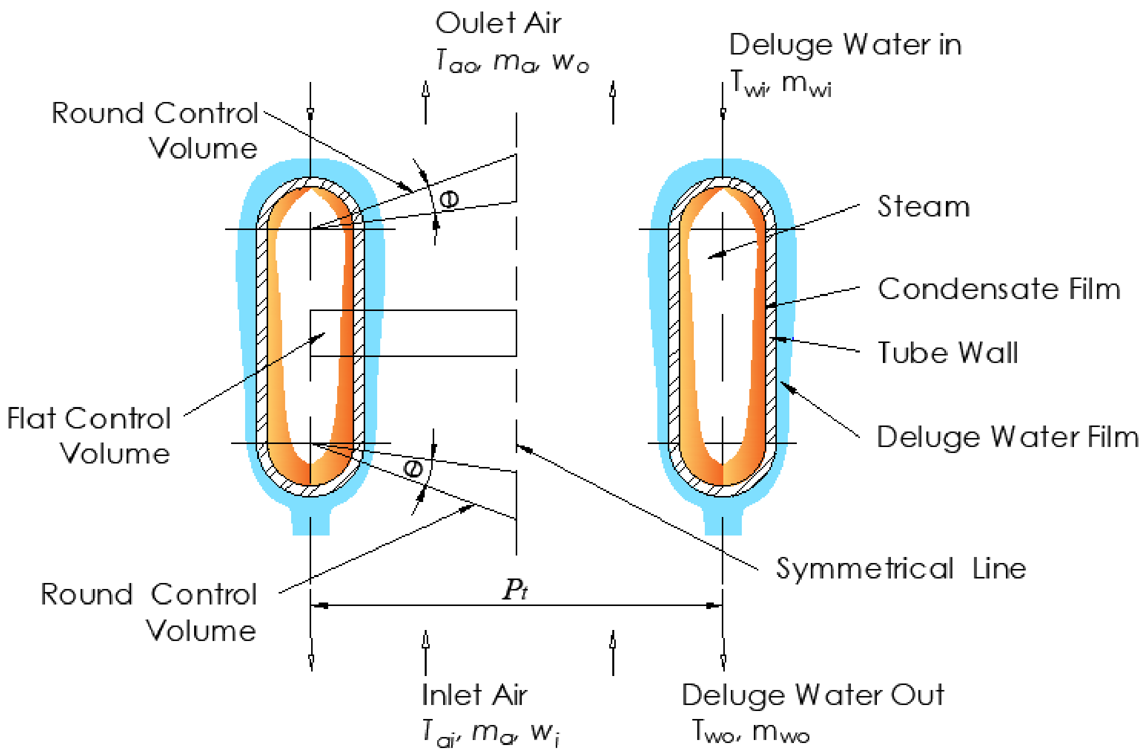

Figure 3. 2: Physical model of CDTB

The flow directions of all the media involved in the heat and mass transfer processes taking place in both control volumes, as well as the parameters, which are essential for governing differential equations derivations are depicted in Figures 3.3 (a) and (b).

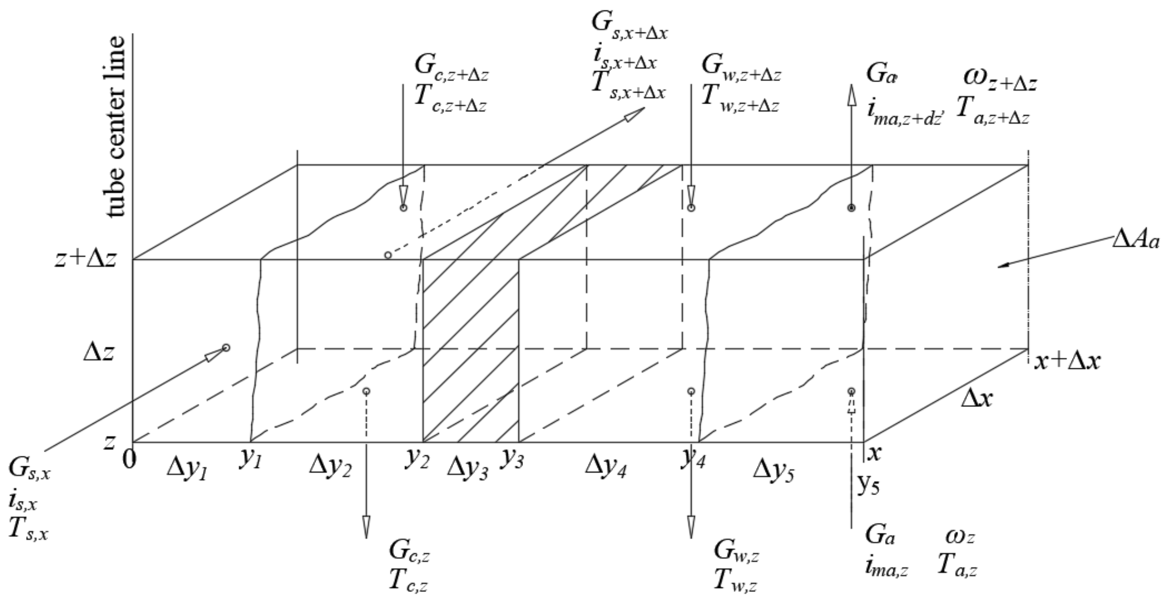

a) Flat section

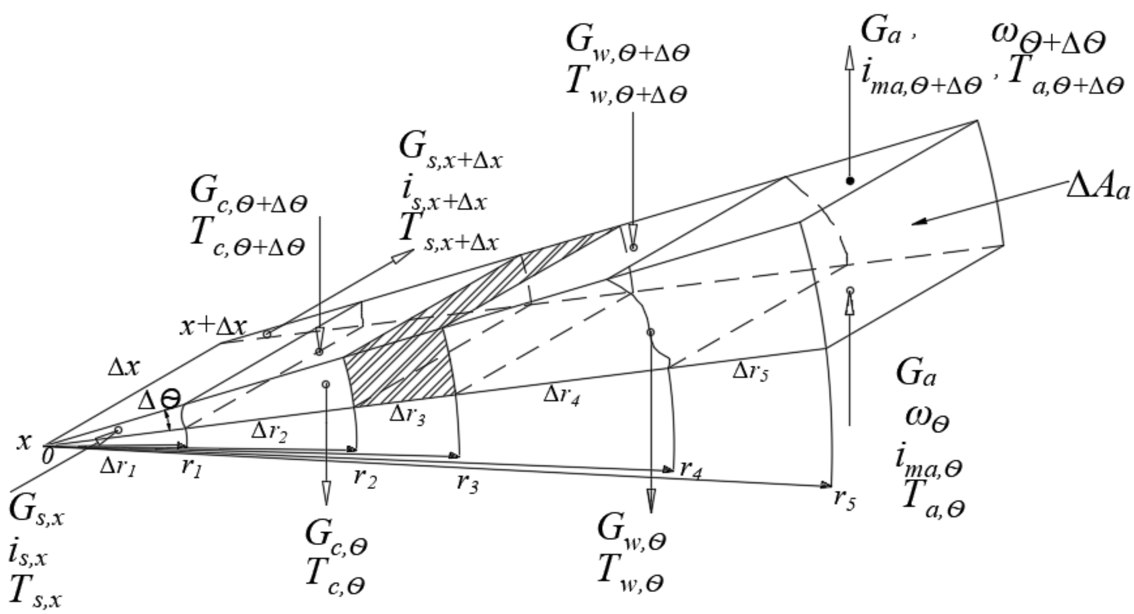

b) Round section

Figure 3. 3: Elementary control volume of the CDTB

The counter-current flow of air and water over the surface of the tubes was considered. This flow arrangement is believed to consume less pumping power. For both control volumes, the steam flows in the *x*-direction, inside the tubes. For flat section, the condensate drains in the negative z-direction. The recirculating deluge water is dispersed over the tube surface in the negative z-direction, while the inlet air is drawn upward from the bottom of the tubes in the z-direction. while the inlet air is drawn upward from the bottom of the tubes in the z-direction. For round control volume, both condensate, deluge water, and air flow along the tube round-end circumferences in their respective directions. In both sections, heat is transferred from the condensed steam through the condensation film, tube wall, deluge water film to the air stream.

Both one-dimensional analytical and two-dimensional numerical models were developed by applying the momentum, mass and energy conservation principles to differential control volumes and the following assumptions were considered.

- Steady, single phase, incompressible fluid flow and heat transfer.
- Negligible radiation heat transfer.
- The deluge water is distributed uniformly along the surface of the tubes.
- The effect of steam velocity on the condensate film is ignored.

3.2. The Governing Equations of a One-Dimensional Analytical Model for CDTB

The one-dimensional analytical model was developed based on Poppe, Merkel as well as heat and mass transfer analogy methods of analysis, and based on the approach presented in Kröger (2004).

3.2.1. Flat control volume

a) The mass balance for the control volume for dry air (Figure 3.3 (a)):

$$\left(G_{a,z+\Delta z} - G_{a,z}\right)\Delta y_5 \Delta \mathrm{x} = 0 \tag{3. 1}$$

Divide with $\Delta x \Delta z \Delta y_5$, and let $\Delta z \rightarrow 0$ to obtain change of dry air mass flux,

$$\frac{\left(G_{a,z+\Delta z} - G_{a,z}\right)}{\Delta z} = \frac{dG_a}{dz} = 0 \tag{3. 2}$$

b) The mass balance for the control volume for water (Figure 3.3 (a)):

$$\left(G_{w,z} - G_{w,z+\Delta z}\right)\Delta y_4 \Delta \mathrm{x} = \left(G_{a,z+\Delta z}\omega_{\mathrm{a,z+\Delta z}} - G_{a,z}\omega_{\mathrm{a,z}}\right)\Delta y_5 \Delta \mathrm{x} \tag{3. 3}$$

Divide with $\Delta x \Delta z \Delta y_5$ and $\Delta x \Delta z \Delta y_4$, let $\Delta z \rightarrow 0$, and consider Eq. (3.2) to obtain change in deluge water mass flux,

$$\frac{dG_w}{dz} = \mathrm{G_a}\frac{d\omega_{\mathrm{a}}}{dz} \tag{3. 4}$$

c) The overall energy balance for the control volume (Figure 3.3 (a)):

$$\begin{aligned}\left(G_{s,x+\Delta x} i_{s,x+\Delta x} - G_{s,x} i_{s,x}\right)\Delta y_1 \Delta \mathrm{z} \\ + c_{pw}\left(G_{w,z} T_{dw,z} - G_{w,z+\Delta z} T_{w,z+\Delta z}\right)\Delta y_4 \Delta \mathrm{x} \\ + \left(G_{a,z+\Delta z} i_{ma,z+\Delta z} - G_{a,z} i_{ma,z}\right)\Delta y_5 \Delta \mathrm{x} = 0\end{aligned} \tag{3. 5}$$

The steam condensation was assumed to happen at constant steam temperature, and therefore $i_{s,x} = i_{s,x+\Delta x}$, and Eq. (3.5) can be simplified as:

$$G_{w,z}\, c_{pw}\frac{dT_w}{dz} + \frac{dG_w}{dz} c_{pw} T_{w,z} = G_s \frac{di_s}{dx} + G_a \frac{di_{ma}}{dz} \tag{3. 6}$$

Hence,

$$\frac{dT_w}{dz} = \frac{1}{G_{w,z}\, c_{pw}} \left(G_s \frac{di_s}{dx} + G_a \ \frac{di_{ma}}{dz} - \frac{dG_w}{dz} c_{pw} T_{w,z} \right) \tag{3. 7}$$

According to Dalton's evaporation law, the evaporation rate of the deluge water into the non-saturated air stream is given as:

$$\frac{dG_w}{dz} = h_d a_w \,(w_{sw} - w) \tag{3. 8}$$

where a_w is volumetric area of deluge water-side. At the air-water interface, the heat transfer is expressed in term of latent and sensible heat as:

$$Q_a = Q_s + Q_l \tag{3. 9}$$

The latent and sensible heat can be defined, respectively as:

$$Q_l = G_a \frac{d\omega_{\mathrm{a}}}{dz} i_v = h_d a_w \,(w_{sw} - w) i_v \tag{3. 10}$$

$$Q_s = h_a a_a (T_w - T_a) \tag{3. 11}$$

where, a_a is volumetric area of air-side, and i_v is the water vapour enthalpy, which is determined at the deluge water film temperature (T_w) as:

$$i_v = i_{fgwo} + c_{pv} T_w \tag{3. 12}$$

where, i_{fgwo} is latent heat evaluated at 0 °C. Therefore, Eq. (3.9) can be re-written as:

$$Q_a = h_a a_a (T_w - T_a) + h_d a_w \, (w_{sw} - w) i_v = G_a \frac{di_{ma}}{dz} \tag{3. 13}$$

The saturated air enthalpy and air-water interface vapour mixture enthalpy are computed respectively as:

$$\begin{aligned} i_{masw} &= c_{pa} T_w + w_{sw} \left(i_{fgwo} + c_{pv} T_w \right) = c_{pa} T_w + w_{sw} i_v \\ &= c_{pa} T_w + w i_v + (w_{sw} - w) i_v \end{aligned} \tag{3. 14}$$

$$i_{ma} = c_{pa} T_a + w \left(i_{fgwo} + c_{pv} T_a \right) \tag{3. 15}$$

Therefore, the temperature differential $(T_w - T_a)$ in Eq. (3.13) can be replaced by the enthalpy differential of saturated air enthalpy at the air-water interface and air-water interface vapour mixture enthalpy per unit of dry air which defined as:

$$i_{masw} - i_{ma} = (c_{pa} + w c_{pv})(T_w - T_a) + (w_{sw} - w) i_v \tag{3. 16}$$

Then Eq. (3.16) can be rearranged as

$$T_w - T_a = [(i_{masw} - i_{ma}) - (w_{sw} - w) i_v] / c_{pma} \tag{3. 17}$$

where

$$c_{pma} = c_{pa} + w c_{pv} \tag{3. 18}$$

Therefore, Eq. (3.13) can be rearranged as:

$$\frac{di_{ma}}{dz} = \frac{h_d a_w}{G_a}\left[\frac{h_a}{c_{pma}h_d}(i_{masw} - i_{ma}) + \left(1 - \frac{h_a}{c_{pma}h_d}\right) i_v (w_{sw} - w)\right] \qquad (3.\ 19)$$

where $h_a/c_{pma}h_d$ is a Lewis factor, which determines the relation between the heat and mass transfer. The heat transfer rate from the condensed steam to the deluge water film can be expressed in term of overall heat transfer coefficient as:

$$G_s \frac{di_s}{dx} = U_a a_a (T_s - T_{ws}) \qquad (3.\ 20)$$

Therefore, the changes in the steam enthalpy can be expressed as:

$$\frac{di_s}{dx} = \frac{U_a a_a}{G_s}(T_s - T_{ws}) \qquad (3.\ 21)$$

The overall heat transfer coefficient is defined as:

$$U_a = \left[\frac{1}{h_c} + \frac{t_t}{k_t} + \frac{1}{h_w}\right]^{-1} \qquad (3.\ 22)$$

The differential equations (3.4), (3.8), (3.13), (3.19) and (3.21) are describing the heat transfer processes taking place within the one-dimensional flat control volume of a CDTB based on Poppe approach.

For Merkel's simplified approach, the Lewis factor is taken to be equal to one, the deluge water evaporation $\left(\frac{dG_w}{dz}\right)$ is considered to be equal to zero, and the deluge water temperature is assumed to be constant $\left(\frac{dT_w}{dz}\right)$. Therefore, Eq. (3.7) and (3.19) become, respectively

$$G_s \frac{di_s}{dx} = G_a \frac{di_{ma}}{dz} \tag{3. 23}$$

$$\frac{di_{ma}}{dz} = \frac{h_d a_a}{G_a}(i_{masw} - i_{ma}) \tag{3. 24}$$

And therefore,

$$G_a \frac{di_{ma}}{dz} = U_a a_a \,(T_s - T_{ws}) \tag{3. 25}$$

$$G_a \frac{di_{ma}}{dz} = h_d a_w (i_{masw} - i_{ma}) \tag{3. 26}$$

Integrate Eq. (3.25) and (3.26) between the inlet and outlet air enthalpy

$$\frac{i_{mao} - i_{mai}}{T_s - T_{ws}} = \frac{U_a A_a}{G_a A_{fr}} \tag{3. 27}$$

$$ln\left(\frac{i_{masw} - i_{mai}}{i_{masw} - i_{mao}}\right) = \frac{h_d A_w}{G_a A_{fr}} = NTU_a \tag{3. 28}$$

The enthalpy of the air at bundle exit can be obtained from Eq. (3.27) and (3.28) as:

$$i_{mao} = i_{mai} + \frac{U_a A_a}{G_a A_{fr}}(T_s - T_{dws}) \tag{3. 29}$$

$$i_{mao} = i_{masw} - (i_{masw} - i_{mai})e^{-NTU_a} \tag{3. 30}$$

The surface temperature of the deluge water can be defined either using Eq. (3.27) or combination of Eq. (3.29) and (3.30) as:

$$T_{ws} = T_s - \frac{G_a A_{\mathrm{fr}}(i_{mao} - i_{mai})}{U_a A_a} \tag{3. 31}$$

$$T_{ws} = T_s - \frac{G_a A_{\mathrm{fr}}(i_{masw} - i_{mai})\left(1 - e^{-NTU_a}\right)}{U_a A_a} \tag{3. 32}$$

3.2.2. Round control volume

a) The mass balance for the control volume for dry air (Figure 3.3 (b)):

$$\left(G_{a,\theta+\Delta\theta} - G_{a,\theta}\right)\Delta r_5 \Delta \mathrm{x} = 0 \tag{3. 33}$$

Divide with $\Delta x \Delta r_5 r_5 \Delta\theta$, and let $\Delta\theta \rightarrow 0$ to obtain change of dry air mass flux,

$$\frac{\left(G_{a,\theta+\Delta\theta} - G_{a,\theta}\right)}{r_5 \Delta\theta} = \frac{1}{r_5}\frac{dG_a}{d\theta} = 0 \tag{3. 34}$$

b) The mass balance for the control volume for water (Figure 3.3 (b)):

$$\left(G_{w,\theta} - G_{w,\theta+\Delta\theta}\right)\Delta r_4 \Delta \mathrm{x} = G_a \left(\omega_{\mathrm{a},\theta+\Delta\theta} - \omega_{\mathrm{a},\theta}\right)\Delta r_5 \Delta \mathrm{x} \tag{3. 35}$$

Divide with $\Delta x \Delta r_4 r_4 \Delta\theta$, and $\Delta x \Delta r_5 r_5 \Delta\theta,$ and let $\Delta\theta \rightarrow 0$ consider Eq. (3.34) to obtain change in deluge water mass flux,

$$\frac{dG_w}{d\theta} = \frac{\mathrm{r}_4}{\mathrm{r}_5} G_a \frac{d\omega_{\mathrm{a}}}{d\theta} \tag{3. 36}$$

c) The overall energy balance for the control volume (Figure 3.3 (b)):

$$\left(G_{s,x+\Delta x} i_{s,x+\Delta x} - G_{s,x} i_{s,x}\right)\Delta \mathrm{r}_1 \mathrm{r}_1 \Delta\theta$$
$$+\ c_{pw}\left(G_{w,\theta} T_{dw,\theta} - G_{w,\theta+\Delta\theta} T_{w,\theta+\Delta\theta}\right)\Delta r_4 \Delta \mathrm{x} \quad (3.\ 37)$$
$$+\left(G_{a,\theta+\Delta\theta} i_{ma,\theta+\Delta\theta} - G_{a,\theta}\ i_{ma,\theta}\right)\Delta r_5 \Delta \mathrm{x} = 0$$

Eq. (3.37) can be simplified to

$$\frac{1}{r_4} G_{w,\theta} c_{pw} \frac{dT_w}{d\theta} + \frac{1}{r_w}\frac{dG_w}{d\theta} c_{pw} T_{w,\theta} = \mathrm{G_{s,x}} \frac{di_s}{dx} + \frac{1}{r_5} G_{a,\theta} \frac{di_{ma}}{d\theta} \quad (3.\ 38)$$

Hence,

$$\frac{dT_w}{d\theta} = \frac{r_4}{G_{w,\theta} c_{pw}}\left(-\frac{1}{r_4}\frac{dG_w}{d\theta} c_{pw} T_{w,\theta} + \mathrm{G_{s,x}}\ \frac{di_s}{dx} + \frac{1}{r_5} G_{a,\theta} \frac{di_{ma}}{d\theta}\right) \quad (3.\ 39)$$

According to by Dalton's evaporation law, deluge water evaporation rate into the non-saturated air stream is:

$$\frac{dG_w}{d\theta} = h_d a_w (w_{sw} - w) \quad (3.\ 40)$$

The heat transfer across the air-water interface is expressed as:

$$Q_a = Q_s + Q_l \quad (3.\ 41)$$

The latent and sensible heat can be defined respectively as:

$$Q_l = \frac{\mathrm{r_4}}{\mathrm{r_5}} G_a \frac{d\omega_\mathrm{a}}{d\theta} i_v = h_d a_w (w_{sw} - w)\ i_v \quad (3.\ 42)$$

$$Q_s = h_a a_a (T_{dw} - T_a) \tag{3. 43}$$

Therefore, Eq. (3.41) can be re-written as:

$$Q_a = h_a a_a (T_{dw} - T_a) + h_d a_w (w_{sw} - w)\, i_v = \frac{1}{r_5} G_{a,\theta} \frac{di_{ma}}{d\theta} \tag{3. 44}$$

Through the same simplification process, as indicated by Eq. (3.13) to (3.18), Eq. (3.44) can be rearranged as:

$$\frac{di_{ma}}{d\theta} = \frac{h_d a_w}{G_{a,\theta}} r_5 \left[\frac{h_a}{c_{pma} h_d}(i_{masw} - i_{ma}) + \left(1 - \frac{h_a}{c_{pma} h_d}\right) i_v (w_{sw} - w)\right] \tag{3. 45}$$

In term of overall heat transfer coefficient, the heat transfer rate from the condensed steam to the deluge water film can be expressed as:

$$G_{\mathrm{s,x}} \frac{di_s}{dx} = U_a a_a (T_s - T_{ws}) \tag{3. 46}$$

The overall heat transfer coefficient is defined as:

$$U_a = \left[\frac{1}{h_c} + \frac{\ln\left(\frac{r_{to}}{r_{ti}}\right)}{2\pi k_t L_t} + \frac{1}{h_w}\right]^{-1} \tag{3. 47}$$

Based on Poppe method, the heat transfer processes taking place within a one-dimensional round control volume of CDTB are defined by Eq. (3.36), (3.39), (3.40), (3.45) and (3.46). By applying Merkel's assumptions, and carrying out the same simplification process as shown by Eq. (3.23) to (3.32), the outlet air enthalpy can be determined by equations similar to Eq. (3.29) and (3.30), while the deluge water surface temperature can be defined by equations similar to Eq. (3.31) and (3.32).

3.2.3. Solution Methods of Governing Equations

For the flat and round control volumes, the differential equations were integrated over the vertical flat height (H_f) and round-end (angle θ) sections of the tube, respectively. The obtained integrated governing equations were solved analytically.

The one-dimensional analytical model was assessed based on Poppe, Merkel, and heat and mass transfer analogy methods. For both methods, the outlet air temperature and humidity ratio, as well as the deluge water inlet and outlet temperature were attained through Gauss-Seidel iteration method. The output performance data for the down round-end section were taken to be the input performance data of the vertical flat section, while the input performance data of the upper round-end section were equal to output performance data of the vertical flat section.

In Merkel approach, the Lewis factor was assumed to be equal to unit, while, in Poppe method, the Lewis factor was defined by using Bosjnakovic (1965) equation as:

$$Le = 0.866^{0.667}\left(\frac{w_{sw}+0.622}{w+0.622} - 1\right)/ln\left(\frac{w+0.622}{w+0.622}\right) \tag{3. 48}$$

Furthermore, in Poppe method, the air at the exit of the bundle was not considered to be saturated. The mass transfer coefficient at the air-water interface was obtained from the relationship between heat and mass transfer coefficient through a Lewis factor as:

$$h_d = h_a / c_{pma} Le \tag{3. 49}$$

For the heat and mass transfer analogy method, the mass transfer convection coefficient is determined from the analogy between heat and mass transfer at the air-water interface by using correlations accessible in Appendix B to F. To define overall the heat transfer coefficient in Eq. (3.22) and (3.47), several correlations presented in Appendix B to F were employed to determine the condensation and deluge water heat transfer coefficients. The flow charts of the iterative loop for one-dimensional model evaluation is shown in Figure 3.4.

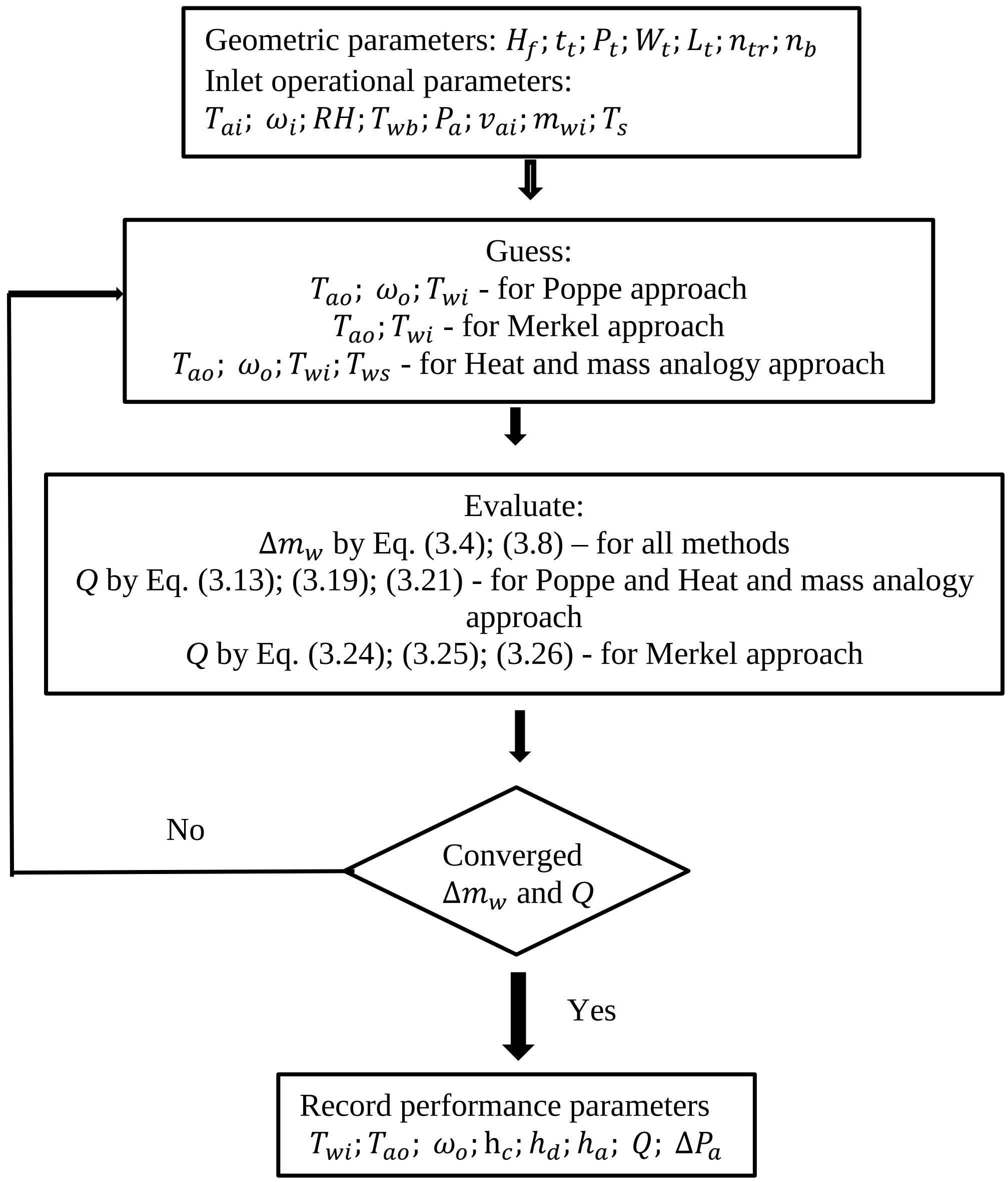

Figure 3. 4: The flow chart of the iterative loop for one-dimensional model evaluation

3.2.4. Validation of Model

The model's validation was carried out based on the following typical designing and operating conditions of a delugeable tube bundle as shown in Table 3.1(Angula, 2015).

Table 3. 1: Typical designing and operating conditions of a delugeable tube bundle

Description	Symbol	Unit	Value
Steam temperature	T_s	℃	45
Atmospheric pressure	p_a	Pa	101325
Ambient inlet air temperature	T_a	℃	15
Relative humidity	ϕ	%	60
Air velocity	v_a	m/s	2
Deluge water mass flow rate	m_w	kg/s	2

Figure 3.5 was considered for the flow on the air-side. The height (H_{BL}) at which two air-side boundary layers meet was calculated. The flow within the boundary layer height (H_{BL}) was considered to be a developing flow. Therefore, the heat transfer rate and air-side pressure drop within this region were determined by employing the external flow theories. The flow in the rest of the air flow channel was considered to be a fully developed flow. However, for the considered tube height ($H_t = 220\ mm$), the height (H_{BL}) was calculated to be 500 mm, which is greater than the tube height (H_t). Therefore, the entire air-side flow was taken to be developing flow. Furthermore, the critical height at which the flow would change from laminar to turbulent was calculated to be 1690 mm, which is also greater than considered tube height (H_t), therefore, the laminar external theories were employed.

For validation of the one-dimensional analytical model, the solutions for each tube section attained from all the methods (Poppe, Merkel and heat and mass transfer analogy) were compared in Table 3.2. In Table 3.3, the comparison of overall solutions as per method are presented. Poppe, Merkel and heat and mass transfer analogy are well-established methods, and their predictive ability have been proven (Rodrigo *et al.*, 2013). The solutions, from all the methods were found to be comparable.

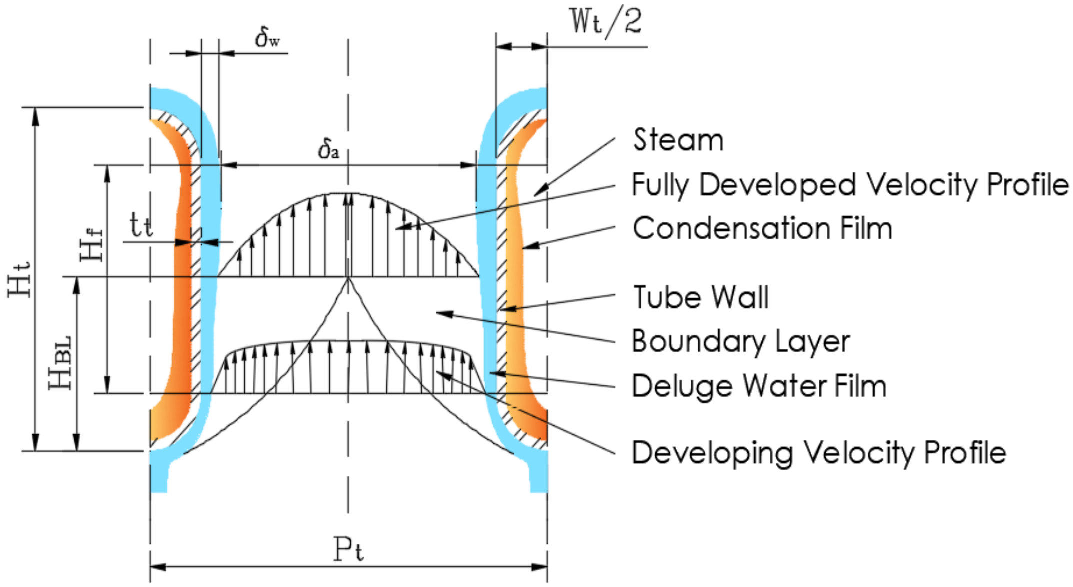

Figure 3. 5: Tube bundle section, illustrating the air-side flow between two adjacent tubes

By comparing the Merkel solutions to Poppe solutions, the outlet air temperature and humidity ratio were found to be 0.24 % and 1.22 % higher and lower, respectively. While by comparing the heat and mass transfer analogy solutions to Poppe solutions, the outlet air temperature and humidity ratio were found to be 0.06 % and 3.2 % lower. Due to the fact that Merkel method assumes saturated air output, the outlet air humidity ratio supposed to be higher than that of Poppe method. However, Rodrigo *et al.* (2013) found that, this is not to be always a case, since this may influence by the air temperature and amount of deluge water.

The highest heat transfer rate was obtained by Poppe method followed by Merkel method, and heat and mass transfer analogy method obtained the lowest heat transfer rate. While slight differences in air-side pressure drop were yielded. This correlate with the conclusion made in Angula (2015), where the performance of the similar tube bundle was analysed, by employing only one control volume with differential governing equations in Cartesian coordinate, which were integrated over entire tube height including the bottom and upper round-end sections. By comparing the Merkel and heat and mass transfer analogy solutions to Poppe solution, 2.94 % and 8.99 % differences in heat transfer rate were achieved, respectively. This is due to the fact that, the deluge water evaporation rate is believed to be higher when Lewis factor is smaller, which results in higher latent heat transfer. The Lewis factor for Poppe method was found to be less than a unity, while the Merkel method assumes that the Lewis factor is equal to one. The Merkel method underestimates the amount of water that evaporates. Hence, the slight inconsistencies between solutions were mainly due to the assumptions made in Merkel model.

From the presented results, it can be said that, one-dimensional model is valid for the analysis of the thermal performance of a CDTB that can be incorporated into the second stage of induced draft HDWD. Furthermore, all the methods can be employed to analyse thermal performance of a CDTB. However, according to Rodrigo *et al.* (2013), when a detail and accurate results and design are required, the Poppe method is the best, whence Merkel method is more appropriate when less accuracy is required. In heat and mass transfer analogy method, the mass transfer convection coefficient is determined from the analogy between heat and mass transfer at the air-water interface, and it does not make use of Lewis factor or any other assumption. In addition to that, the heat and mass transfer analogy was found to be easier to use (Zou *et al.*, 2016).

Table 3. 2: Comparison of one-dimensional model results per section of the tube

	Description	Condensation heat transfer coefficient	Deluge water inlet temperature,	Deluge water heat transfer coefficient	Outlet air temperature,	Outlet air humidity ratio	Air-side heat transfer coefficient	Mass transfer coefficient	Heat transfer rate	Air-side pressure drop
	Symbol	h_c	T_{wi}	h_w	T_{ao}	ω_{ao}	h_a	h_d	Q_a	ΔP_a
	Units	$\mathrm{W/m^2\,K}$	℃	$\mathrm{W/m^2\,K}$	℃	$\mathrm{kg/kg}$	$\mathrm{W/m^2\,K}$	$\mathrm{W/m^2\,K}$	W	$\mathrm{p_a}$
Upper Round Section	Merkel Approach	17236.43	43.896	21156.13	16.48	0.0088	26.16	0.02557	145.73	≈0
	Pope Approach	16984.85	43.838	21144.71	16.44	0.00900	26.18	0.02706	151.54	≈0
	Heat and Mass Transfer Analogy Approach	17471.16	43.831	21143.32	16.43	0.00871	26.15	0.02445	139.48	≈0
Flat Section	Merkel Approach	24203.38	-	871.86	-	-	18.33	0.01795	556.48	0.6044
	Pope Approach	23923.41	-	871.31	-	-	18.33	0.01902	556.48	0.6045
	Heat and Mass Transfer Analogy Approach	24840.96	-	872.92	-	-	18.32	0.01749	514.77	0.6042
Down Round Section	Merkel Approach	17037.27	-	21136.22	-	-	26.11	0.02562	150.42	24.85
	Pope Approach	17040.38	-	20985.332	-	-	26.12	0.02711	150.66	24.87
	Heat and Mass Transfer Analogy Approach	17240.37	-	21154.80	-	-	26.11	0.0245	145.16	24.85

Table 3. 3: Comparison of one-dimensional model results per approaches

Description	Condensation heat transfer coefficient	Deluge water inlet temperature	Deluge water heat transfer coefficient	Outlet air temperature	Outlet air humidity ratio	Air-side heat transfer coefficient	Mass transfer coefficient (critical region)	Heat transfer rate	Air-side pressure drop
Symbol	h_c	T_{wi}	h_w	T_{ao}	ω_{ao}	h_a	h_d	Q_a	ΔP_a
Units	$\mathrm{W/m^2\,K}$	℃	$\mathrm{W/m^2\,K}$	℃	kg/kg	$\mathrm{W/m^2\,K}$	$\mathrm{W/m^2\,K}$	W	$\mathrm{p_a}$
Merkel Approach	19492.31	43.89	14388.07	16.48	0.00889	23.54	0.02305	852.65	24.91
Pope Approach	19316.21	43.84	14333.79	16.44	0.00900	23.54	0.02440	878.45	25.47
Heat and Mass Transfer Analogy Approach	19850.83	43.83	14390.35	16.43	0.00871	23.53	0.02217	799.42	25.45

3.3. The Governing Equations of a Two-dimensional Numerical Model for CDTB

The two-dimensional numerical model was developed in order to analyze the heat transfer in the y and z- directions for flat section, and in radial (r) and transverse (θ) directions for round-end sections. The heat transfer in the z- and transverse (θ) directions are mainly due to enthalpies carried by fluids, and in the y- and radial (r) directions are due to the conduction and convection through the tube wall and fluids. The axial heat transfer in the x-direction and along the tube length was neglected. For the two-dimensional numerical model, both round-end and flat sections elementary control volumes, in Figure 3.3, were further divided into five sub-elementary control volumes. These are steam-side, condensate-side, tube wall-side, deluge water-side and air-side. Then, the conservation principles of mass, momentum and energy were applied to each individual sub-elementary control volume to derive the governing differential equations which describe the fluid flow and heat and mass transfer processes taking place in each sub-elementary control volume.

3.3.1. Flat Control Volume

3.3.1.1. Steam-side elementary control volume

The steam-side elementary control volume is shown in Figure 3.6.

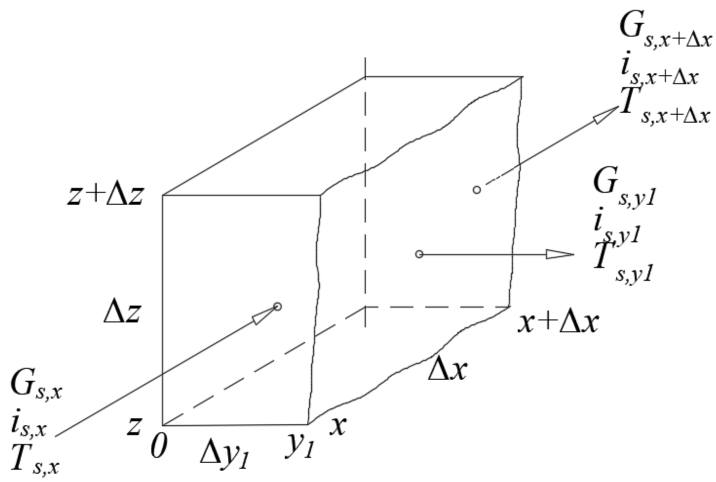

Figure 3. 6: Steam-side elementary control volume

a) The mass balance for the elementary control volume (Figure 3.6):

$$\left(G_{s,x} - G_{s,x+\Delta x}\right)\Delta y_1 \Delta \mathrm{z} = G_{s,y_1} \Delta z \Delta x \quad (3.\ 50)$$

That can be simplified as:

$$\Delta G_{sx} \Delta y_1 \Delta \mathrm{z} = G_{s,y_1} \Delta z \Delta x \quad (3.\ 51)$$

Divide with $\Delta x \Delta z \Delta y_1$, and take the limit as $\Delta x \rightarrow 0$ to obtain the change in mass flux of steam as:

$$\frac{\partial G_{sx}}{\partial x} = \frac{G_{s,y_1}}{\Delta y_1} \quad (3.\ 52)$$

b) The energy balance for the elementary control volume (Figure 3.6):

$$\left(G_{s,x}i_{s,x} - G_{s,x+\Delta x}i_{s,x+\Delta x}\right)\Delta y_1 \Delta \mathrm{z} = G_{s,y_1}i_{s,y_1}\Delta z \Delta x \tag{3. 53}$$

The pressure differences within the steam flow are usually small that the saturated temperature of the steam can be assumed constant. Therefore, steam condensation was presumed to happen at constant steam temperature, so that $i_{s,x} = i_{s,x+\Delta x} = i_{s,y_1}$ then Eq. (3.53) becomes,

$$\Delta G_{sx}i_{s,x}\Delta y_1 \Delta \mathrm{z} = G_{s,y_1}i_{s,y_1}\Delta z \Delta x \tag{3. 54}$$

Divide with $\Delta x \Delta z \Delta y_1$, and take the limit as $\Delta x \rightarrow 0$ to obtain energy accompanied by steam as:

$$\frac{\partial G_s}{\partial x} i_{s,x} = \frac{G_{s,y_1}}{\Delta y_1} i_{s,y_1} \tag{3. 55}$$

c) The heat transfer balance for the thermal resistance (Figure 3.7):

$$G_{s,y_1}\Delta \mathrm{z}\Delta \mathrm{x} i_{s,y_1} = Q_{s,s-cs} \tag{3. 56}$$

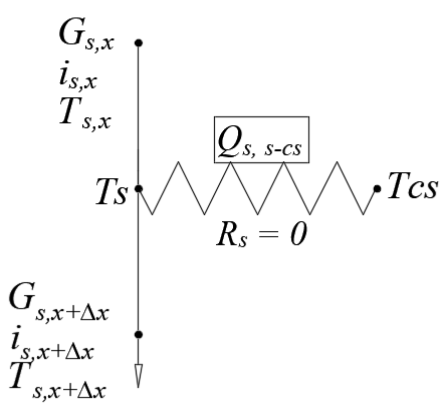

Figure 3. 7: Steam-side thermal resistance

3.3.1.2. Condensate-side elementary control volume

The condensate-side elementary control volume is presented in Figure 3.8.

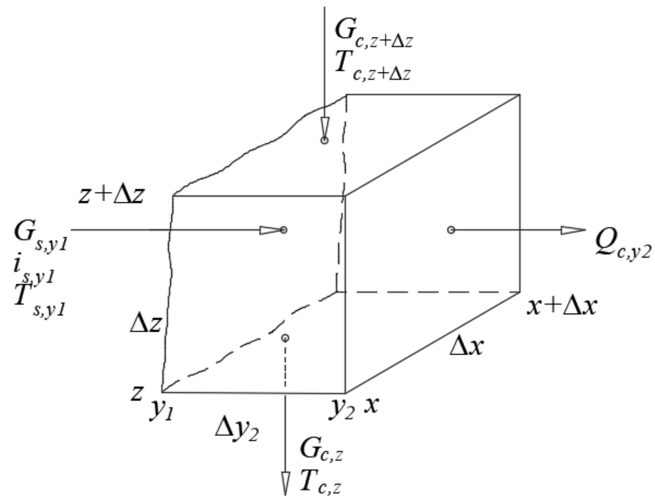

Figure 3. 8: Condensate-side elementary control volume

a) The mass balance for the elementary control volume (Figure 3.8):

$$\left(G_{c,z} - G_{c,z+\Delta z}\right)\Delta y_2 \Delta \mathrm{x} = G_{s,y_1}\Delta z \Delta x \tag{3. 57}$$

That can be simplified as:

$$\Delta G_{cz}\Delta y_2 \Delta \mathrm{x} = G_{s,y_1}\Delta z \Delta x \tag{3. 58}$$

Divide with $\Delta x \Delta z \Delta y_2$, and take the limit as $\Delta z \rightarrow 0$ to obtain the change in condensate mass flux as:

$$\frac{\partial G_{cz}}{\partial \mathrm{z}} = \frac{G_{s,y_1}}{\Delta y_2} \tag{3. 59}$$

Substitute Eq. (3.55) into (3.59) to yield the changes in steam mass flux:

$$\frac{\partial G_{sx}}{\partial x} = \frac{\partial G_{cz}}{\partial \mathrm{z}} \frac{\Delta y_2}{\Delta y_1} \tag{3. 60}$$

b) The energy balance for the elementary control volume (Figure 3.8):

$$G_{s,y_1} \Delta \mathrm{z} \Delta \mathrm{x} i_{s,y_1} + G_{c,z+\Delta z} \Delta y_2 \Delta \mathrm{x} c_{pc} T_{c,z+\Delta z} = Q_{c,y_2} + G_{c,z} \Delta y_2 \Delta \mathrm{x} c_{pc} T_{c,z} \tag{3. 61}$$

That can be simplified as:

$$\begin{aligned} G_{s,y_1}(\Delta \mathrm{z} \Delta \mathrm{x}) i_{s,y_1} - Q_{c,y_2} & \\ &= G_{c,z} \Delta y_2 \Delta \mathrm{x} c_{pc} T_{c,z} \\ &- \left(G_{c,z} - \Delta G_{cz}\right) \Delta y_2 \Delta \mathrm{x} c_{pc} \left(T_{c,z} + \Delta T_{cz}\right) \\ &= \Delta G_{cz} \Delta y_2 \Delta \mathrm{x} c_{pc} T_{c,z+\Delta z} - G_{c,z} \Delta y_2 \Delta \mathrm{x} c_{pc} \Delta T_{cz} \end{aligned} \tag{3. 62}$$

Substitute Eq. (3.58) into (3.62) and simplify

$$Q_{c,y_2} = \Delta G_{cz} \Delta y_2 \Delta \mathrm{x} \left(i_{s,y_1} - c_{pc} T_{c,z+\Delta z}\right) + G_{c,z} \Delta y_2 \Delta \mathrm{x} c_{pc} \Delta T_{cz} \tag{3. 63}$$

c) The heat transfer balance for the thermal resistance (Figure 3.9):

$$Q_{c,z+\Delta z-cm} + Q_{c,cs-cm} = Q_{c,cm-ti} + Q_{c,cm-z} \tag{3. 64}$$

where

$$Q_{c,cs-cm} = \frac{k_c \Delta x \Delta z (T_{cs} - T_{cm})}{\Delta y_{2,1}} \tag{3. 65}$$

$$Q_{c,cm-ti} = \frac{k_c \Delta x \Delta z (T_{cm} - T_{ti})}{\Delta y_{2,2}} = \frac{k_c \Delta x \Delta z (T_s - T_{ti})}{\Delta y_2} \tag{3. 66}$$

$$Q_{c,z+\Delta z-cm} = G_{c,z+\Delta z} \Delta y_2 \Delta x c_{pc} \left(T_{c,z+\Delta z} - T_{cm}\right) \tag{3. 67}$$

$$Q_{c,cm-z} = G_{c,z} \Delta y_2 \Delta x c_{pc} (T_{cm} - T_{c,z}) \tag{3. 68}$$

$$\Delta y_2 = \Delta y_{2,1} + \Delta y_{2,2} \tag{3. 69}$$

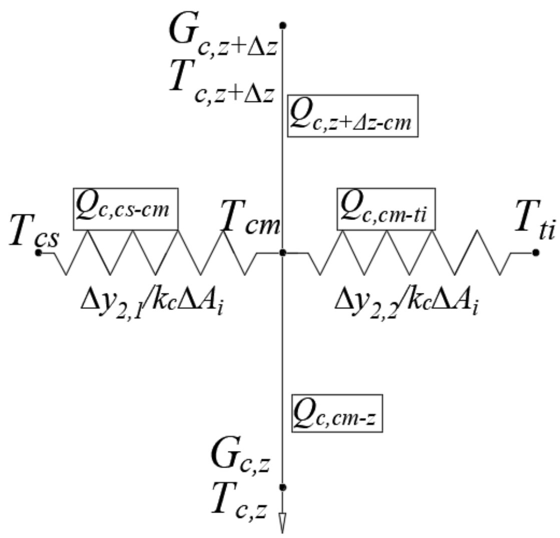

Figure 3. 9: Condensate-side thermal resistance

d) Coupling of the elementary control volume to thermal resistance (Figure 3.8 and 3.9):

$$Q_{c,cs-cm} = Q_{s,s-cs} \tag{3. 70}$$

$$Q_{c,cm-ti} = Q_{c,y_2} \tag{3. 71}$$

e) The momentum balance of the elementary control volume (Figure 3.10):

The momentum balance was carried out to define the weighted mean temperature of the condensate. Consider the control volume ($y^* \Delta x \Delta z$) shown in Figure 3.10. The forces acting in the control volume are due to buoyancy (F_B), gravity (F_g) and friction which is due to viscosity (F_τ).

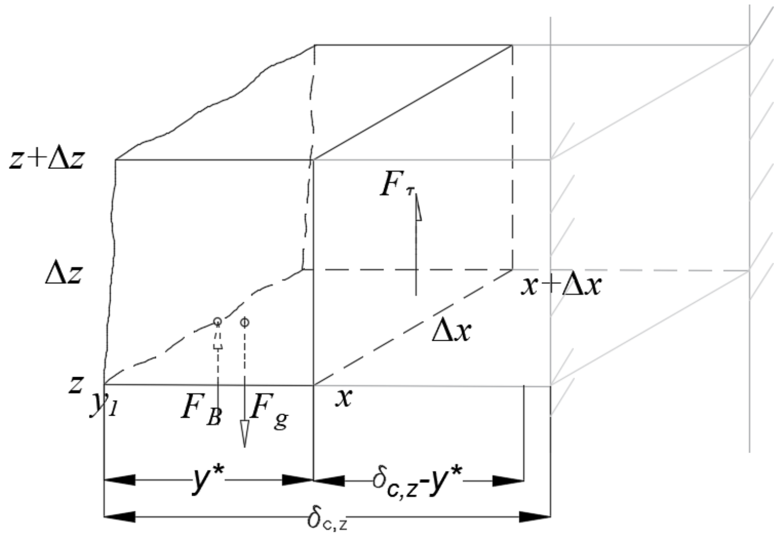

Figure 3. 10: Free body diagram for the control volume in the condensation film

The force balance for the free body diagram shown in Figure 3.10 can be written as:

$$\rho_c g(y^*\Delta x\Delta z) = \mu_c \frac{du_c}{dy^*}(\Delta x\Delta z) + \rho_s g(y^*\Delta x\Delta z) \tag{3. 72}$$

The changes of the condensate velocity over y^* was achieved by dividing Eq. (3.72) by $(\Delta x\Delta z)$ as:

$$\frac{du_c}{dy^*} = \frac{g(\rho_c - \rho_s)}{\mu_c} y^* \tag{3. 73}$$

The condensate velocity profile inside the condensation film, can be obtained by integrating the Eq. (3.73), so that at y_1 where $y^* = 0$, $\frac{du_c}{dy^*} = 0$, and at y_2 where $y^* = \delta_{c,z}$, $u_c = 0$, which led to the velocity profile of the condensate to be:

$$u_c(y^*) = \frac{g(\rho_c - \rho_s)}{2\mu_c} {y^*}^2 \tag{3. 74}$$

The mass flow rate of the condensate at the location z, where the film thickness is $\delta_{c,z}$, and was defined as:

$$G_{c,z}\Delta x\delta_{c,z} = \int_0^{\delta_{c,z}} \rho_c u_c(y^*)\Delta x dy^* = \frac{\rho_c g\Delta x(\rho_c - \rho_s)}{2\mu_c}\int_0^{\delta_{c,z}} {y^*}^2 dy^*$$
$$= \frac{\rho_c g\Delta x(\rho_c - \rho_s)}{6\mu_c}{\delta_{c,z}}^3 \tag{3. 75}$$

The enthalpy transferred by the condensate as it flows through the cross section $(\Delta x\delta_{c,z})$, can be written as:

$$G_{c,z}\Delta x\delta_{c,z}c_{pc}T_{cm} = c_{pc}\int_0^{\delta_c} \rho_c u_c(y^*)T_c(y^*)\Delta x dy^* \tag{3. 76}$$

Since the temperature profile within the condensation film in the y-direction was assumed to be linear, it can be expressed so that $T_c(y^*) = T_{cs}$ at y_1, where $y^* = 0$, and $T_c(y^*) = T_{ti}$ at y_2, where $y^* = \delta_{c,z}$. Therefore,

$$T_c(y^*) = T_{cs} - \frac{(T_{cs} - T_{ti})}{\delta_{c,z}} y^* \tag{3. 77}$$

And Eq. (3.76) can be re-written as:

$$G_{c,z}\Delta x\delta_{c,z}T_{cm} = \rho_c\frac{g(\rho_c-\rho_s)}{2\mu_c}\int_0^{\delta_c} y^{*2}\left(T_{cs}-\frac{(T_{cs}-T_{ti})}{\delta_{c,z}}y^*\right)\Delta x dy^* \tag{3. 78}$$

which can be simplified as:

$$G_{c,z}\Delta x\delta_{c,z}T_{cm} \qquad = \frac{\rho_c g\Delta x(\rho_c-\rho_s){\delta_c}^3}{2\mu_c}\left[\frac{T_{cs}}{3}-\frac{(T_{cs}-T_{ti})}{4}\right] \tag{3. 79}$$

Combine Eq. (3.75) and (3.79) as:

$$\begin{aligned}&\frac{\rho_c g\Delta x(\rho_c-\rho_s)}{6\mu_c}{\delta_{c,z}}^3 T_{cm}\\ &\qquad = \frac{\rho_c g\Delta x(\rho_c-\rho_s){\delta_{c,z}}^3}{2\mu_c}\left[\frac{T_{cs}}{3}-\frac{(T_{cs}-T_{ti})}{4}\right]\end{aligned} \tag{3. 80}$$

Therefore, the weighted mean temperature of the condensate in the condensation film is

$$T_{cm} = T_{cs}-\frac{3}{4}(T_{cs}-T_{ti}) \tag{3. 81}$$

3.3.1.3. Tube wall-side elementary control volume

The tube wall-side elementary control volume and thermal resistance diagram are illustrated in Figures 3.11 and 3.12, respectively.

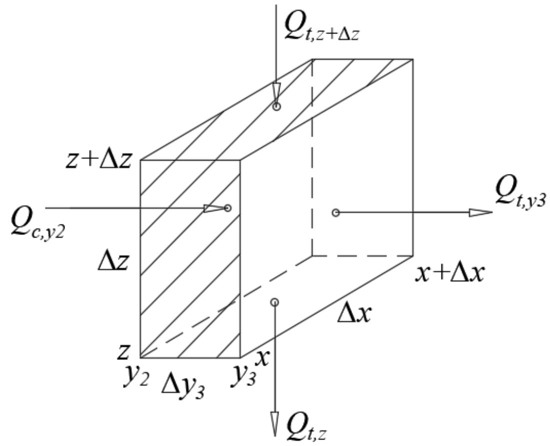

Figure 3. 11: Tube wall-side elementary control volume

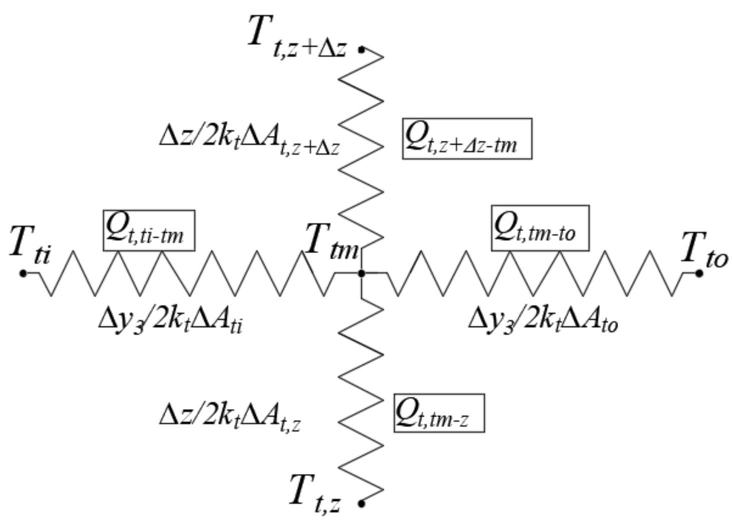

Figure 3. 12: Tube wall-side thermal resistance

a) The heat transfer balance for the thermal resistance (Figure 3.11):

$$Q_{t,ti-tm} + Q_{t,z+\Delta z-tm} = Q_{t,tm-to} + Q_{t,tm-z} \tag{3. 82}$$

where

$$Q_{t,ti-tm} = \frac{2k_t \Delta x \Delta z (T_{ti} - T_{tm})}{\Delta y_3} \tag{3. 83}$$

$$Q_{t,z+\Delta z-tm} = \frac{2k_t \Delta y_3 \Delta x (T_{t,z+\Delta z} - T_{tm})}{\Delta z} \tag{3. 84}$$

$$Q_{t,tm-to} = \frac{2k_t \Delta x \Delta z (T_{tm} - T_{to})}{\Delta y_3} \tag{3. 85}$$

$$Q_{t,tm-z} = \frac{2k_t \Delta y_3 \Delta x (T_{tm} - T_{t,z})}{\Delta z} \tag{3. 86}$$

b) Coupling of the elementary control volume to thermal resistance (Figure 3.11 and 3.12):

$$Q_{t,ti-tm} = Q_{c,y_2} \tag{3. 87}$$

$$Q_{t,z+\Delta z-tm} = Q_{t,z+\Delta z} \tag{3. 88}$$

$$Q_{t,tm-to} = Q_{t,y_3} \tag{3. 89}$$

$$Q_{t,tm-z} = Q_{t,z} \tag{3. 90}$$

3.3.1.4. Water-side elementary control volume

The deluge water-side elementary control volume is presented in Figure 3.13.

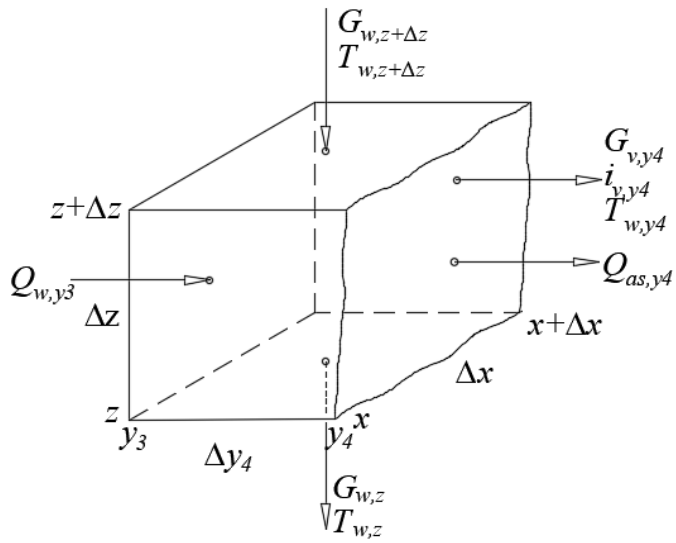

Figure 3. 13: Deluge water-side elementary control volume

a) The water mass balance for the elementary control volume (Figure 3.13):

$$\left(G_{w,z+\Delta z} - G_{w,z}\right)\Delta y_4 \Delta \mathrm{x} = G_{v,y_4}\Delta z \Delta x \tag{3. 91}$$

That can be simplified as:

$$\Delta G_{wz}\Delta y_4 \Delta \mathrm{x} = G_{v,y_4}\Delta z \Delta x \tag{3. 92}$$

Divide with $\Delta x \Delta z \Delta y_4$, and take the limit as $\Delta z \rightarrow 0$ to obtain the change in deluge water mass flux as:

$$\frac{\partial G_{wz}}{\partial z} = \frac{G_{v,y_4}}{\Delta y_4} \tag{3. 93}$$

b) The energy balance for the elementary control volume (Figure 3.13):

$$Q_{w,y_3} - \left(Q_{s,y_4} + G_{v,y_4}\Delta z\Delta x i_{v,y_4}\right) = G_{w,z}\Delta y_4 \Delta x c_{pw} T_{w,z} - G_{w,z+\Delta z}\Delta y_4 \Delta x c_{pw} T_{w,z+\Delta z} \tag{3. 94}$$

Let's the heat transfer leaving the control volume to be Q_{w,y_4}, which is the sum of sensible and latent heat crossing the air-water interface.

$$Q_{w,y_4} = Q_{s,y_4} + G_{v,y_4}\Delta z\Delta x i_{v,y_4} \tag{3. 95}$$

Substitute Q_{w,y_4} into Eq. (3.94) and re-arrange terms

$$\begin{aligned} Q_{w,y_4} &= Q_{w,y_3} + G_{w,z+\Delta z}\Delta y_4 \Delta x c_{dw} T_{dw,z+\Delta z} - G_{w,z}\Delta y_4 \Delta x c_{pw} T_{w,z} \\ &= Q_{w,y_3} + \left(G_{w,z} + \Delta G_{wz}\right)\Delta y_4 \Delta x c_{pw}\left(T_{w,z} - \Delta T_{wz}\right) - G_{w,z}\Delta y_4 \Delta x c_{pw} T_{w,z} \\ &= Q_{w,y_3} - G_{w,z}\Delta y_4 \Delta x c_{pw}\Delta T_w + \Delta G_w \Delta y_4 \Delta x c_{pw} T_{w,z+\Delta z} \end{aligned} \tag{3. 96}$$

c) The heat transfer balance for the thermal resistance (Figure 3.14):

$$Q_{w,to-wm} + Q_{w,z+\Delta z-wm} = Q_{w,wm-ws} + Q_{w,wm-z} \tag{3. 97}$$

where

$$Q_{w,to-wm} = \frac{k_w \Delta x \Delta z (T_{to} - T_{wm})}{\Delta y_{4,1}} \tag{3. 98}$$

$$\mathrm{Q_{w,wm-ws}} = \frac{\mathrm{k_w}\Delta x \Delta z (\mathrm{T_{wm}} - \mathrm{T_{ws}})}{\Delta y_{4,2}} = \frac{k_w \Delta x \Delta z (T_{to} - T_{ws})}{\Delta y_4} \tag{3. 99}$$

$$Q_{w,z+\Delta z-wm} = G_{w,z+\Delta z}\Delta y_4 \Delta \mathrm{x} c_{pw}(T_{w,z+\Delta z} - T_{wm}) \quad (3.\ 100)$$

$$Q_{w,wm-z} = G_{w,z}\Delta y_4 \Delta \mathrm{x} c_{pw}(T_{wm} - T_{w,z}) \quad (3.\ 101)$$

$$\Delta y_4 = \Delta y_{4,1} + \Delta y_{4,2} \quad (3.\ 102)$$

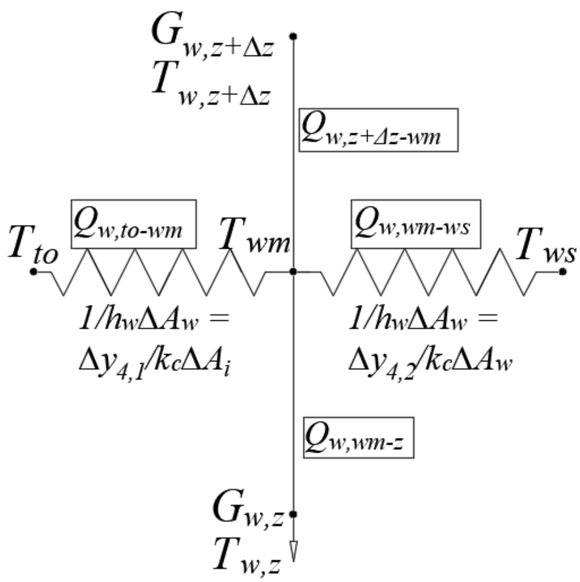

Figure 3. 14: Deluge water-side thermal resistance

d) Coupling of the elementary control volume to thermal resistance (Figure 3.13 and 3.14):

$$Q_{w,to-wm} = Q_{w,y_3} \quad (3.\ 103)$$

$$Q_{w,wm-ws} = Q_{w,y_4} \quad (3.\ 104)$$

e) The momentum balance on the water-side

The momentum balance of water-side control volume was carried out in order to determine the weighted mean temperature of the deluge water, and was conducted in the similar manner as that of condensate-side control volume. The weighted mean temperature of the deluge water was computed as:

$$T_{wm} = T_{to} - \frac{5}{8}(T_{to} - T_{ws}) \quad (3.\ 105)$$

3.3.1.5. Air - side elementary control volume

The air-side elementary control volume is shown in Figure 3.15, and the air was assumed to be moist and unsaturated.

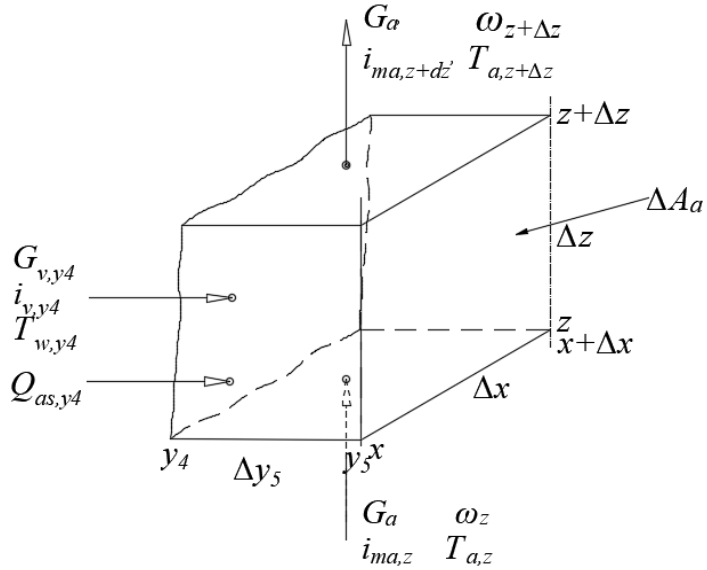

Figure 3. 15: Air-side elementary control volume

a) The water vapour mass balance for the elementary control volume (Figure 3.15):

$$G_{v,y_4}\Delta z\Delta x = G_a\Delta y_5\Delta \mathrm{x}[(1+\omega_{z+\Delta z}) - (1+\omega_z)] \quad (3.\ 106)$$

That can be simplified as:

$$G_{v,y_4}\Delta z\Delta x = G_a\Delta y_5\Delta \mathrm{x}\Delta\omega_z \quad (3.\ 107)$$

Divide with $\Delta x \Delta z \Delta y_5$, and take the limit as $\Delta z \to 0$ to obtain the change in humidity ratio as:

$$\frac{G_{v,y_4}}{G_a \Delta y_5} = \frac{\partial \omega_z}{\partial z} \tag{3. 108}$$

b) The energy balance for the elementary control volume (Figure 3.15):

$$\left(Q_{s,y_4} + G_{v,y_4} \Delta \mathrm{z} \Delta \mathrm{x} i_{v,y_4}\right) = G_a \Delta y_5 \Delta \mathrm{x} \left(i_{ma,z+\Delta z} - i_{ma,z}\right) \tag{3. 109}$$

Substitute Eq. (3.95) into (3.109) and simplify

$$Q_{w,y_4} = G_a \Delta y_5 \Delta \mathrm{x} \Delta i_{ma} \tag{3. 110}$$

c) The heat transfer balance for the thermal resistance (Figure 3.16):

$$Q_{as,ws-am} = h_a \Delta x \Delta z (T_{ws} - T_{am}) \tag{3. 111}$$

$$Q_{al,ws-am} = h_d \Delta x \Delta z i_{v,y_4} (\omega_{sw} - \omega_{zm}) \tag{3. 112}$$

Eq. (3.110) can now re-written as

$$\begin{aligned} Q_{w,y_4} &= h_a \Delta x \Delta z (T_{ws} - T_{am}) + h_d \Delta x \Delta z i_{v,y_4} (\omega_{sw} - \omega_{zm}) \\ &= G_a \Delta y_5 \Delta \mathrm{x} \Delta i_{ma} \end{aligned} \tag{3. 113}$$

Divide with $\Delta x \Delta z \Delta y_5$, and take the limit as $\Delta z \to 0$ to obtain the changes in moist air enthalpy.

$$\frac{\partial i_{ma}}{\partial z} = \frac{h_a}{G_a \Delta y_5} \ (T_{ws} - T_{am}) + \frac{h_d}{G_a \Delta y_5} i_{v,y_4}(\omega_{sw} - \omega_{zm}) \qquad (3.\ 114)$$

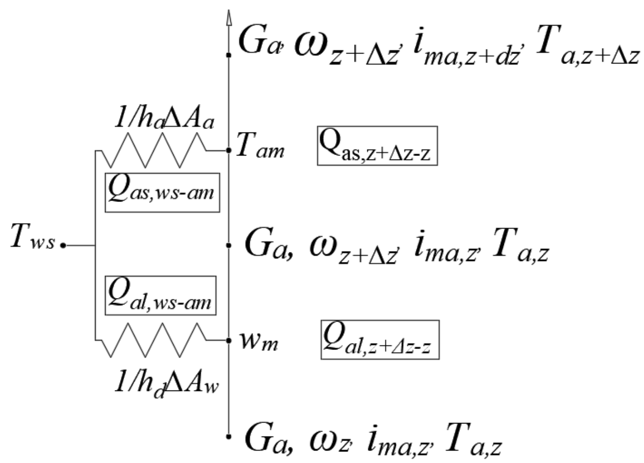

Figure 3. 16: Air-side thermal resistance

d) Coupling of the elementary control volume to thermal resistance (Figure 3.15 and 3.16):

$$Q_{al,ws-am} = Q_{l,z+\Delta z-z} \qquad (3.\ 115)$$

$$Q_{as,ws-am} = Q_{s,z+\Delta z-z} \qquad (3.\ 116)$$

3.3.2. Round control volume

3.3.2.1. Steam-side elementary control volume

The steam-side elementary control volume is presented in Figure 3.17.

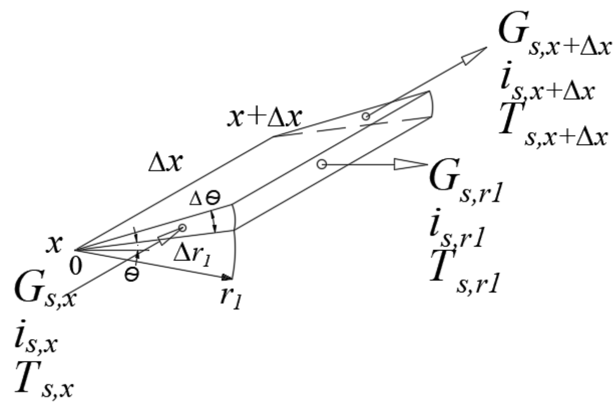

Figure 3. 17: Steam-side elementary control volume

a) The mass balance for the elementary control volume (Figure 3.17):

$$\left(G_{s,x} - G_{s,x+\Delta x}\right)\Delta \mathrm{r}_1 \mathrm{r}_1 \Delta\theta = G_{s,r_1} r_1 \Delta\theta \Delta x \quad (3.\ 117)$$

Divide with $\Delta x \Delta r_1 r_1 \Delta\theta$, and take the limit as $\Delta x \rightarrow 0$ to obtain the changes in steam mass flux as

$$\frac{\partial G_{sx}}{\partial x} = \frac{G_{s,r_1} r_1}{\Delta r_1} \quad (3.\ 118)$$

b) The energy balance for the elementary control volume (Figure 3.17):

$$\left(G_{s,x} i_{s,x} - G_{s,x+\Delta x} i_{s,x+\Delta x}\right)\Delta \mathrm{r}_1 \mathrm{r}_1 \Delta\theta = G_{s,r_1} r_1 \Delta\theta \Delta x i_{s,r_1} \quad (3.\ 119)$$

Since steam condensation was considered to happen at steam constant temperature, it can be assumed that $i_{s,x} = i_{s,x+\Delta x} = i_{s,r_1}$ then,

$$\left(G_{s,x}i_{s,x} - G_{s,x+\Delta x}i_{s,x}\right)\Delta \mathrm{r}_1 \mathrm{r}_1 \Delta\theta = G_{s,r_1} r_1 \Delta\theta \Delta x i_{s,r_1} \tag{3. 120}$$

Divide with $\Delta x \Delta r_1 r_1 \Delta\theta$, and take the limit as $\Delta x \rightarrow 0$ to obtain the change in steam mass flux as:

$$\frac{\partial G_s}{\partial x} i_{s,x} = \frac{G_{s,r_1} r_1}{\Delta r_1} i_{s,r_1} \tag{3. 121}$$

c) The heat transfer balance for the thermal resistance (Figure 3.18):

$$G_{s,r_1} r_1 \Delta\theta \Delta x i_{s,r_1} = Q_{s,s-cs} \tag{3. 122}$$

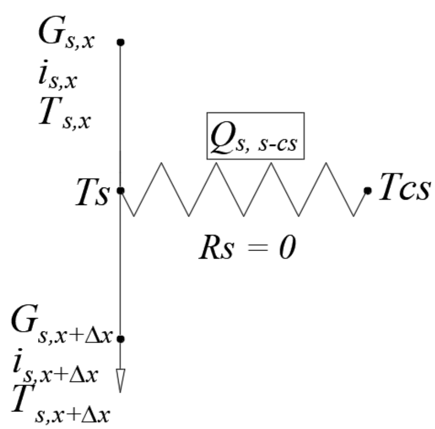

Figure 3. 18: Steam-side thermal resistance

3.3.2.2. Condensate-side elementary control volume

The condensate-side elementary control volume is illustrated in Figure 3.19.

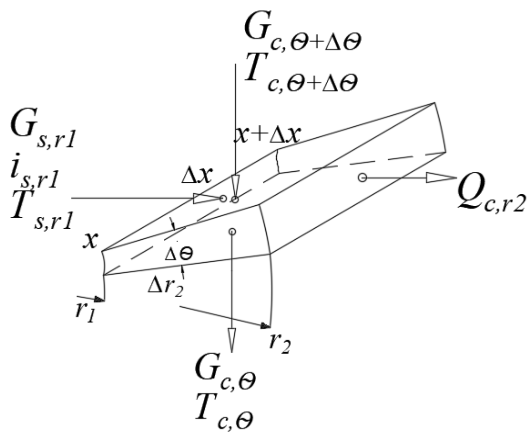

Figure 3. 19: Condensate-side elementary control volume

a) The mass balance for the elementary control volume (Figure 3.19):

$$\left(G_{c,\theta} - G_{c,\theta+\Delta\theta}\right)\Delta r_2 \Delta \mathrm{x} = G_{s,r_1} r_1 \Delta\theta\Delta x \tag{3. 123}$$

Divide with $\Delta x \Delta r_2 r_2 \Delta\theta$, and take the limit as $\Delta\theta \rightarrow 0$ to obtain the change in condensate mass flux as:

$$\frac{\partial G_{c,\theta}}{\partial \theta} = \frac{G_{s,r_1} r_1}{\Delta r_2} \tag{3. 124}$$

Substitute Eq. (3.121) into (3.124) to yield the changes in steam mass flux:

$$\frac{\partial G_{sx}}{\partial x} = \frac{\partial G_{c,\theta}}{\partial \theta}\frac{\Delta r_2}{\Delta r_1} \tag{3. 125}$$

b) The energy balance for the elementary control volume (Figure 3.19):

$$G_{s,r_1} r_1 \Delta\theta \Delta x i_{s,r_1} + G_{c,\theta+\Delta\theta} \Delta r_2 \Delta \mathrm{x} c_{pc} T_{c,\theta+\Delta\theta} = Q_{c,r_2} + G_{c,\theta} \Delta r_2 \Delta \mathrm{x} c_{pc} T_{c,\theta} \quad (3.126)$$

That can be simplified as:

$$G_{s,r_1} r_1 \Delta\theta \Delta x i_{s,r_1} - Q_{c,r_2} = G_{c,\theta} \Delta r_2 \Delta \mathrm{x} c_{pc} T_{c,\theta} - \left(G_{c,\theta} - \Delta G_{c,\theta}\right) \Delta r_2 \Delta \mathrm{x} c_{pc} \left(T_{c,\theta} + \Delta T_{c\theta}\right) = \Delta G_{c,\theta} \Delta r_2 \Delta \mathrm{x} c_{pc} T_{c,\theta+\Delta\theta} - G_{c,\theta} \Delta r_2 \Delta \mathrm{x} c_{pc} \Delta T_{c\theta} \quad (3.127)$$

Substitute Eq. (3.123) into (3.127) and simplify

$$Q_{c,r_2} = \Delta G_{c,\theta} \Delta r_2 \Delta \mathrm{x} \left(i_{s,r_1} - c_{pc} T_{c,\theta+\Delta\theta}\right) + G_{c,\theta} \Delta r_2 \Delta \mathrm{x} c_{pc} \Delta T_{c\theta} \quad (3.128)$$

c) The heat transfer balance for the thermal resistance (Figure 3.20):

$$Q_{c,\theta+\Delta\theta-cm} + Q_{c,cs-cm} = Q_{c,cm-ti} + Q_{c,cm-\theta} \quad (3.129)$$

where

$$Q_{c,cs-cm} = \frac{k_c \Delta x \Delta\theta (T_{cs} - T_{cm})}{ln\left(\frac{r_1 + \Delta r_{2,1}}{r_1}\right)} \quad (3.130)$$

$$Q_{c,cm-ti} = \frac{k_c \Delta x \Delta\theta (T_{cm} - T_{ti})}{ln\left(\frac{r_2}{r_1 + \Delta r_{2,1}}\right)} = \frac{k_c \Delta x \Delta\theta (T_{cs} - T_{ti})}{ln\left(\frac{r_2}{r_1}\right)} \quad (3.131)$$

$$Q_{c,\theta+\Delta\theta-cm} = G_{c,\theta+\Delta\theta} \Delta r_2 \Delta \mathrm{x} c_{pc} \left(T_{c,\theta+\Delta\theta} - T_{cm}\right) \quad (3.132)$$

$$Q_{c,cm-\theta} = G_{c,\theta} \Delta r_2 \Delta \mathrm{x} c_{pc} (T_{cm} - T_{c,\theta} \quad (3.133)$$

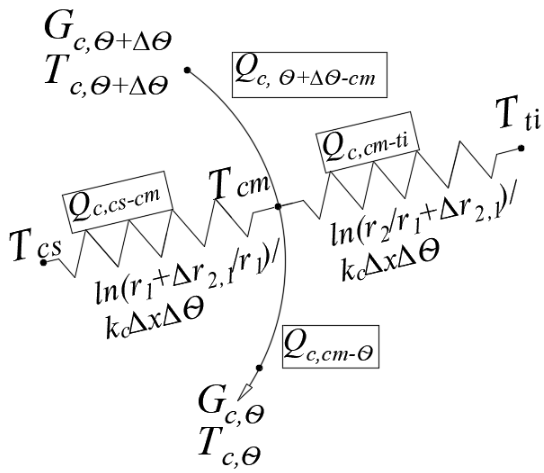

Figure 3. 20: Condensate-side thermal resistance

d) Coupling of the elementary control volume to thermal resistance (Figure 3.19 and 3.20):

$$Q_{c,cs-cm} = G_{s,r_1} r_1 \Delta\theta \Delta x i_{s,r_1} \tag{3. 134}$$

$$Q_{c,cm-ti} = Q_{c,r_2} \tag{3. 135}$$

e) The momentum balance of the elementary control volume (Figure 3.21):

The momentum balance was carried out to define the weighted mean temperature of the condensate. Consider the control volume $(r^*\Delta x\Delta\theta)$ shown in Figure 3.21. The forces acting in the control volume are due to buoyancy (F_B), gravity (F_g) and friction which is due to viscosity (F_τ).

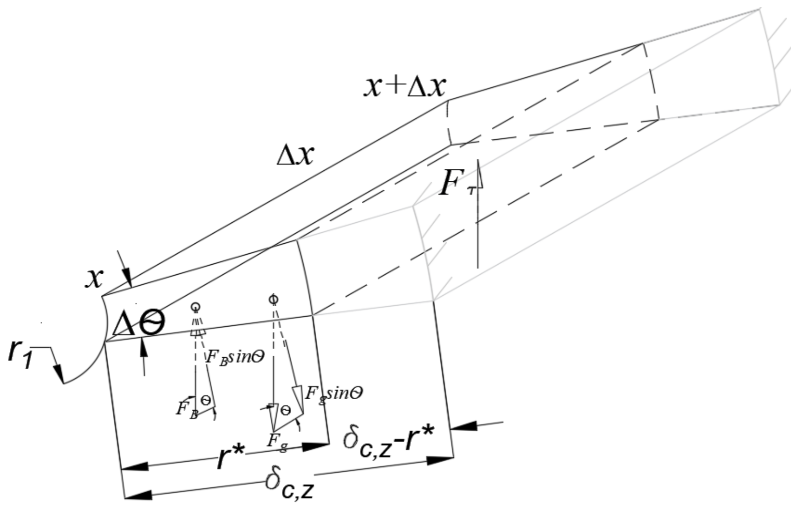

Figure 3. 21: Free body diagram for the control volume in the condensation film

The force balance for the free body diagram can be written as

$$\rho_c g(r^*\Delta x(r_1 + r^*)\Delta\theta)\sin(\theta) = \mu_c \frac{du_c}{dr^*}(\Delta x(r_1 + r^*)\Delta\theta) + \rho_s g(r^*\Delta x(r_1 + r^*)\Delta\theta)\sin(\theta) \tag{3. 136}$$

The changes of the condensate velocity over r^* was achieved by dividing Eq. (3.136) by $(\Delta x(r_1 + r^*)\Delta\theta)$ as:

$$\frac{du_c}{dr^*} = \frac{g(\rho_c - \rho_s)}{\mu_c} r^* \sin(\theta) \tag{3. 137}$$

The condensate velocity profile inside the condensation film, can be obtained by integrating the Eq. (3.137), so that at r_1 where $r^* = 0$, $\frac{du_c}{dr^*} = 0$, and at $r_2 = r_1 + \delta_{c,\theta}$ where $r^* = \delta_{c,\theta}$, $u_c = 0$, which led to the velocity profile of the condensate to be:

$$u_c(r^*) = \frac{g(\rho_c - \rho_s)}{2\mu_c} \sin(\theta)\, r^{*2} \tag{3. 138}$$

The mass flow rate of the condensate at the location θ, where the film thickness is $\delta_{c,\theta}$, and was define as:

$$G_{c,\theta}\Delta x\delta_{c,\theta} = \int_0^{\delta_{c,\theta}} \rho_c u_c(r^*)\Delta x dr^*$$

$$= \frac{\rho_c g\Delta x(\rho_c - \rho_s)}{2\mu_c}\sin(\theta)\int_0^{\delta_{c,\theta}} r^{*2} dr^* \tag{3. 139}$$

$$= \frac{\rho_c g\Delta x(\rho_c - \rho_s)}{6\mu_c} sin(\theta)\, {\delta_{c,\theta}}^3$$

The enthalpy transferred by the condensate as it flows through the cross section $\left(\Delta x\delta_{c,\theta}\right)$, can be written as:

$$G_{c,\theta}\Delta x\delta_{c,\theta}c_{pc}T_{cm} = c_{pc}\int_0^{\delta_{c,\theta}} \rho_c u_c(r^*)T_c(r^*)\Delta x dr^* \tag{3. 140}$$

Since the temperature profile within the condensation film in the *r*adial direction was assumed to be logarithmic, it can be expressed so that $T_c(r^*) = T_{cs}$ at r_1, where $r^* = 0$, and $T_c(r^*) = T_{ti}$ at r_2, where $r^* = \delta_{c,\theta}$. Therefore:

$$T_c(r^*) = T_{cs} - \frac{(T_{cs} - T_{ti})}{\ln\left(\frac{r_1 + \delta_{c,\theta}}{r_1}\right)} ln\left(\frac{r_1 + r^*}{r_1}\right) = T_{cs} - \frac{(T_{cs} - T_{ti})}{\ln\left(\frac{\delta_{c,\theta}}{r_1}\right)} ln\left(\frac{r^*}{r_1}\right) \tag{3. 141}$$

Therefore, Eq. (3.140) can be re-written as:

$$G_{c,\theta}\Delta x\delta_{c,\theta}T_{cm} = \rho_c \frac{g\Delta x(\rho_c-\rho_s)}{2\mu_c}\sin(\theta)\int_0^{\delta_{c,\theta}} r^{*2}\left(T_{cs} - \frac{(T_{cs}-T_{ti})}{\ln\left(\frac{\delta_{c,\theta}}{r_1}\right)} ln\left(\frac{r^*}{r_1}\right)\right)dr^* \tag{3. 142}$$

which can be simplified as:

$$G_{c,\theta}\Delta x\delta_{c,\theta}T_{cm} = \frac{\rho_c g\Delta x(\rho_c-\rho_s){\delta_{c,\theta}}^3}{2\mu_c}\sin(\theta)\left[\frac{T_{cs}}{3} - \frac{(T_{cs}-T_{ti})}{4}\right] \tag{3. 143}$$

Combine Eq. (3.139) and (4.143) as

$$\begin{aligned}\frac{\rho_c g\Delta x(\rho_c-\rho_s)}{6\mu_c}\sin(\theta)\,{\delta_{c,\theta}}^3T_{cm}\\ = \frac{\rho_c g\Delta x(\rho_c-\rho_s){\delta_{c,\theta}}^3}{2\mu_c}\sin(\theta)\left[\frac{T_{cs}}{3} - \frac{(T_{cs}-T_{ti})}{4}\right]\end{aligned} \tag{3. 144}$$

Therefore, the weighted mean temperature of the condensate in the condensation film is:

$$T_{cm} = T_{cs} - \frac{3}{4}(T_{cs}-T_{ti}) \tag{3. 145}$$

3.3.2.3. Tube wall-side elementary control volume

The tube wall-side elementary control volume and thermal resistance diagram are shown in Figures 3.22 and 3.23, respectively.

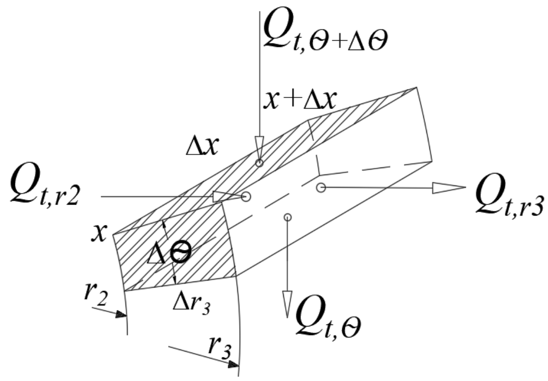

Figure 3. 22: Tube wall-side elementary control volume

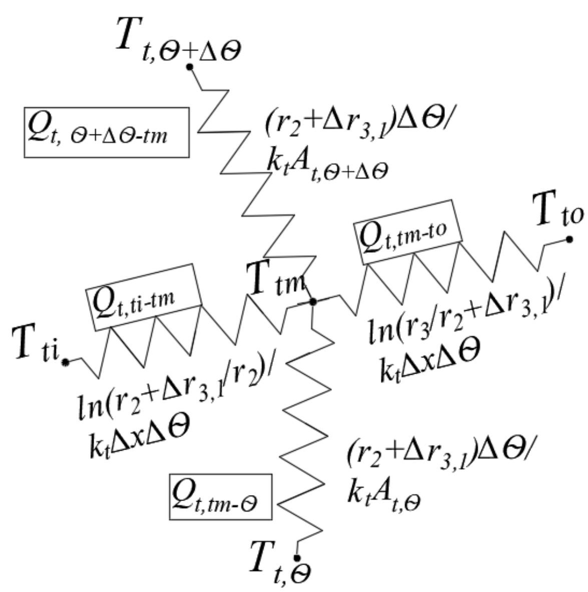

Figure 3. 23: Tube wall-side thermal resistance

a) The heat transfer balance for the thermal resistance (Figure 3.23):

$$Q_{t,ti-tm} + Q_{t,\theta+\Delta\theta-tm} = Q_{t,tm-to} + Q_{t,tm-\theta} \tag{3. 146}$$

where

$$Q_{t,ti-tm} = \frac{k_t \Delta x \Delta\theta (T_{ti} - T_{tm})}{ln\left(\frac{r_2 + \frac{\Delta r_3}{2}}{r_2}\right)} \tag{3. 147}$$

$$Q_{t,\theta+\Delta\theta-tm} = \frac{k_t \Delta r_3 \Delta x (T_{t,\theta+\Delta\theta} - T_{tm})}{\left(r_2 + \frac{\Delta r_3}{2}\right)\Delta\theta} \tag{3. 148}$$

$$Q_{t,tm-to} = \frac{k_t \Delta x \Delta\theta (T_{tm} - T_{to})}{ln\left(\frac{r_3}{r_2 + \frac{\Delta r_3}{2}}\right)} \tag{3. 149}$$

$$Q_{t,tm-\theta} = \frac{k_t \Delta r_3 \Delta x (T_{tm} - T_{t,\theta})}{\left(r_2 + \frac{\Delta r_3}{2}\right)\Delta\theta} \tag{3. 150}$$

b) Coupling of the elementary control volume to thermal resistance (Figure 3.22 and 3.23):

$$Q_{t,ti-tm} = Q_{c,r_2} \tag{3. 151}$$

$$Q_{t,\theta+\Delta\theta-tm} = Q_{t,\theta+\Delta\theta} \tag{3. 152}$$

$$Q_{t,tm-to} = Q_{t,r_3} \tag{3. 153}$$

$$Q_{t,tm-\theta} = Q_{t,\theta} \tag{3. 154}$$

3.3.2.4. Water-side elementary control volume

The deluge water-side elementary control volume is presented in Figure 3.24.

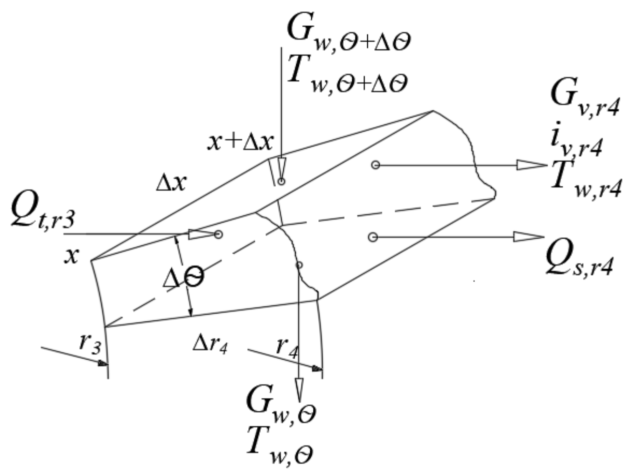

Figure 3. 24: Deluge water-side elementary control volume

a) The water mass balance for the elementary control volume (Figure 3.24):

$$\left(G_{w,\theta+\Delta\theta} - G_{w,\theta}\right)\Delta r_4 \Delta \mathrm{x} = G_{v,r_4} r_4 \Delta\theta\Delta x \tag{3. 155}$$

Divide with $\Delta x \Delta r_4 r_4 \Delta\theta$, and take the limit as $\Delta\theta \rightarrow 0$ to obtain the deluge water mass flux changes as:

$$\frac{\partial G_{w,\theta}}{\partial\theta} = \frac{G_{v,r_4} r_4}{\Delta r_4} \tag{3. 156}$$

b) The energy balance for the elementary control volume (Figure 3.24):

$$\begin{aligned} &Q_{w,r_3} + G_{w,\theta+\Delta\theta}\Delta r_4 \Delta \mathrm{x} c_{pw} T_{w,\theta+\Delta\theta} \\ &\qquad = \left(Q_{s,r_4} + G_{v,r_4} r_4 \Delta\theta\Delta x i_{v,r_4}\right) + G_{w,\theta}\Delta r_4 \Delta \mathrm{x} c_{pw} T_{w,\theta} \end{aligned} \tag{3. 157}$$

Let's the heat transfer leaving the control volume to be Q_{w,r_4}, which is the sum of sensible and latent heat crossing the air-water interface.

$$Q_{w,r_4} = Q_{s,r_4} + G_{v,r_4} r_4 \Delta\theta \Delta x i_{v,r_4} \tag{3. 158}$$

Substitute Q_{w,r_4} into Eq. (3.157) and re-arrange terms.

$$\begin{aligned} Q_{w,r_4} &= Q_{w,r_3} + \left(G_{w,\theta} + \Delta G_{w,\theta}\right)\Delta r_4 \Delta \mathrm{x} c_{pw}\left(T_{w,\theta} + \Delta T_{w\theta}\right) \\ &\quad - G_{w,\theta}\Delta r_4 \Delta \mathrm{x} c_{pw} T_{w,\theta} \\ &= Q_{w,r_3} - G_{w,\theta}\Delta r_4 \Delta \mathrm{x} c_{pw} \Delta T_{w\theta} \\ &\quad + \Delta G_{w,\theta}\Delta r_4 \Delta \mathrm{x} c_{pw} T_{w,\theta+\Delta\theta} \end{aligned} \tag{3. 159}$$

c) The heat transfer balance for the thermal resistance (Figure 3.25):

$$Q_{w,to-wm} + Q_{w,\theta+\Delta\theta-wm} = Q_{w,wm-ws} + Q_{w,wm-\theta} \tag{3. 160}$$

where

$$Q_{w,to-wm} = \frac{k_w \Delta x \Delta\theta (T_{to} - T_{wm})}{ln\left(\frac{r_3 + \Delta r_{4,1}}{r_3}\right)} \tag{3. 161}$$

$$\mathrm{Q_{w,wm-ws}} = \frac{k_w \Delta x \Delta\theta (T_{wm} - T_{ws})}{ln\left(\frac{r_4}{r_3 + \Delta r_{4,1}}\right)} = \frac{k_w \Delta x \Delta\theta (T_{to} - T_{ws})}{ln\left(\frac{r_4}{r_3}\right)} \tag{3. 162}$$

$$Q_{w,\theta+\Delta\theta-wm} = G_{w,\theta+\Delta\theta}(\Delta r_4 \Delta \mathrm{x}) c_{pw} (T_{w,\theta+\Delta\theta} - T_{wm}) \tag{3. 163}$$

$$Q_{w,wm-\theta} = G_{w,\theta}(\Delta r_4 \Delta \mathrm{x}) c_{pw} (T_{wm} - T_{w,\theta}) \tag{3. 164}$$

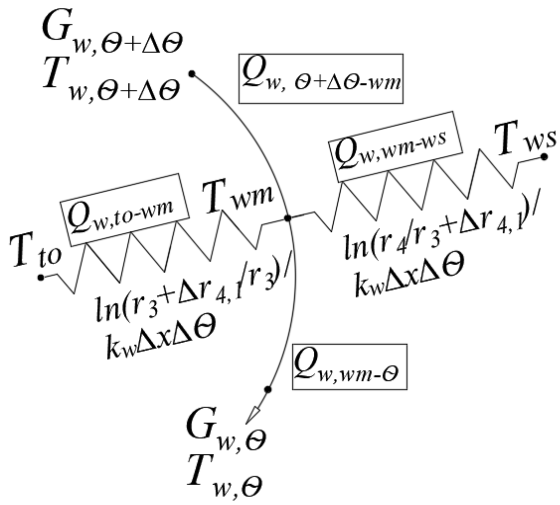

Figure 3. 25: Deluge water-side thermal resistance

d) Coupling of the elementary control volume to thermal resistance (Figure 3.24 and 3.25):

$$Q_{w,to-wm} = Q_{w,r_3} \tag{3. 165}$$

$$Q_{w,wm-ws} = Q_{w,r_4} \tag{3. 166}$$

e) The momentum balance on the water-side

The momentum balance of water-side control volume was carried out in the similar manner as that of condensate-side control volume, and with aim of determining the weighted mean temperature of the deluge water as:

$$T_{wm} = T_{to} - \frac{5}{8}(T_{to} - T_{ws}) \tag{3. 167}$$

3.3.2.5. Air - side elementary control volume

The air-side elementary control volume is shown in Figure 3.26, and the air was assumed to be moist and unsaturated.

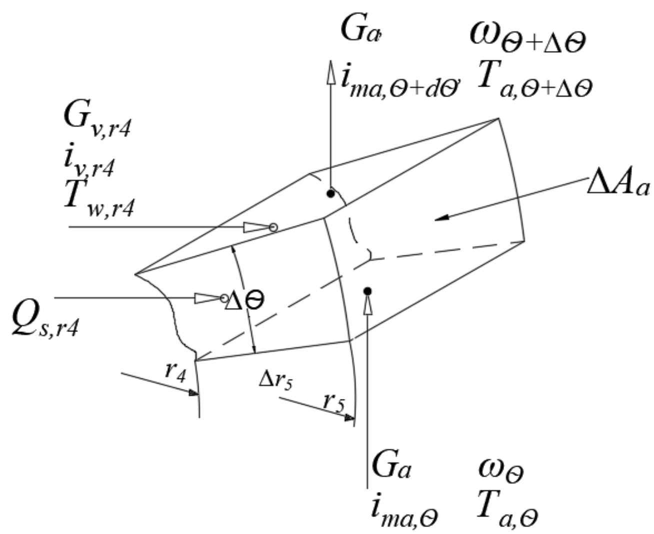

Figure 3. 26: Air-side elementary control volume

a) The water vapour mass balance for the elementary control volume (Figure 3.26):

$$G_{v,r_4} r_4 \Delta\theta \Delta x = G_a \Delta r_5 \Delta \mathrm{x}[(1+\omega_{\theta+\Delta\theta}) - (1+\omega_\theta)] \tag{3. 168}$$

Divide with $\Delta x \Delta r_5 r_5 \Delta\theta$, and take the limit as $\Delta\theta \rightarrow 0$ to obtain the change in humidity ratio as:

$$\frac{\partial \omega_\theta}{\partial \theta} = \frac{G_{v,r_4} r_4}{G_a \Delta r_5} \tag{3. 169}$$

Combine Eq. (3.156) and (3.169)

$$\frac{\partial \omega_\theta}{\partial \theta} = \frac{\partial G_{w,\theta}}{\partial \theta} \frac{\Delta r_4}{G_a \Delta r_5} \tag{3. 170}$$

b) The energy balance for the elementary control volume (Figure 3.26):

$$\left(Q_{s,r_4} + G_{v,r_4} r_4 \Delta\theta \Delta x i_{v,r_4}\right) = G_a \Delta r_5 \Delta \mathrm{x}\left(i_{ma,\theta+\Delta\theta} - i_{ma,\theta}\right) \tag{3. 171}$$

Substitute Eq. (3.158) into (3.171) and simplify

$$Q_{w,r_4} = G_a \Delta r_5 \Delta \mathrm{x} \Delta i_{ma\theta} \tag{3. 172}$$

c) The heat transfer balance for the thermal resistance (Figure 3.27):

$$Q_{s,ws-am} = h_a r_5 \Delta\theta \Delta x (T_{ws} - T_{am}) \tag{3. 173}$$

$$Q_{l,ws-am} = h_d r_5 \Delta\theta \Delta x i_{v,r_4} (\omega_{sw} - \omega_{\theta m}) \tag{3. 174}$$

Eq. (3.158) can now re-written as:

$$\begin{aligned} Q_{w,r_4} &= h_a r_5 \Delta\theta \Delta x (T_{ws} - T_{am}) + h_d r_5 \Delta\theta \Delta x i_{v,r_4} \left(\omega_{sw} - \omega_{\theta,m}\right) \\ &= G_a \Delta r_5 \Delta \mathrm{x} \Delta i_{ma,\theta} \end{aligned} \tag{3. 175}$$

Divide with $\Delta x \Delta r_5 r_5 \Delta\theta$, and take the limit as $\Delta\theta \rightarrow 0$ to obtain the change in moist air enthalpy as:

$$\frac{\partial i_{ma,\theta}}{\partial \theta} = \frac{h_a r_5}{G_a \Delta r_5} (T_{ws} - T_{am}) + \frac{h_d r_5}{G_a \Delta r_5} i_{v,r_4} \left(\omega_{sw} - \omega_{\theta,m}\right) \tag{3. 176}$$

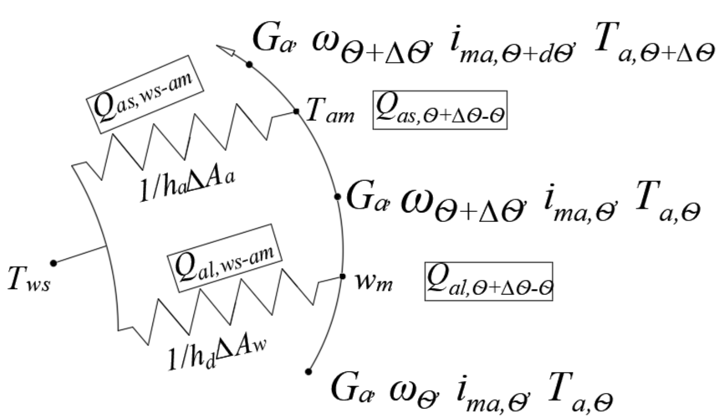

Figure 3. 27: Air-side thermal resistance

d) Coupling of the elementary control volume to thermal resistance (Figure 3.26 and 3.27):

$$Q_{l,ws-am} = Q_{l,\theta+\Delta\theta-\theta} \tag{3. 177}$$

$$Q_{s,ws-am} = Q_{s,\theta+\Delta\theta-\theta} \tag{3. 178}$$

3.3.3. Coupling of governing equations for Flat control volume

Some of the governing differential equations that describing the heat and mass transfer in the vertical flat section of the tube were obtained by coupling and simplifying the differential equations derived in sections 3.3.1.

3.3.3.1. Steam-condensate-side

Substitute Eq. (3.52) and (3.65) into (3.70)

$$\frac{k_c \Delta x \Delta z (T_{cs} - T_{cm})}{\Delta y_{2,1}} = G_{s,y_1} \Delta \mathrm{z} \Delta \mathrm{x} i_{s,y_1} = \Delta G_{cz} \Delta y_2 \Delta \mathrm{x} i_{s,y_1} \tag{3. 179}$$

Divide with $\Delta \mathrm{z} \Delta \mathrm{x} \Delta y_2$ and let $\Delta z \rightarrow 0$ and re-arrange terms to obtain the changes in condensate mass flux as:

$$\frac{\partial G_{cz}}{\partial \mathrm{z}} = \frac{k_c (T_{cs} - T_{cm})}{\Delta y_2 \Delta y_{2,1} i_{s,y_1}} \tag{3. 180}$$

The condensation film thicknesses can be attained from Eq. (3.66) as:

$$\frac{k_c \Delta x \Delta z (T_{cm} - T_{ti})}{\Delta y_{2,2}} = \frac{k_c \Delta x \Delta z (T_s - T_{ti})}{\Delta y_2} \tag{3. 181}$$

$$\Delta y_{2,2} = \frac{(T_{cm} - T_{ti})}{(T_s - T_{ti})} \Delta y_2 \tag{3. 182}$$

$$\Delta y_{2,1} = \Delta y_2 - \frac{(T_{cm} - T_{ti})}{(T_s - T_{ti})} \Delta y_2 \tag{3. 183}$$

Let the mass flow rate of the condensate per unit length Δx to be $\Gamma(z)$:

$$G_{c,z}\delta_c = \frac{\rho_c g(\rho_c - \rho_s)}{6\mu_c} {\delta_{c,z}}^3 = \Gamma(z) \tag{3. 184}$$

Therefore, the heat flux through the condensate film can be defined as:

$$\frac{\Gamma(z)}{\Delta z} i_{s,y_1} = \frac{k_c(T_{cs} - T_{ti})}{\delta_{c,z}} \tag{3. 185}$$

Substitute Eq. (3.184) into (3.185) and integrate to obtain the condensate film thickness as:

$$\frac{\rho_c g(\rho_c - \rho_s)}{2\mu_c} {\delta_{c,z}}^2 \frac{\Delta\delta_c}{\Delta z} = \frac{k_c(T_{cs} - T_{ti})}{\delta_{c,z} i_{s,y_1}} \tag{3. 186}$$

$$\delta_{c,z} = \left[\frac{8\mu_c k_c(T_{cs} - T_{ti})z}{\rho_c g(\rho_c - \rho_s) i_{s,y_1}}\right]^{1/4} = \Delta y_2 \tag{3. 187}$$

3.3.3.2. Tube wall

Combine Eqs. (3.66) and (3.83) and re-arrange terms to obtain the tube wall mean temperature as:

$$\frac{2k_t\Delta x\Delta z(T_{ti}-T_{tm})}{\Delta y_3}=\frac{2k_c\Delta x\Delta z(T_{cm}-T_{ti})}{\Delta y_2} \quad (3.\ 188)$$

$$T_{tm}=T_{ti}-\frac{k_c}{k_t}\frac{\Delta y_3}{\Delta y_2}(T_{cm}-T_{ti}) \quad (3.\ 189)$$

3.3.3.3. Deluge water-side

Combine Eqs. (3.92) and (3.107), and simplify to get the changes in deluge water mass flux over z-direction as:

$$\frac{\Delta G_{w,z}}{\Delta z}=G_a\frac{\Delta\omega_z}{\Delta z}\frac{\Delta y_5}{\Delta y_4} \quad (3.\ 190)$$

The deluge water film's thicknesses were attained from Eqs. (3.99), (3.99) and (3.102) as:

$$\frac{\mathrm{k_w}\Delta x\Delta z(\mathrm{T_{wm}}-\mathrm{T_{ws}})}{\Delta y_{4,2}}=\frac{k_w\Delta x\Delta z(T_{to}-T_{ws})}{\Delta y_4} \quad (3.\ 191)$$

$$\Delta y_{4,2}=\frac{(\mathrm{T_{wm}}-\mathrm{T_{ws}})}{(T_{to}-T_{ws})}\Delta y_4 \quad (3.\ 192)$$

$$\Delta y_{4,1}=\Delta y_4-\frac{(\mathrm{T_{wm}}-\mathrm{T_{ws}})}{(T_{to}-T_{ws})}\Delta y_4 \quad (3.\ 193)$$

From Eq. (3.104) deluge water surface temperature can be obtained as:

$$\frac{\mathrm{k_w}\Delta x\Delta z(\mathrm{T_{wm}}-\mathrm{T_{ws}})}{\Delta y_{4,2}}=Q_{w,y_4} \quad (3.\ 194)$$

$$\mathrm{T_{ws}} = \mathrm{T_{wm}} - \frac{Q_{w,y_4}\Delta y_{4,2}}{\mathrm{k_w}\Delta x \Delta z} \tag{3. 195}$$

3.3.3.4. Air-side

The changes in air humidity ratio can be attained by simplifying Eq. (3.115), dividing with $\Delta\mathrm{z}\Delta\mathrm{x}\Delta y_5$ and let $\Delta z \rightarrow 0$ as follow:

$$h_d \Delta\mathrm{z}\Delta\mathrm{x} i_{v,y_4}(\omega_{sw} - \omega_m) = G_a \Delta y_5 \Delta\mathrm{x} \Delta\omega_z i_{v,y_4} \tag{3. 196}$$

$$\frac{\partial \omega_z}{\partial z} = \frac{h_d}{G_a \Delta y_5}(\omega_{sw} - \omega_{zm}) \tag{3. 197}$$

3.3.4. Coupling of governing equations for Round control volume

The additional governing equations that define the heat and mass transfer in the round-end section of the tube were determined in the same way as that of vertical section. Therefore, after the coupling and simplification of several equations derived in section 3.3.2, the following governing equations were achieved.

3.3.4.1. Steam-condensate-side

The changes in condensate mass flux was defined from Eqs. (3.122), (3.124) and (3.130) as:

$$\frac{\partial G_{c,\theta}}{\partial \theta} = \frac{k_c(T_{cs} - T_{cm})}{ln\left(\frac{r_1 + \Delta r_{2,1}}{r_1}\right)\Delta r_2 i_{s,r_1}} \tag{3. 198}$$

The condensation film thicknesses can be attained from Eq. (3.131) as:

$$\frac{k_c \Delta x \Delta \theta (T_{cm} - T_{ti})}{ln\left(\frac{r_2}{r_2 - \Delta r_{2,2}}\right)} = \frac{k_c \Delta x \Delta \theta (T_{cs} - T_{ti})}{ln\left(\frac{r_2}{r_1}\right)}$$

$$\Delta r_{2,2} = r_2 \left[1 - \frac{1}{\exp\left(\frac{(T_{cm} - T_{ti})}{(T_{cs} - T_{ti})} ln\left(\frac{r_2}{r_1}\right)\right)}\right] \tag{3. 199}$$

$$\Delta r_{2,1} = \Delta r_2 - \Delta r_{2,2} \tag{3. 200}$$

3.3.4.2. Tube wall-side

From the combination of Eqs. (3.131) and (3.147), the tube wall mean temperature was obtained as:

$$\frac{k_t \Delta x \Delta \theta (T_{ti} - T_{tm})}{ln\left(\frac{r_2 + \frac{\Delta r_3}{2}}{r_2}\right)} = \frac{k_c \Delta x \Delta \theta (T_{cm} - T_{ti})}{ln\left(\frac{r_2}{r_1 + \Delta r_{2,1}}\right)}$$

$$T_{tm} = T_{ti} - \frac{k_c ln\left(\frac{r_2 + \frac{\Delta r_3}{2}}{r_2}\right)}{k_t ln\left(\frac{r_2}{r_1 + \Delta r_{2,1}}\right)} (T_{cm} - T_{ti}) \tag{3. 201}$$

3.3.4.3. Deluge water-side'

The changes in deluge water mass flux over angle θ was obtained from Eq. (3.170) as:

$$\frac{\partial G_{w\theta}}{\partial \theta} = G_a \frac{\partial \omega_\theta}{\partial \theta} \frac{\Delta r_5}{\Delta r_4} \tag{3. 202}$$

The deluge water film's thicknesses were attained from Eq. (3.162) as:

$$\frac{k_w \Delta x \Delta\theta (T_{wm} - T_{ws})}{ln\left(\frac{r_4}{r_4 - \Delta r_{4,2}}\right)} = \frac{k_w \Delta x \Delta\theta (T_{to} - T_{ws})}{ln\left(\frac{r_4}{r_3}\right)}$$

$$\Delta r_{4,2} = r_4 \left[1 - \frac{1}{\exp\left(\frac{(T_{wm} - T_{ws})}{(T_{to} - T_{ws})} ln\left(\frac{r_4}{r_3}\right)\right)}\right] \tag{3. 203}$$

$$\Delta r_{4,1} = \Delta r_4 - \Delta r_{4,2} \tag{3. 204}$$

From Eq. (3.162) and (3.166) deluge water surface temperature can be obtained as:

$$\frac{k_w \Delta x \Delta\theta (T_{wm} - T_{ws})}{ln\left(\frac{r_4}{r_3 + \Delta r_{4,1}}\right)} = Q_{w,r_4}$$

$$\mathrm{T_{ws}} = \mathrm{T_{wm}} - \frac{Q_{w,r_4} ln\left(\frac{r_4}{r_3 + \Delta r_{4,1}}\right)}{\mathrm{k_w} \Delta x \Delta\theta} \tag{3. 205}$$

3.3.4.4. Air-side

The changes in air humidity ratio can be attained by combining and simplifying Eqs. (3.169), (3.174) and (3.177).

$$\frac{\partial \omega_\theta}{\partial \theta} = \frac{h_d r_5}{G_a \Delta r_5} (\omega_{sw} - \omega_{\theta m}) \tag{3. 206}$$

3.3.5. Discretization of Governing Equations

The domain (tube), in Figure 3.28, was divided into discretized control volumes (grids) in the *z*-direction for the vertical flat section, and in the transverse direction for round-end sections. The nodal/grid points were place at the center and face/ interface of the control volumes as depicted in Figure 3.29 (a, b). The discretized equations were obtained by integrating the governing differential equations over the corresponding individual control volumes, and maintaining the conservation laws. The discretization of governing equations enable the analysis of the local variation of every parameter easier (Corberán *et al.*, 2000).

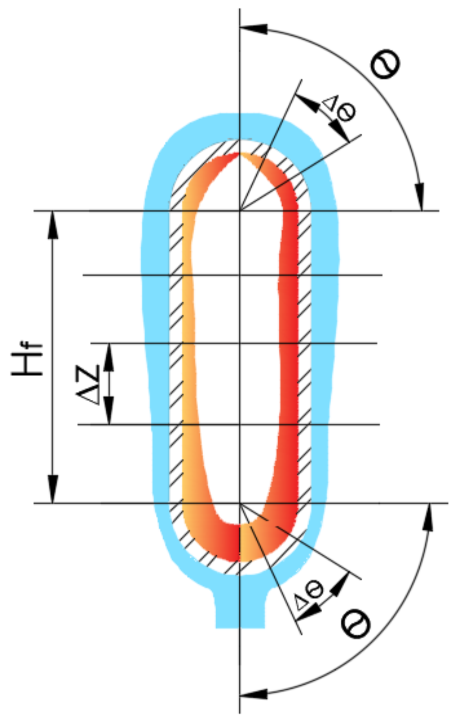

Figure 3. 28: Air-flow over domain (tube)

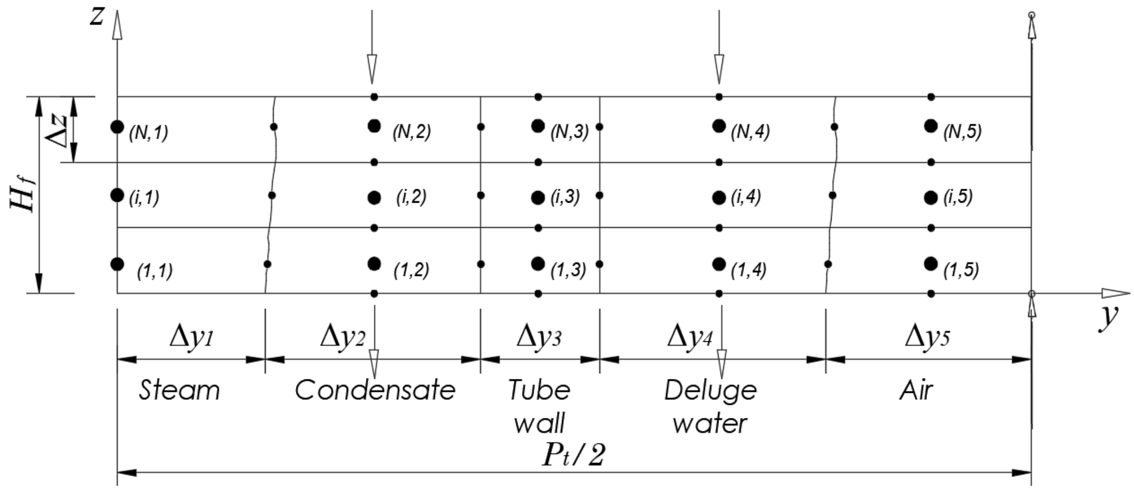

a) Flat section

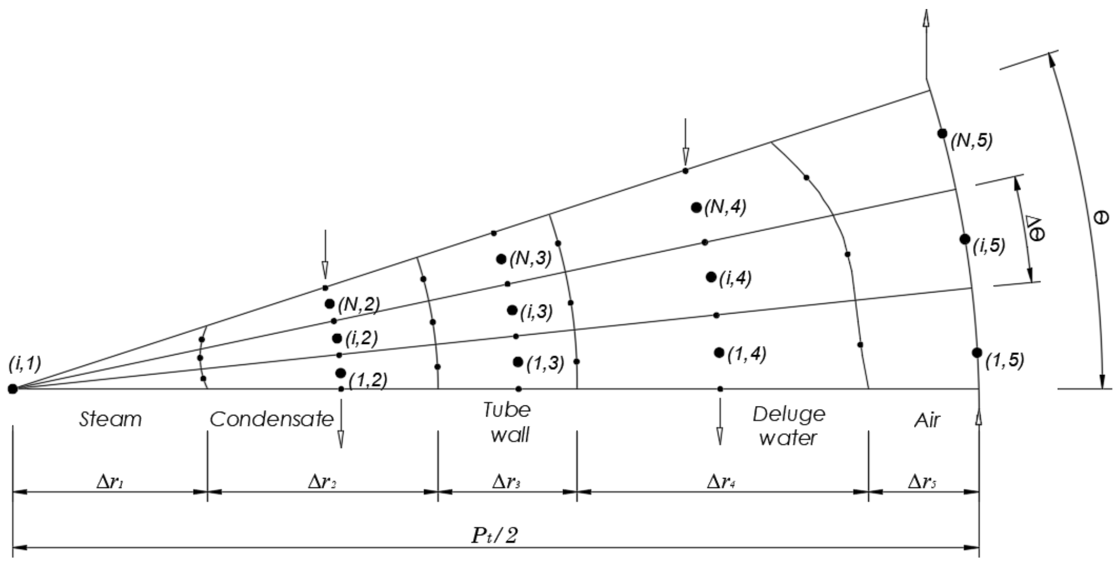

b) Round-end section

Figure 3. 29: Grid points network

The linear upwind differencing method was used to discretize the governing differential equations. The linear upwind differencing scheme is the mostly common method used for the convection dominated flows, because it provides the numerical stable solutions and considers the flow direction (Suhas, 1980).

Discretization of the governing equations of the *i-th* row/interval for the vertical flat section of the tube is shown below. The subscript i of the index's notation used in Figure 3.29 denotes the grid point index in the *z*-direction, and the number after a comma, denotes the grid point index in the *y*- or transverse direction.

The height of each grid cell was determined as:

$$\Delta z = H_t / N_r \tag{3. 207}$$

where, H_t is tube height and N_r is the number of intervals in the *z*-direction.

$$\begin{aligned} Q_{c,(i,2-1)} &= \left(G_{c(i+1,2)} - G_{c(i-1,2)}\right)\Delta y_2 \Delta x i_{s(i,2-1)} \\ &= \frac{k_{c(i,2)}\Delta x \Delta z\left(T_{c(i,2-1)} - T_{c(i,2)}\right)}{\Delta y_{2,1}} \end{aligned} \tag{3. 208}$$

$$\frac{\left(G_{c(i+1,2)} - G_{c(i-1,2)}\right)}{\Delta \mathrm{z}} = \frac{k_{c(i,2)}\left(T_{c(i,2-1)} - T_{c(i,2)}\right)}{\Delta y_2 \Delta y_{2,1} i_{s(i,2-1)}} \tag{3. 209}$$

$$\Delta y_{2,2} = \frac{\left(T_{c(i,2)} - T_{t(i,3-1)}\right)}{\left(T_{c(i,2-1)} - T_{t(i,3-1)}\right)}\Delta y_2 \tag{3. 210}$$

$$
\begin{aligned}
Q_{c,(i,2+1)} &= \left(G_{c(i+1,2)} - G_{c(i-1,2)}\right)\Delta y_2 \Delta \mathrm{x}\left(i_{s(i,2-1)} - c_{pc(i,2)} T_{c(i+1,2)}\right) \\
&\quad + G_{c(i-1,2)}\Delta y_2 \Delta \mathrm{x} c_{pc(i,2)}\left(T_{c(i+1,2)} - T_{c(i-1,2)}\right) \\
&= Q_{c,(i,2-1)} + Q_{c,(i+1,2)} - Q_{c,(i-1,2)} \\
&= \frac{k_{c(i,2)}\Delta x \Delta z\left(T_{c(i,2)} - T_{t(i,3-1)}\right)}{\Delta y_{2,2}}
\end{aligned}
\tag{3. 211}
$$

$$
T_{c(i,2)} = T_{c(i,2-1)} - \frac{3}{4}\left(T_{c(i,2-1)} - T_{t(i,3-1)}\right) \tag{3. 212}
$$

$$
T_{t(i,3)} = T_{t(i,3-1)} - \frac{k_{c(i,2)}}{k_{t(i,3)}}\frac{\Delta y_3}{\Delta y_2}\left(T_{c(i,2)} - T_{t(i,3-1)}\right) \tag{3. 213}
$$

$$
\begin{aligned}
Q_{t(i,3+1)} &= Q_{t(i,3-1)} + Q_{t(i+1,3)} - Q_{t(i-1,3)} \\
&= \frac{2k_{t(i,3)}\Delta x \Delta z(T_{t(i,3)} - T_{t(i,3+1)})}{\Delta y_3}
\end{aligned}
\tag{3. 214}
$$

$$
G_{w(i+1,4)} - G_{w(i-1,4)} = G_a\left(\omega_{z(i+1,4)} - \omega_{z(i-1,4)}\right)\frac{\Delta y_5}{\Delta y_4} \tag{3. 215}
$$

$$
\Delta y_{4,2} = \frac{\left(\mathrm{T}_{\mathrm{w}(i,4)} - \mathrm{T}_{\mathrm{w}(i,4+1)}\right)}{\left(T_{t(i,3+1)} - \mathrm{T}_{\mathrm{w}(i,4+1)}\right)}\Delta y_4 \tag{3. 216}
$$

$$\begin{aligned}
\mathrm{Q}_{\mathrm{w}(i,4+1)} &= \mathrm{Q}_{\mathrm{w}(i,4-1)} + Q_{w(i+1,4)} - Q_{w(i-1,4)} \\
&= \frac{k_{w(i,4)}\Delta x \Delta z\left(\mathrm{T}_{\mathrm{w}(i,4)} - \mathrm{T}_{\mathrm{w}(i,4+1)}\right)}{\Delta y_{4,2}} \\
&= \mathrm{Q}_{\mathrm{w}(i,4-1)} - G_{w(i-1,4)}\Delta y_4 \Delta \mathrm{x} c_{pw(i,4)}(T_{w(i+1,4)} \\
&- T_{w(i-1,4)}) + (G_{w(i+1,4)} \\
&- G_{w(i-1,4)})\Delta y_4 \Delta \mathrm{x} c_{pw(i,4)} T_{w(i+1,4)}
\end{aligned} \tag{3. 217}$$

$$\mathrm{T}_{\mathrm{w}(i,4)} = T_{t(i,3+1)} - \frac{5}{8}\left(T_{t(i,3+1)} - \mathrm{T}_{\mathrm{w}(i,4+1)}\right) \tag{3. 218}$$

$$\mathrm{T}_{\mathrm{w}(i,4+1)} = \mathrm{T}_{\mathrm{w}(i,4)} - \frac{\mathrm{Q}_{\mathrm{w}(i,4+1)}\Delta y_{4,2}}{k_{w(i,4)}\Delta x \Delta z} \tag{3. 219}$$

$$\begin{aligned}
i_{ma(i+1,5)} &= i_{ma(i-1,5)} + \frac{h_a \Delta \mathrm{z}}{G_a \Delta y_5}\left(T_{w(i,4+1)} - T_{a(i,5)}\right) \\
&+ \frac{h_d \Delta \mathrm{z}}{G_a \Delta y_5} i_{v(i,5-1)}\left(\omega_{sw(i,4+1)} - \omega_{(i,5)}\right)
\end{aligned} \tag{3. 220}$$

$$\begin{aligned}
\mathrm{Q}_{\mathrm{w}(i,5-1)} &= h_a \Delta x \Delta z\left(T_{w(i,4+1)} - T_{a(i,5)}\right) \\
&+ h_d \Delta x \Delta z i_{v(i,5-1)}\left(\omega_{sw(i,4+1)} - \omega_{(i,5)}\right) \\
&= G_a \Delta y_5 \Delta \mathrm{x}\left(i_{ma(i+1,5)} - i_{ma(i-1,5)}\right)
\end{aligned} \tag{3. 221}$$

$$\omega_{z(i+1,5)} = \omega_{z(i-1,5)} + \frac{h_d \Delta z}{G_a \Delta y_5}\left(\omega_{sw(i,5-1)} - \omega_{(i,5)}\right) \tag{3. 222}$$

Discretization of the governing equations of the *i-th* row/interval for the round section of the tube is shown below. The angle of each grid cell was determined as:

$$\Delta\theta = \theta/N_r \tag{3. 223}$$

where, θ is angle of the round-end section.

$$\frac{\left(G_{c(i+1,2)} - G_{c(i-1,2)}\right)}{\Delta\theta} = \frac{k_{c(i,2)}\left(T_{c(i,2-1)} - T_{c(i,2)}\right)}{ln\left(\frac{r_1 + \Delta r_{2,1}}{r_1}\right)\Delta r_2 i_{s(i,2-1)}} \tag{3. 224}$$

$$\Delta r_{2,2} = r_2\left[1 - \frac{1}{\exp\left(\frac{\left(T_{c(i,2)} - T_{t(i,3-1)}\right)}{\left(T_{c(i,2-1)} - T_{t(i,3-1)}\right)} ln\left(\frac{r_2}{r_1}\right)\right)}\right] \tag{3. 225}$$

$$Q_{c(i,2-1)} = \left(G_{c(i+1,2)} - G_{c(i-1,2)}\right)\Delta r_2 \Delta \mathrm{x} i_{s(i,2-1)} \tag{3. 226}$$

$$\begin{aligned} Q_{c(i,2+1)} = \frac{k_{c(i,2)}\Delta x\Delta\theta\left(T_{c(i,2)} - T_{t(i,3-1)}\right)}{ln\left(\frac{r_2}{r_1 + \Delta r_{2,1}}\right)} \\ = \left(G_{c(i+1,2)} - G_{c(i-1,2)}\right)\Delta r_2 \Delta \mathrm{x}\left(i_{s(i,2-1)} - c_{pc(i,2)} T_{c(i+1,2)}\right) \\ + G_{c(i-1,2)}\Delta r_2 \Delta \mathrm{x} c_{pc(i,2)}\left(T_{c(i+1,2)} - T_{c(i-1,2)}\right) \\ = Q_{c(i+1,2)} + Q_{c(i,2-1)} - Q_{c(i-1,2)} \end{aligned} \tag{3. 227}$$

$$T_{c(i,2)} = T_{c(i,2-1)} - \frac{3}{4}\left(T_{c(i,2-1)} - T_{t(i,3-1)}\right) \tag{3. 228}$$

$$T_{t(i,3)} = T_{t(i,3-1)} - \frac{k_{c(i,2)}}{k_{t(i,3)}} \frac{ln\left(\frac{r_2 + \frac{\Delta r_3}{2}}{r_2}\right)}{ln\left(\frac{r_2}{r_1 + \Delta r_{2,1}}\right)}\left(T_{c(i,2)} - T_{t(i,3-1)}\right) \tag{3. 229}$$

$$Q_{t(i,3+1)} = Q_{t(i,3-1)} + Q_{t(i+1,3)} - Q_{t(i-1,3)} = \frac{k_{t(i,3)}\Delta x\Delta\theta\left(T_{t(i,3)} - T_{t(i,3+1)}\right)}{ln\left(\frac{r_3}{r_2+\frac{\Delta r_3}{2}}\right)} \tag{3. 230}$$

$$G_{w(i+1,4)} - G_{w(i-1,4)} = G_a\left(\omega_{\theta(i+1,4)} - \omega_{\theta(i-1,4)}\right)\frac{\Delta r_5}{\Delta r_4} \tag{3. 231}$$

$$\Delta r_{4,2} = r_4\left[1 - \frac{1}{\exp\left(\frac{\left(\mathrm{T}_{\mathrm{w}(i,4)} - \mathrm{T}_{\mathrm{w}(i,4+1)}\right)}{\left(T_{t(i,3+1)} - \mathrm{T}_{\mathrm{w}(i,4+1)}\right)}ln\left(\frac{r_4}{r_3}\right)\right)}\right] \tag{3. 232}$$

$$\begin{aligned}
\mathrm{Q}_{\mathrm{w}(i,4+1)} &= \mathrm{Q}_{\mathrm{w}(i,4-1)} + Q_{w(i+1,4)} - Q_{w(i-1,4)} \\
&= \frac{k_{w(i,4)}\Delta x\Delta\theta\left(\mathrm{T}_{\mathrm{w}(i,4)} - \mathrm{T}_{\mathrm{w}(i,4+1)}\right)}{ln\left(\frac{r_4}{r_3 + \Delta r_{4,1}}\right)} \\
&= \mathrm{Q}_{\mathrm{w}(i,4-1)} - G_{w(i-1,4)}\Delta r_4\Delta \mathrm{x} c_{pw(i,4)}(T_{w(i+1,4)} \\
&- T_{w(i-1,4)}) + (G_{w(i+1,4)} \\
&- G_{w(i-1,4)})\Delta r_4\Delta \mathrm{x} c_{pw(i,4)}T_{w(i+1,4)}
\end{aligned} \tag{3. 233}$$

$$\mathrm{T}_{\mathrm{w}(i,4)} = T_{t(i,3+1)} - \frac{5}{8}\left(T_{t(i,3+1)} - \mathrm{T}_{\mathrm{w}(i,4+1)}\right) \tag{3. 234}$$

$$\mathrm{T}_{\mathrm{w}(i,4+1)} = \mathrm{T}_{\mathrm{w}(i,4)} - \frac{\mathrm{Q}_{\mathrm{w}(i,4+1)}ln\left(\frac{r_4}{r_3+\Delta r_{4,1}}\right)}{k_{w(i,4)}\Delta x\Delta\theta} \tag{3. 235}$$

$$i_{ma(i+1,5)} = i_{ma(i-1,5)} + \frac{h_a r_5}{G_a \Delta r_5} \left(T_{w(i,4+1)} - T_{a(i,5)}\right) + \frac{h_d r_5}{G_a \Delta r_5} i_{v(i,5-1)} \left(\omega_{sw(i,4+1)} - \omega_{(i,5)}\right) \tag{3. 236}$$

$$\begin{aligned} \mathrm{Q}_{\mathrm{w}(i,5-1)} &= h_a r_5 \Delta\theta \Delta x \left(T_{w(i,4+1)} - T_{a(i,5)}\right) \\ &+ h_d r_5 \Delta\theta \Delta x i_{v(i,5-1)} \left(\omega_{sw(i,4+1)} - \omega_{(i,5)}\right) \\ &= G_a \Delta r_5 \Delta \mathrm{x} \left(i_{ma(i+1,5)} - i_{ma(i-1,5)}\right) \end{aligned} \tag{3. 237}$$

$$\omega_{\theta(i+1,5)} = \omega_{\theta(i-1,5)} + \frac{h_d r_5 \Delta\theta}{G_a \Delta r_5} \left(\omega_{sw(i,5-1)} - \omega_{(i,5)}\right) \tag{3. 238}$$

3.3.6. Solution of Governing Equations and Grid Dependency

A two-dimensional numerical model was analysed based on heat and mass transfer analogy method, and following the procedures in Figure 3.30. The heat and mass transfer analogy was found to be easier to use (Zou *et al.*, 2016). Initially, the bundle's geometric parameters and the inputs parameters were given. Then, some of the output parameters were guessed. The steam, water, and air properties were evaluated at steam, and mean water and air temperatures, respectively. The dimensionless parameters (Re, P_r, Sc, N_u, Sh) were computed, using correlations available in the literatures. Sequentially, the heat, mass and overall heat transfer coefficients were calculated.

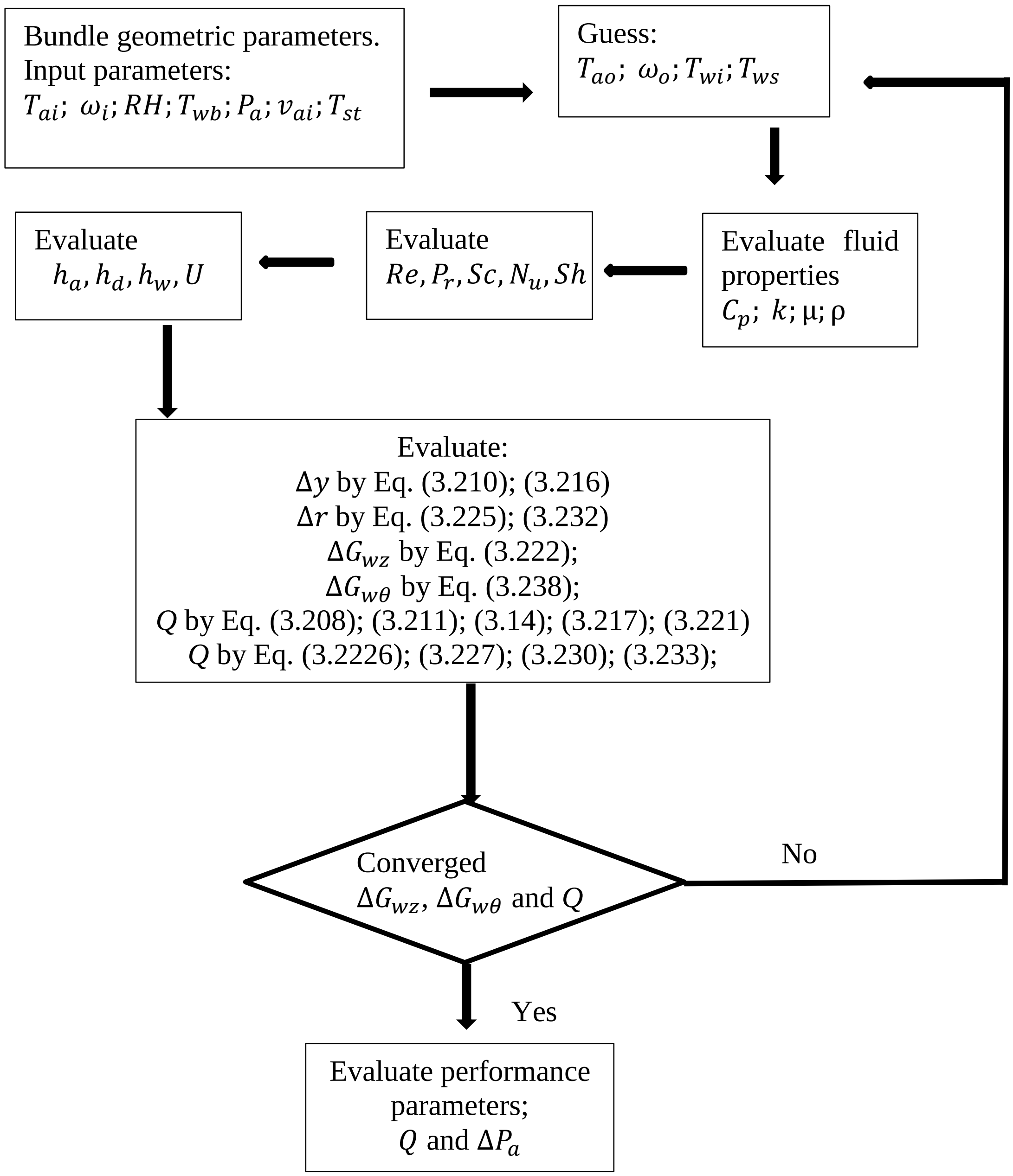

Figure 3. 30: The general algorithm which describes the two-dimensional model solutions procedures

The grid dependency of the two-dimensional numerical solutions on the grid cell sizes was performed at same operating conditions that were used in one-dimensional model validation, and as presented in the Table 3.1. The flow on the air-side was considered as shown is Figure 3.5. The manual grid dependency was carried out. The tube was divided into several intervals/rows as indicated in Figure 4.29. The larger the number of the intervals, the smaller the size of the grid cells, and variations in the numerical solutions. Some of the calculated variables for both round-end (down and upper) and flat tube sections were normalised and plotted against the number of intervals as shown in Figure 3.31 (a, b, c). From all Figures, it can be seen that the numerical solution started to be stable at interval number 15, ($N_r = 15$). Therefore, the solutions at this interval number were taken to be two-dimensional model's solutions, and were compared to one-dimensional model's solutions.

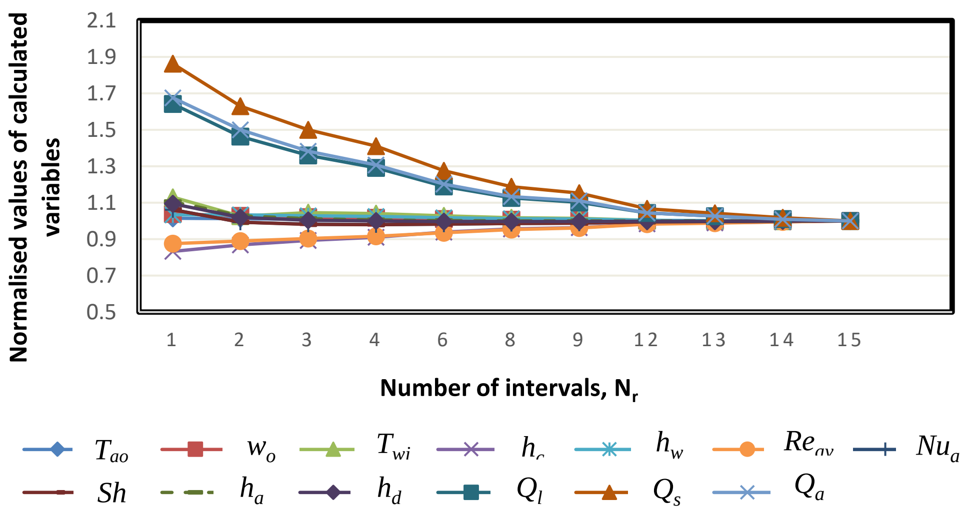

a) Down round-end section

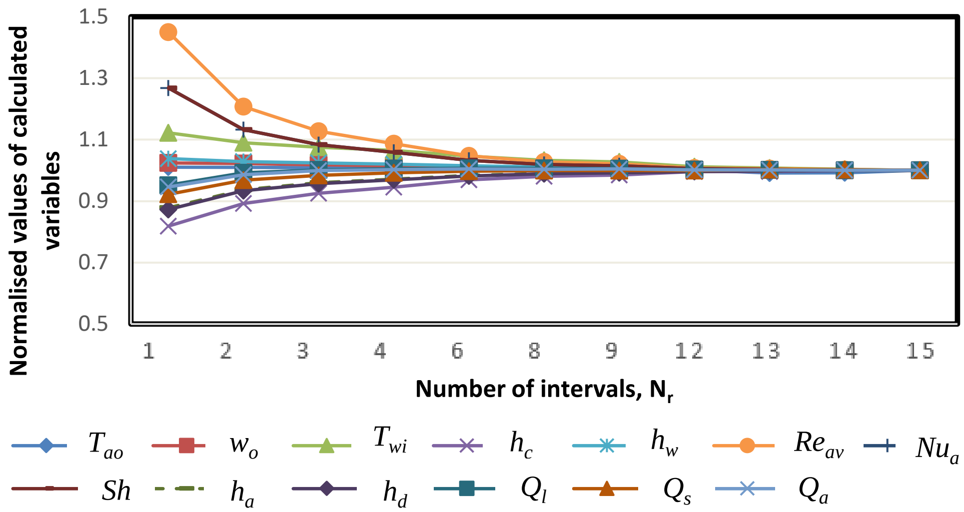

b) Flat section

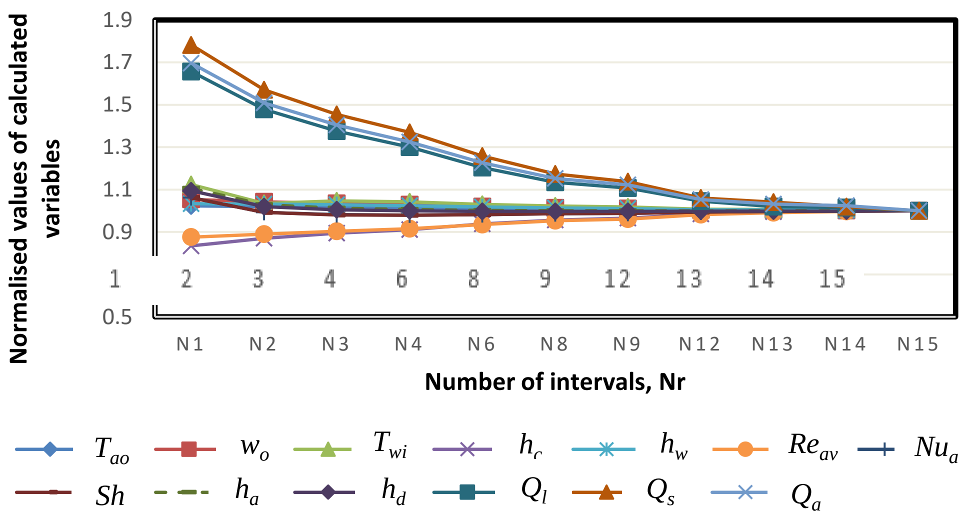

c) Upper round-end section

Figure 3. 31: The grid dependency of the two-dimensional numerical solutions

3.3.7. Validation of Model

For the validation of the two-dimensional numerical model, its results were compared to that of one-dimensional analytical model obtained from heat and mass transfer analogy method as depicted in Tables 3.4 and 3.5. Both heat transfer rate and air-side pressure drop yielded from one-dimensional model were found to be 4.83 % and 1 % higher than that of two-dimensional model. The differences between the solutions were primarily due to the variation of air and water properties in two-dimensional model. Furthermore, the drag coefficient (C_D) in two-dimensional model was computed by employing the equation presented in Khan *et al.* (2004), while in one-dimensional the drag coefficient (C_D) was obtained from the drag coefficient (C_D) – Reynold number (Re_D) graph of Schlichting (1979) as presented in Yunus and Afshin (2011). This might also lead to the discrepancy in the air-side pressure drop values. Hence, with these insignificant differences it can be concluded that, the two-dimensional model is valid for the analysis of the thermal performance of a CDTB. Furthermore, it can be concluded that, using either model, will not affect the thermal performance of a CDTB.

Moreover, the two-dimensional model results were compared to that of Angula (2015), in which the modelling was performed under an assumption that the tube has flat ends, and not round, and therefore, the governing differential equations were derived using Cartesian coordinates, and were integrated over the entire tube height. The heat transfer rate and the air-side pressure drop of the current model was found to be 1.9 % and 10% high and low, respectively than that of Angula (2015). Therefore, it can be also concluded that, considering the tube round ends to be as flat ends, does not have much impact the thermal performance of the tube bundle.

Table 3. 4: Comparison of one and two-dimensional model results as per section of the tube

	Description	Condensation heat transfer coefficient	Deluge water inlet temperature	Deluge water heat transfer coefficient	Outlet air temperature	Outlet air humidity ratio	Air-side heat transfer coefficient	Mass transfer coefficient (critical region)	Heat transfer rate	Air-side pressure drop
	Symbol	h_c	T_{wi}	h_w	T_{ao}	ω_{ao}	h_a	h_d	Q_a	ΔP_a
	Units	$\mathbf{W/m^2\,K}$	℃	$\mathbf{W/m^2\,K}$	℃	**kg/kg**	$\mathbf{W/m^2\,K}$	$\mathbf{W/m^2\,K}$	**W**	$\mathbf{p_a}$
Round Upper Section	1D Heat and Mass Transfer Analogy Approach	17471.16	43.83	21143.32	16.44	0.00871	26.16	0.02445	139.49	**≈0**
	2D Heat and Mass Transfer Analogy Approach	17675.27	29.75	18255.28	16.42	0.00857	33.13	0.03233	136.26	**≈0**
Flat Section	1D Heat and Mass Transfer Analogy Approach	24840.96	-	872.92	-	-	18.32	0.01749	514.77	0.6042
	2D Heat and Mass Transfer Analogy Approach	32656.61	-	842.54	-	-	18.06	0.0173	479.87	0.5259
Down Round Section	1D Heat and Mass Transfer Analogy Approach	17240.37	-	21154.80	-	-	26.11	0.024581	145.17	24.85
	2D Heat and Mass Transfer Analogy Approach	17420.63	-	18122.34	-	-	33.13	0.03262	143.93	24.69

Table 3. 5: Comparison of average one and two-dimensional model solutions

Description	Condensation heat transfer coefficient	Deluge water inlet temperature,	Deluge water heat transfer coefficient	Outlet air temperature,	Outlet air humidity ratio	Air-side heat transfer coefficient	Mass transfer coefficient (critical region)	Heat transfer rate	Air-side pressure drop
Symbol	h_c	T_{wi}	h_w	T_{ao}	ω_{ao}	h_a	h_d	Q_a	ΔP_a
Units	$\mathrm{W/m^2\,K}$	℃	$\mathrm{W/m^2\,K}$	℃	$\mathrm{kg/kg}$	$\mathrm{W/m^2\,K}$	$\mathrm{W/m^2\,K}$	W	$\mathrm{p_a}$
1D Heat and Mass Transfer Analogy Approach	19850.83	43.83	14390.35	16.44	0.00871	23.53	0.02217	799.42	25.45
2D Heat and Mass Transfer Analogy Approach	22584.17	29.75	12406.72	16.42	0.00857	28.11	0.02742	760.83	25.22

Chapter 4: Design Optimization of Conventional Delugeable Tube Bundle Thermal Performance

4.1. Introduction

This Chapter details the design optimization and geometric parameters adjustment of the Conventional Delugeable Tube Bundles (CDTB). This was performed in order to identify the best configuration for the HDWD second stages tube bundle (CDTB), as well as to determine the overall size of HDWD that can replace the CD in an existing ACC system of the local considered generating unit. The design optimization and dimensions adjustment were conducted in two steps, and using the two-dimensional model. In the first step, the optimization was performed and validated by comparing CDTB performance to that of the Delugeable Round Tube Bundle (DRTB) presented in Anderson (2014) study, which was the latest upgraded version of both Heyns (2008) and Owen (2013)'s DRTB, and which later was modified by to Plessis and Owen (2020) to become a single-stage HDWD. In the second step, the geometric parameters of the best CDTB configuration from the first step were adjusted, so that they correspond to that of the first stage tube bundle, which was constructed using the geometric parameters of the A-frame CD units for ACC system of a local generating unit. The width, length and steam flow area for the CDTB were adjusted and adapted based on the space created after the shortening of the tubes of first stage from the original length of CD tubes. The heat transfer rate and air-side pressure drop were used as critical performance measures during both optimisation and dimensions adjustment.

The identification of the HDWD's configuration had been performed by several researchers. In Heyns (2008) study, the geometric parameters of the first stage tube bundle were determined by using the geometric parameters of the A-frame array CD unit. The length of the finned tubes of CD unit was reduced from 7.52 m to 4.5 m in order to accommodate the second stage multi-row horizontal round tube bundle of 10.8 m length. Similarly, through the analytical evaluation, Owen (2013) identified the best second stage tube bundle configuration of an induced HDWD. The critical performance measures used were heat transfer rate, steam-side pressure drop and ejector loading. The configuration that provided the high heat transfer rate, low steam-side pressure drop, and minimal ejector loading was considered to be the best. Anderson (2014) incorporated Owen (2013) best configuration tube bundle, however, during performance analysis the critical performance measures were heat transfer rate and air-side pressure drop. Unlikely in Owen (2013), the air-side pressure drop was not defined by employing Niitsu, Naito and Anzai (1967) correlation as it was found to underestimate the pressure drop over the tube bundle.

Since one of the main functions of the dephlegmator is to provide an additional vapour flow, in order to avoid vapor backflow in the primary condenser units, a careful design of the HDWD is essential. The vapor backflow in primary condenser units is mainly due to row effects and inlet loss coefficient distributions (Smit, 2000). This occurs when the pressure drop over two tubes of the same vapor pass are different. This shows that full condensation has happened in the tube with the highest pressure drop. Therefore, the dephlegmator should be designed to overcome the row effects and inlet loss coefficient distributions. If the dephlegmator consists of the multi-rows tube bundle, dephlegmator itself can be subjected to row effects. Therefore, the ejector is required to remove the non-condensable gases as well as eject adequate vapor to prevent backflow in the upstream dephlegmator tubes row. The row effects can be eliminated by using the single-row tube pass (Owen, 2013).

4.2. Tube bundle optimization

In most of the literatures, the heat exchangers or tube bundles performance optimisations were based on the operating costs, which was defined through a comparison of pressure drops of different alternatives. For this approach, the objective function is only taking into account the operational costs parameters. However, for power plant heat exchangers applications, this optimisation approach was found not to be adequate. Therefore, a different approach that comprises of the objective function which influenced also by the heat transfer ability of the heat exchanger should be used (McLellan, 2015). Different response parameters or value of comparison have been used in several studies in which heat exchanger optimisations were conducted. Catton (2010) used heat exchanger effectiveness, pumping power and heat transfer rate as key and response parameters during the shell and tube heat exchanger optimisation. This value was defined as heat transfer divided by the pumping power per change in temperature. The heat generation cost was used as a value of comparison by (Orozaliev *et al.,* 2010).

Different optimisation techniques such as: Artificial Neural Network (ANN), global sensitivity analysis, harmony search algorithm and Generic Algorithm have been used by numerous researchers. Xie *et al.* (2007) used back propagation (BP) neural network algorithm to analyse the heat exchanger temperature differences and heat transfer rate. Naphon and Arisariyawong (2018) and Reynoso-Jardón *et al.* (2019) used ANN approach to evaluate optimal thermal design for heat exchangers. However, in Reynoso-Jardón *et al.* (2019) study, the material type of a heat exchanger was considered as part of the variables. The usage exploration of global sensitivity analysis and harmony search algorithm for shell and tube heat exchangers design optimization was conducted by Fesanghary *et al.* (2009). Generic Algorithm is one of the most commonly used techniques. In this technique, the population comprises of several heat exchanger designs, which consist of different values of all the considered design parameters (Catton, 2010). Furthermore, Generic Algorithm was found having advantage over other techniques in attaining numerous results of same quality, as well as providing quiet enhancement in the optimal designs than traditional designs (Resat *et al.*, 2006).

The objective of the design optimization was reached by maximining the heat transfer rate and minimizing the air-side pressure drop, by ensuring that it is not exceeding the pressure drop of similar delugeable tube bundles in the literatures to which it is being compared. In addition to these key parameters, the available space for installation of the proposed induced HDWD was also considered as a crucial parameter.

4.2.1. Design Evaluation Method

The heat exchangers can be analysed using two methods: the log mean temperature difference (LMTD) and the effectiveness-number of transfer units (ε-NTU) methods. The LMTD method was employed during the CDTB thermal optimisation. The LMTD method was found to be suitable for heat exchanger performance calculations (McLellan, 2015).

Since, the outlet conditions were unknown, the values of outlet parameters were initial guessed, and through iterative method, the final values were obtained. The optimization of the CDTB thermal performance was performed by means of a validated two-dimensional numerical model which was based on heat and mass transfer analogy method. This model was well presented in Chapter 3. This model requires solution of both thermal-based function and friction-based function. The steam temperature and pressure, deluge water inlet flow rate, and all air operating inlet conditions were kept constant during optimisation. For the condensate and deluge water, the bulk mean temperatures were determined. The output parameters such as outlet air temperature, heat transfer rate and air-side pressure drop were computed.

4.2.2. Optimization validation and design variables

The optimization validation was accomplished by adapting the tube bundle's geometric parameters and operating conditions for DRTB presented in Anderson (2014). The frontal area ($7.172\,\mathrm{m}^2$), steam flow area ($0.368\,\mathrm{m}^2$), and fan power (476.58 W), were kept constant and equivalent to that of DRTB. The deluge water mass flow rate was considered to be seven and half times the evaporation rate similar to the one for the DRTB. The considered DRTB is multi-row which is 2.87 m wide, 1 m high and 2.5 m long and its performance data are 5.126 MW and 22.703 Pa, heat transfer rate and air-side pressure drop, respectively. The row effects are believed to be the main cause of vapour flow back in most of dephlegmators. According to Owen (2013), this can be eliminated by considering the single-row bundle. Thus, in this study, the single-row CDTB configuration was considered, and the tube's height was taken to be 1 m, which is equal to DRTB's height.

Since the outer size of the tube bundle was fixed, the pitch between the tubes was the only variables that was considered, and varied, in order to determine the bundle's tube number, and tube outer width as well as the tube pitch that delivers optimum performance. The tube pitches of 25 mm, 30 mm and 38 mm were considered and their effects on the thermal design performance of the bundle were assessed. These tube pitches were selected based on the recommendations in literatures (Kroger (2004), Heyns (2008), Owen (2013)). For each tube pitch, the corresponding tube outside width and number of the tubes per row were calculated. Furthermore, the heat transfer rate, air-side pressure drop and minimum air flow area along the tube height in both entrance and fully developed regions were computed.

4.2.3. Response parameters and algorithm

The response parameters or values of comparison were computed by Eq. (4.1), (4.2) and (4.3).

$$\mathrm{R_Q} = \frac{Q_r}{Q_f} \tag{4.1}$$

$$\mathrm{R_P} = \frac{\Delta P_r}{\Delta P_f} \tag{4.2}$$

whereby (Q_r/Q_f) and $(\Delta P_r/\Delta P_f)$ are the heat transfer rate and air-side pressure drop ratios of the DRTB and CDTB, respectively which were obtained as the tube pitch was varied. Since the value of Q_r and ΔP_r were constant and equal to that of DRTB, parameters R_Q

and R_P decreased as Q_f and ΔP_f increased. However, since the objective of the optimisation was to maximise heat transfer rate and minimise air-side pressure drop, for optimum design, parameters R_Q and R_P should be high and low, respectively. This can be achieved if the configuration of CDTB provides a high rate of heat transfer at a reasonable air-side pressure drop. The Thermal Performance Index (*TPI*) was used to analyse the overall performance of the CDTB by taking into account both thermal and hydrodynamic performances.

$$TPI = \varepsilon/\Delta P_a \tag{4.3}$$

where, ε is bundle effectiveness and ΔP_a is air-side pressure drop.

The solutions procedure used is described by general algorithm in the flow diagram, Figure 3.30. Generic Algorithm was used since it was found to be one of the most common used techniques (Catton, 2010). For each tube pitch, the corresponding tube outside width and number of the tubes per row were calculated, and shown in Figure 4.1. As the tube pitch increased, the tube outside width and number of the tubes per row were found to increase and decrease, respectively. This means that, as the tube outside width increases, the number of the tubes per row in bundle decreases. From Figure 4.2, it was found that at small tube pitches, the heat transfer rate was higher in fully developed region than in entrance region, and it was the opposite for larger tube pitches. This was due to the fact that, the entrance tube height, as shown in Figure 4.3 increased with tube pitches. Furthermore, at smaller tube pitches, the numbers of the tubes per row were many, which led to large surface heat transfer area.

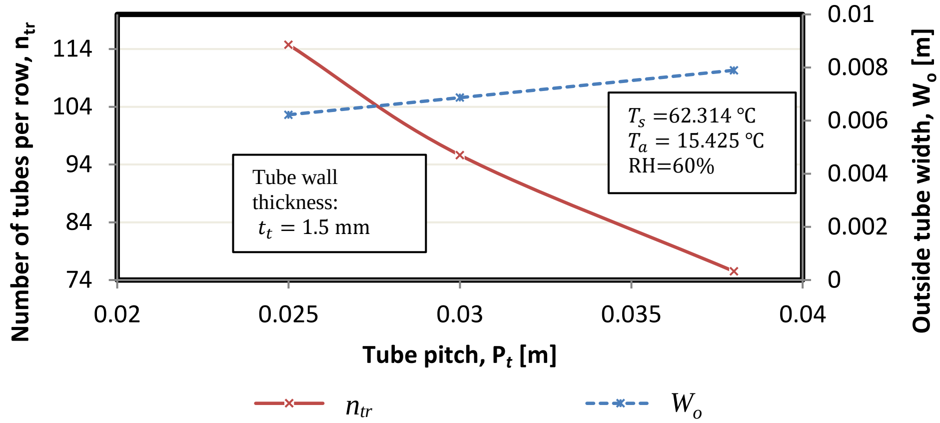

Figure 4. 1: Number of tubes per row and outside tube width per tube pitch for the CDTB configuration

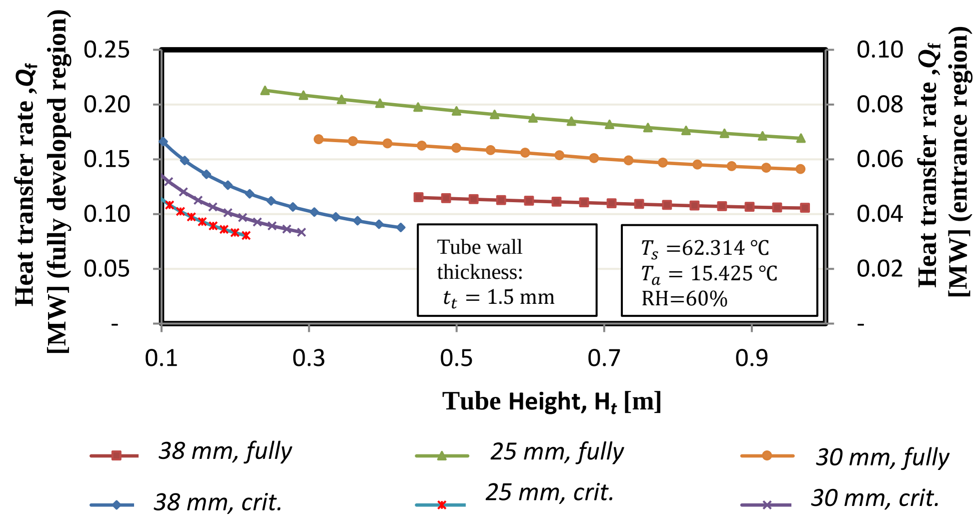

Figure 4. 2: Heat transfer rate along the CDTB height at different tube pitches

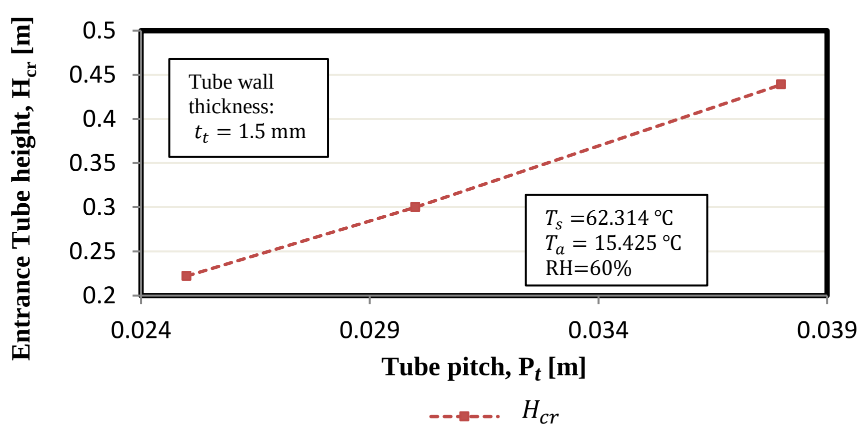

Figure 4. 3: Tube pitch effect on the entrance tube height

Since, the steam flow area was constant and the numbers of the tubes per row were many at smaller tube pitches, the outside tube width had to reduce in order to meet the targeted value of the steam flow area. As shown in Figure 4.4, the air-side pressure drop was found to decrease with tube pitch in both fully developed and entrance regions. This was due to the fact that, at smaller tube pitches, the minimum airflow area was smaller which led to higher air velocity in the channel/ minimum airflow area, and subsequently to higher air-side pressure drop (Figure 4.5).

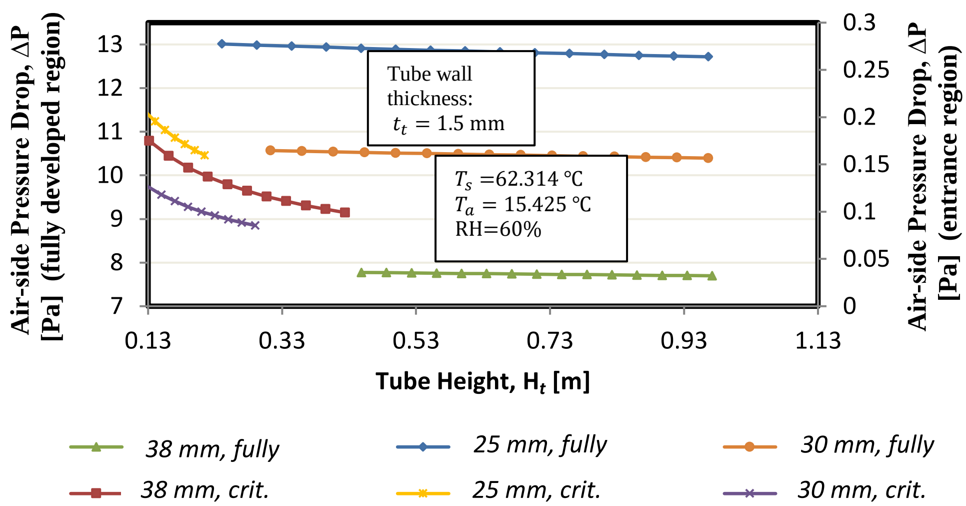

Figure 4. 4: Air-side pressure drop along the CDTB height at different tube pitches

As indicated in Figures 4.6 and 4.7, both heat transfer rate (Q_r/Q_f) and air-side pressure drop ($\Delta P_r/\Delta P_f$) ratios were found to increase with tube pitch. The maximum deviations between DRTB and conventional CDTB data were 52 % and 55 % for heat transfer rate and air-side pressure drop, respectively as presented in Figure 4.8. At tube pitch 28 mm, the deviations between the bundle's data for both heat transfer rate and air-side pressure drop were the same and equal to 36 %.

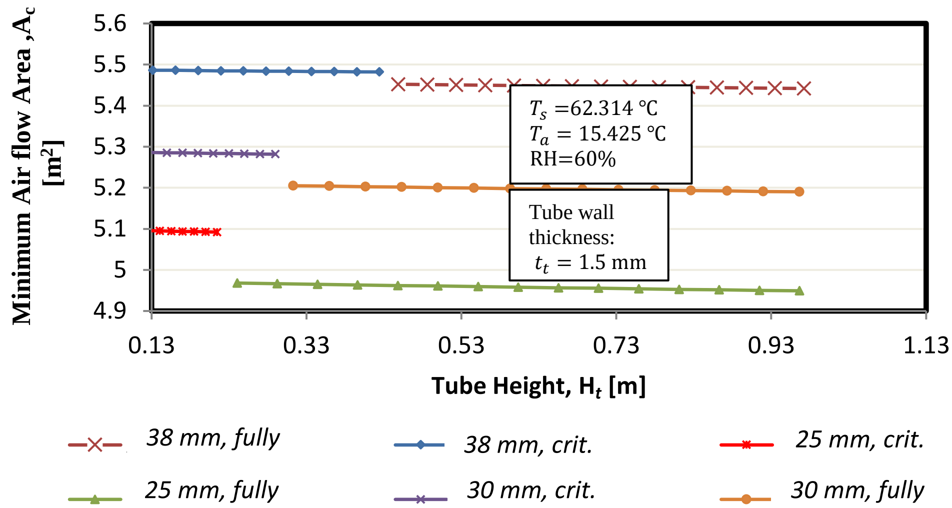

Figure 4. 5: Minimum air flow area along the CDTB height at different tube pitches

Furthermore, the bundle effectiveness was found to decrease as the tube pitch increased, as depicted in Figure 4.9 together with air-side pressure drop. As a result, the *TPI* was found also to decrease as the tube pitch increased, Figure 4.10. This indicates that, the effectiveness was a dominant in determination of *TPI*, and the CDTB performs better at smaller tube pitches; however, this comes at the cost of high air-side pressure drop. Therefore, it can be concluded that, the tube pitch has a significant effect on the bundle's performance.

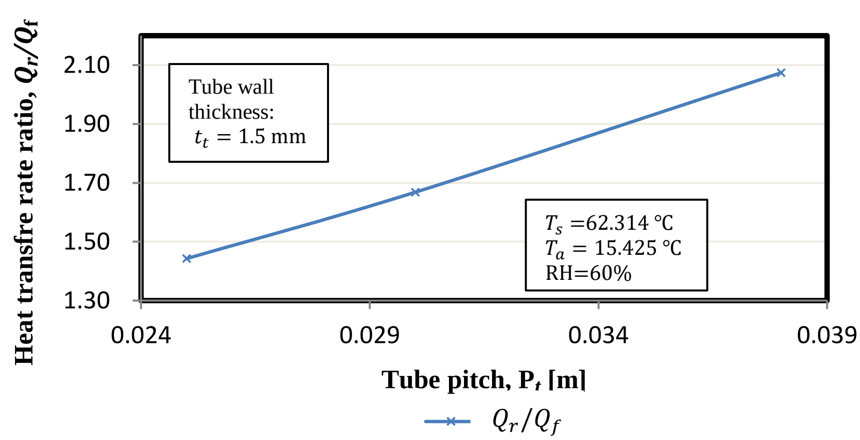

Figure 4. 6: Tube pitch effect on the heat transfer rate ratios of DRTB and CDTB

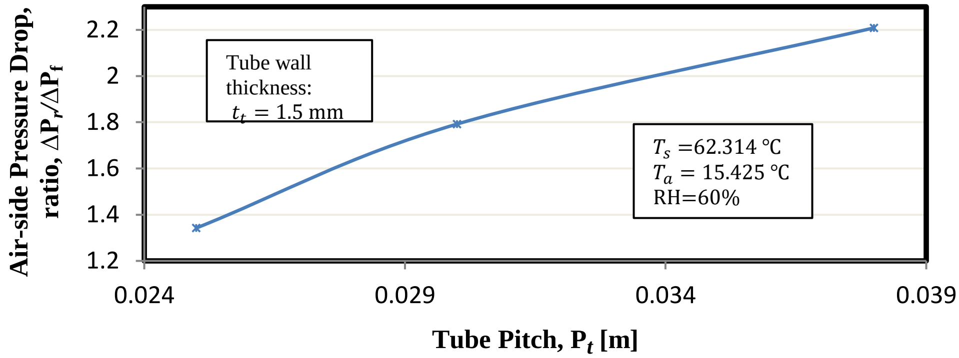

Figure 4. 7: Tube pitch effect on the air-side pressure drop ratios of DRTB and CDTB

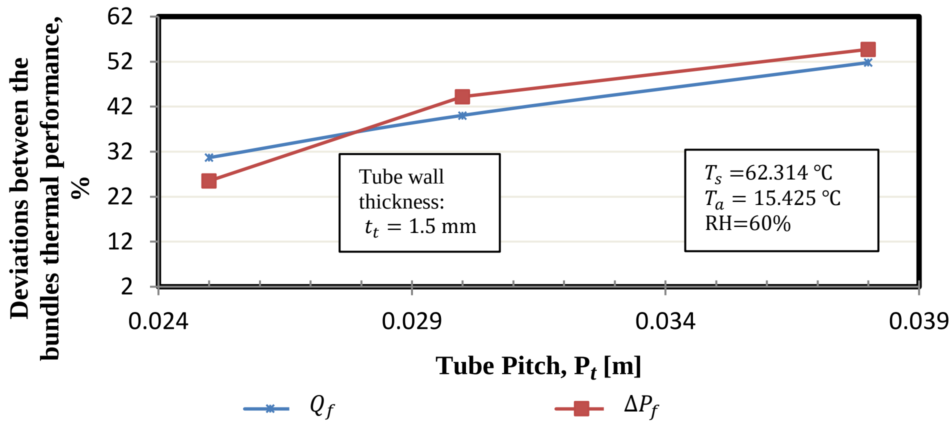

Figure 4. 8: Deviations between performance data of DRTB and CDTB

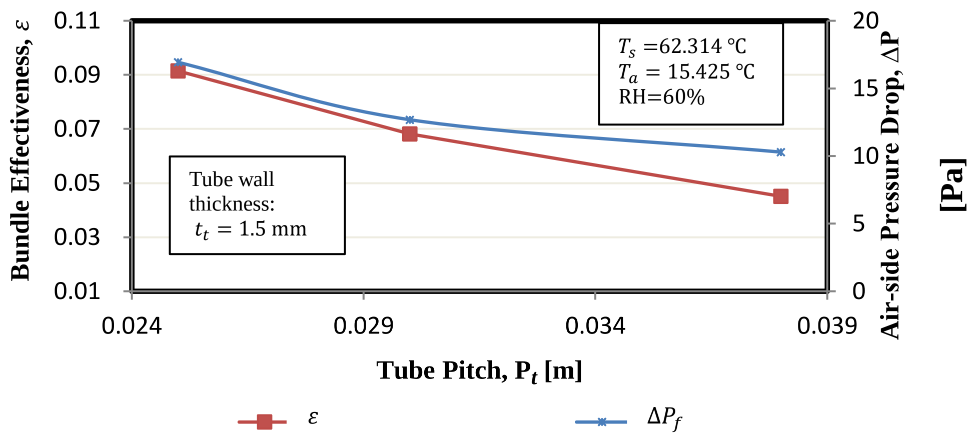

Figure 4. 9: Tube pitch effect on the bundle effectiveness and air-side pressure drop

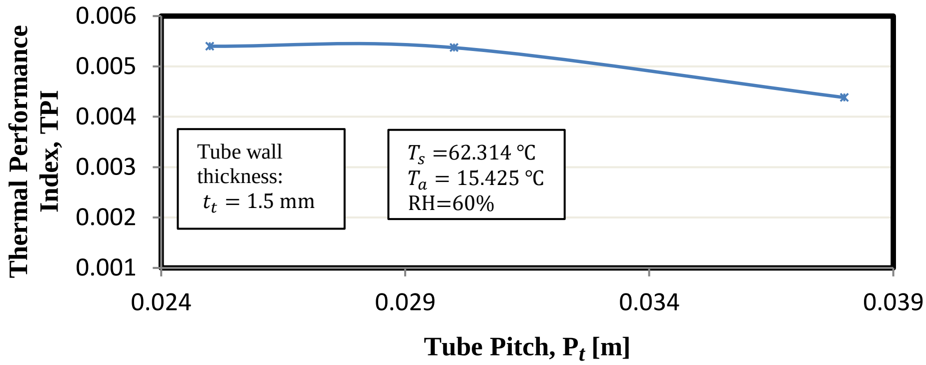

Figure 4. 10: Tube pitch effect on the Thermal Performance Index

4.2.4. Tube Bundle Selection

It was found out that, the small tube pitches deliver high performance than large pitches. Since, the CDTB air-side pressure drop was lower than that of DRTB even at small tube pitches, where the air-side pressure drop was high, the chosen CDTB configuration has a tube pitch of 25 mm. Furthermore, the *TPI* of the bundle was also found to be higher at small tube pitches.

The chosen CDTB configuration (here after referred as CDTB ‘1’) has a height, length and width of 1000 mm, 2500 mm and 2870 mm, respectively. It consists of 115 number of tubes per row of 3.22 mm and 6.23 mm inside and outside width, respectively. The heat transfer rate and air-side pressure drop of the chosen CDTB configuration were found to be 31 % and 25 % lower than that of DRTB. The tube layout and dimensions of the CDTB ‘1’s configuration are illustrated in Figure 4.11.

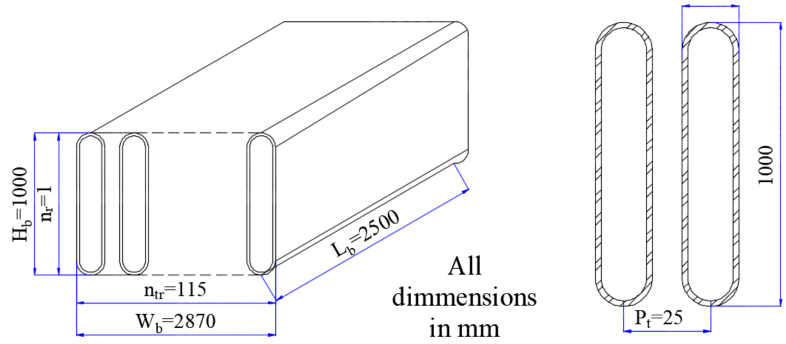

Figure 4. 11: The tube layout and dimensions of the CDTB '1's configuration

4.3. Dimensions Adjustment of the CDTB '1' Configuration

The HDWD was designed in such way that it can replace the CD of an existing ACC system coupled to a 30 MW steam turbine of the local generating unit. The proposed HDWD should be able to perform the duty of the CD for an existing ACC system. Therefore, as shown in Figure 4.12, the CD geometric dimensions were used to configure the first stage tube bundle as well as the second stage tube bundle (CDTB) of the induced HDWD, and ensure that flooding in the first stage is avoided.

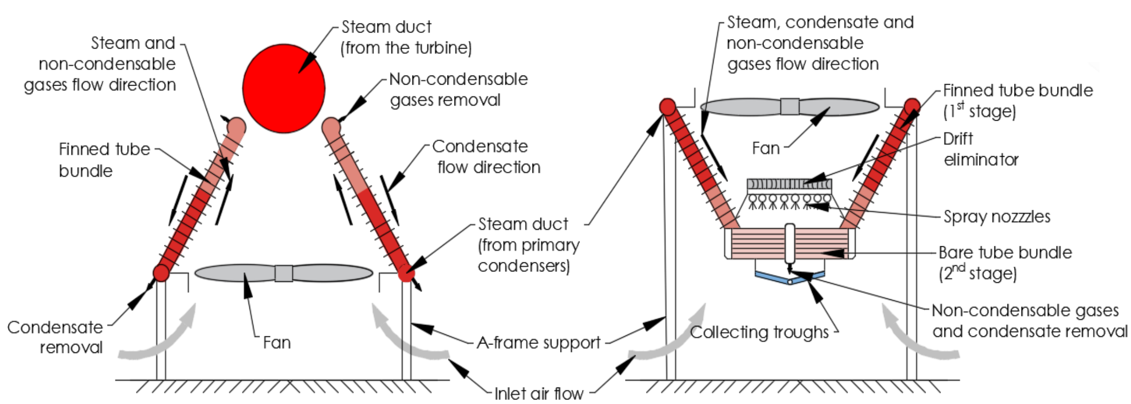

a) CD **b) HDWD**

Figure 4. 12: Schematic diagrams of CD and induced HDWD

The considered generation unit consists of three (3) ACC "streets" which are in an A-frame shape with 30° half-apex angle. Each "street" comprises of three (3) A-frame primary condenser units (condensing units) and one (1) A-frame CD (secondary condenser) unit. Each primary condenser and dephlegmator units consist of six (6) tube bundles, three (3) on each side of A-frame. By excluding the fixtures and supporters, dephlegmator tube bundles are 2320 mm wide, 293 mm high and 6440 mm long as shown in Figure 4.13. Each bundle consists of 183 elliptically core tubes with rectangular fins threaded on, and are arranged in three rows. The row I has 47 tubes, row II has 37 tubes and row III has 57 tubes, which are installed at fin pitch of 4 mm, 3 mm and 2.5 mm, respectively (GEA, 1978).

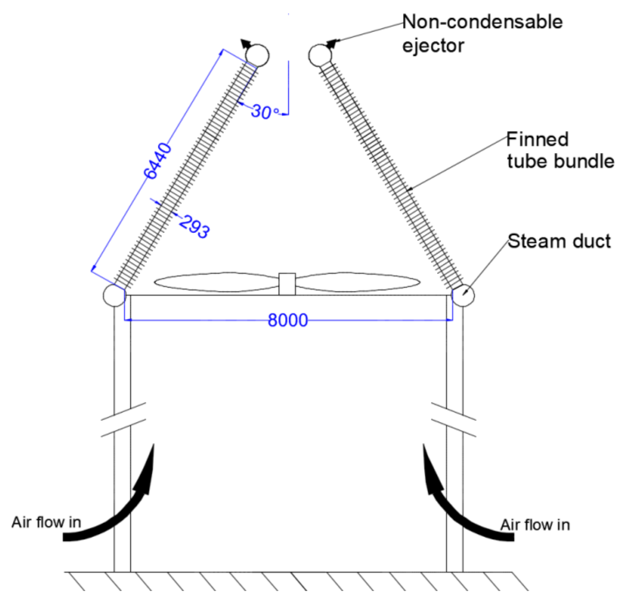

Figure 4. 13: Geometric parameters of CD for ACC system coupled to 30 MW steam turbine

The CDTB '1' design was found to be characterized by the following parameters: bundle width, length, height, and steam flow area, as well as by the tube pitch, width, length, and height. These geometric parameters were adjusted accordingly. The considered values for these parameters, are presented in Table 4.1, and were selected mainly based on the geometrical dimensions of the existing CD, and suggestions and recommendations from literatures (Heyns (2008), Owen (2013), Anderson (2014)).

Table 4. 1: Design parameter values for the CDTB optimization

Design parameter	Unit	value
Tube bundle Width	mm	2320; 2870; 4640
Tube bundle Length	mm	2500; 3178; 3838
Tube bundle steam flow area	m^2	0.142; 0.284; 0.426; 0.368

4.3.1. Tube Bundle Width Adjustment

Since, the CDTB ‘1’ was connected in series to the first stage tube bundle, it was wise to ensure that the CDTB ‘1’ width was adjusted and corresponding to that of first stage tube bundle. The size for the first stage tube bundle was taken to be the same as that of existing CD’s tube bundles, but, with shortened tubes, in order to create a room for the second stage bundle (CDTB). Therefore, the effect of the tube bundle width on the CDTB ‘1’ performance was investigated, by considering three (3) tube bundle widths: 2320 mm, 2870 mm and 4640 mm, which are equivalent to first stage tube bundle width, Anderson (2004) tube bundle width, and two times the first stage tube bundle width, respectively. The rest of the CDTB ‘1’ geometric parameters were kept constant as shown in Figure 4.11, while the deluge water flow rate was considered to be equal to evaporation rate.

From Figure 4.14, the number of tubes per row, as well as the air frontal area were found to increase with tube bundle width. This results in larger surface heat transfer area and air mass flow rate into the bundle. As a consequence, the heat transfer rate was also found to increase with tube bundle width as depicted in Figure 4.15. In addition to that, the heat transfer rate decreases along the tube bundle height in both entrance and fully developed regions as presented in Figure 4.16 for different tube bundle widths. This is due to the increasing of the air temperature, as it flows through the bundle.

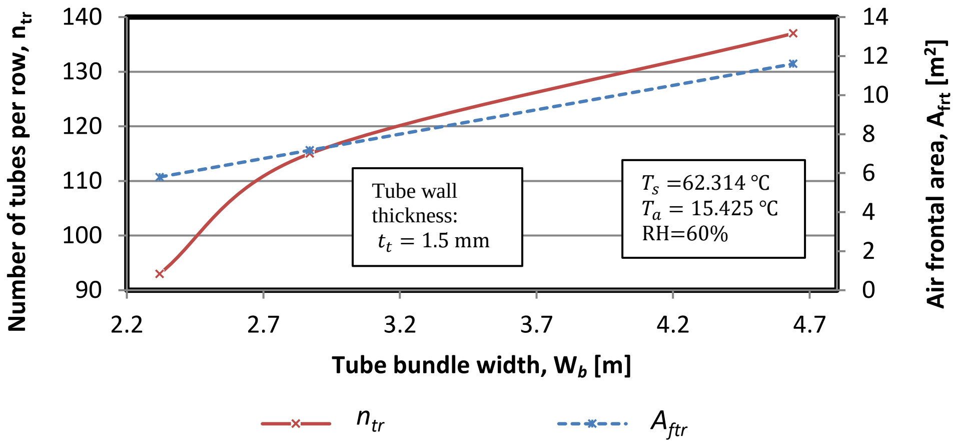

Figure 4. 14: Tube bundle width effect on number of tubes per row and air frontal area for CDTB '1'

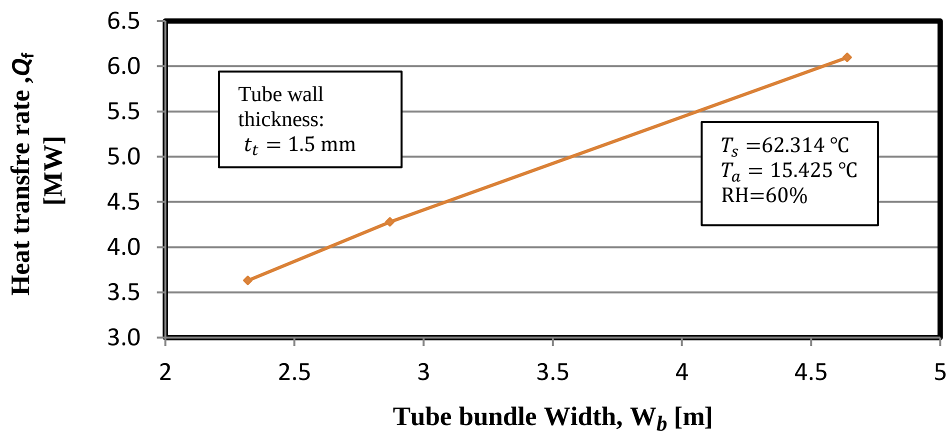

Figure 4. 15: Tube bundle width effect on heat transfer rate for CDTB '1'

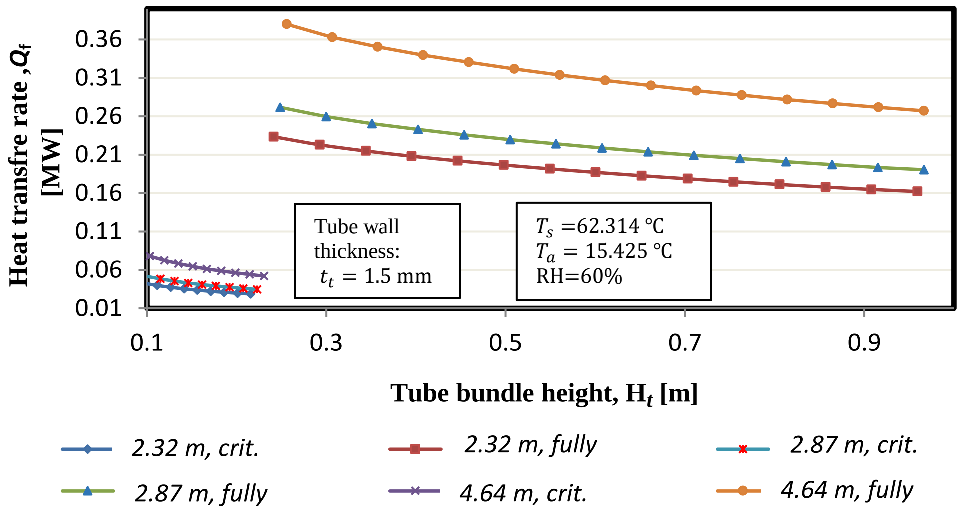

Figure 4. 16: Heat transfer rate along the CDTB '1' height at different tube bundle widths

As shown in Figure 4.17, the air minimum flow area between the adjusted tubes was found to increase with bundle width. This is due to the fact that, during the analysis, the tube pitch was kept constant. This results in decrease of air-side pressure drop as illustrated in Figure 4.18. Along the tube bundle height, the air minimum flow area between the adjusted tubes, was found to slightly decrease in both entrance and fully developed regions as presented in Figure 4.19 for different tube bundle widths. This is due to the fact that, the deluge water film thickness was found to decrease against the height. Therefore, as shown in Figure 4.20, the air-side pressure drop was found to slightly increasing in fully developed region.

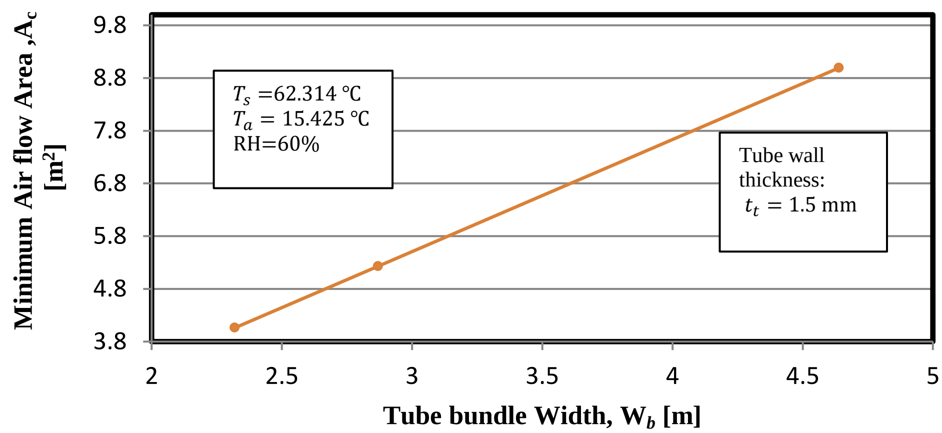

Figure 4. 17: Tube bundle width effect on the minimum air flow area for CDTB '1'

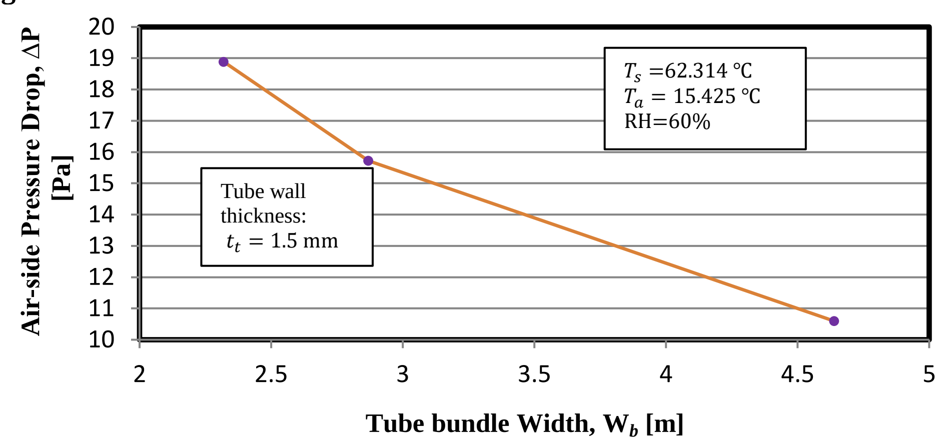

Figure 4. 18: Tube bundle width effect on air-side pressure drop for CDTB '1'

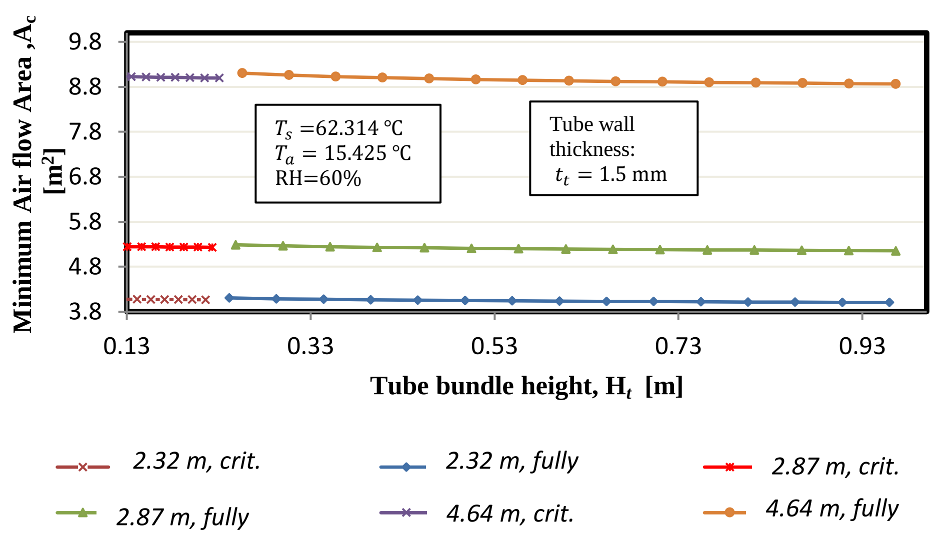

Figure 4. 19: Minimum air flow area along the CDTB '1' height at different tube bundle widths

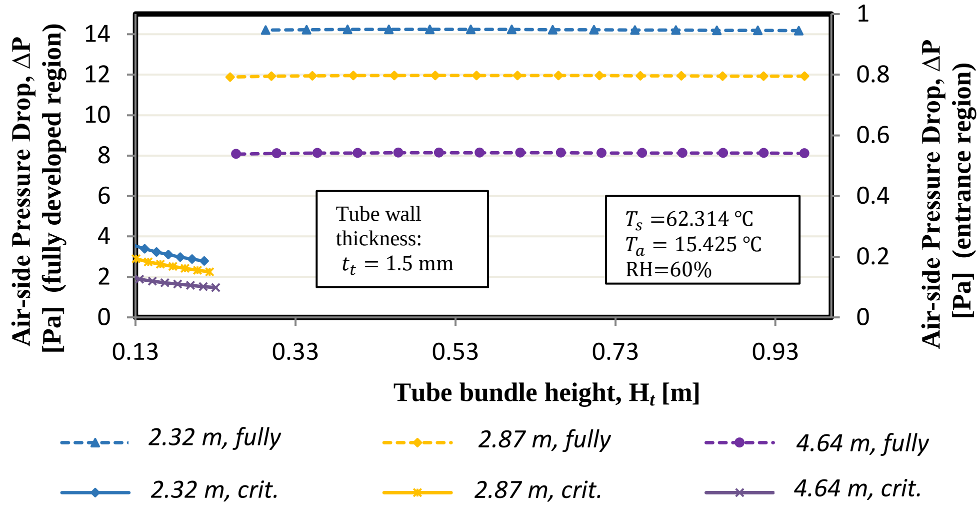

Figure 4. 20: Air-side pressure drop along the CDTB '1' height at different tube bundle widths

As it is illustrated above, the heat transfer and air-side pressure drop were found to increase and decrease, respectively with the tube bundle width, which is a desirable aspect. However, at same, the outside tube width and number of tubes per row were found to decrease and increase, respectively with the tube bundle width. Too many tubes in the bundle and too small outside tube width may lead to high manufacturing and construction costs, and large space for the installation. Therefore, the CDTB '1' configuration with 2320 mm width, (here after referred as CDTB '2'), as depicted in Figure 4.21, was selected for further design adjustment. However, with noting that as the CDTB '1' width changed from 2870 mm to 2320 mm, the heat transfer rate and air-side pressure drop decreased and increased by 15 % and 20 %, respectively.

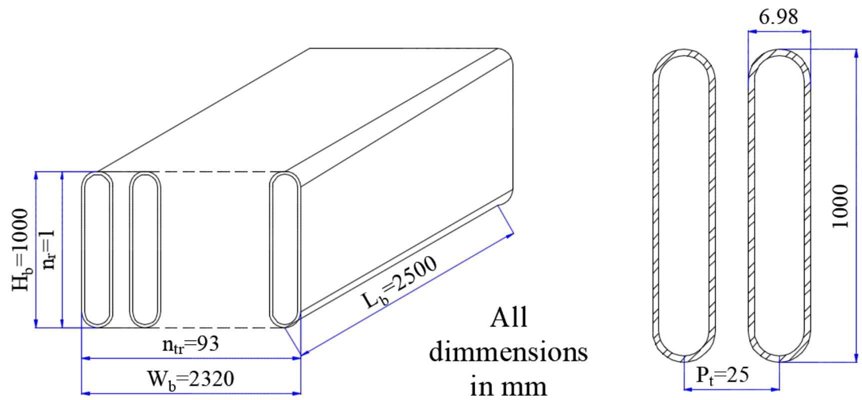

Figure 4. 21: The tube layout and dimensions of the CDFB '2's configuration

4.3.2. Tube Bundle Length Adjustment

The tube bundle length was adjusted in order to assess its impact on the thermal performance of CDTB '2', as well as to determine the length of both first and second stages tube bundles of HDWD. Therefore, as above-mentioned, the length of tubes of the CD was reduced to create space for the CDTB. The CDTB '2' was placed at three different positions (A, B, C) as indicated in Figure 4.18.

- Position A - the base of CDTB '2' was placed at the end of CD finned tubes,
- Position B - the length of first stage tubes was equal to 4.5 m, as it was considered in Heyns (2008) and Owen (2013),
- Position C - the CD finned tube length were shortened by 40.2 % as it was considered in Andersons (2014).

For each position, the new lengths for the CDTB '2', as well as for the first stage tube bundle were determined as indicated in Figure 4.22 and summarised in Table 4.2. The defined new lengths for the CDTB '2' were then used in performance analysis.

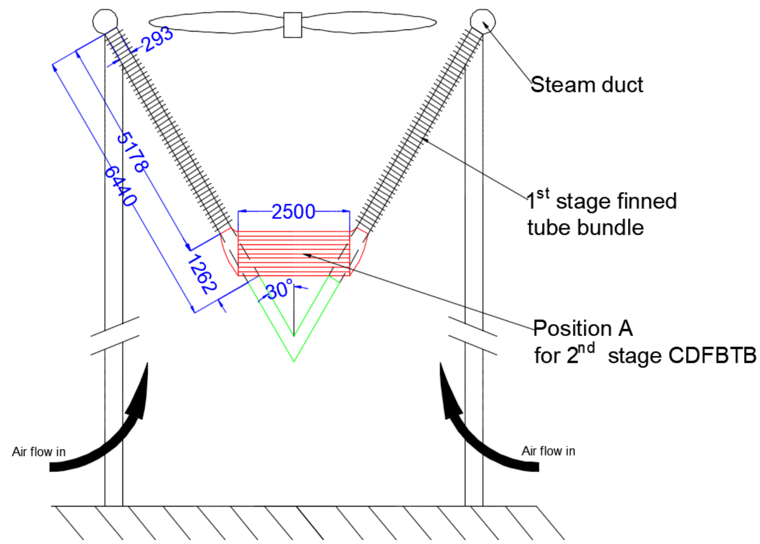

a) Position A

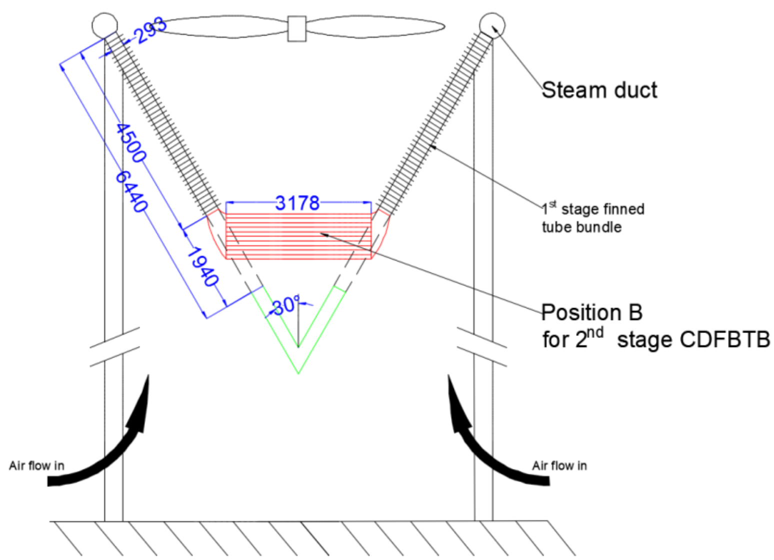

b) Position B

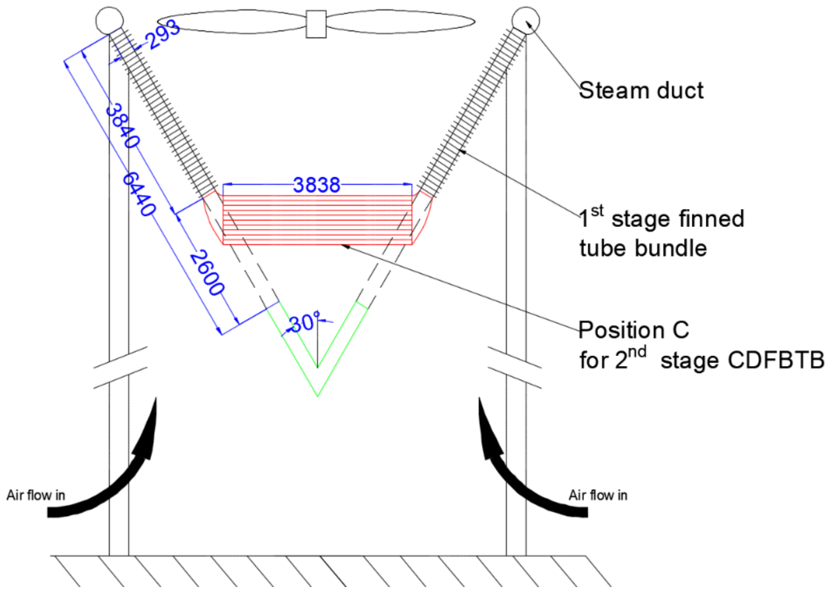

c) Position C

Figure 4. 22: Different positions of CDTB '2'

Table 4. 2: Summary of bundles dimensions at different positions

Position	First stage tubes length, mm	Second stage tubes length (CDTB), mm	Reduced CD length, mm
A	5178	2500	1262
B	4500	3178	1940
C	3840	3838	2600

From the results shown in Figures 4.23, the heat transfer rate increased with tube bundle length. This is obvious due to the fact that, increasing of the tube bundle length results on larger heat surface area. However, along the tube bundle height, in both entrance and fully developed regions, the heat transfer rate was found to decrease as shown in Figure 4.24 for different tube bundle lengths. Figure 4.25 shows that, the air-side pressure drop decreased with tube bundle length. This is due to the fact that, the air minimum flow area was found to increase with tube bundle length as presented in Figure 4.26. However, as depicted in Figure 4.27, along the tube bundle height, the minimum air flow area was found to decrease, which is resulted on slightly increase of the air-side pressure drop along the tube bundle height as shown in Figure 4.28.

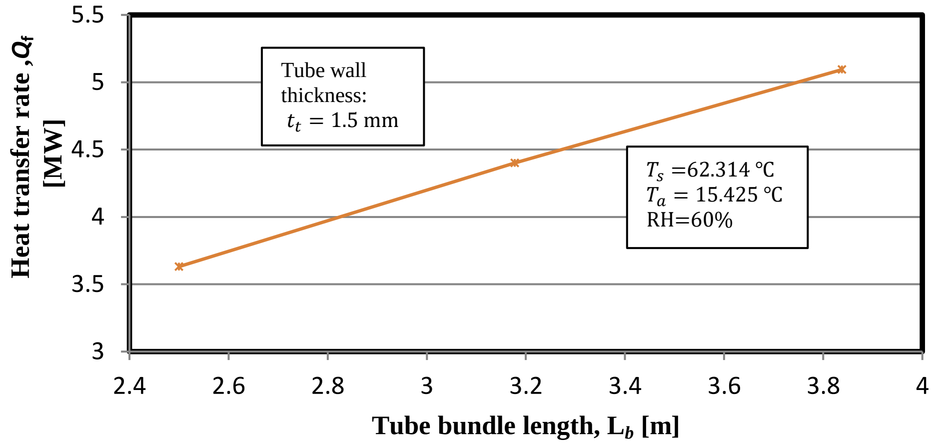

Figure 4. 23: Tube bundle length effect on heat transfer rate for CDTB '2'

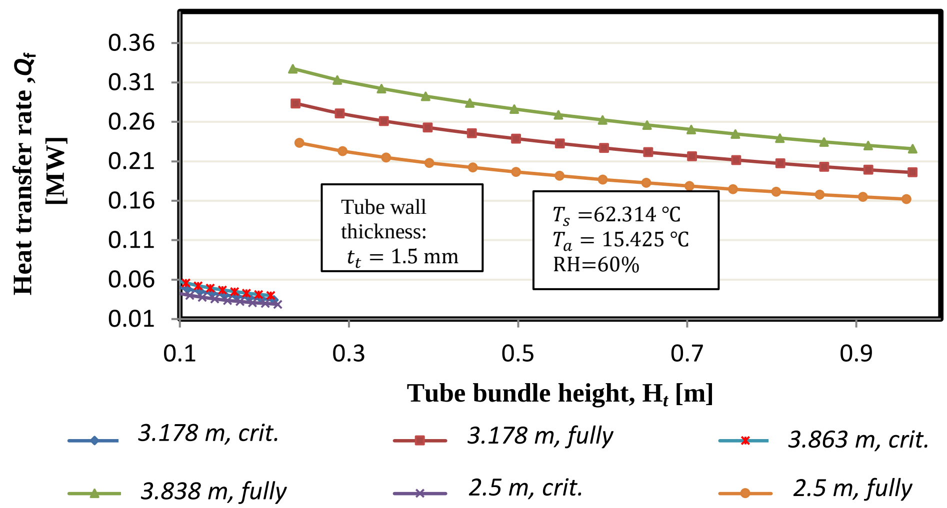

Figure 4. 24: Heat transfer rate along the CDTB '2' height at different tube bundle lengths

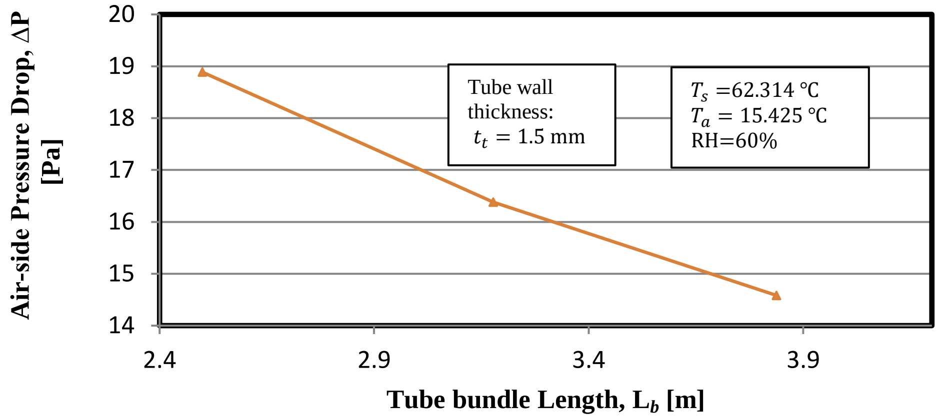

Figure 4. 25: Tube bundle length effect on air-side pressure drop for CDTB ‘2’

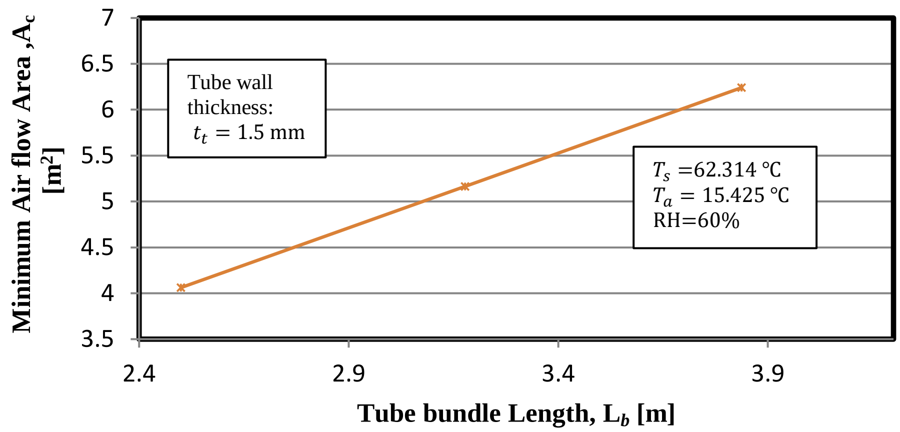

Figure 4. 26: Tube bundle length effect on minimum air flow area for CDTB ‘2’

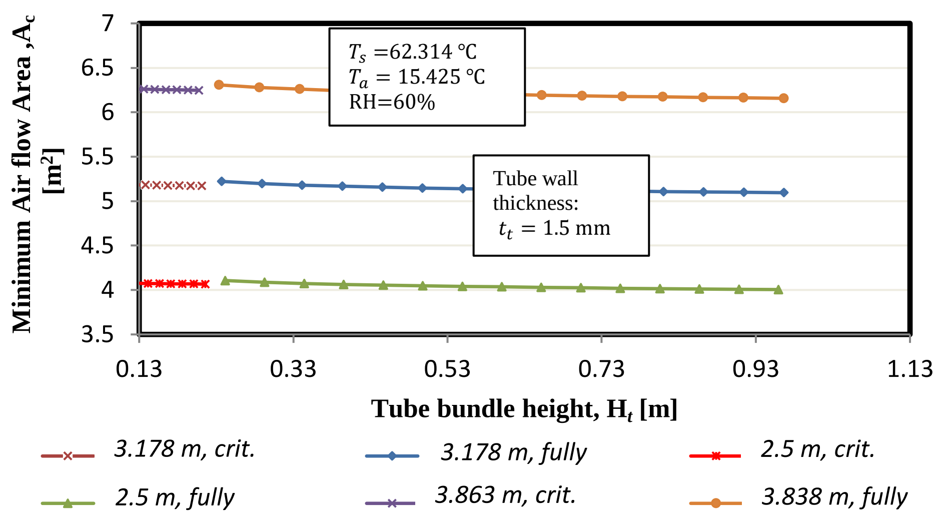

Figure 4. 27: Minimum air flow area along the CDTB ‘2’ height at different tube bundle lengths

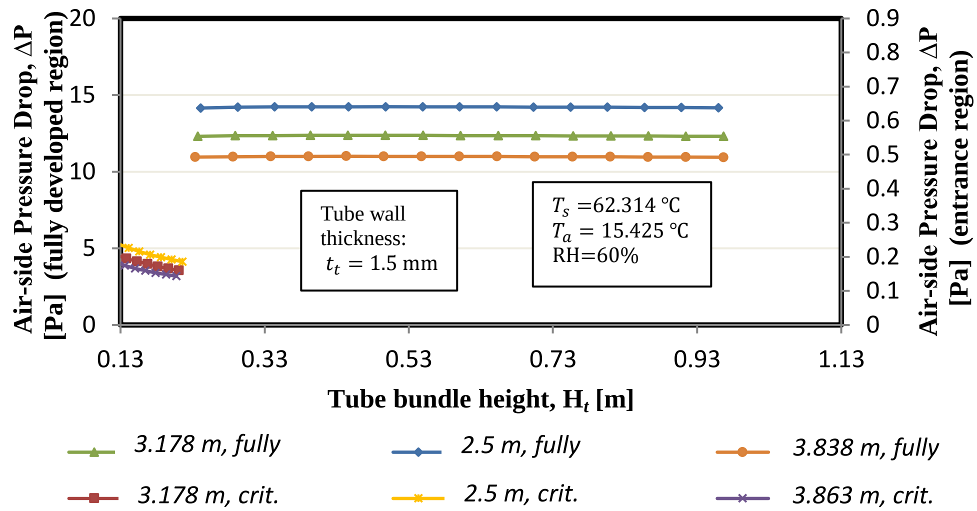

Figure 4. 28: Air-side pressure drop along the CDTB '2' height at different tube bundle lengths

As it is presented above, the heat transfer and air-side pressure drop were found to increase and decrease, respectively with the tube bundle length, which is a desirable aspect. Therefore, any of the considered tube bundle length can be selected. Hence, the CDTB '2' configuration (here after referred as CDTB '3') attained for position B was selected. For this position, as the bundle length changed from 2500 mm to 3178 mm, the heat transfer rate and air-side pressure drop increased and decreased by 21 % and 13 %, respectively. For position C, an increasing and decreasing of 40 % and 23 %, for the heat transfer rate and air-side pressure drop, respectively were achieved. However, for this position, the length of first stage tube bundle was found to be too short, which may result in insufficient performance of the bundle, and overloading of the second stage bundle at high ambient air temperature (Owen, 2013). The CDTB '3' is illustrated in Figure 4.29.

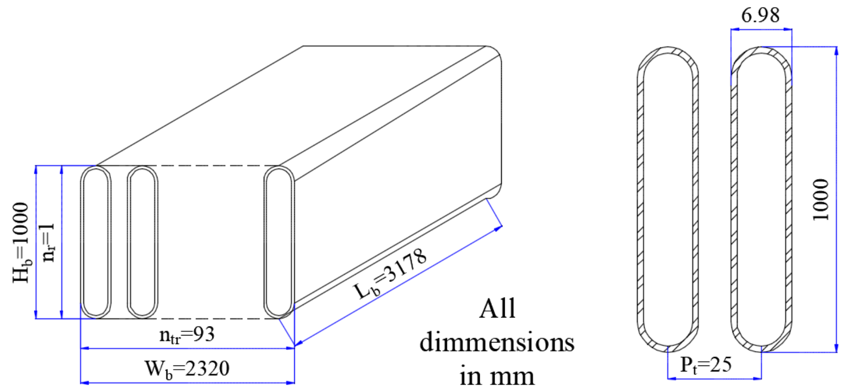

Figure 4. 29: The tube layout and dimensions of the CDTB '3''s configuration

4.3.3. Tube bundle steam flow area adjustment

The effect of the steam flow area on the CDTB '3' thermal performance was examined by considering four (4) steam flow areas. The first steam flow area (A_{st1}) is equal to the first stage tube bundle steam flow area, which is equal to steam flow area of an existing CD tube bundle: $A_{st1} = 0.142\, m^2$; $A_{st2} = 2 \times A_{st1}$; $A_{st3} = 3 \times A_{st1}$ and $A_{st4} =$ Andreson (2014). As indicated in Figure 4.30, as the steam flow area increased, the overall heat transfer rate was found decreasing. Figure 4.31 shows that, along the tube bundle height, the heat transfer rate was found slightly increasing in fully developed region, and slightly decreased in entrance region, which resulted in overall heat transfer rate to decrease as the bundle steam flow area increased. Since, the tube pitch was fixed, the minimum air flow area was found to decrease as the steam flow area increased, which resulted in increasing of air-side pressure drop as presented in Figures 4.32. The effects of the steam flow area on the minimum air flow area is shown in Figure 4.33. As depicted in Figure 4.34, along the tube bundle height, the minimum air flow area was found to slightly increase in the entrance region and slightly decreasing in fully developed region, which resulted in slightly decreasing and increasing of the air-side pressure drop in the entrance and fully developed regions, respectively as shown in Figure 4.35.

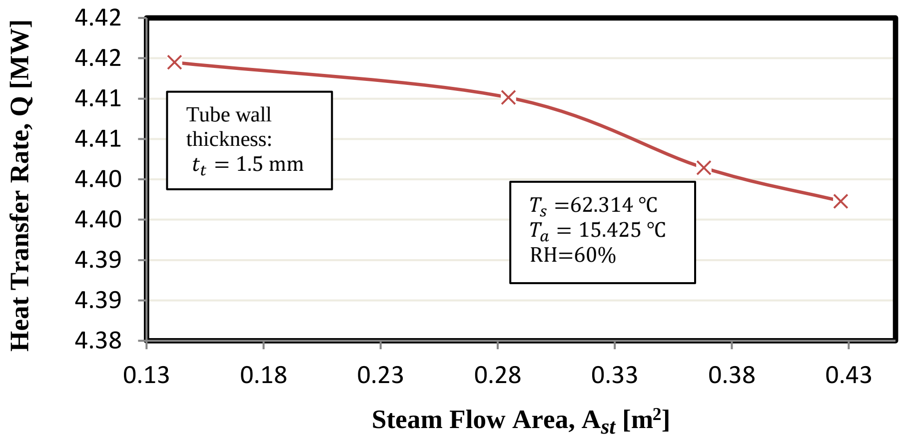

Figure 4. 30: Tube bundle steam flow area effect on the overall heat transfer rate for CDTB '3'

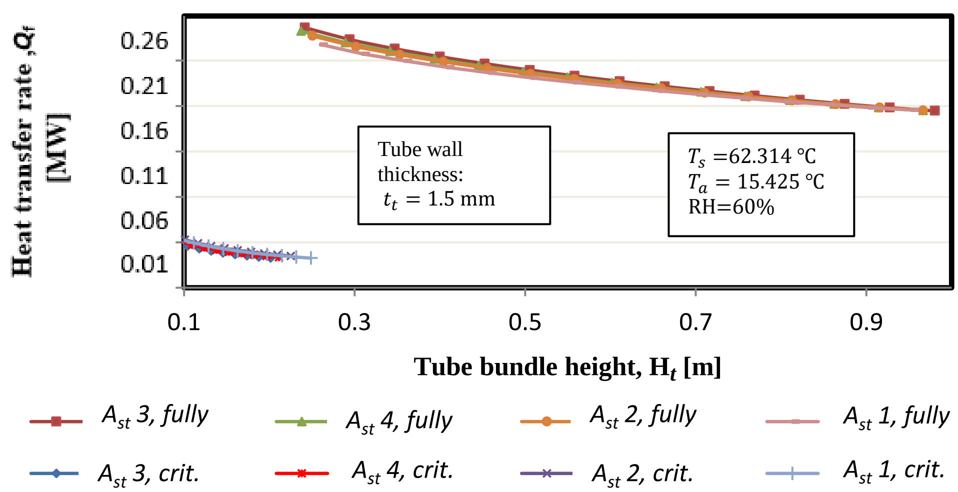

Figure 4. 31: Heat transfer rate along CDTB '3' height at different steam flow areas

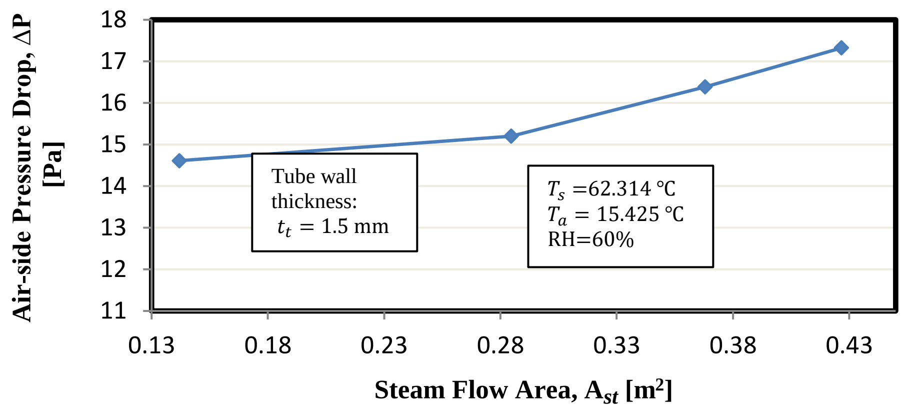

Figure 4. 32: Tube bundle steam flow area effect on air-side pressure drop for CDTB '3'

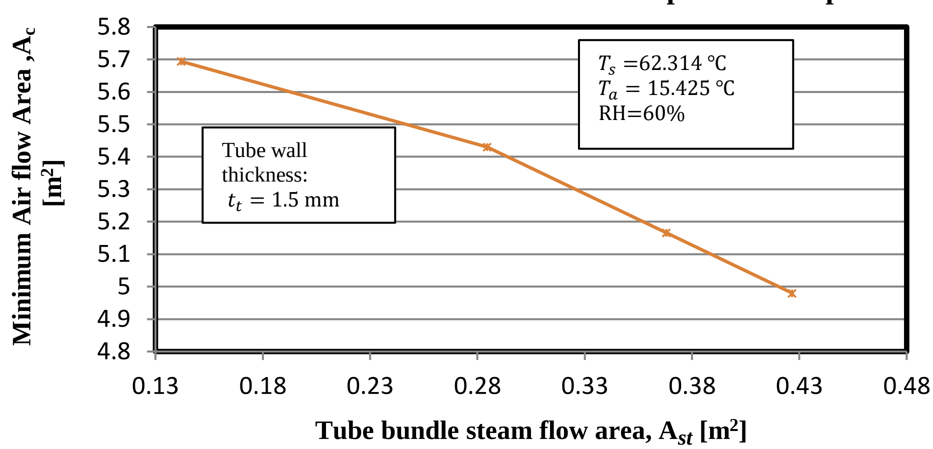

Figure 4. 33: Tube bundle steam flow area effect on minimum air flow area for CDTB '3'

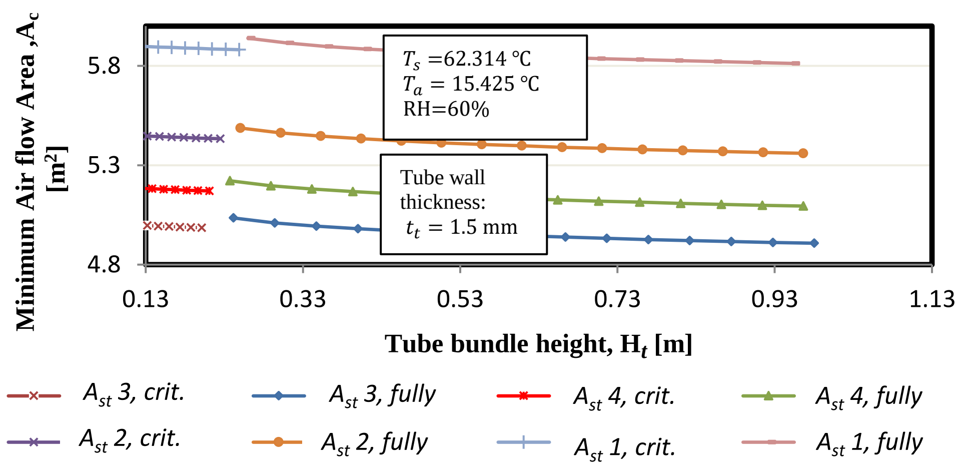

Figure 4. 34: Minimum air flow area along CDTB '3' height at different steam flow areas

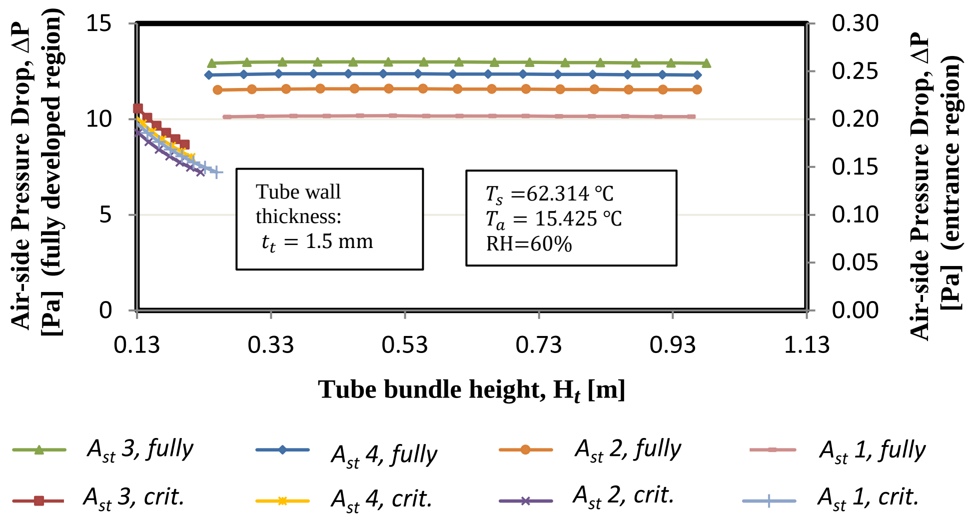

Figure 4. 35: Air-side pressure drop along CDTB '3' height at different steam flow areas

As illustrated above, the high heat transfer rate and low air-side pressure drop were attained at smaller steam flow areas. Moreover, as the bundle steam flow area reduced from 0.368 m^2 to 0.142 m^2, the heat transfer rate and air-side pressure drop increased and decreased by 0.3 % and 11 %, respectively. However, as depicted in Figure 4.36, the outside tube width decreased with steam flow area, thus at $A_{st1} = 0.142\ m^2$, the outside tube width was 4.5 mm, which may lead to manufacturing complications or the tube may be regarded as microchannel tube (Ozdemir, 2006). Therefore, further geometric adjustment was required in order to attain the reasonable outside tube width. For that reason, the tube height was adjusted until the reasonable outside tube width was achieved. At constant steam flow area ($A_{st1} = 0.142\ m^2$), as the tube height decreased, the outside tube width increased, as illustrated in Figure 4.37. Hence, to outage the manufacturing complications, the tube height of 300 mm, which resulted on outside tube width of 6.95 mm was selected. Therefore, the bundle obtained when the steam flow area of CDTB '3' was equal to that of the first stage bundle ($A_{st1} = 0.142\ m^2$) and tube height is 300 mm was selected, and is presented in Figure 4.38.

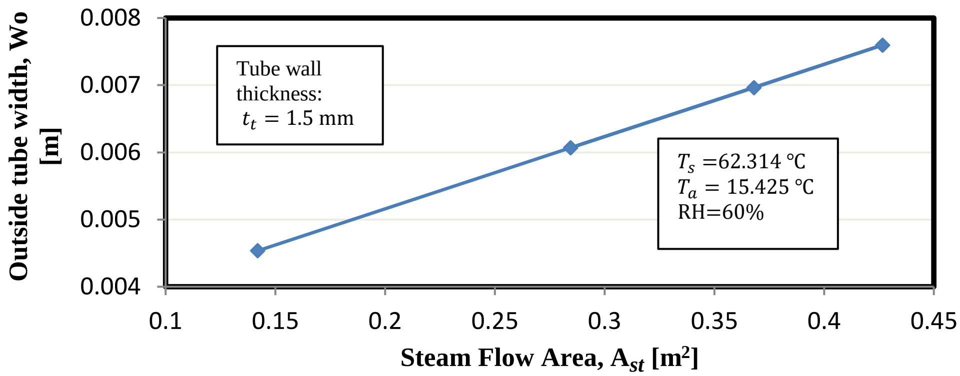

Figure 4. 36: Tube steam flow area effect on the outside tube width

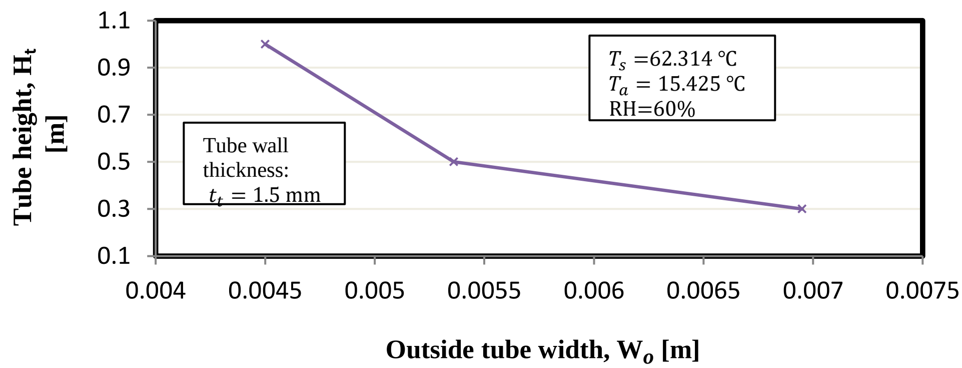

Figure 4. 37: Tube height effect on the outside tube width

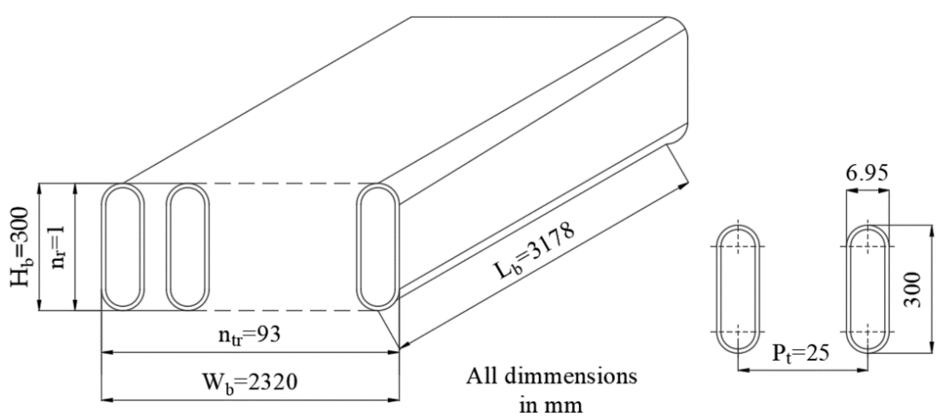

Figure 4. 38: The tube layout and dimensions of the final CDTB's configuration

Since the performance of HDWD incorporated with CDTB is to be compared to that of CD of an ACC system coupled to a 30 MW steam turbine, at local generating unit, and its performance is also to be analysed at the operating conditions for that ACC system, it was advised to perform a performance analysis of the CD prior to that of CDTB and HDWD incorporated with CDTB. Thus, in the next Chapter, a performance analysis of the CD was conducted and presented.

Chapter 5: Analysis of Conventional Dephlegmator Thermal Performance

5.1. Introduction

This Chapter provides the development and validation of a mathematical model of a direct air-cooling generating unit's cold-end system coupled to 30 MW steam turbine. Furthermore, the sensitivity of the ACC performance to the high ambient air temperature, and the fan rotational speed, as well as outlining of the CD performance, are also presented in this Chapter.

Energy efficiency of a thermal power plant strongly depends on its boiler-condenser operation conditions; however, this study focused on the dependence of the power plant performance on the condenser operation conditions. The condenser creates a vacuum which extracts more steam from low pressure turbine exhaust, and thus create a natural suction phenomenon. The condenser reduces the turbine exhaust pressure and increase the specific output of the turbine (Masiwal *et al.*, 2017). Moreover, the performance of the power plant is mainly depending on the cold-end system of the steam turbine (Lakovic et al., 2010), which comprises of the last stage of the turbine, ACC, ambient air, and the air ejection system, whereby, the ACC is the key component.

The maximum generated power and the heat transfer rate are mostly impacted by the ACC operating conditions, which is determined by the operating conditions of the cooling ambient air. ACC performance depends on its air-side and steam-side characteristic parameters, as well as on condenser design, latent heat amount to be removed, maintenance of the condenser, and the air ejection system. The air-side characteristic parameters include: ambient air flow rate (fan rotational speed) and temperature; air-side pressure drop; and heat transfer coefficient. While, steam-side characteristic parameters include: condensing temperature and pressure, steam-side pressure drop, steam flow rate and condensation rate.

The turbo-generator can be turbine-follow mode or boiler-follow mode controlled. However, according to Putman and Harpster (2000) the effects of the condensing pressure in both modes are similar. In the turbine-follow mode-controlled power plant, the generator load is controlled by turbine governor. So, in order to maintain the steam parameters at the turbine throttle as close as possible to their design values, the fuel firing rate and other parameters are adjusted by steam boiler control system. Therefore, the condenser pressure rise will result in enthalpy rise and enthalpy change drops at the end point or turbine exit. However, in order to maintain the generated power at the designed level, the throttle and exhaust flows will be increased by turbine governor. As a consequence, the fuel firing rate will be increased by steam boiler control system. This leads to the increase of the specific heat rate of the turbo generator unit (Laković *et al.*, 2010). However, high fuel firing rate increases the fuel consumption rate, and operational cost of the plant. Otherwise, without corrective measurements, condenser pressure falling leads to the reduction of generated power and the heat transfer rate. Therefore, the plant should operate at the optimum air flow rate, which depends on ambient air temperature and power demand (Kromhout, *et al*., 2001).

The content of this Chapter is focused into three aspects: Firstly, the mathematical model of a direct air-cooling generating unit’s cold-end system was developed. This includes the models of steam turbine low pressure cylinder, array of axial fans and ACC. The ACC model comprises of energy, draft and steam-side pressure drop equations. The complex relations among the components of the cold-end system were also emphasized. Secondly, the developed mathematical model of cold-end system was validated by comparing its results to the design parameters of the considered generating unit. Finally, the sensitivity analysis was carried out in order to quantify the impacts of the high ambient air temperature, and the fan rotational speed on the ACC performance, generating unit output power, and efficiency loss due condenser performance. This was conducted at maximum plant load.

5.2. Description of the considered direct air-cooling generating unit

The ACC system coupled to a 30 MW steam turbine of a local direct air-cooling generating unit which is situated in Windhoek City was considered, and its design parameters are presented in Table 5.1(GEA, 1978).

Table 5. 1: Design characteristics for the generating unit

Parameter	Unit	Value
Nominal power	MW	30
Minimum stable load	MW	11
Number of revolutions	RPM	3000
Live steam pressure	Bar	62.83
Live steam temperature	℃	482
Live steam flow	kg/s	33.33
Turbine vacuum	kPa	13.1
Exhaust steam flow at LP cylinder	kg/s	26.39
Exhaust steam pressure	kPa	19.62
Exhaust Steam enthalpy at LP cylinder	kJ/kg	2395
Exhaust steam content	%	91.3
Number of extractions ports	-	5

As shown in a schematic diagram in Figure 5.1, the considered generating unit comprises of drum boiler type and a single shaft direct air-cooling condensing steam turbine.

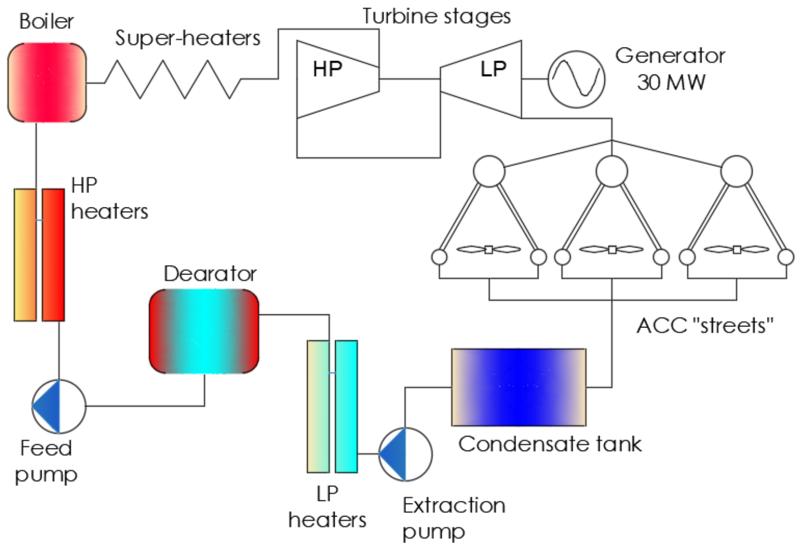

Figure 5. 1: Schematic diagram of the considered generating unit

The saturated steam produced in the boiler is superheated in the primary and secondary super-heaters to high pressure and temperature. This steam is initially partially expanded in the High Pressure (HP) turbine stage, and further expanded to the ACC's pressure in Low Pressure (LP) turbine stage the steam. In ACCs the steam is condensed to liquid by the air provided by forced draft axial fans, there-after it is piped to the condensate tank before it is pumped to the feed water heaters. The boiler feed water is pre-heated in the feed water heaters by the steam which is extracted at different turbine ports. This enhances the cycle thermal efficiency. The design data for ACC unit are depicted in Table 5.2 (GEA, 1978).

Table 5. 2: Design parameters for the ACC unit

Parameter	Unit	Value
Maximum Condenser heat removal rate	MW	63.44
Cooling air temperature	℃	32.2
Air pressure	kPa	82646
Power consumption at fan shaft	kW	600

Furthermore, each "street" has four (4) axial fans, whereby three (3) fans are supplying air to primary condenser units and one (1) is supplying air to dephlegmator unit. According to the operating manuals (GEA, 1978), the fan speeds for all primary condenser units are set at same value, however, the speed of dephlegmator unit fan should not be lower than that of the condensing units. The fan design performance characteristics are depicted in Table 5.3.

Table 5. 3: Fan design performance characteristics for the ACC's unit

Parameter	Unit	Value
Fan type	-	6 300 PFS/6
Volumetric flow rate	m^3/s	256
Static pressure	Pa	100
Power consumption	kW	46
Speed	rpm	182

Both primary condenser and CD units are comprised of tube bundles, which consist of elliptically core tubes with rectangular fins threaded on and are arranged in three rows. The ACC geometrical characteristics are presented in Table 5.4.

Table 5. 4: ACC geometrical characteristics

Parameter	Unit	Primary condenser Unit	CD Unit
Transversal pitch	mm	38	38
Longitudinal pitch	mm	42.5	42.5
Tube length	mm	7200	6440
Tube height	mm	55	55
Tube width	mm	18	18

Tube thickness	-	1.7	1.7
Number of tube rows per condenser unit	-	3	3
Fin pitch per row	mm	4; 3; 2.5	4; 3; 2.5
Tube bundles per condenser unit	-	3	3
Tube bundles per "street"	-	9	3
Tube bundles per ACC unit	-	27	9
Tube bundles width	mm	2320	2320
Tube bundles height	mm	293	293

5.3. Cold-end System Mathematic Modelling

5.3.1. Direct ACC Modelling

A detailed performance evaluation of the ACC was conducted in order to outline the performance of the CD of the ACC unit, which is the component of interest. The CD's performance was compared to the proposed HDWD in order to signify how HDWD can improve the ACC's performance during the hot periods. Furthermore, the effect of ACC's performance on the turbine power output was outlined. The ACC of the considered generation unit, comprises of primary and CD. In order to analyse the performance of the CD units, the performance of the primary condenser units should be performed first. The conditions of the steam at the exit of the primary condenser units was considered as the steam conditions at the inlet of the CD units.

The model for ACC was adapted from model presented in Kröger (2004). This model was evaluated based on UA-AMTD and Effectiveness-NTU methods. The heat transfer performance calculations of an ACC require simultaneous solution of the energy and draft equations. The calculations were performed through iterative solution procedure, where the initial values were guessed and iterated until they converged. The steam at both entrance and exit of ACC is in two-phase region; therefore, dryness along the ACC tubes was employed as a crucial variable to define the dynamic condensation process of the steam. The adapted model was adjusted based on the Figure 5.2, which shows the typical ACC tubes rows allocated between the dividing and combining headers. The steam-side performance parameters for each tube row were defined at different locations of the tubes as labelled *i*, *ii*, *iii* and *iv*, whereas tube rows are labelled as *1*, *2* and *3* in Figure 5.2.

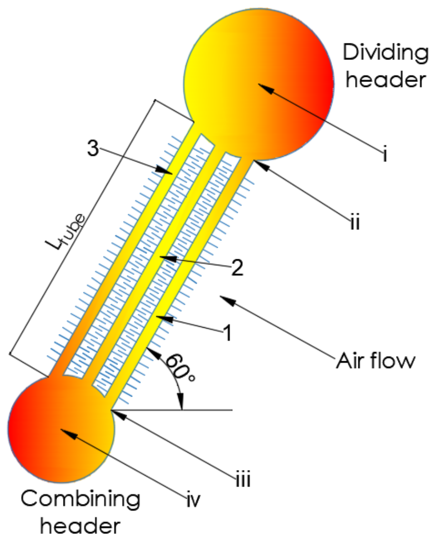

Figure 5. 2: Tubes rows between the dividing and combining headers

5.3.1.1. Energy equation

In ACC, the heat is transferred from the condensing steam inside the inclined tubes to the ambient airflows over the tubes. Therefore, the energy equation formulates the heat transfer rates balance between the air- and steam-sides is:

$$Q = \sum_{i=1}^{n_r} m_a c_{pa(i)} \left(T_{ao(i)} - T_{ai(i)}\right) = \sum_{i=1}^{n_r} m_{c(i)} i_{fg} = \sum_{i=1}^{n_r} m_a c_{pa(i)} e_{(i)} \left(T_{vm(i)} - T_{ai(i)}\right) \tag{5.1}$$

where i in this case represents the tube row number (*1,2,3*), m_a is the mass flow rate of the ambient air flows through the ACC tube bundle, $T_{ai(i)}$ and $T_{ao(i)}$ are the air inlet and outlet temperatures, respectively, m_c is the condensation rate, and $e_{(i)}$ is the ACC finned tube bundle heat transfer effectiveness, which was determined as:

$$e_{(i)} = 1 - \exp\left(-\frac{UA_{(i)}}{\mathrm{m_a c_{pa(\mathit{i})}}}\right) \tag{5.2}$$

where $UA_{(i)}$ is the overall heat transfer coefficient between the steam and the air.

$$UA_{(i)} = \left(\frac{1}{h_{ae(i)}A_{a(i)}} + \frac{1}{h_{c(i)}A_{c(i)}}\right)^{-1} \tag{5.3}$$

Kröger (2004) proposed the formula for determining experimentally the air-side thermal conductance for a specific finned tube as:

$$h_{ae(i)}A_{a(i)} = \mathrm{N_{y(\mathit{i})} k_{a(\mathit{i})} A_{fr(\mathit{i})} P_{ra(\mathit{i})}^{1/3}} \tag{5.4}$$

where N_y is the determined experimentally characteristic heat transfer parameter and its given form is:

$$\mathrm{N_{y(\mathit{i})}} = \mathrm{aR}_{\mathrm{y}(i)}^{b} \tag{5.5}$$

where R_y is the characteristic flow parameter and defined as:

$$\mathrm{R_{y(\mathit{i})}} = m_{a(i)}/\mu_{a(i)}A_{fr(i)} \tag{5.6}$$

where $A_{fr(i)}$ is the effective frontal area of ACC tube bundle. The condensation heat transfer coefficient for inclined tubes was defined by Groenewald (1993) correlation as:

$$h_{c(i)} = 0.9245\left[\frac{L_t k_{c(i)}^3 \rho_{c(i)}^2 g cos(\theta) i_{fg(i)}}{\mu_{c(i)} m_{a(i)} c_{pa(i)}\left(T_{vm(i)} - T_{ai(i)}\right)\left[1 - \exp\left(-\frac{U_{c(i)} H_t L_t A_{(i)}}{m_{at} c_{pa(i)}}\right)\right]}\right]^{0.25} \quad (5.7)$$

The air temperature at the exit of the ACC tube bundle can be defined from Eq. (5.1) as:

$$T_{ao(i)} = T_{ai(i)} + e_{(i)}(T_{vm(i)} - T_{ai(i)}) \quad (5.8)$$

5.3.1.2. Draft equation

The draft equation signifies the losses of mechanical energy that the air experiences as it flows through the ACC's tube bundles. These losses should be overcome by the additional mechanical energy supplied by the fan. The fan performance characteristic was used to determine the amount of mechanical energy to be added by the fan. This was achieved by employing the fan static pressure to the volume flow rate of air curves. The air-side loss over the ACC unit generally consists of losses over the ACC tube bundles, however, the obstacles up- and downstream of the bundles and fan, also add some losses (Owen, 2013). The air-side losses over the ACC tube bundles were defined as:

$$\Delta p_{Fs} - \left(\Delta p_{ts} + \Delta p_{up-do}\right) = \Delta p_a \quad (5.9)$$

$$\Delta p_a = K_{\theta t} \rho_{am} v_{am}^2 / 2 \quad (5.10)$$

$$\Delta p_{Fs} = K_{Fs} \frac{\left(\frac{m_a}{A_{cas} n_F}\right)^2}{2\rho_{am}} \tag{5.11}$$

where Δp_{ts} and $\Delta p_{up/do}$, are the losses over the unit tower supports and obstacles up- and downstream of the fan respectively. K_{Fs}, n_F and A_{cas} are static loss coefficient, number of fan and fan casing area, respectively. While, ρ_{am} and v_{am} are the mean air density and velocity through the bundle, respectively.

For a forced draft system, the K_{ot} is expressed as:

$$\begin{aligned} K_{\theta t} = K_{he} &+ \frac{2(\rho_{ai} - \rho_{ao})}{\sigma_{min}^2(\rho_{ai} - \rho_{ao})} \\ &+ \frac{2\rho_{ao}}{(\rho_{ai} - \rho_{ao})}\left(\frac{1}{\sin\theta_m} - 1\right)\left(\frac{1}{\sin\theta_m} - 1 + 2K_c^{0.5}\right) \\ &+ \frac{2\rho_{ai}(K_{dj} + K_o)}{(\rho_{ai} - \rho_{ao})} \end{aligned} \tag{5.12}$$

where Khe is the loss coefficient for normal isothermal flow through the finned-tube bundle which consider the contraction and expansion losses through the bundle. K_{dj} takes into account the losses due to the turbulent decay of the jet after the bundles, while K_o takes into account losses during the final mixing process as the flow leaves the ACC (Owen, 2013).

5.3.1.3. Steam-side pressure drop

The steam-side pressure changes as steam is condensed. This is due to condensation process and the effects of the frictional, momentum and gravitational force through the condenser tubes as shown in Eq. (5.13).

$$\Delta p_s = \Delta p_{st} + \Delta p_m + \Delta p_f \tag{5.13}$$

where, Δp_{st} is the elevation head pressure drop; Δp_m is the momentum pressure term. This is a momentum recovery for condensing steam flows, because at the inlet, the steam is less- dense, therefore, its kinetic energy is greater than that of the more-dense liquid condensate at outlet. Δp_f is the pressure drop due to friction, which normally defined by employing the empirically-based models. According to O'Donovan and Grimes (2015), the momentum recovery can reduce the pressure drop through the tube bundle by offsetting the frictional losses. However, this phenomenon is always not a case, because different empirical models showed inconsistent results.

The excessive frictional pressure loss may result on the limitation on the vacuum level obtained at turbine outlet, which can lead to plant output reduction (O'Donovan at el, 2012). Additionally, extreme pressure drop decreases the temperature difference between the saturated steam and ambient air ($\Delta T = T_{vm} - T_{ai}$). This is because the temperature and pressure of the saturated steam flowing through the condenser tubes are co-dependent. Low ΔT in ACC can badly affect the ACC heat transfer characteristics. According to Palen (1993) through Donovan *et al.* (2012), the overall change of condenser steam-side pressure should not be greater than 20 % of the operating pressure. The momentum and gravitational/ static pressure drop are given respectively as:

$$\Delta p_{st} = \rho_{vii} g L_t \sin\theta \tag{5.14}$$

$$\Delta p_m = \rho_{vii}(v_{viii}^2 - v_{vii}^2) \tag{5.15}$$

Regardless, multiple studies conducted to determine friction pressure drop in two-phase liquid-vapor flow, no accurate method or analytical model was yet to be found (Donovan *et al.*, 2012). Most of the available models are based on the experimental approach, and therefore they were developed for a particular set of fluids/flow conditions/geometries. For that reason, these models perform and predict the pressure drop well only on limited range of the database which corresponds to the conditions in which they were established. Therefore, the inconsistence of about 50% was found between some empirical models (Moreno *et al.,* 2003). In attempt to validate the most applicable model, Lockhart and Martinelli (1949) theoretical two-phase pressure drop models was compared to the experimental value. In general, the results agreed however, at higher steam flow rates there were some discrepancies (Donovan *et al.*, 2012 and O'Donovan and Grimes, 2015).

Therefore, in this study, the equation used in Honing (2009) study to calculate the pressure difference in ACC tubes between dividing and combining headers was adopted. This equation was initially derived by Kröger (2004). However, Kröger (2004) assumed the complete condensation of all the steam entering the tubes, which was not a case in Honing (2009).

$$dP_{vf} = f_{De}\rho_v v_v^2 \frac{dz}{2d_e} \tag{5.16}$$

where f_{De} is interfacial friction factor which is determined as:

$$f_{De} = f_D(a_1 + a_2/Re_v) \tag{5.17}$$

By integrating Eq. (5.16) over the entire tube length, it became:

$$\Delta p_f = \frac{0.1582\mu_{vii}^2 L_t}{\rho_{vii} d_e^3 (Re_{viii} - Re_{vii})}\left[\frac{a_1}{2.75}\left(Re_{viii}^{2.75} - Re_{vii}^{2.75}\right) + \frac{a_2}{1.75}\left(Re_{viii}^{1.75} - Re_{vii}^{1.75}\right)\right] \tag{5.18}$$

where d_e is the hydraulic diameter of the tube, and value a_1 and a_2 are expressed as:

$$a_1 = 1.0649 + 1.0411 \times 10^{-3} Re_{vn} - 2.011 \times 10^{-7} Re_{vn}^3 \tag{5.19}$$

$$a_2 = 290.1479 + 59.3153 Re_{vn} + 1.5995 \times 10^{-2} Re_{vn}^3 \tag{5.20}$$

This equation neglects the changes in thermos-physical properties. It is believed that vapor laminarization of the flow during condensation tends to occur at $Re_v < 2300$; however, this has a less effects on the friction pressure drop in practical ACC tubes (Kröger, 2004). The Reynolds number normal to the surface are defined as:

$$\mathrm{Re}_{vn} = \frac{Re_{vii} W_t}{2L_t} - \frac{Re_{viii} W_t}{2L_t} \tag{5.21}$$

And the local Reynolds number can now be expressed as:

$$\mathrm{Re_{viii}} = \frac{\rho_{viii} v_{viii} d_e}{\mu_{viii}} \tag{5.22}$$

5.3.2. Array of Axial Fans Modelling

The axial fan array rotation speed is used to regulate the turbine back pressure, by stimulating the condensation process of steam. This is because the turbine back pressure is associated with the temperature of the exhaust steam. According to Huang *et al.* (2020) the turbine back pressures can be calculated using Eq. (5.23), when the steam pressures drop from the turbine to the condenser is not considered.

$$p_B = 0.00981 \left(\frac{T_s + 100}{57.66}\right)^{7.46} \tag{5.23}$$

where T_s is a steam temperature. During the actual operation, the axial flow fans speeds are kept at the same value. The characteristic parameters of axial fans change with operating states. Therefore, the performance of fan at off-design condition can be attained by employing the fan laws of dimensional similarity at the design conditions as in Eq. (5.24) to (5.26).

$$\frac{V_f}{V_{fm}} = \left(\frac{D_f}{D_{fm}}\right)^3 \frac{N_f}{N_{fm}} \tag{5.24}$$

$$\frac{\Delta P_{sf}}{\Delta P_{sfm}} = \frac{\rho_a}{\rho_{am}} \left(\frac{D_f}{D_{fm}}\right)^2 \left(\frac{N_f}{N_{fm}}\right)^2 \tag{5.25}$$

$$\frac{P_f}{P_{fm}} = \frac{\rho_a}{\rho_{am}} \left(\frac{D_f}{D_{fm}}\right)^5 \left(\frac{N_f}{N_{fm}}\right)^3 \tag{5.26}$$

where, V_f, ΔP_{sf}, P_f, ρ_a, D_f and N_f, are volumetric flow rate, static pressure rises, power consumption, density of air, fan diameter and rotational speed, respectively. When the fan is operating under designed conditions, its operating parameters are equal to that with subscript *'m'*. Since, in this study the performance of the same axial fan is analysed at different speeds and ambient air temperatures, Eq. (5.24), (5.25), and (5.26) are simplified as:

$$\frac{V_f}{V_{fm}} = \frac{N_f}{N_{fm}} \tag{5.27}$$

$$\frac{\Delta P_{sf}}{\Delta P_{sfm}} = \frac{\rho_a}{\rho_{am}} \left(\frac{N_f}{N_{fm}}\right)^2 \tag{5.28}$$

$$\frac{P_f}{P_{fm}} = \frac{\rho_a}{\rho_{am}} \left(\frac{N_f}{N_{fm}}\right)^3 \tag{5.29}$$

5.3.3. Steam Turbine Low Pressure Cylinder Modelling

In this Section, the models for determining the turbine exhaust mass flow rate and enthalpy were developed. This is essential because the changes in turbine exhaust mass flow rate and enthalpy significantly affect the backpressure of the generating unit which sequentially affects the power generation of the steam turbine low pressure section.

5.3.3.1. Exhaust steam mass flow rate calculation

The calculation of turbine exhaust steam mass flow rate was performed by employing the methods that are used to carry out the turbine off-design calculations. The method of regenerative system heat balance was used. This method was considered to be the most accurate as well as it is convenient to implement (Zhang *et al.*, 2019). This method incorporates the mass and energy conservation principles to derive the general matrix equation of steam-water distribution (Yan *et al.*, 2000).

The steam turbine of considered generating unit, has five (5) extraction ports/ stages, one (1) on the HP turbine, and four (4) on the LP turbine stage. The extracted steam is fed to five (5) different heaters, as shown in the schematic diagram of the regenerative extraction cycle of the unit in Figure 5.3. The cycle is made up of four (4) surface heaters (2 HP and 2 LP) and one (1) direct contact heater (deaerator).

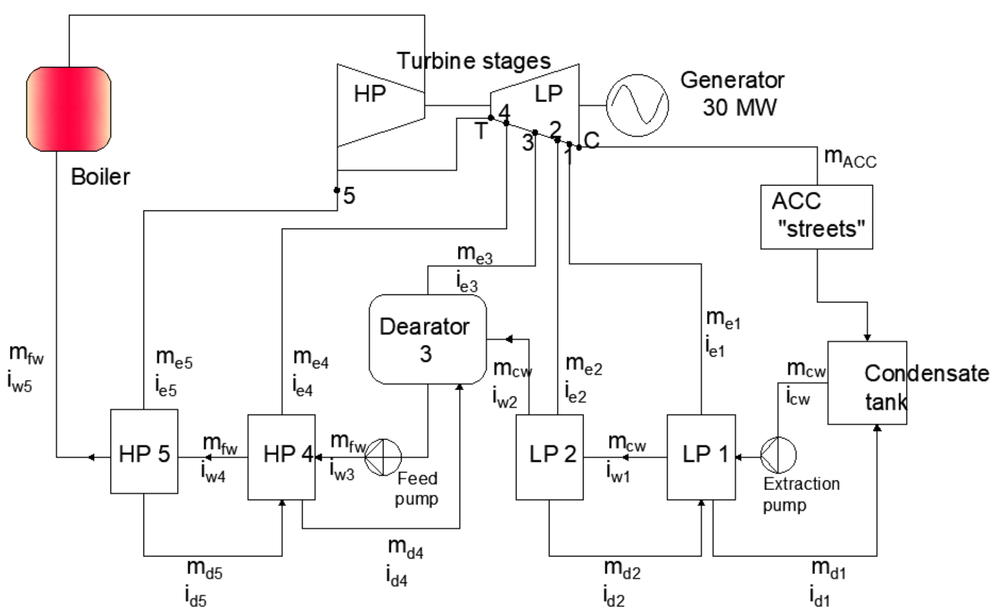

Figure 5. 3: Schematic diagram of the unit regenerative extraction cycle

In order to derive the equations that, describe the mass and energy balance of each heater, the control volumes were taken around each heater, and the mass and energy conservation principles were applied to each control volumes. The extraction steam enthalpy changes(q_e) were expressed as:

For the surface heater:

$$q_{ei} = i_{ei} - i_{di} \tag{5.30}$$

For direct contact heater:

$$q_{ei} = i_{ei} - i_{wi} \tag{5.31}$$

The feed water enthalpy changes$\left(q_{fw}\right)$ for both surface and direct contact heaters were expressed as:

$$q_{fwi} = i_{wi} - i_{wi+1} \tag{5.32}$$

The drainage flow enthalpy changes(q_d) were expressed as:

For the surface heater:

$$q_{di} = i_{di+1} - i_{di} \tag{5.33}$$

For direct contact heater:

$$q_{di} = i_{di+1} - i_{wi} \tag{5.34}$$

where subscript i is number of extraction stage; i_e is extraction enthalpy; i_d is drainage enthalpy; i_w is heated water enthaply. Since, the aim was to compute the turbine exhaust steam mass flow rate, the derivation of equations began at the heater with extraction from HP turbine stage, and then proceeded to the one that taps from LP turbine stage toward the turbine exit.

Surface heater 5, HP:

$$m_{\mathrm{e5}}(i_{\mathrm{e5}} - i_{\mathrm{d5}}) = m_{fw}(i_{\mathrm{w5}} - i_{\mathrm{w4}}) \tag{5.35}$$

Surface heater 4, HP:

$$m_{\mathrm{e5}}(i_{\mathrm{d5}} - i_{\mathrm{d4}}) + m_{\mathrm{e4}}(i_{\mathrm{e4}} - i_{\mathrm{d4}}) = m_{fw}(i_{\mathrm{w4}} - i_{\mathrm{w3}}) \tag{5.36}$$

Direct contact heater 3:

$$\begin{aligned} m_{\mathrm{e5}}(i_{\mathrm{d4}} - i_{\mathrm{w3}}) + m_{\mathrm{e4}}(i_{\mathrm{d4}} - i_{\mathrm{w3}}) + m_{\mathrm{e3}}(i_{\mathrm{e4}} - i_{\mathrm{w4}}) \\ = m_{cw}(i_{\mathrm{w3}} - i_{\mathrm{w2}}) \end{aligned} \tag{5.37}$$

Surface heater 2, LP:

$$m_{\mathrm{e2}}(i_{\mathrm{e2}} - i_{\mathrm{d2}}) = m_{cw}(i_{\mathrm{w2}} - i_{\mathrm{w1}}) \tag{5.38}$$

Surface heater 1, LP:

$$m_{\mathrm{e2}}(i_{\mathrm{d2}} - i_{\mathrm{d1}}) + m_{\mathrm{e1}}(i_{\mathrm{e1}} - i_{\mathrm{d1}}) = m_{cw}(i_{\mathrm{w1}} - i_{\mathrm{cw}}) \tag{5.39}$$

where m_{ei}, m_{fw}, m_{cw} and i_{cw} are the steam mass flow rate of i^{th} extraction stage; boiler feed water flow; condensate water flow; enthalpy of condensate water, respectively.

Eq. (5.35) to (5.39) can be re-written into matrix form as:

$$A.m_e = m_w.B \tag{5.40}$$

where A, B, m_e and m_w are expressed, respectively as:

$$A = \begin{bmatrix} q_{e5} & 0 & 0 & 0 & 0 \\ q_{d4} & q_{e4} & 0 & 0 & 0 \\ q_{d3} & q_{d3} & q_{e3} & 0 & 0 \\ 0 & 0 & 0 & q_{e2} & 0 \\ 0 & 0 & 0 & q_{d1} & q_{e1} \end{bmatrix} \tag{5.41}$$

$$B = \begin{bmatrix} q_{fw5} \\ q_{fw4} \\ q_{fwi3} \\ q_{fw2} \\ q_{fw1} \end{bmatrix} \tag{5.42}$$

$$m_e = \begin{bmatrix} m_{e5} \\ m_{e4} \\ m_{e3} \\ m_{e2} \\ m_{e1} \end{bmatrix} \tag{5.43}$$

$$m_w = \begin{bmatrix} m_{fcw} & 0 & 0 & 0 & 0 \\ 0 & m_{fcw} & 0 & 0 & 0 \\ 0 & 0 & m_{cw} & 0 & 0 \\ 0 & 0 & 0 & m_{cw} & 0 \\ 0 & 0 & 0 & 0 & m_{cw} \end{bmatrix} \tag{5.44}$$

From Eq. (5.40), the steam mass flow rate from each extraction stage can be calculated as:

$$m_e = A^{-1}.m_w.B \tag{5.45}$$

Then the flow rate of the exhausted steam to ACC can be computed as:

$$m_{ACC} = m_B - \sum m_e \tag{5.46}$$

where the m_B is the turbine live steam mass flow rate from the boiler.

5.3.3.2. Exhaust steam enthalpy calculation

The exhaust steam is in two- phase region, therefore it is essential for its dryness to be defined. The changes in backpressure of the turbine influence the pressure ratio in the last stage of the turbine, and as a consequence, the exhaust steam enthalpy alters. The enthalpy at the turbine exit (i_{ACC}) is a function of the turbine exhaust pressure, which mainly depends on the condensing pressure and temperature of the ACC. For the ideal conditions, the ACC condensing pressure is equal to the turbine exhaust pressure. However, when the pressure drop on the steam-side is considered, the condensing pressure is less than turbine exhaust pressure. The condensing temperature or mean temperature (T_{vm}) for both primary and dephlegmator were computed by employing Eq. (5. 47).

$$T_{vm} = \frac{T_{a,out} - T_{a,in}}{\varepsilon} + T_{a,in} \tag{5.47}$$

For the entire ACC the condensing temperature was defined from the total heat transfer rate as:

$$Q_T = \dot{m}_c i_{fg}(T_{vm})$$
$$= \left[\dot{m}_a C_{pa}\left(T_{a,out} - T_{a,in}\right)\right]_{primary} + \left[\dot{m}_a C_{pa}\left(T_{a,out} - T_{a,in}\right)\right]_{dephlegmator} \quad (5.48)$$

where m_c is total condensation rate, and is defined as:

$$\dot{m}_c = m_{c,primary} + m_{c,dephlegmator} \quad (5.49)$$

and $i_{fg}(T_{vm})$ is enthalpy of vaporization corresponding to the condensing temperature which is expressed as:

$$i_{fg}(T_{vm}) = (3.4831814 \times 10^6 - 5.8627703 \times 10^3 T_{vm} + 12.139568 {T_{vm}}^2 - 1.40290431 \times 10^{-2}\, T_{vm}^3)\,(10^{-3}), kJ/kg \quad (5.50)$$

Knowing the steam-side pressure drop and condensing pressure, the turbine exhaust pressure can be determined. Steam mass flow rate in the HP and LP turbine stages were expressed respectively, as:

$$m_B = m_{\mathrm{e5}} + m_{\mathrm{T}} \quad (5.51)$$

$$m_{\mathrm{T}} = m_{\mathrm{e4}} + m_{\mathrm{e3}} + m_{\mathrm{e2}} + m_{\mathrm{e1}} + m_{\mathrm{ACC}} \quad (5.52)$$

The power generated at each extraction port or stage was calculated as:

$$W_{\mathrm{B-5}} = m_{\mathrm{B}}(i_{\mathrm{B}} - i_{\mathrm{e5}}) \tag{5.53}$$

$$W_{\mathrm{5-T}} = (m_{\mathrm{B}} - m_{\mathrm{e5}})\,(i_{\mathrm{e5}} - i_{\mathrm{T}}) \tag{5.54}$$

$$W_{\mathrm{T-4}} = \dot{m}_{\mathrm{T}}(i_{\mathrm{T}} - i_{\mathrm{e4}}) \tag{5.55}$$

$$W_{\mathrm{4-3}} = (\dot{m}_{\mathrm{T}} - \dot{m}_{\mathrm{e4}})\,(i_{\mathrm{e4}} - i_{\mathrm{e3}}) \tag{5.56}$$

$$W_{\mathrm{3-2}} = (\dot{m}_{\mathrm{T}} - \dot{m}_{\mathrm{e4}} - \dot{m}_{\mathrm{e3}})\,(i_{\mathrm{e3}} - i_{\mathrm{e2}}) \tag{5.57}$$

$$W_{\mathrm{2-1}} = (\dot{m}_{\mathrm{T}} - \dot{m}_{\mathrm{e4}} - \dot{m}_{\mathrm{e3}} - \dot{m}_{\mathrm{e2}})\,(i_{\mathrm{e2}} - i_{\mathrm{e1}}) \tag{5.58}$$

$$W_{\mathrm{1-ACC}} = (\dot{m}_{\mathrm{T}} - \dot{m}_{\mathrm{e4}} - \dot{m}_{\mathrm{e3}} - \dot{m}_{\mathrm{e2}} - m_{\mathrm{e1}})\,(i_{\mathrm{e1}} - i_{\mathrm{ACC}}) \tag{5.59}$$

The power generated in the HP and LP turbine stages, respectively are

$$W_{HP} = W_{\mathrm{B-5}} + W_{\mathrm{5-T}} \tag{5.60}$$

$$W_{LP} = W_{\mathrm{T-4}} + W_{\mathrm{4-3}} + W_{\mathrm{3-2}} + W_{\mathrm{2-1}} + W_{\mathrm{1-ACC}} \tag{5.61}$$

In terms of exhaust steam mass flow rate (m_{ACC}), the gross turbine output power is:

$$W_T = 1.307047601\dot{m}_{\mathrm{ACC}}(i_{\mathrm{B}} - i_{\mathrm{e5}}) + 1.2411925\dot{m}_{\mathrm{ACC}}(i_{\mathrm{e5}} - i_{\mathrm{T}}) + \tag{5.62}$$

$$1.24119251\dot{m}_{\mathrm{ACC}}(i_{\mathrm{T}} - i_{\mathrm{e4}}) + 1.187117\dot{m}_{\mathrm{ACC}}(i_{\mathrm{e4}} - i_{\mathrm{e3}}) +$$

$$1.13532172\dot{m}_{\mathrm{ACC}}\,(i_{\mathrm{e3}} - i_{\mathrm{e2}}) + 1.056814408\dot{m}_{\mathrm{ACC}}(i_{\mathrm{e2}} - i_{\mathrm{e1}}) +$$

$$1.003426541\dot{m}_{\mathrm{ACC}}(i_{\mathrm{e1}} - i_{\mathrm{ACC}})$$

5.4. Validation of cold-end system mathematic model

To test the precision of the developed model, its performance was validated against the design performance data of the considered generation unit. Therefore, the model was run at design operating conditions of the ACC system as indicated in Tables 5.1, 5.2 and 5.3, as well as using the geometrical characteristics in Table 5.4. The maximum heat transfer rate of ACC was calculated by using the steam content, mass flow and the corresponding enthalpy of the exhaust steam. In this case the exhaust steam enthalpy was that corresponding to exhaust steam pressure.

$$Q_{max} = m_s i_{fg} = 26.389 \times 2404 = 63439\ \mathrm{kW} = 63.44\ \mathrm{MW} \tag{5.63}$$

According to the operating manuals, when the steam-side pressure drop is considered, the condensate temperature may be about 2 – 5 K lower that the exhaust steam temperature. Therefore, by using the exhaust steam temperature of 60.6 ℃, the condensate temperature was in the range of 58.06 – 55.06 ℃.

The comparison of the model performance data to design performance data of ACC and turbine exhaust conditions is presented in Table 5.5. The percentage error was computed as:

$$Error = \left(\frac{design\ parameter - calculated\ parameter}{design\ parameter}\right) \times 100\% \tag{5.64}$$

Table 5. 5: Comparison of model and design performance data of ACC and turbine exhaust conditions

Parameter	Unit	Design performance data	Model performance data	Error, %
Net Power	MW	30	30.52	-1.73
Exhaust steam pressure	Pa	19620	19368.73	1.28
Exhaust steam temperature	℃	60.06	59.38	2.34
Enthalpy of exhaust steam	kJ/kg	2404	2403.23	-0.34
Exhaust steam flow, ($\boldsymbol{m_{ACC}}$)	kg/s	26.389	26.12	1.02
Uncondensed steam flow	kg/s	0	0.199	
Heat transfer rate	MW	63.20	61.85	2.14

From the results in Table 5.5, it is clearly that, the developed model predicts the ACC and generating unit performance reasonably, with negligible discrepancies. These discrepancies may due to the accuracy of the correlations used to predict the steam-side pressure drop, and specifically, the frictional steam-side pressure drop. The average steam-side pressure drop of the model is 736.78 Pa, which is about 4 % of the condensing pressure ($P_{vm} = 19000.34\ P_a$). This is less than 20% as it was indicated by Palen (1993) through Donovan *et al*. (2012), that the overall change of condenser steam-side pressure drop should not be greater than 20 % of the operating pressure.

Due to the pressure drop considerations, the obtained exhaust steam pressure is less than the designed one. This leads to the decrease in exhaust steam pressure by 2.51 mbar, which results in an increase of the enthalpy difference at the turbine exit. Thus, the turbine power output is higher than the designed one by 1.73 %. Furthermore, the decrease of the condensing pressure and corresponding temperature, results in the dropping of temperature difference between condensing and ambient air temperature ($\Delta T = T_{vm} - T_{ai}$) consequently, the heat transfer rate drops. Thus, 0.75 % of steam is uncondensed and it will be ejected into the atmosphere. Similar trend of results was achieved by Zhang *et al*, (2019) on their performance analysis of ACC cold-end system modelling.

Some of the calculated variables for each tube bundle row and for both primary condenser and CD units, as well for entire ACC units are shown in Figure 5.4 to 5.9. From Figure 5.4, it is clear that the highest heat transfer rate was achieved in the first tube row (row 1), which comes into contact with the ambient air first. This is due to the high temperature difference between the condensing and air temperature in the first tube row, which decreases as the air flows through the tube bundle as presented in Figure 5.5. Figure 5.6 shows that the steam-side pressure drop was high in tube row *1*. This is due to the higher condensation of steam in this tube row as shown in Figure 5.7, which results on higher steam velocity at the inlet of tube row *1*. This clearly depicted in Figure 5.8.

As it can be seen in Figure 5.9, the momentum pressure loss is a negative term, thus it is a pressure recovery for steam condensation. The momentum recovery was found to be in the same order of magnitude as the friction pressure drop. This concurs with O'Donovan *et al.* (2012) findings in their study of the steam-side characterization of modular ACC. Furthermore, in O'Donovan *et al.* (2012) study, it was found that this closer or same order of magnitude leads to small pressure drop in the tube bundle, when the geodetic pressure drops were not considered. This is also shown in Figure 5.9 as ΔP_t. As stated by O'Donovan and Grimes (2015), the momentum recovery phenomenon is always not a case as this depends on empirical model used to define friction pressure drop. Thus, in tube row *1 and 3* the momentum recovery does not completely offset the effect of friction pressure drop. Most of the above-discussed phenomena was applicable to both primary condenser and CD units.

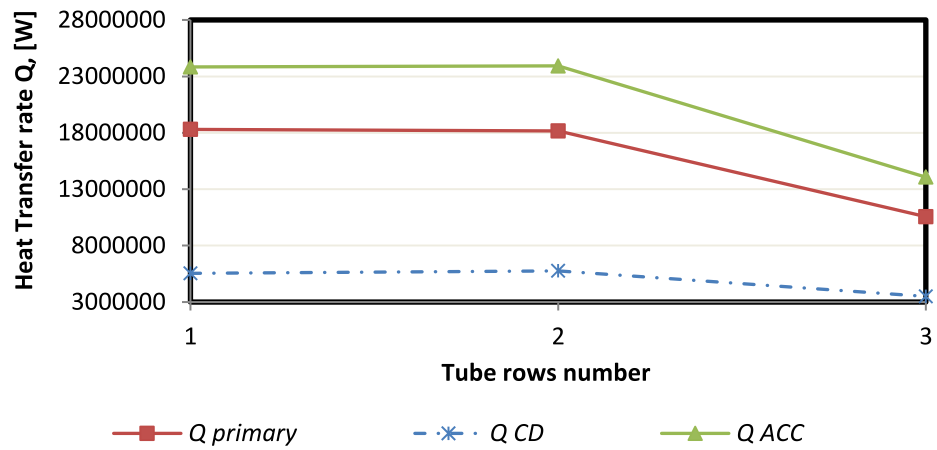

Figure 5. 4: Heat transfer rate per tube row

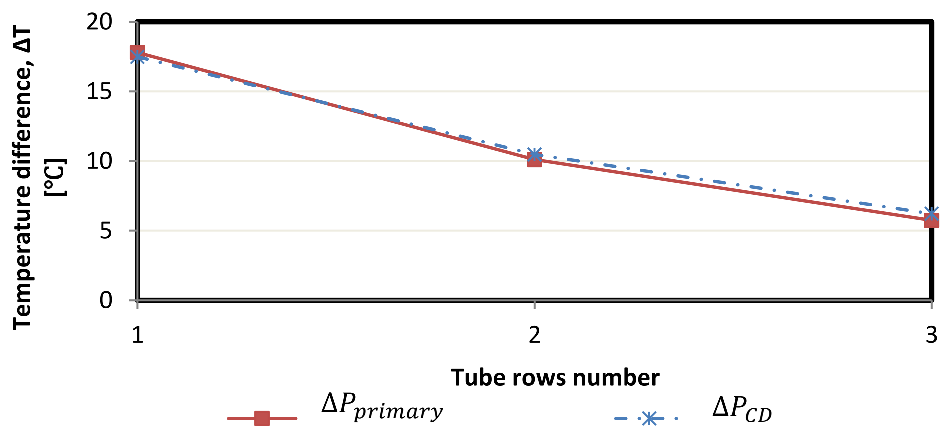

Figure 5. 5: Temperature difference between condensing and ambient air per tube row

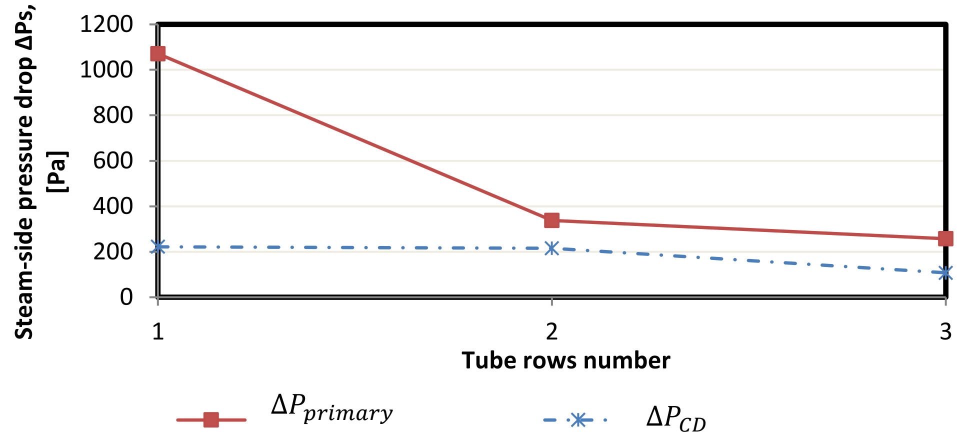

Figure 5. 6: Steam-side pressure drop per tube row

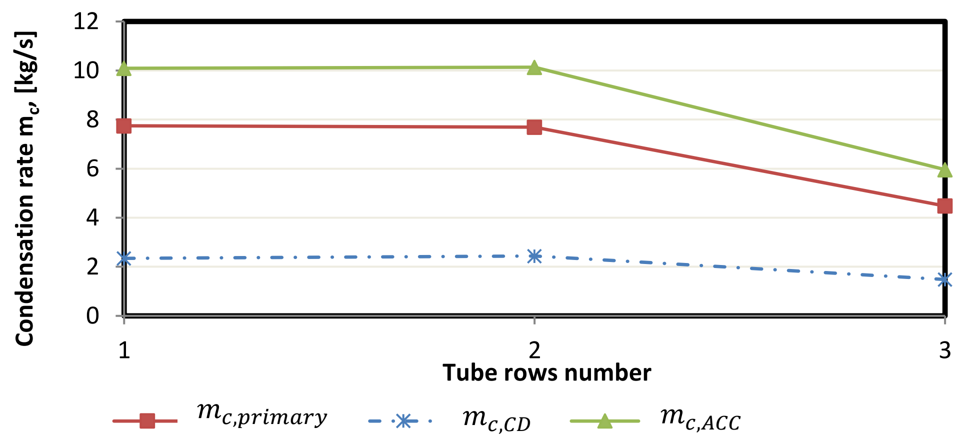

Figure 5. 7: Condensation rate per tube row

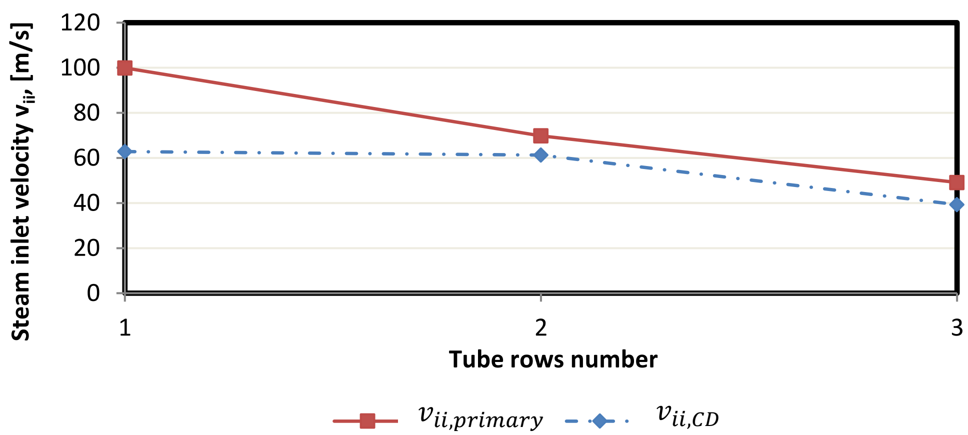

Figure 5. 8: Steam inlet velocity per tube row

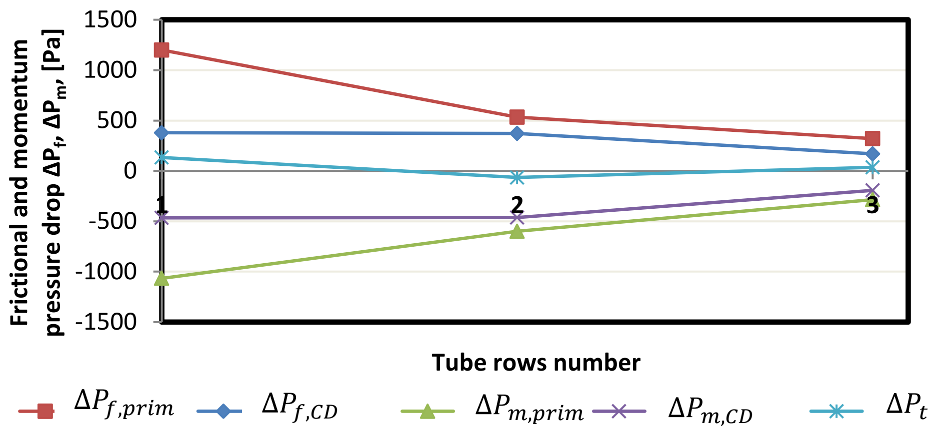

Figure 5. 9: Frictional and momentum pressure losses per tube row

5.5. Sensitivity Analysis

The sensitivity study of the ACC performance to the ambient air temperature and rotational fan speed during the hot periods was assessed through parametric study that was conducted under two conditions. In the first condition, the ambient air temperature was varied from the design operating value of 32.2 ℃ to 40 ℃, while the rotational fan speed was kept constant. In the second condition, rotational fan speed was altered from 50 rpm to 250 rpm; while the ambient air temperature remain unchanged. According to Moore *et al.* (2014), the plant output and efficiency can be maximized by changing the rotational fan speed. Thus, a 10 % increase in fan speed can result in an increase of 10 % of plant output.

The considered rotational axial fan speed range was selected so that at design ambient air temperature (T_{ai} = 32.2 ℃), when the volumetric flow rate is less than the optimum, the design steam turbine exhaust pressure (19620 Pa) is achieved. While, at highest considered air temperature (T_{ai} = 40 ℃), when the volumetric flow rate is greater than the optimum, the design steam turbine exhaust pressure (19620 Pa) is achieved. For both conditions, the steam flow was kept constant and equal to the design value of 26.389 kg/s. In addition to that, for the CD units only 150, 182 and 225 rpm rotational fan speeds were considered, due to the fact that at higher ambient air temperature and lower rotational fan speed, the CD unit were flooded with steam, while at higher rotational fan speed and ambient air temperature closer to the design value (32.2 ℃ and 34 ℃), the CD unit were starved.

All the operating parameters which define the performance of the ACC on both steam and air-sides, were recorded for both primary condenser and CD unit. On the air- side, the performance of the ACC was defined in terms of the heat transfer rate, air-side pressure drop, fan power consumption, and outlet air temperature, which is mainly governed by air volumetric flow rates. On the steam-side, the ACC performance was determined in terms of condensing pressure and temperature, steam-side pressure drop, steam velocity, condensation rate, and amount of uncondensed steam ejected out of the condenser.

Furthermore, the turbine output power was computed, and the effect of the ACC performance on the steam turbine output power was outlined. The net power plant output was calculated by subtracting the total fan power consumption from the steam turbine output power as:

$$W_{net} = W_t - P_F \tag{5.65}$$

The plant performance was also expressed in terms of the efficiency loss due to condenser performance as (Moore *et al.*, 2014):

$$\eta_{loss} = \left(1 - \frac{W_{net}}{W_{net,max}}\right) \times 100\% \tag{5.66}$$

where W_{net} and $W_{net,max}$ were obtained net power output at different ambient air temperatures and fan speeds and net power output attained by the validated model at design operating conditions, respectively. The obtained performance parameters for both primary condenser and CD units were analysed and discussed in chapter 8.

5.6 CD performance data

Initial performance analysis for both primary condenser and CD units was conducted at constant rotational speed of 182 rpm, which is equal to the design operating value. However, at low ambient air temperatures, the rejected steam from the primary condenser units became insignificant. Furthermore, the fans consume more energy when operated at high speeds. That means, as recommended in GEA (1978), the fan speed on the primary condenser units-side should be lower than that of the dephlegmator unit-side. By employing this measurement, more steam from the primary condenser units, and less energy was consumed by primary condenser units-side fans. For that reason, the fan speed on primary condenser units' side was considered to be 125 rpm, while the fan speed on the CD units-side was kept at 140 rpm. The CD performance data obtained at this fan speed, and at different ambient air temperatures, as shown in Table 5.6, were compared to that of HDWD, whose performance was analysed in Chapter 6. Furthermore, the primary condenser unit's performance data attained at same operation conditions, and presented in Table 5.7 were combined with that of CD units, in order to achieved the overall ACC performance, which is shown in Table 5.8, as well as to signify the ACC effect on the steam turbine and net power output of the generating unit, depicted in Table 5.9. Furthermore, these performance data were illustrated graphically, scrutinised, and discussed in detail in Chapter 8.

Table 5. 6: CD units performance data

Parameter	Unit	Value			
Ambient Air Temperature, T_{ai}	°C	32.2	36	40	44
Heat Transfer rate, Q	MW	11.16	9.74	7.18	5.33
Outlet air temperature, T_{ao}	°C	47.12	48.77	49.50	50.50
Air-side pressure drop, $\Delta \boldsymbol{p_a}$	Pa	158.95	157.21	151.79	146.79
Fan power, P_F	kW	68.27	67.44	66.57	65.57
Inlet steam flow rate, m_i	kg/s	12.214	13.608	15.863	18.08
Ejected steam flow rate, m_e	kg/s	7.50	9.49	12.83	15.83
Condensation rate, m_c	kg/s	4.72	4.12	3.03	2.24
Steam-side pressure drop, $\Delta \boldsymbol{p_s}$	Pa	1,810.04	2,574.22	4,653.80	6,653.80
Condensing pressure, P_c	Pa	17,022.88	17,255.00	16,102.41	14,102.41

Table 5. 7: Primary condenser units performance data

Parameter	Unit	Value			
Ambient Air Temperature, T_{ai}	°C	32.2	36	40	44
Heat Transfer rate, Q	MW	33.48	30.18	24.85	19.62
Outlet air temperature T_{ao}	°C	49.22	51.06	52.55	54.00
Air-side pressure drop, $\Delta \boldsymbol{p_a}$	Pa	106.91	105.85	104.58	103.34
Fan power, P_F	kW	145.79	143.99	142.15	140.36
Inlet steam flow rate, m_i	kg/s	26.389	26.389	26.388	26.39
Ejected steam flow rate, m_e	kg/s	12.21	13.61	15.86	18.08
Condensation rate, m_c	kg/s	14.18	12.78	10.53	8.31
Steam-side pressure drop, $\Delta \boldsymbol{p_s}$	Pa	755.73	804.96	944.00	1099.20

Table 5. 8: ACC incorporated with CD performance data

Parameter	Unit	Value			
Ambient Air Temperature, T_{ai}	°C	32.2	36	40	44
Heat Transfer rate, Q	MW	44.64	39.92	32.03	24.95
Average outlet air temperature, T_{ao}	°C	48.17	49.92	51.02	52.25
Air-side pressure drop, $\Delta \boldsymbol{p_a}$	Pa	132.93	131.53	128.19	125.06
Fan power, P_F	kW	214.07	211.43	208.73	205.94
Inlet steam flow rate, m_i	kg/s	26.389	26.389	26.389	26.389
Ejected steam flow rate, m_e	kg/s	7.50	9.49	12.83	15.83
Condensation rate, m_c	kg/s	18.89	16.90	13.56	10.55
Condensing pressure, P_c	kPa	18.278	18.541	18.376	18.015
Steam-side pressure drop, $\Delta \boldsymbol{p_s}$	kPa	2.565	3.379	5.597	7.753

Table 5. 9: Generating unit with ACC incorporated with CD performance data

Parameter	Unit	Value			
Ambient Air Temperature, T_{ai}	°C	32.2	36	40	44
Turbine exhaust pressure, P_i	Pa	19,561.46	20,230.84	21,175.81	21,891.70
Turbine output power, W_t	MW	30.512	30.474	30.422	30.383
Plant/ unit fan power, P_F	kW	214.07	211.43	208.73	205.94
Plant/ unit net output power, W_{net}	MW	30.30	30.26	30.21	30.18

Chapter 6: Analysis of Thermal Performance for HDWD incorporated with Conventional Delugeable Tube Bundle

6.1. Introduction

This Chapter provides the thermal performance analysis of the CDTB, as well as of HDWD incorporated with CDTB into its second stage. Furthermore, the Chapter offers the comparison of thermal performance of the CD (which was analysed in Chapter 5), and HDWD incorporated with CDTB. The CDTB which was modelled in Chapter 3 and optimized in Chapter 4 was incorporated into the second stage of HDWD. As mentioned in Chapter 1, the HDWD has two stages, connected in series and combined in one condenser unit. The first stage has inclined finned tubes shorter compared to the CD tubes, and second stage has horizontal bare flat tubes. The first stage tubes are shortened in order to accommodate the second stage tube bundle (CDTB). The second stage can operate in the dry and wet modes during cold or off-peak and hot or peak periods, respectively. With this arrangement, the uncondensed steam from the primary condenser units are initially condensed in the first stage tubes, and further uncondensed steam is finally condensed in CDTB, which is the second stage of HDWD. The geometric parameters of the CDTB are presented in Table 6.1.

Table 6. 1: CDTB geometric parameters

Parameter	Unit	Value
Bundle width, W_b	mm	2320
Bundle length, L_b	mm	3178
Bundle height, H_b	mm	300
Bundle steam flow area, A_{stb}	m^2	0.142
Tube height, H_t	mm	300
Tube length, L_t	mm	3178

Tube width, W_t	mm	6.95
Tube pitch, P_t	mm	25
Tube thickness, t_t	mm	1.5
Number of tubes, n_{tr}	-	93
Material	Carbon steel	

6.2. Performance Assessment

Since, the first stage operates on dry mode, and as primary condenser and CD units, the performance of the first stage of the HDWD was analysed by employing the developed and validated model for the CD in Chapter 5. The CDTB performance was assessed based on the heat and mass transfer analogy method, presented in Chapter 3. The HDWD performance was assessed and conducted at operation conditions of the ACC of the considered generating unit as described in Chapter 5, and at different ambient air temperatures as it was performed for the CD and primary condenser units in Chapter 5.

During the wet operating mode conditions, a large amount of steam is condensed by the second stage (CDTB) of the HDWD than by the first stage. This is due to substantial inlet/outlet and friction losses in the first stage than in the second stage tube bundle, which results in drawing of large amount of vapor through it by the wet second stage. In the end, this leads to significant net steam-side pressure drop over the first stage. Furthermore, the higher condensation rate results in more pressure recovery in the second stage tube bundle, and therefore, the net steam-side pressure drop in the second stage is considerably less than in the first stage. Moreover, according to Owen (2013), the first stage of HDWD contributes about 67 % to the steam-side pressure drop in the HDWD. Therefore, by neglecting the steam-side pressure drop in the second stage tube bundle, might not have a significant impact on its performance prediction.

The considered generating unit is allocated in the district town (Windhoek) with the average relative humidity in the range of 30% to 32%. Therefore, the CDTB performance analysis was performed at relative humidity of 30%. The fan rotational speed on the HDWD side was kept at 140 rpm, which is the same speed at which the CD performance was conducted. The conditions of the steam at the exit of the primary condenser units obtained in Chapter 5, and presented in Table 6.2, were employed as the operating conditions of the steam in the dividing headers of the HDWD first stage tube bundle.

Table 6. 2: Operating conditions at the exit of the primary condenser units

Parameter	Unit	Value			
Air Temperature	°C	32.2	36	40	44
Steam pressure	Pa	18,269.28	18,916.95	18,863.21	18,799.23
Saturation temperature	°C	58.11	58.87	58.81	58.74
Steam mass flow rate	kg/s	12.213	13.609	15.863	18.078
Steam quality	-	0.49	0.53	0.61	0.69

After, the first stage tube bundle thermal performance was performed, the operating conditions at its exit, and presented in Table 6.3, were taken to be operating conditions at the entrance of the CDTB.

Table 6. 3: Operating conditions at the exit of the first stage tube bundle of HDWD

Parameter	Unit	Value			
Air Temperature	°C	32.2	36	40	44
Steam pressure	Pa	16,803.73	16,831.59	15,185.51	12,062.60
Saturation temperature	°C	56.33	56.38	54.21	49.51
Steam mass flow rate	kg/s	7.83	9.76	12.96	16.27
Steam quality	-	0.64	0.72	0.82	0.9

The ACC with a HDWD was found to use less water which is about 20 %, compared to adiabatic cooling (Heyns, 2008). During the performance assessment of HDWD, the deluge water was considered to be equal to the evaporation rate, at deluge water mass flux, of $1.7\ \mathrm{kg/m^2.s}$. This deluge water mass flux is greater or equal to the deluge water mass flux of $1.6\ \mathrm{kg/m^2.s}$ and $1.7\ \mathrm{kg/m^2.s}$ at which, according to Niitsu *et al.* (1967) and Heyns (2008), respectively, the uniform wetting of tubes occurs. Furthermore, the deluge water mass flux, recommended by Niitsu *et al.* (1967) and Heyns (2008), were obtained by employing the empirical correlations which were derived for the round tube bundles not for flat tube bundle as considered in this study.

All the performance parameters at bundle (1^{st} and 2^{nd} stages), component (primary condenser units, and HDWD) and system level (ACC incorporated with HDWD) were recorded, tabulated, illustrated graphically, and analysed. Furthermore, the turbine and net power output were computed, and the impact of the performance of ACC incorporated with HDWD on the steam turbine performance characteristics was outlined. On the air-side, the HDWD performance data were presented in terms of the heat transfer rate, air-side pressure drop, fan power consumption, and outlet air temperature driven by flow rates of ambient air. On the steam-side, the HDWD performance data were presented in terms of the inlet steam flow rate, ejected steam flow rate, condensation rate, steam-side pressure drop, and condensing pressure.

6.3. Performance Data

The performance data for the first stage tube bundle, CDTB, HDWD incorporated with CDTB, and ACC incorporated with HDWD are depicted in Tables 6.4 to 6.7. In addition to that, the steam turbine performance characteristics were assessed, and presented in Table 6.8. Furthermore, these performance data were illustrated graphically, scrutinised, and discussed in detail in Chapter 8.

Table 6. 4: First stage tube bundle performance data

Parameter	Unit	Value			
Ambient Air Temperature, T_{ai}	°C	32.2	36	40	44
Heat Transfer rate, Q	MW	10.36	9.08	6.88	4.29
Air-side pressure drop, $\Delta \boldsymbol{p_a}$	Pa	317.57	314.22	309.90	305.04
Outlet air temperature, T_{ao}	°C	45.62	47.56	48.83	49.50
Fan power, P_F	kW	68.27	67.44	66.57	65.73
Inlet steam flow rate, m_i	kg/s	12.21	13.61	15.86	18.08
Ejected steam flow rate, m_e	kg/s	7.83	9.77	12.96	16.27
Condensation rate, m_c	kg/s	4.38	3.84	2.90	1.81
Steam-side pressure drop, $\Delta \boldsymbol{p_s}$	Pa	1,477.89	2,092.92	3,677.82	6,737.40

Table 6. 5: CDTB performance data

Parameter	Unit	Value			
Ambient Air Temperature, T_{ai}	°C	32.2	36	40	44
Heat Transfer rate, Q	MW	17.65	17.26	14.99	11.00
Air-side pressure drop, $\Delta \boldsymbol{p_a}$	Pa	0.28	0.32	0.36	0.38
Outlet air temperature, T_{ao}	°C	34.07	37.54	40.99	44.26
Fan power, P_F	kW	66.58	66.00	65.52	65.18
Inlet steam flow rate, m_i	kg/s	7.83	9.77	12.96	16.27
Ejected steam flow rate, m_e	kg/s	0.381	2.48	6.64	11.66
Condensation rate, m_c	kg/s	7.45	7.29	6.32	4.61

Table 6. 6: HDWD incorporated with CDTB performance data

Parameter	Unit	Value			
Ambient Air Temperature, T_{ai}	°C	32.2	36	40	44
Heat Transfer rate, Q	MW	28.01	26.34	21.87	15.29
Outlet air temperature, T_{ao}	°C	39.85	42.55	44.91	46.88
Air-side pressure drop, $\Delta \boldsymbol{p_a}$	Pa	317.84	314.54	310.26	305.42
Fan power, P_F	kW	67.43	66.72	66.04	65.46
Inlet steam flow rate, m_i	kg/s	12.21	13.608	15.862	18.078
Ejected steam flow rate, m_e	kg/s	0.3808	2.4808	6.6429	11.6556
Condensation rate, m_c	kg/s	11.83	11.13	9.22	6.42
Steam-side pressure drop, $\Delta \boldsymbol{p_s}$	Pa	1,477.89	2,092.92	3,677.82	6,737.40
Condensing pressure, P_c	Pa	16937.60	17000.17	15622.83	12826.15

Table 6. 7: ACC incorporated with HDWD performance data

Parameter	Unit	Value			
Ambient Air Temperature, T_{ai}	°C	32.2	36	40	44
Heat Transfer rate, Q	MW	61.49	56.51	46.72	34.91
Average outlet air temperature, T_{ao}	°C	44.53	46.80	48.73	50.44
Air-side pressure drop, $\Delta \boldsymbol{p_a}$	Pa	424.75	420.39	414.83	408.75
Ejected heat transfer rate, Q_e	MW	0.90	5.87	15.76	27.79
Fan power, P_F	kW	213.21	210.72	208.20	205.82
Inlet steam flow rate, m_i	kg/s	26.39	26.39	26.39	26.39
Ejected steam flow rate, m_e	kg/s	0.38	2.48	6.64	11.66
Condensation rate, m_c	kg/s	26.01	23.91	19.75	14.73
Steam-side pressure drop, $\Delta \boldsymbol{p_s}$	Pa	2233.62	2897.88	4621.82	7836.60
Condensing pressure, P_c	Pa	17856.37	18035.61	17373.63	16097.52

Table 6. 8: Generating unit with ACC incorporated with HDWD performance data

Parameter	Unit	Value			
Ambient Air Temperature, T_{ai}	°C	32.2	36	40	44
Turbine exhaust pressure, P_i	Pa	18973.18	19484.55	19684.54	20015.82
Turbine output power, W_t	MW	30.546	30.516	30.505	30.486
Unit fan power, P_F	kW	213.22	210.72	208.20	205.82
Unit net output power, W_{net}	MW	30.333	30.305	30.297	30.280

6.4 Comparison of Performance Data of CD and HDWD Incorporated with CDTB

This section offers the comparison of thermal performance of the CD and HDWD incorporated with CDTB, which were analysed in Chapter 5 and 6, respectively. In addition to that, the CD and HDWD performance data presented in Tables 5.6 and 6.6 respectively, were combined with that of the primary condenser units in Table 5.7. This was performed, in order to obtain the overall performance of the ACC, incorporated with either CD or HDWD as shown in Tables 5.8 and 6.7, respectively, as well as to signify their effects on the steam turbine and net power output of the generating unit as depicted in Table 6.8.

The performance data of the CD and HDWD, were compared at both component (CD and HDWD) and system (ACC incorporated with either CD or HDWD) levels. Furthermore, the first stage tube bundle of HDWD and CD performance data were compared, in order to outline the HDWD performance, when it operates on the dry mode. On the air- side, the comparison of performance data at both component and system levels were performed in terms of the heat transfer rate, and air-side pressure drop. While, on the steam-side the comparison was conducted for turbine exist pressure, turbine and net power output. When the CDTB operates on wet mode, it transfers heat that is more than the heat that could be transferred by the finned-tube heat exchanger portion it replaced. The detailed discussion of the performance data comparison is presented in Chapter 8.

Chapter 7: Analysis of Microchannel Delugeable Tube Bundle Thermal Performance

7.1. Introduction

This Chapter presents the performance analysis of the MDTB. Furthermore, the performance of the HDWD incorporated with MDTB into its second stage was outlined. The Chapter also offers the comparison of thermal performances of the CDTB (which was analysed in Chapter 6) and MDTB. The applications for MHXs in energy system, electronic cooling, fuel cell automobiles, etc, have become wide. This is due to their small size, light in weight, less materials, and high heat transfer coefficients (Ren *et al.*, 2020).

The MDTB performance was predicted by employing the semi-empirical model which was validated using the literatures. The crucial characteristics for accuracy, for semi-empirical model, are heat-transfer and pressure-drop correlations (Yin *et al.*, 2015). Therefore, to improve the accuracy of the model, the existing correlations in the literatures for the steam-side microscale heat transfer and pressure drop inside the microchannel were extensively evaluated and compared.

Like the CDTB, the MDTB also consists of the horizontal flat bare tubes, however, with rectangular microchannels/ports on the steam-side as presented in Figure 7.1. In the heat exchanger industry, the most commonly used microchannels/ ports are rectangular and circular (Fung and Majnis, 2019). However, according to Ozdemir (2006), the local single-phase Nusselt number of round microchannels were found to be about 15 % lower than that of straight rectangular microchannel. Furthermore, the rectangular microchannel geometry attained the lowest thermal resistance compared to the triangular and trapezoidal geometries (Gunnasegaran *et al.*, 2010), (Wang *et al*., 2016). Therefore, in this study, the rectangular microchannels were considered.

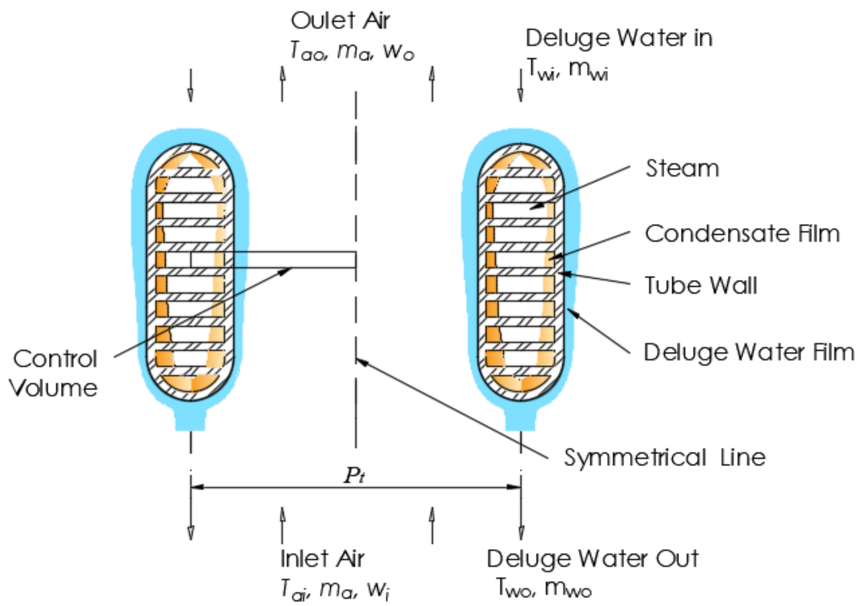

Figure 7. 1: Two adjacent tube in MDTB

The analysis of the transition, between micro- and macro-scale, has been fully performed by several authors. Therefore, according to Ribatski (2013), the micro- to macro-transitional is as follow:

- Conventional channels: $D_h > 3\ mm$
- Mini-channels: $0.2\ mm < D_h \leq 3\ mm$
- Microchannels:$0.2\ mm\ \geq D_h > 0.01\ mm$
- Nanochannels: $D_h \leq 0.01\ mm$

where D_h is the hydraulic diameter of the channel.

The flow patterns have been highlighted in many condensations inside small-diameter channels studies, to be one of the factors that influences the transfer processes of heat and momentum (Ribatski and Jaqueline, 2015). Kim and Mudawar (2012) proposed the flow pattern transition during condensation inside small-diameter channels as shown in Figure 7.2.

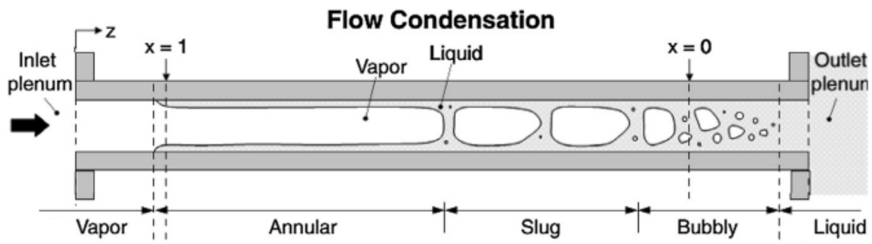

Figure 7. 2: Condensation flow patterns in a horizontal tube (Kim and Mudawar, 2012)

Most of the common models in the literatures are annular flow model (Kim and Mudawar, 2012), (Al-Zaidi *et al.*, 2018) (Keniar 2020). This is due to the wide range of qualities covered by this regime during condensation, even for channels with small diameters (Keniar, 2020). Furthermore, annular flow is the main regime during flow condensation, and most correlations were developed and proposed for this flow regime (Al-Zaidi, *et al.*, 2018). The annular flow model's applicability depends on restriction of the applied assumptions. Semi-empirical, analytical, and Computational Fluid Dynamics approaches have been used by several researchers to model annular condensation (Bandhauer *et al.*, 2006), (Chen et al., 2009), (Keniar, 2020). The semi- empirical models do not involve significant computational power, and applicable to conditions similar to their base data, and mainly used for the design of heat exchangers (Keniar, 2020). On the other hand, the analytical models can cover a wide range of condensation conditions, however, they were developed for a specific geometry, and new model is always needed every time a new geometry is considered (Keniar, 2020).

In this study, the single-phase flow and heat transfer in microchannel tube bundle was considered, because of inconsistences and conflicted results have been reported for two-phase flow and heat transfer (Cheng and Xia, 2017). Furthermore, the effect of the gravity on the pressure drop is not considered, since it was reported to be negligible for a single-phase fluid in a microchannel heat exchanger (Dang *et al.*, 2010).

7.2. Modelling

The semi- empirical model was employed in predicting the flow and heat characteristics for the MDTB. The model uses the relevant and validated correlations from literatures. The empirical correlations have been used in several studies, whose findings agreed very well with experimental data (Zhang *et al.*, 2014 a); (Sahar *et al.*, 2017); (Al-Zaidi *et al.*, 2018); (Ren *et al.*, 2020); (Hsieh *et al.*, 2021). The geometrical design and environment conditions that impact on thermal performance, were investigated by employing the validated semi-empirical model. Based on the conclusions made in Chapter 3, for MDTB modelling, a one-dimensional model was considered, and separate modelling of the round-end sections was not taken into account.

7.2.1. MDTB Description

The considered MDTB had several microchannel flat bare tubes with identical geometrical parameters. As shown in Figure 7.1, the steam flows inside the microchannels/ ports, while the water and air flow outside the tubes in counter-flow directions. The detailed geometrical parameters of the flat microchannel tube are shown in Figure 7.3.

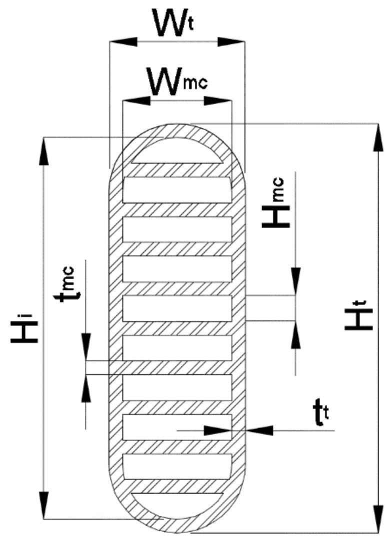

Figure 7. 3: The geometrical parameters of the flat microchannel tube

Each flat tube consists of numerous rectangular channels or ports on the steam-side with a defined height (H_{mc}) and width (W_{mc}). For the considered flat tube, the width (W_t) and height (H_t) were kept constant, while, the sizes of the channels were varied by changing the channel height. For each number of channel (N_{mc}) in a microchannel tube, the hydraulic diameter for channels was defined in order to identify the number of channels, at which the size of the channels falls under microchannel category as presented in Ribatski (2013). The obtained microchannel categories are presented in Table 7.1. The cross-sectional flow area and perimeter were defined as:

$$A_{mc} = H_{mc}W_{mc} \tag{7. 1}$$

$$P_{mc} = 2H_{mc}+2W_{mc} \tag{7. 2}$$

The hydraulic diameter was determined as:

$$D_h = \frac{4A_{mc}}{P_{mc}} \tag{7. 3}$$

Table 7. 1: The microchannel categories

Number of Channels, N_{mc}	**Hydraulic diameter, D_h [mm]**	**Classification**
1 to 75	7.8 to 3.05	Convectional Channels
76 to 186	3.05 t 0.201	Mini-channels
186 to 198	0.201 to 0.01	Microchannel
>198	<0.01	Nanochannel

From Table 7.1, it is clear that the channel's sizes fall into microchannel category, when the number of channels in microchannel is in the range between 186 and 198.

7.2.2. Governing Equations

As showed in Figure 7.1, the steam flows through the parallel microchannel, and condensed by the help of the counter-current flow of air and water over the tubes. The control volume was drawn from the centerline of the tube to the symmetry line between the two adjacent tubes, as illustrated in Figure 7.1. The layout of a typical control volume of a tube for a MDTB, and its resistance diagram are shown in Figure 7.4 and 7.5 respectively. On the air-water side, the tube was taken to have a single control volume as depicted in Figure 3.5.

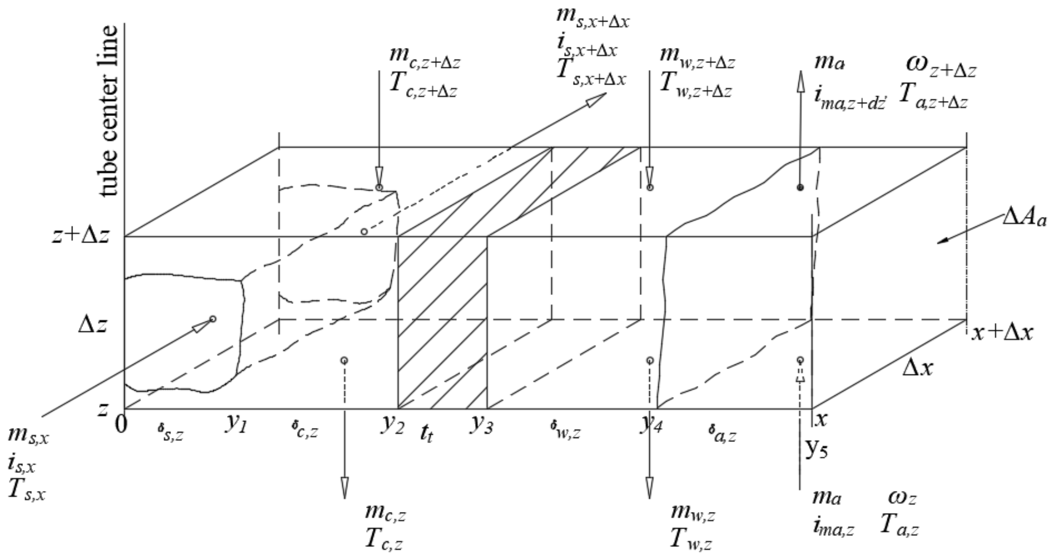

Figure 7. 4: Typical control volume for a MDTB

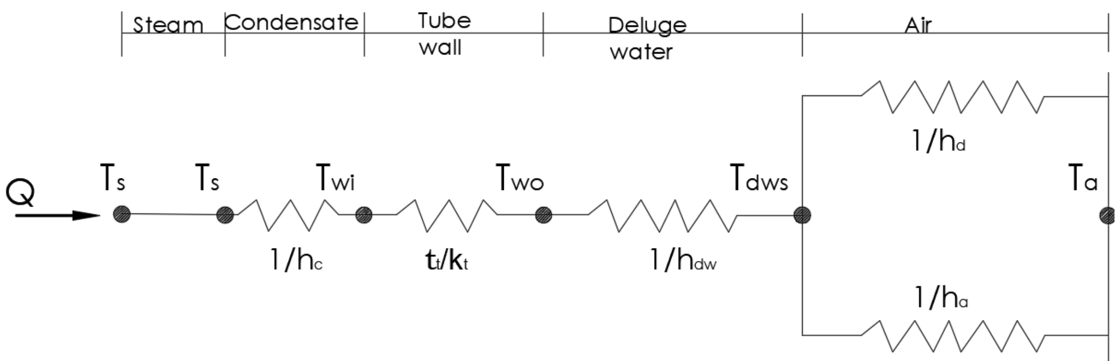

Figure 7. 5: The resistance diagram

In general, the MDTB modelling was performed in the same manner as that of the CDTB. The main difference was with the empirical correlations used to define the flow and heat transfer on the steam-side, inside the microchannels. The developed model calculates the heat transfer from steam to the inside tube wall of microchannel, then from the outside tube wall to air and water. Therefore, the inside tube wall temperature is crucial for accurate calculation. However, in microchannel condenser, the change of the tube wall temperature along the direction of airflow was found to be insignificant, thus it can be ignored (Yin *et al.*, 2015). Further, the microchannel tube width is quite shorter compared to its length, therefore, the change in air properties during airflow crossing over a tube is minimum.

The following assumptions were applied in the calculations:

- The annular condensing flow is single phase, steady and incompressible,
- There is one-dimensional steam flow in a segment,
- There is no maldistribution in steam flow rate between the microchannels,
- The longitudinal conduction and heat transfer between ports are ignored,
- Pressure is uniform across the microchannel's cross-sectional area,
- Thermophysical properties are based on local saturation pressure,
- The liquid film interface is smooth, and
- Gravity effects are negligible.

A balance of steam and water-air-side enthalpy variation is required for the total energy conservation for a control volume. On the steam-side, the energy conservation is represented by:

$$Q_c = m_s(i_{s,x+\Delta x} - i_{s,x}) \tag{7. 4}$$

which can be also represented as:

$$Q_c = h_c A_{cs}(T_s - T_{wi}) \tag{7. 5}$$

Through the tube wall, the total heat transfer is defined as:

$$Q_k = \mathrm{k_t} \frac{A_t (T_{wi} - T_{wo})}{t_t} \quad (7.\ 6)$$

For the air-water-side, the total heat transfer can be computed as:

$$Q_a = m_a (i_{ao} - i_{ai}) \quad (7.\ 7)$$

This can be also expressed as:

$$Q_a = Q_s + Q_l \quad (7.\ 8)$$

whereby latent and sensible heat can be defined respectively as:

$$Q_l = \Delta m_{dw} i_v = h_d \mathrm{A_a} (w_{sw} - w) i_v = m_a (\omega_o - \omega_i) i_v \quad (7.\ 9)$$

$$Q_s = h_a A_a (T_{dws} - T_a) \quad (7.\ 10)$$

where Δm_{dw} is the changes in deluge water mass flow rate. In terms of the overall heat transfer coefficient, the heat transfer is expressed as:

$$Q = \mathrm{UA}(\mathrm{T_s} - T_{dws}) \quad (7.\ 11)$$

And the overall heat transfer coefficient is defined as:

$$U = \left[\frac{1}{h_c} + \frac{t_t}{k_t} + \frac{1}{h_{dw}} \right]^{-1} \quad (7.\ 12)$$

The deluge water heat transfer coefficient is defined as:

$$h_w = \frac{k_w}{\delta_w} \tag{7. 13}$$

The deluge water film can be expressed as:

$$\delta_w = \left[\frac{3\,\mu_w m_{wi}}{(g\,\rho_w\,L_t\,(\rho_w - \rho_a))}\right]^{1/3} \tag{7. 14}$$

7.2.3. Solution Methods

On the steam-side, the obtained governing equations were applied to all channels as several control volumes. While, the water-air-side was considered as a single control volume, and therefore, the governing equations were applied over the entire tube height (H_t). The deluge water properties were determined at deluge water mean temperature. Water-air-side heat transfer coefficients and air side pressure drop were predicted by using the external flow theories in conjunction with heat and mass transfer analogy method. The flow on the air-side was considered as shown in Figure 3.5. The governing equations were solved analytically and iteratively using Log Mean Temperature Difference (LMTD) method. The initial outlet air, tube wall and deluge water surface temperatures were guessed, and through looping tool, the governing equations were solved. The parameters such as heat transfer rate, effectiveness, pressure drop, and performance index were determined.

7.3. Validation

The employed empirical model was validated against Doan *et al.* (2020) experimental data. Doan *et al.* (2020) experimentally investigated single-phase flow and heat transfer analysis in a microchannel condenser. During the validation, the emphases was more on the steam-side performance characteristics. This is because, on the air-water-side, the model had already proven to work in Chapters 3 and 6, therefore, in this Chapter the steam-side is the side of interest. Hence, the steam-side Nusselt number and friction factor were computed using relevant correlations. The geometric and operating data which were used in Doan *et al.* (2020) study are shown in Tables 7.2 and 7.3, and the considered working fluid and coolant were steam and water, respectively.

Table 7. 2: Geometric parameters

Geometric parameters	Unit	Value
Hydraulic diameter	μm	500
Channel width	μm	500
Tube conductivity	W/m.K	237
Channel thickness	μm	200
Channel length	mm	32
Number of channels	-	10
Channel shape	-	square
Tube material	-	Al

Table 7. 3: Operating conditions

Operating conditions	Unit	Value
Steam temperature	℃	108
Ambient air Temperature	℃	31
Steam mass flow rate	g/s	0.01 – 0.06
Air mass flow rate	g/s	3.244

7.3.1. Heat Transfer

Figure 7.6 shows the predicted heat transfer rate of the model, which was compared to the experimental data of Doan *et al.* (2020). As the steam mass flow rate increased from 0.01 g/s to 0.06 g/s, the heat transfer rate increased from 22 W to 133 W. It can be seen that the empirical model predictions were in good agreement with the experimental data of Doan *et al.* (2020), who predicted the heat transfer rate of 24 W to 138 W, as the steam mass flow rate increased from 0.01 g/s to 0.06 g/s.

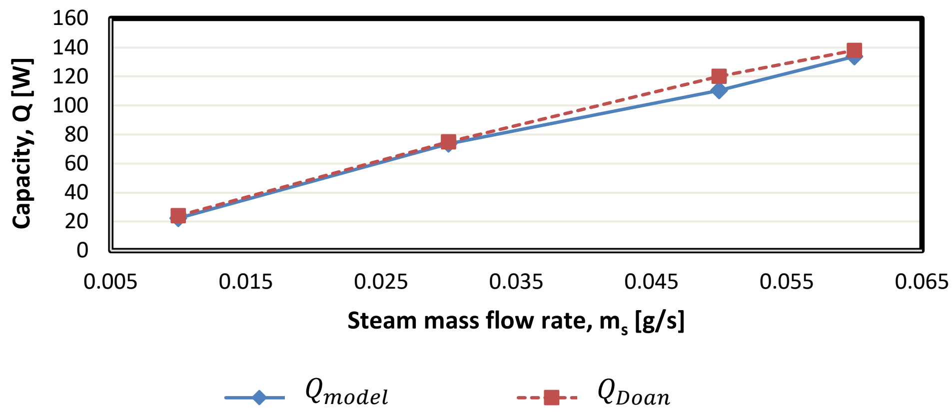

Figure 7. 6: The effect of the steam flow rate on the heat transfer rate

Furthermore, the predicted Nusselt number which were attained using Gnielinski (1976); Shah and London (1978); and Adams *et al.* (1997) correlations were analysed and compared to each other. As shown in Figure 7.7, for all the considered correlations, the Nusselt number was found to increase with Reynolds number. The trend of the results concurs with Sahar *et al.* (2017), and Al-zaidi *et al.* (2018) results. Sahar *et al.* (2017) validated and compared their numerical results to Shah and London (1978), and Bejan (2004) correlations. While, Al-zaidi *et al.* (2018) validated their work using Peng and Peterson (1996) and Bejan (2004) correlations.

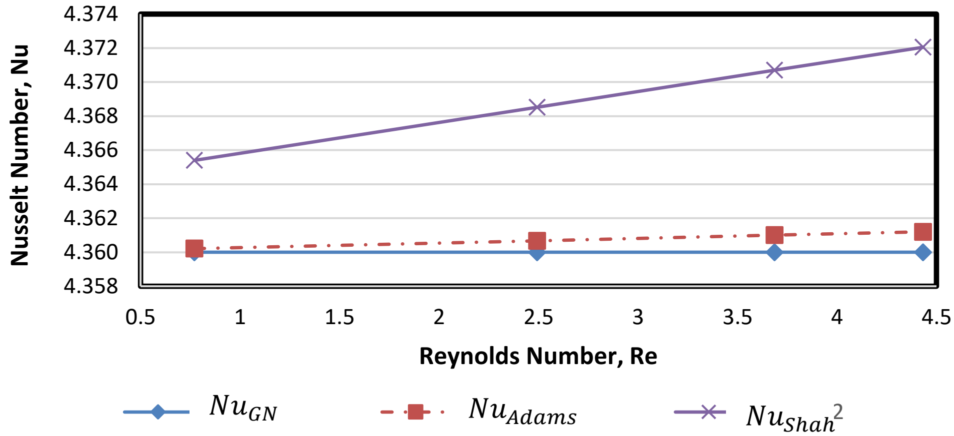

Figure 7. 7: Predicted Nusselt number using existing correlations

7.3.2. Friction Factor and Pressure Drop

Figure 7.8 shows the validation of the empirical results of the steam-side pressure drop against the experimental data of Doan *et al.* (2020). The steam-side pressure drop data were obtained using Shah and London (1978) and Xing *et al.* (2013) friction factor correlations. It is obvious that the empirical model results agreed very well with the Doan *et al.* (2020) experimental data, almost for all the considered correlations. The steam-side pressure drop was found increasing with steam mass flow rate. Similar results were also reported in Hsieh *et al.* (2021) experimental study, in which the convective heat transfer coefficient and friction factor for single phase rectangular microchannels, with deionized water as the cooling fluid, was analysed.

Moreover, as depicted in Figure 7.9, the change in friction factor predicted by the empirical model was found to decrease with increasing Reynolds number. This concurs with Sahar *et al.* (2017), Al-zaidi *et al.* (2018) and Ali *et al.* (2019) findings. In these studies, the validations of the work were performed against either Shah and London (1978) or Xing *et al.* (2013) correlations.

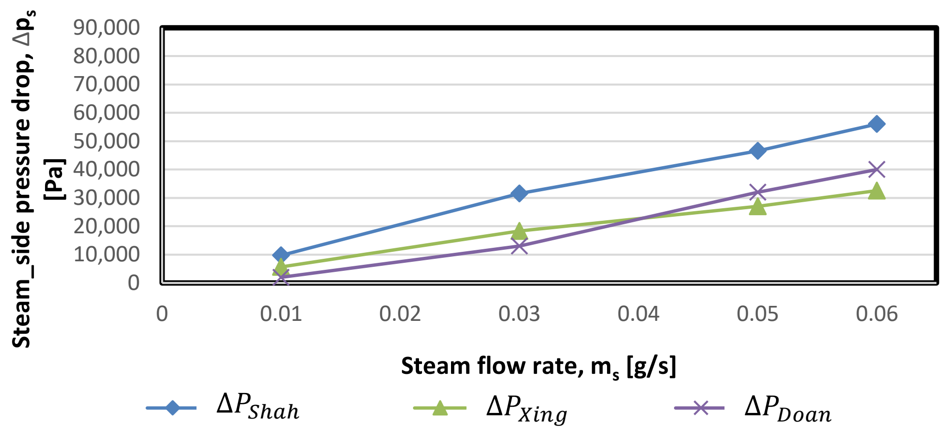

Figure 7. 8: The effect of the steam flow rate on the condenser pressure drop

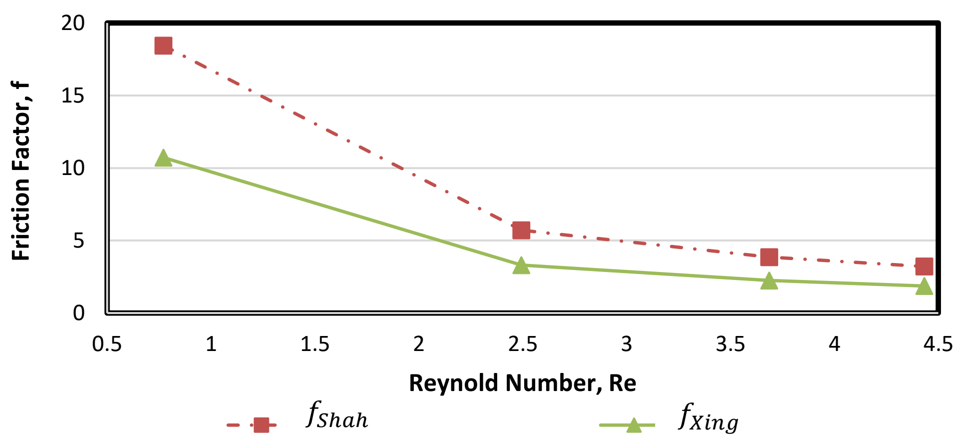

Figure 7. 9: Predicted friction factor using existing correlations

7.4. Performance Analysis

The performance analysis of the MDTB was conducted in order to establish the understanding of the design and control parameters' effects, such as channel geometry and air-side conditions on fluid flow and heat transfer. The size and the dimensions of the considered MDTB was equivalent to that of CDTB, which was optimized and analysed in Chapter 4 and 6, respectively. The only difference was that, the MDTB has microchannel/ports on the steam-side. In a microchannel condenser, the condensation flow is dominant in the heat transfer mechanism compared to the air-side flow. Hence, for the MDTB performance analysis the emphasis was placed more on the steam-side flow.

The influences of the hydraulic diameter of microchannel ports, number of microchannel ports in one flat tube, and inlet ambient air temperature on the hydrodynamic entry length**,** condensation heat transfer coefficient, heat transfer rate, steam-side pressure drop, and thermal performance index were investigated. The hydraulic diameter and number of microchannel ports in one flat tube were varied in range from 10 to 200 μm and 186 to 198 ports, respectively. The analysis was conducted for ambient air temperature in the range of 32 ℃ to 44 ℃. The microchannel tube geometric parameters are summarized in Table 7.4.

Table 7. 4: The microchannel tube geometric parameters

Parameter	**Unit**	**Value**
Hydraulic diameter of channel, D_h	μm	10 to 200
Channel height, H_{mc}	mm	0.008 to 0.11
Channel width, W_{mc}	mm	3.95
Channel thickness, t_{mc}	mm	1.5
Number of Channel, N_{mc}	-	186 to 198
Tube height, H_t	mm	300
Tube width, W_t	mm	6.95
Tube length, L_t	m	3.178
Tube thickness, t_t	mm	1.5

The MDTB thermal performance evaluation was performed at same design operating conditions, as the thermal performance analysis of CDTB was conducted. Since, the MDTB is to be incorporated into second stage of HDWD, the steam condition at the MDTB entrance was corresponding to that at the exit of the first stage of HDWD as show in Table 6.3.

7.5. Performance Data

The performance data for the MDTB, HDWD incorporated with MDTB, and ACC incorporated with HDWD are depicted in Tables 7.5 to 7.7. In addition to that, the steam turbine performance characteristics, for the generating unit with ACC incorporated with HDWD (MDTB) were assessed, and the performance data are presented in Table 7.8. Furthermore, these performance data were illustrated graphically, scrutinised, and discussed in detail in Chapter 8.

Table 7. 5: MDTB performance data

Parameter	Unit	Value			
Ambient Air Temperature, T_{ai}	°C	32.2	36	40	44
Heat Transfer rate, Q	MW	18.03	17.60	15.23	11.04
Air-side pressure drop, $\Delta \boldsymbol{p_a}$	Pa	25.58	29.28	33.51	37.94
Outlet air temperature, T_{ao}	°C	34.11	37.58	41.02	44.28
Fan consumption power, P_F	kW	66.57	16.94	19.26	21.64
Inlet steam flow rate, m_i	kg/s	7.83	9.77	12.96	16.27
Ejected steam flow rate, m_e	kg/s	0.22	2.33	6.54	11.64
Condensation rate, m_c	kg/s	7.62	7.44	6.42	4.63

Table 7. 6: HDWD incorporated with MDTB performance data

Parameter	Unit	Value			
Ambient Air Temperature, T_{ai}	°C	32.2	36	40	44
Heat Transfer rate, Q	MW	28.39	26.68	22.11	15.33
Outlet air temperature, T_{ao}	°C	39.86	42.56	44.92	46.89
Air-side pressure drop, $\Delta \boldsymbol{p_a}$	Pa	343.15	343.50	343.40	342.98
Fan consumption power, P_F	kW	67.42	66.71	66.04	65.45
Inlet steam flow rate, m_i	kg/s	12.21	13.61	15.86	18.08
Ejected steam flow rate, m_e	kg/s	0.22	2.33	6.54	11.64
Condensation rate, m_c	kg/s	11.99	11.28	9.33	6.44
Steam-side pressure drop, $\Delta \boldsymbol{p_s}$	kPa	168.41	211.32	289.04	393.37
Condensing pressure, P_c	kPa	16.85	16.91	15.50	12.79

Table 7. 7: ACC incorporated with HDWD(MDTB) performance data

Parameter	Unit	Value			
Ambient Air Temperature, T_{ai}	°C	32.2	36	40	44
Heat Transfer rate, Q	MW	61.87	56.86	46.96	34.96
Average outlet air temperature, T_{ao}	°C	44.54	46.815	48.73	50.44
Air-side pressure drop, $\Delta\boldsymbol{p_a}$	Pa	450.05	449.35	447.98	446.32
Ejected heat transfer rate, Q_e	MW				
Fan power, P_F	kW	213.21	210.71	208.20	205.81
Inlet steam flow rate, m_i	kg/s	26.389	26.389	26.388	26.389
Ejected steam flow rate, m_e	kg/s	0.22	2.33	6.54	11.64
Condensation rate, m_c	kg/s	26.17	24.06	19.85	14.75
Steam-side pressure drop, $\Delta\boldsymbol{p_s}$	kPa	169.17	212.13	289.99	394.47
Condensing pressure, P_c	kPa	17.70	18.18	17.50	15.96

Table 7. 8: Generating unit with ACC incorporated with HDWD(MDTB) performance data

Parameter	Unit	Value			
Ambient Air Temperature, T_{ai}	°C	32.2	36	40	44
Turbine exhaust pressure, P_i	kPa	18.82	19.63	19.81	19.88
Turbine output power, W_t	MW	30.555	30.507	30.497	30.493
Plant/ unit fan power, P_F	kW	213.21	210.71	208.20	205.81
Plant/ unit net output power, W_{net}	MW	30.34	30.30	30.29	30.29

7.6. Comparison of Performance data of CDTB and MDTB

This section presents thermal performance comparison of the CDTB and MDTB. The MDTB performance parameters, considered during comparison, were the one that were achieved for hydraulic diameter of 140 μm. This is due to the factor that, the Thermal Performance Index (TPI) was found to be reasonable for hydraulic diameter of 140 μm, by comparing to that attained for 200 and 80 μm. The performance data of the CDTB and MDTB were compared at bundle (CDTB and MDTB, as presented in Tables 6.4 and 7.5), component (HDWD incorporated with either CDTB or MDTB, as provided in Tables 6.5 and 7.6) and system (ACC incorporated with either HDWD(CDTB) or HDWD(MDTB), as offered in Tables 6.6 and 7.7) levels. Furthermore, the steam turbine performance characteristics, (depicted in Tables 6.7 and 7.8) for the considered generating unit, which were yielded when the HDWD (with either CDTB or MDTB) were incorporated into ACC, were also compared.

Chapter 8: Results and Discussions

This Chapter presents the results for the thermal performances evaluations of CD, CDTB and MDTB at all levels, as well as their performance comparisons. In addition to that, the analyses, scrutinization, and discussions of the results are also included in this Chapter. Furthermore, the results discussed in this Chapter are tabulated in Appendix G.

8.1. Conventional Dephlegmator Thermal Performance

8.1.1. Air - side Performance Characteristics of the ACC

On the air- side, the performance of the ACC was defined in terms of the heat transfer rate, air-side pressure drop, fan power consumption, and outlet air temperature, which mainly governed by air volumetric flow rates. As shown in Figure 8.1, for a particular fan speed, as the ambient air temperature increased, the air mass flow rate slightly decreased. This is due to the decreasing of the air density as the air temperature increases.

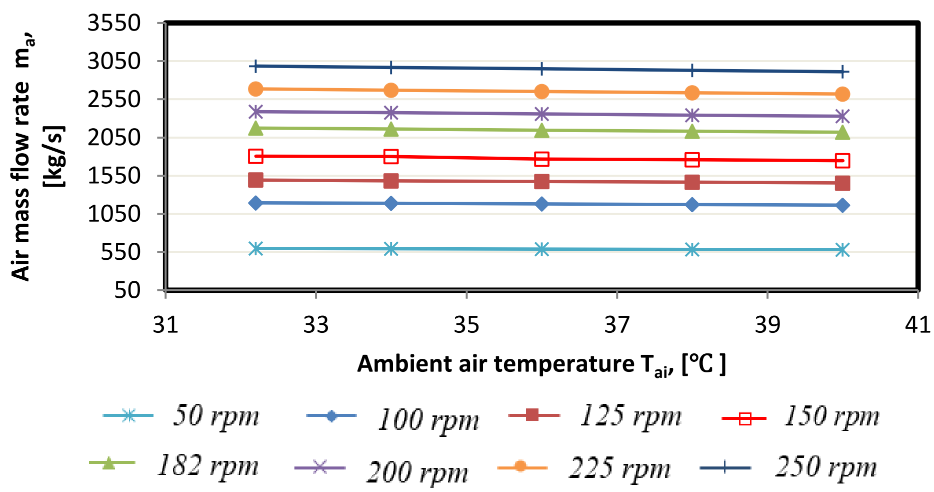

Figure 8. 1: Effects of ambient air temperature on the air mass flow rate at different rotational fan speeds

a) Condenser heat transfer rate

From Figure 8.2 (a, b, c), for both primary condenser and CD units, as well as for the ACC incorporated with CD, the heat transfer rate was found to decrease as the ambient air temperature increased. With air temperature increased, the temperature difference between condensing temperature and ambient air decreased, and thus, the heat transfer rate decreased. Then, as a result, the air exits the tube bundles at higher temperature as shown in Figure 8.3, and a large amount of steam is ejected into the atmosphere as demonstrated in Figure 8.4.

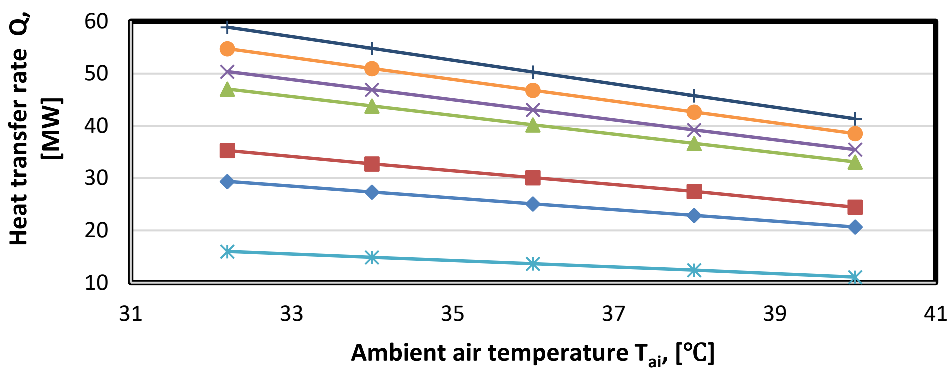

a) Primary condenser units

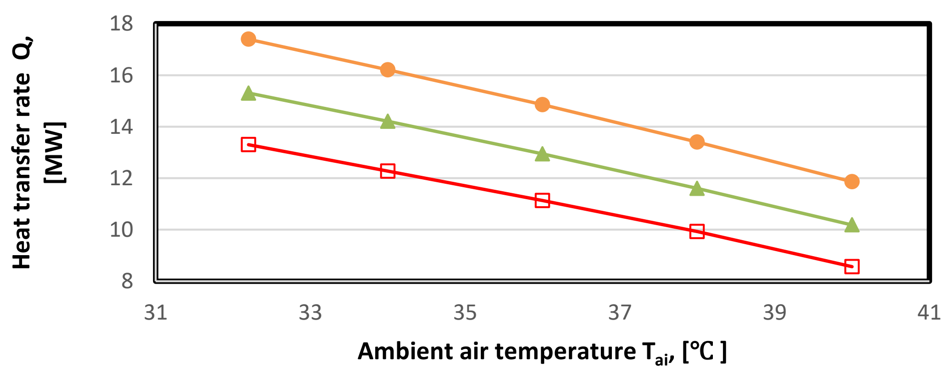

b) CD units

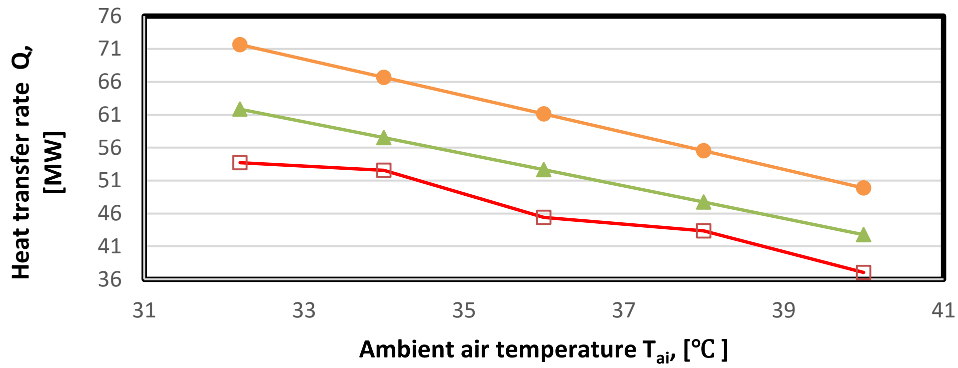

c) ACC system incorporated with CD

50 rpm *100 rpm* *125 rpm* *150 rpm*
182 rpm *200 rpm* *225 rpm* *250 rpm*

Figure 8. 2: Effects of ambient air temperature on the heat transfer rate at different rotational fan speeds

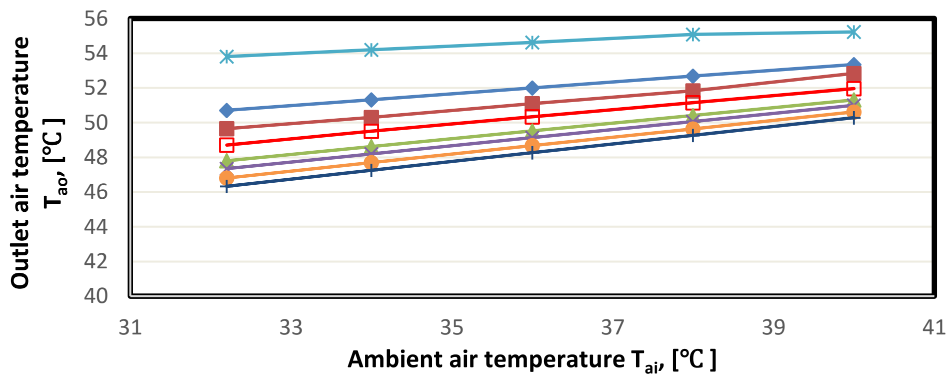

a) Primary condenser units

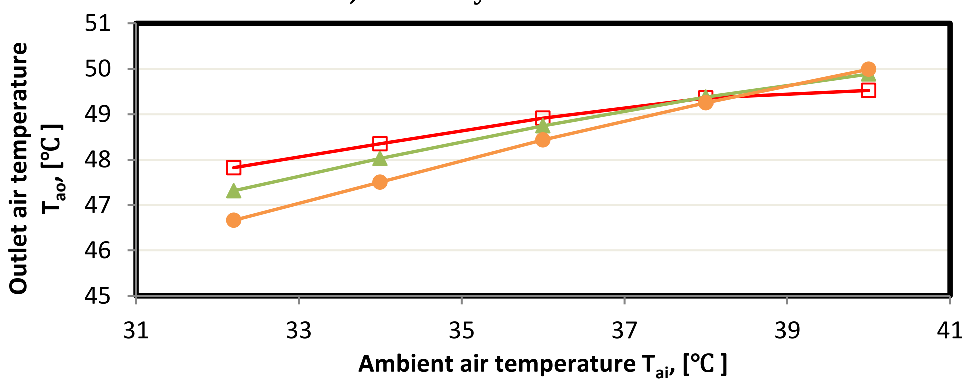

b) CD units

50 rpm *100 rpm* *125 rpm* *150 rpm*
182 rpm *200 rpm* *225 rpm* *250 rpm*

Figure 8. 3: Effects of ambient air temperature on the outlet air temperature at different rotational fan speeds

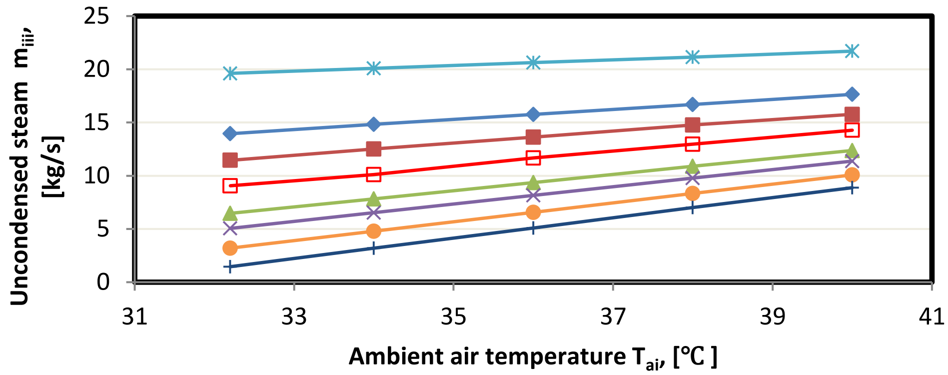

a) Primary condenser units

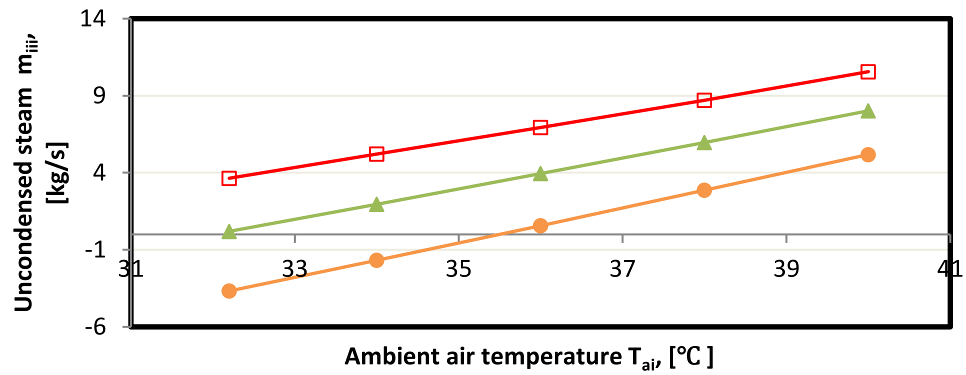

b) CD units

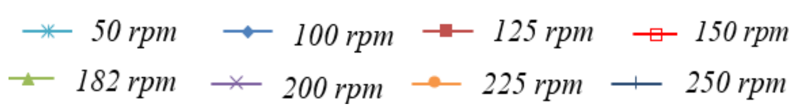

Figure 8. 4: Effects of ambient air temperature on the uncondensed steam at different rotational fan speeds

As corrective measurement, in order to attain the designed heat transfer rate as the ambient air temperature increases, the air mass flow rate should be increased. This was achieved by increasing the rotational fan speed. The air mass flow rate was found to be absolutely linked to ACC cooling performance (Huang *et al.*, 2020). For example, to achieve the designed heat transfer rate at T_{ai} = *36* °C, the mass flow rate should be 2724 kg/s, which is attained by set the fan speed at 231 rpm. Thus, in Figure 8.5, the heat transfer rate increased with rotational fan speed. As a result, the air exits the tube bundle at lower temperature and the amount of ejected steam reduced as shown in Figures 8.6 and 8.7, respectively.

Moreover, the heat rejection improvement coefficient, which was defined by Eq. (8.1) was found to increase with the rotational fan speed as depicted in Figure 8.8. Similar trend of results was obtained by Huang *et al.* (2020).

$$\varepsilon_Q = \frac{Q - Q_m}{Q_m} \times 100\% \qquad (8.\ 1)$$

where Q and Q_m are heat transfer rate at different ambient air temperatures and fan speeds, and heat transfer rate attained at design operating conditions, respectively.

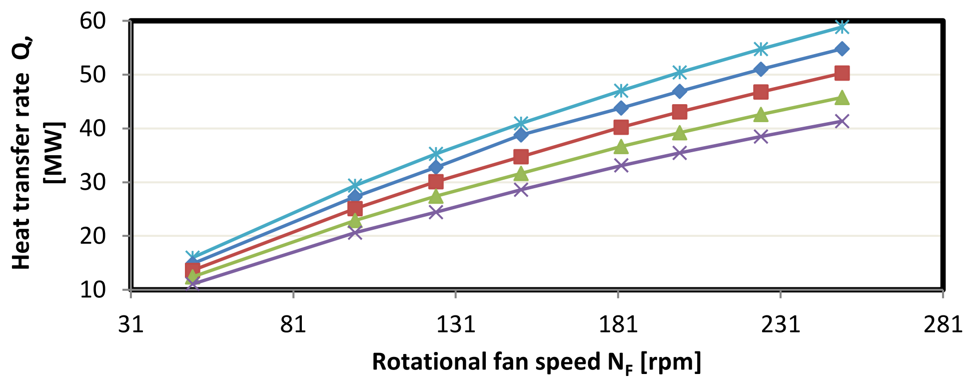

a) Primary condenser units

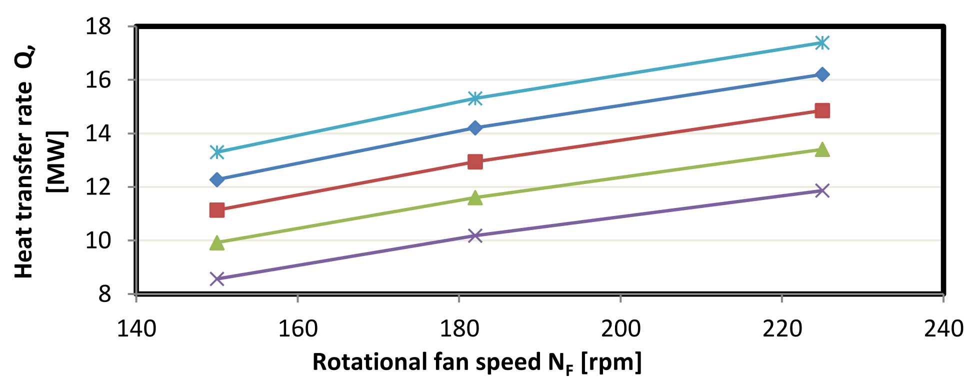

b) CD units

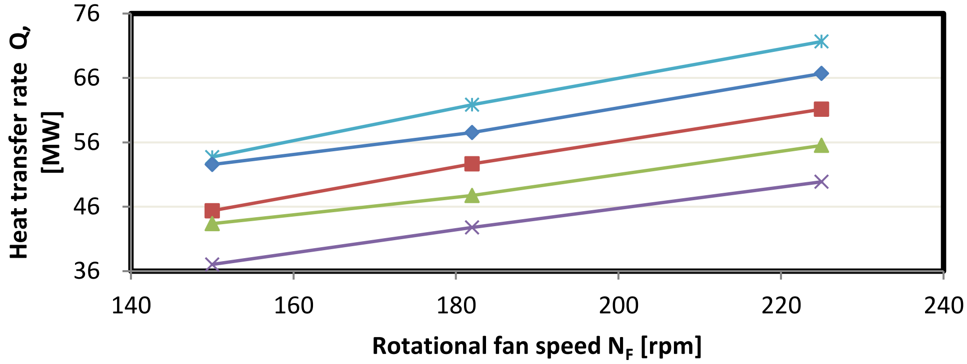

c) ACC system incorporated with CD

32 °C 34 °C 36 °C 38 °C 40 °C

Figure 8. 5: Effects of rotational fan speed on the heat transfer rate at different ambient air temperatures

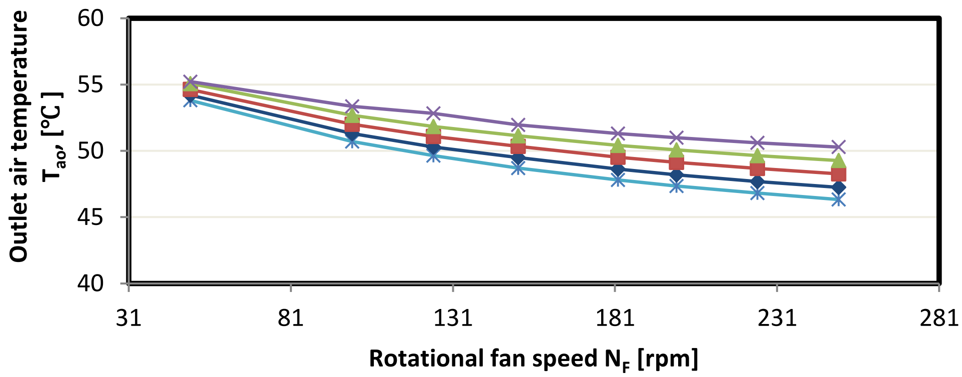

a) Primary condenser units

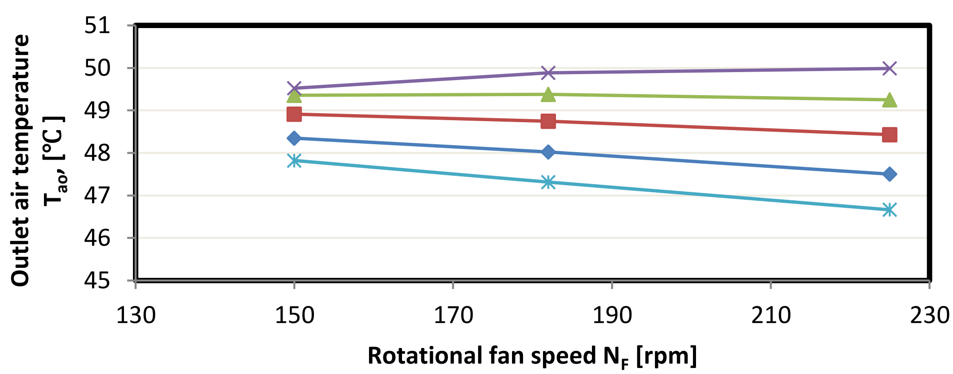

b) CD units

32 °C 34 °C 36 °C 38 °C 40 °C

Figure 8. 6: Effects of rotational fan speed on the outlet air temperature at different ambient air temperatures

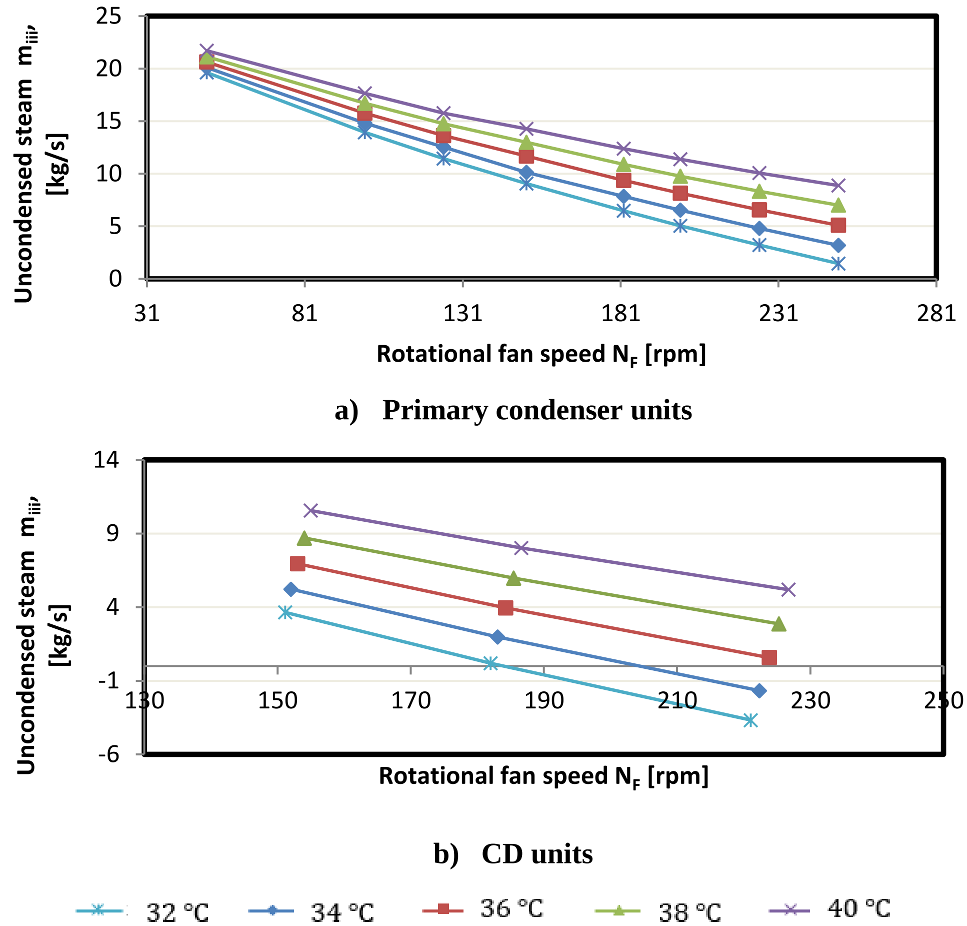

a) Primary condenser units

b) CD units

Figure 8. 7: Effects of rotational fan speed on the uncondensed steam at different ambient air temperatures

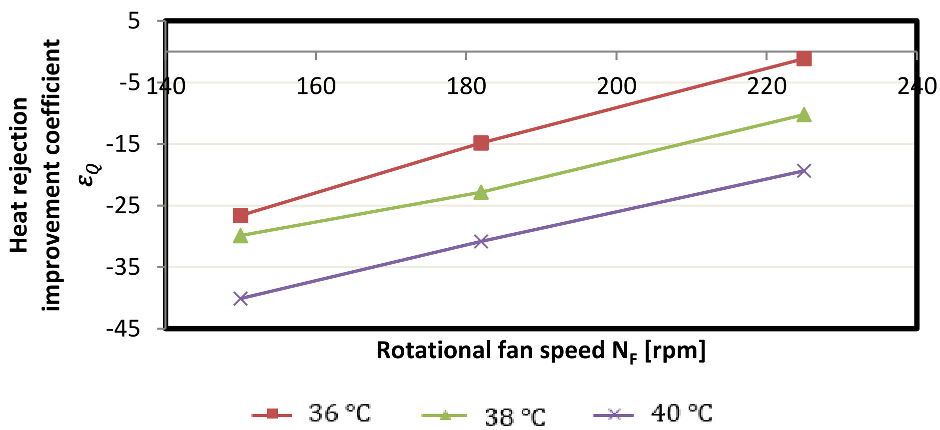

Figure 8. 8: Effects of rotational fan speed on the heat rejection improvement coefficient at different ambient air temperatures

b) Air-side pressure drop

With a closer look, Figure 8.9 (a) shows that, as the ambient air temperature increases, the air-side pressure drop decreases. This is due to the decreasing of the air density as its temperature increases, which results in the static pressure dropping. However, if the analysis was conducted at constant air mass flow rate, air-side pressure drop was found to slightly increase as the ambient air temperature increases. This is presented in Figure 8.9 (b) for CD only. As shown in Figure 8.10, for both primary condenser and CD units, the air-side pressure drop increases with the fan speed. This is due to the fact that, through fan laws, the static pressure is direct proportional to fan speed.

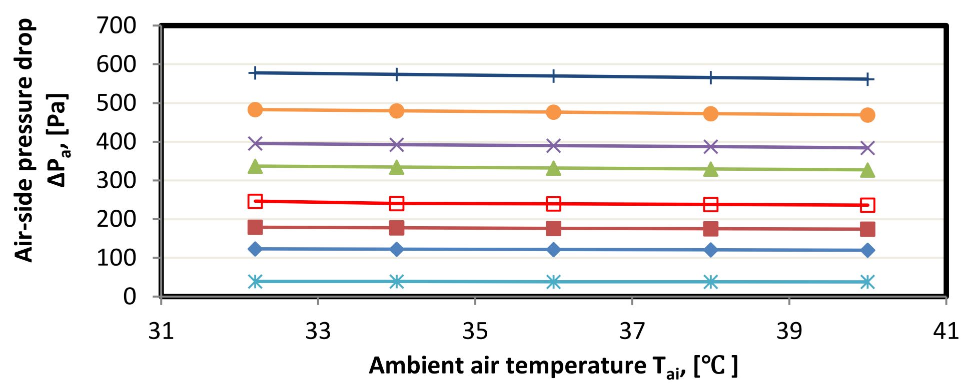

a) Primary condenser

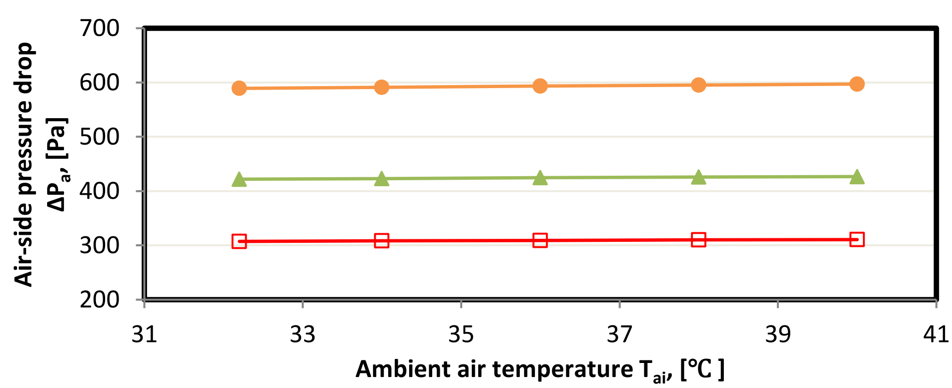

b) CD units

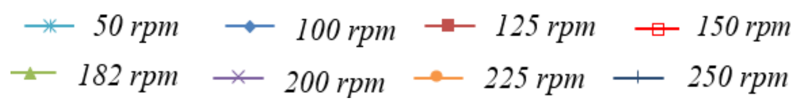

Figure 8. 9: Effects of ambient air temperature on the air-side pressure drop at different rotational fan speeds

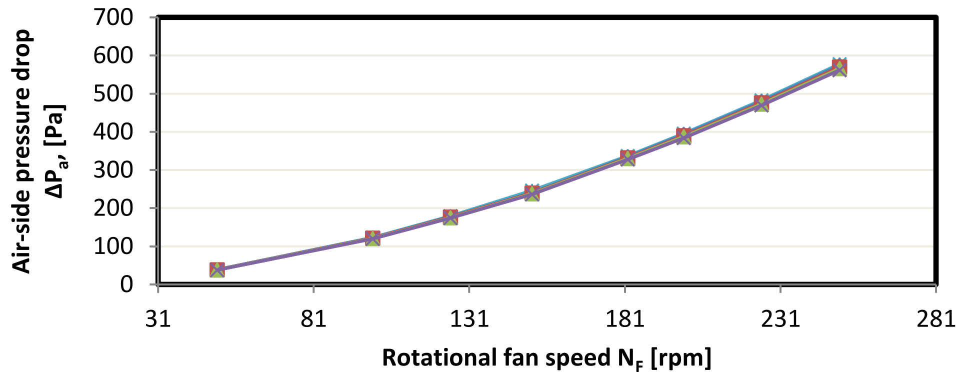

a) Primary condenser

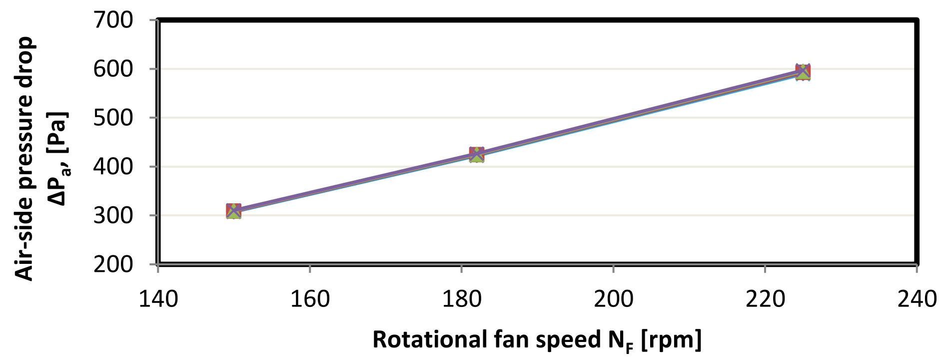

b) CD units

Figure 8. 10: Effects of rotational fan speed on the air-side pressure drop at different ambient air temperatures

c) Fan power consumption

The air-side pressure drop is directly related to fan power consumption. For that reason, from Figure 8.11 (a) it is clear that as the ambient air temperature increases, the fan power consumption slightly decreases. Again here, the opposite results were achieved when the fan speed increases as shown in Figure 8.12. However, as presented in Figure 8.11 (b, c), when the analysis was carried out at constant air mass flow rate, the volumetric flow rate increases with the ambient air temperature. This leads to the rise of fan power consumption with the ambient air temperature.

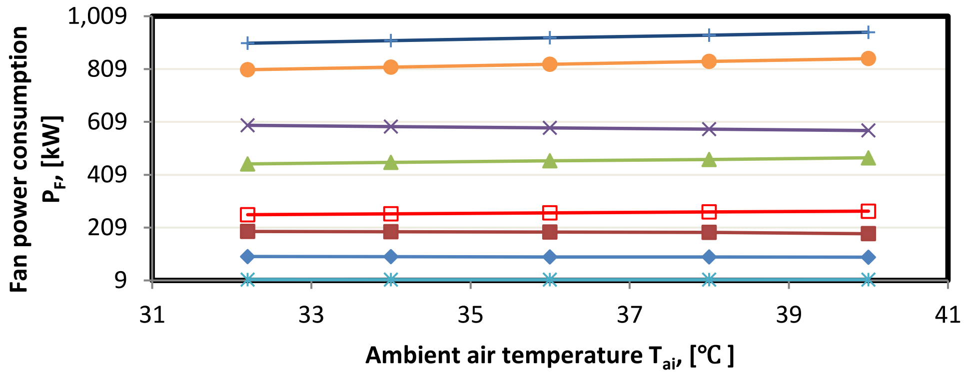

a) Primary condenser units

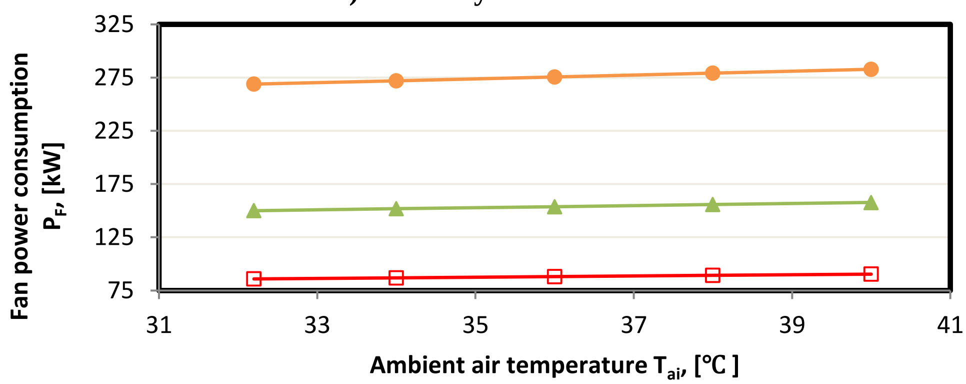

b) CD units

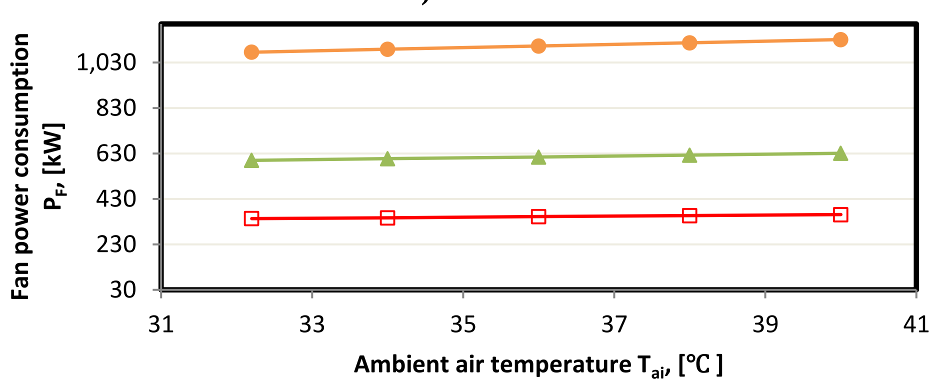

c) ACC system incorporated with CD

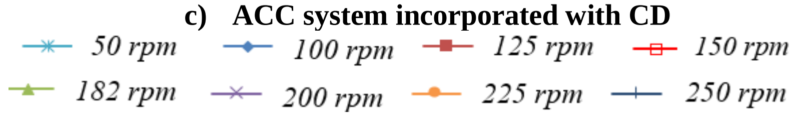

Figure 8. 11: Effects of ambient air temperature on the fan power consumption at different rotational fan speeds

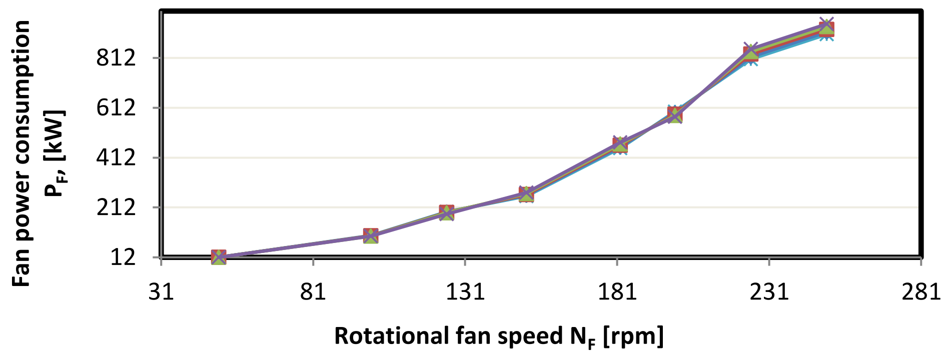

a) Primary condenser units

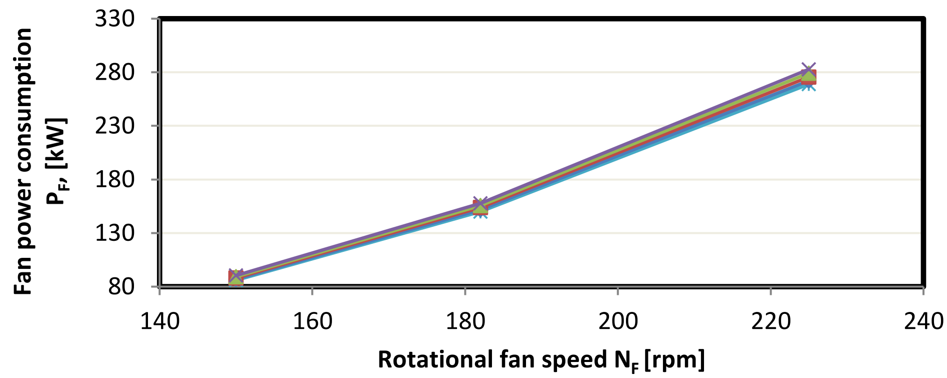

b) CD units

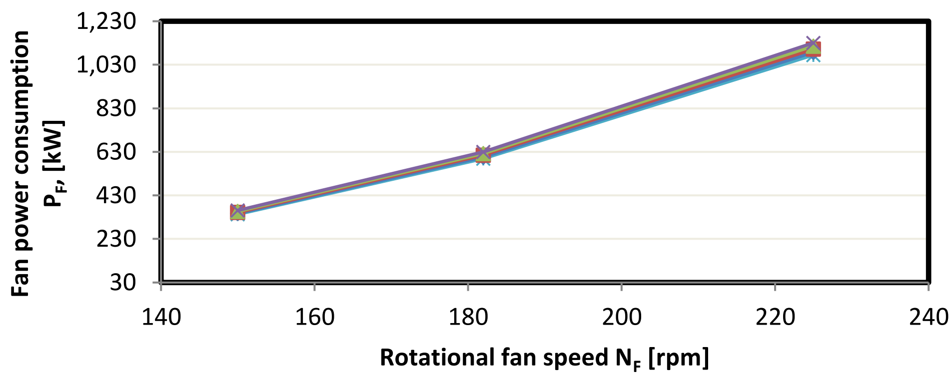

c) ACC system incorporated with CD

32 °C 34 °C 36 °C 38 °C 40 °C

Figure 8. 12: Effects of rotational fan speed on the fan power consumption at different ambient air temperatures

8.1.2. Steam – side Performance Characteristics of the ACC

On the steam-side, the ACC performance was determined in terms of condensing pressure and temperature, steam-side pressure drop, steam velocity, condensation rate, and amount of uncondensed steam ejected out of the condenser.

a) Condensing pressure

The dependence of the condensing pressure on the ambient air temperature was achieved for different fan speeds. As shown in Figures 8.13 (a) and (b), the condensing pressure increased with the ambient air temperature in primary condenser units, while decreased with the ambient air temperature in CD units. This badly affects the condensation rate in both primary condenser and CD units as shown in Figure 8.14. Lower condensation rate in primary condenser leads to more steam flows to the CD units as illustrated in Figure 8.15. Lower condensation rate in CD units results on lower heat transfer rate which is due to large enthalpy of vaporization required to balance the heat energy equations. The large enthalpy of vaporization corresponds to small pressure and temperature, thus, the condensing pressure in the CD units decreased as the ambient air temperature increased as shown in Figure 8.13 (b). Furthermore, the higher inlet steam flow rates were found to cause condensing pressure reduction (O'Donovan *et al.*, 2014).

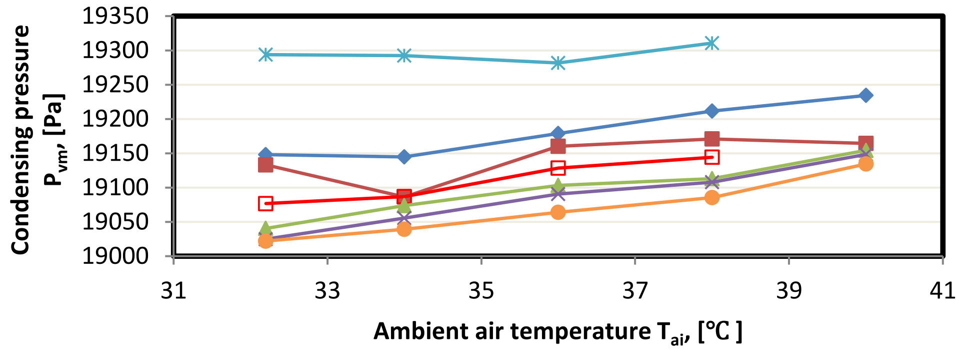

a) Primary condenser units

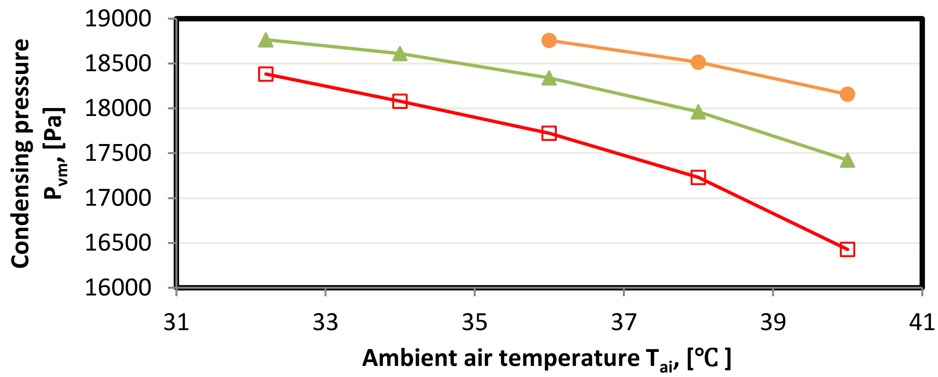

b) CD units

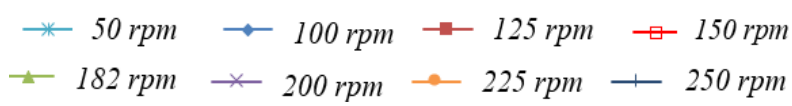

Figure 8. 13: Effects of ambient air temperature on the condensing pressure at different rotational fan speeds

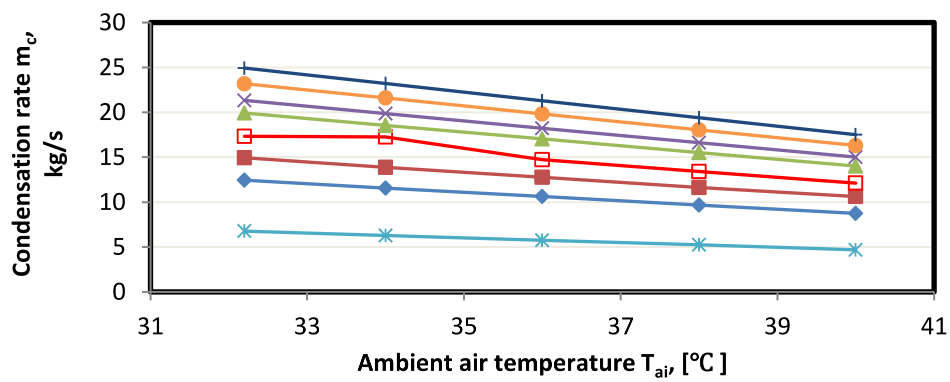

a) Primary condenser units

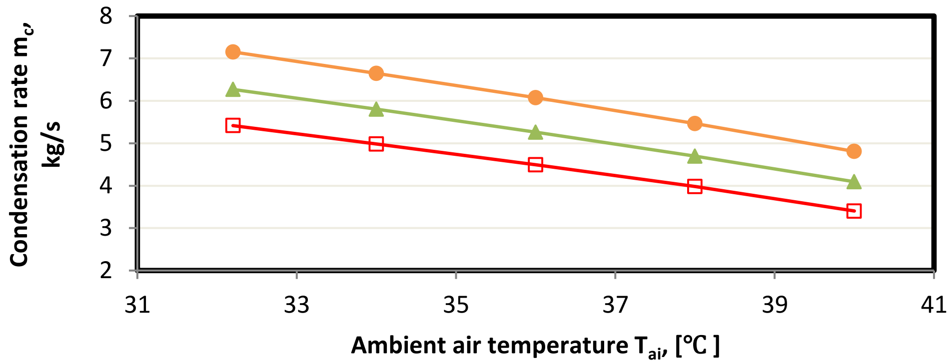

b) CD units

Figure 8. 14: Effects of ambient air temperature on the condensation rate at different rotational fan speeds

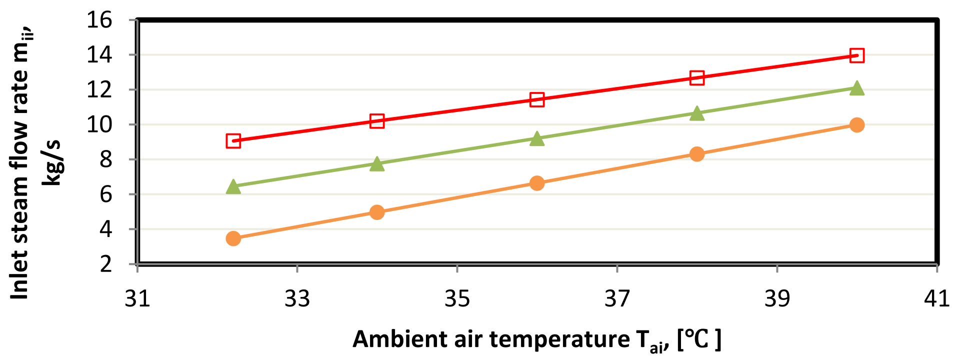

Figure 8. 15: Effects of ambient air temperature on the inlet steam flow rate for a CD units at different rotational fan speeds

To maintain the condensing pressure at designed value, when the ambient air temperature was greater than the designed, the air mass flow rate through the condenser tube bundles should be adjusted through fan speed. Thus, Figure 8.16 (a) shows the decreasing in condensing pressure as the fan speed increased. However, as show in Figure 8.16 (b) the condensing pressure for the CD units was found to increase with fan speed, because the amount of steam flow into the CD units was not constant, as in primary condenser units, and reduced as the fan speed increased, (Figure 8.17). The condensation rates in both primary condenser and CD units increased with fan speed as depicted in Figure 8.18.

However, as presented in Figure 8.19, at the constant air mass flow rate, the condensing pressure in the CD units was found to decrease as the fan speed increases, since at constant air mass flow rate, the inlet steam flow rate was found to increase with the fan speed. This condensing pressure reduction was more pronounced at higher steam flow rates.

In conclusion, the steam flow rate's effects on the condensing pressure can be seen clearly in the CD unit's results, because the amount of steam entering the CD units at different ambient air temperatures is not the same. This is due to different condensation rates in primary condenser units as well as the constant steam flow into the primary condenser units.

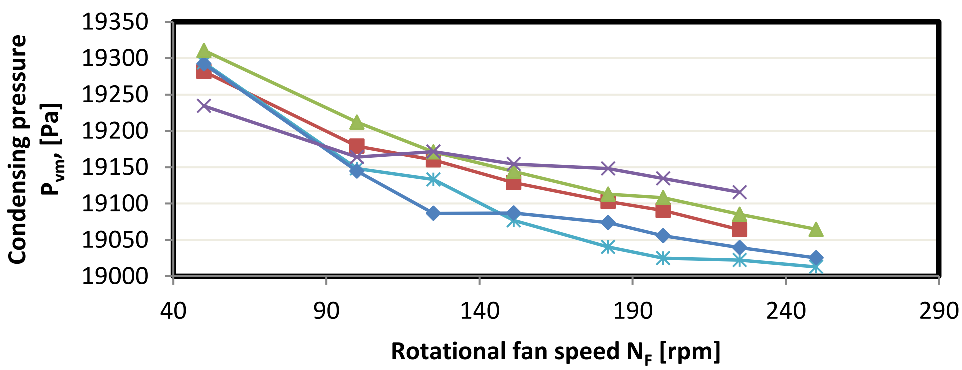

a) Primary condenser units

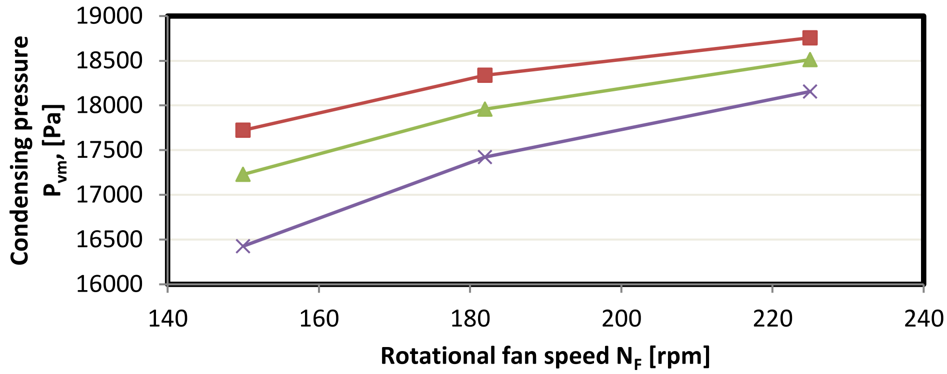

b) CD units

Figure 8. 16: Effects of rotational fan speed on the condensing pressure at different ambient air temperatures

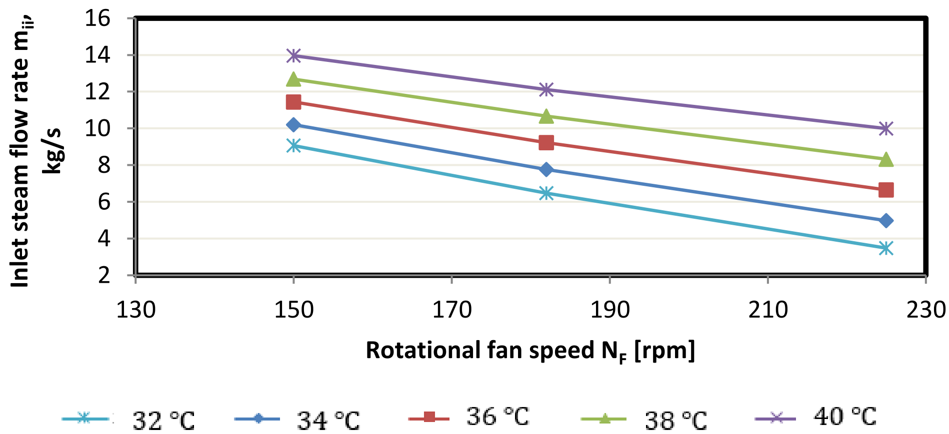

Figure 8. 17: Effects of rotational fan speed on the inlet steam flow rate for CD units at different ambient air temperatures

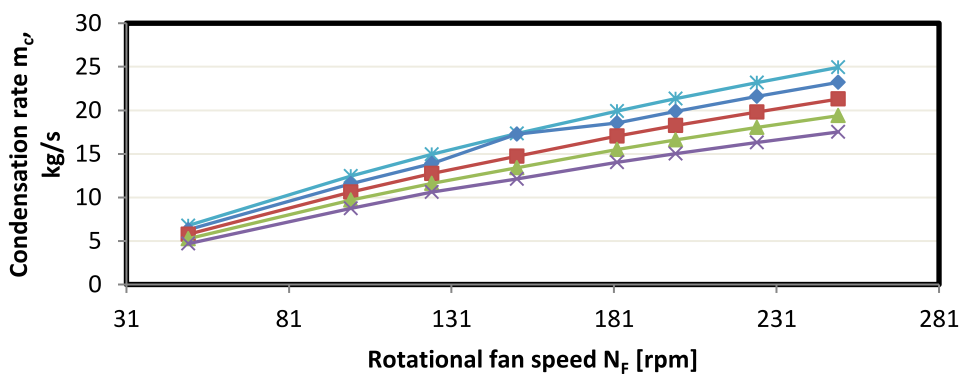

a) Primary condenser units

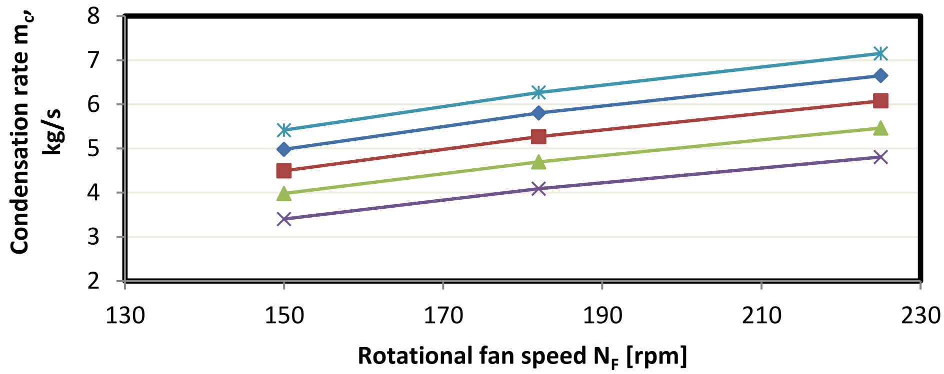

b) CD units

Figure 8. 18: Effects of rotational fan speed on the condensation rate at different ambient air temperatures

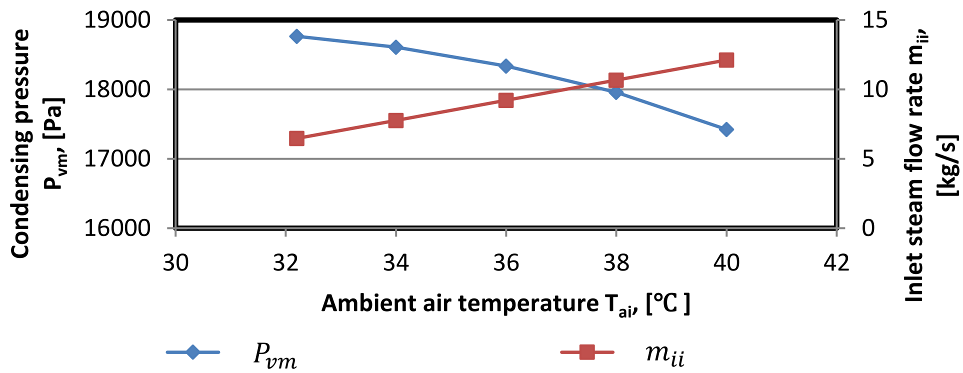

Figure 8. 19: Effects of air temperatures on the condensing pressure for CD at constant air mass flow rate of 2173 kg/s

b) Steam-side pressure drop

For a fixed steam mass flow rate, by increasing the fan speed the condensing pressure, as well as the frictional pressure losses decreases as shown in Figure 8.20. This is due to the increase of air-side heat transfer coefficient, which causes the steam/condensate temperature and pressure to decrease. As a result, due to continuity, the steam density reduces, which causes the inlet steam velocity to increases as presented in Figure 8.21 (a).

However, the inlet steam velocity in CD units was found to decrease as the fan speed increased, because of the inlet steam mass flow rate that also decreased as the fan speed increased (Figure 8.21 (b)).

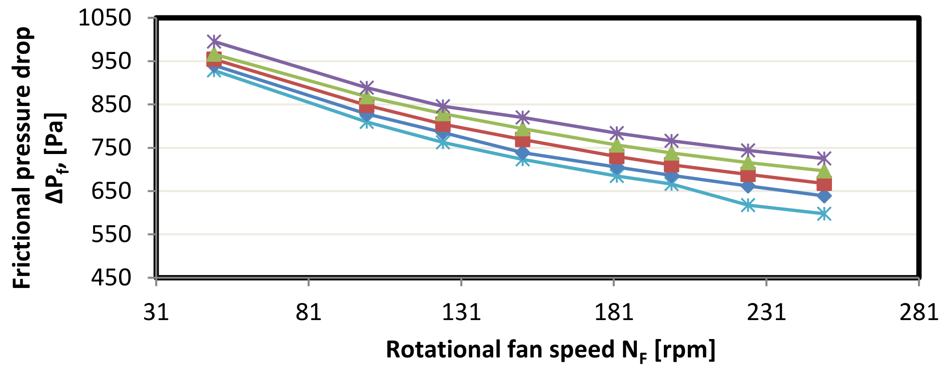

a) Primary condenser units

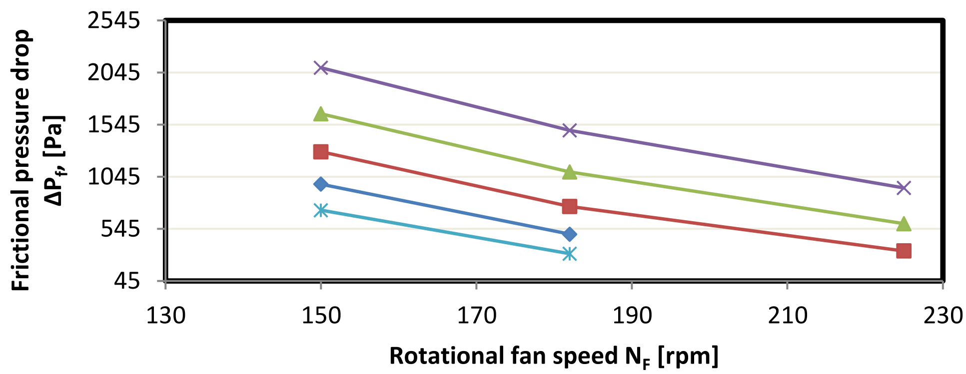

b) CD units

Figure 8. 20: Effects of rotational fan speed on the frictional pressure drop at different ambient air temperatures

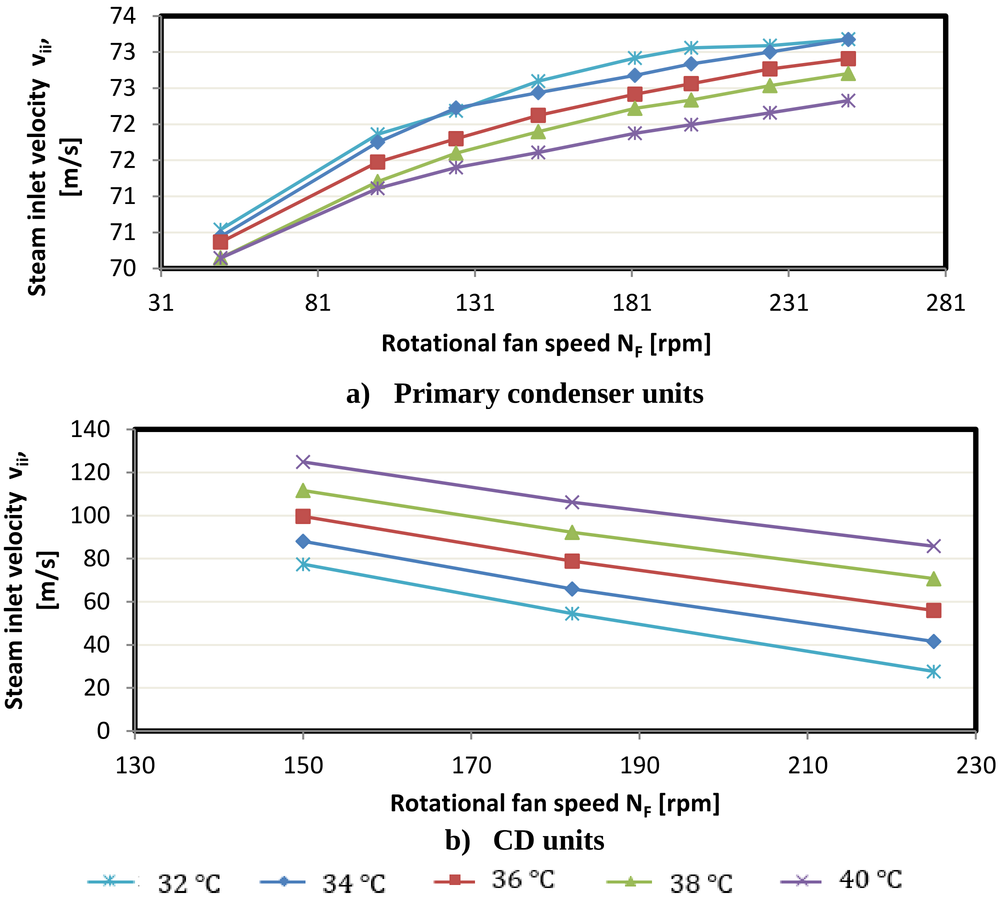

a) Primary condenser units

b) CD units

Figure 8. 21: Effects of rotational fan speed on the steam inlet velocity at different ambient air temperatures

Furthermore, the correlation used to define the frictional pressure drop did not make use of the condensate velocity which increased at the tube's exit, but rather it used the steam velocity at the exit of the tubes, which as shown in Figure 8.22 decreases as the fan speed increases. This results in decreasing of the frictional pressure losses as the fan speed increases. According to Kroger (2004), it is believed that vapor laminarization of the flow during condensation tends to occur at $Re_v < 2300$. However, this has a less effects on the frictional pressure losses in practical ACC tubes. Additionally, it was found that frictional pressure drop increased with ambient air temperature as illustrated in Figure 8.23.

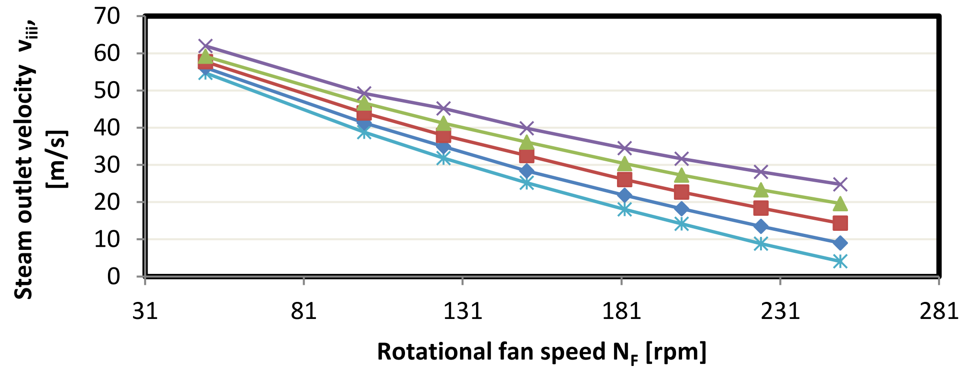

a) Primary condenser units

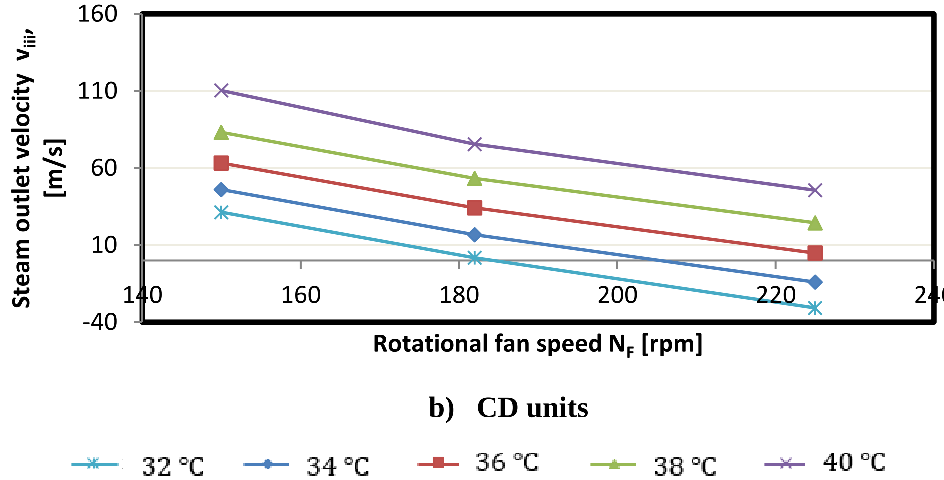

b) CD units

Figure 8. 22: Effects of rotational fan speed on the steam outlet velocity at different ambient air temperatures

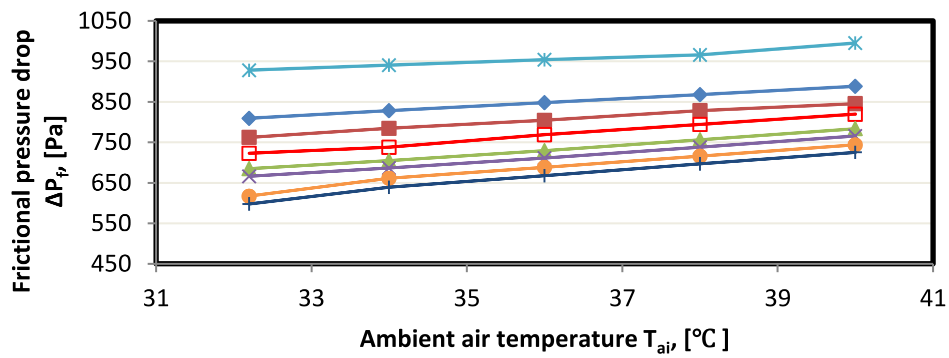

a) Primary condenser units

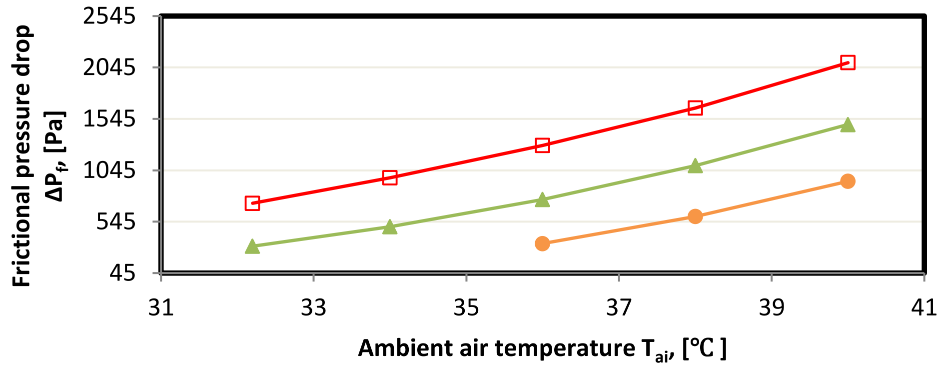

b) CD units

Figure 8. 23: Effects of ambient air temperature on the frictional pressure drop at different rotational fan speeds

Apart from frictional pressure drop, the momentum pressure drop was found to have a huge impact on the overall pressure drop in the tubes. As discussed early, the momentum pressure drop has a negative sign, thus it is a pressure recovery for condensation, which has almost the same magnitude as frictional term especial at large fan speeds. As shown, in Figure 8.24, the combination of the two, resulted in a relatively small pressure drop. This is more noticeable at higher fan speeds, since the sum value of the two is closer to zero. This means the momentum recovery effect was more effective at higher fan speeds.

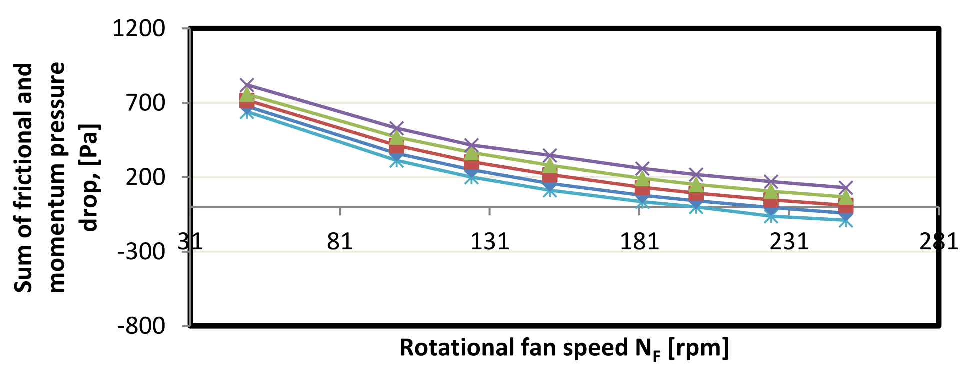

a) Primary condenser units

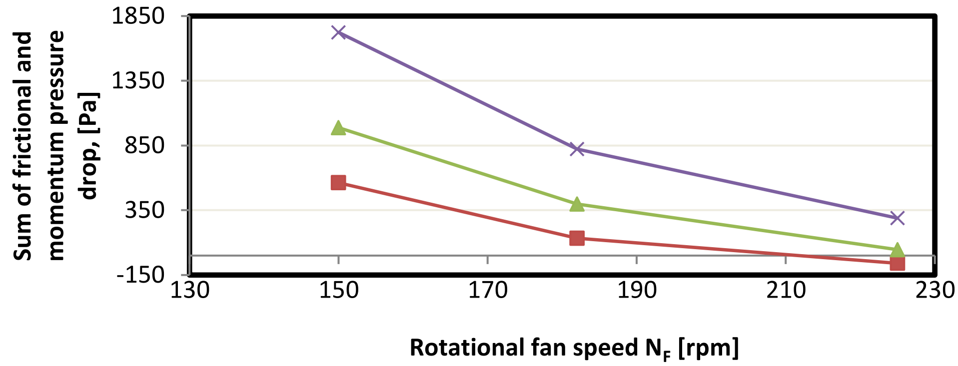

c) CD units

Figure 8. 24: Effects of rotational fan speed on the sum of frictional and momentum pressure drop at different ambient air temperatures

By considering all other pressure drop terms, the total pressure drop between the dividing and combining headers is presented in Figures 8.25 and 8.26. It is clear that the pressure drop behaves in the same manner as the condensing pressure. The total pressure drop was found to increase with ambient air temperature; and decreased as the fan speed increased.

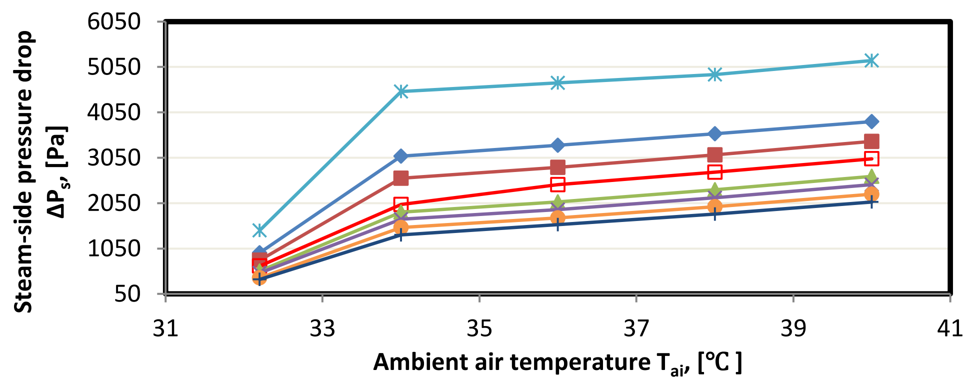

a) Primary condenser units

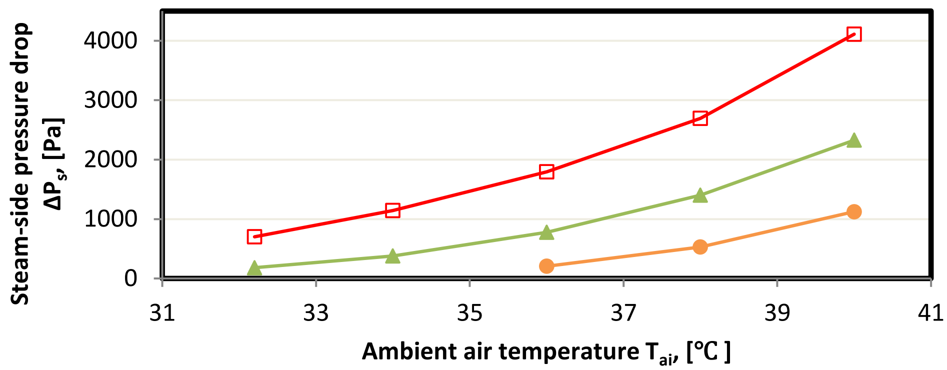

b) CD units

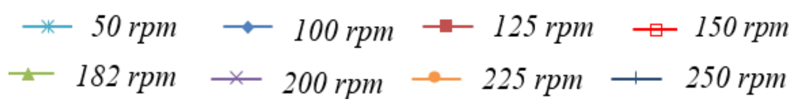

Figure 8. 25: Effects of ambient air temperature on the steam-side pressure drop at different rotational fan speeds

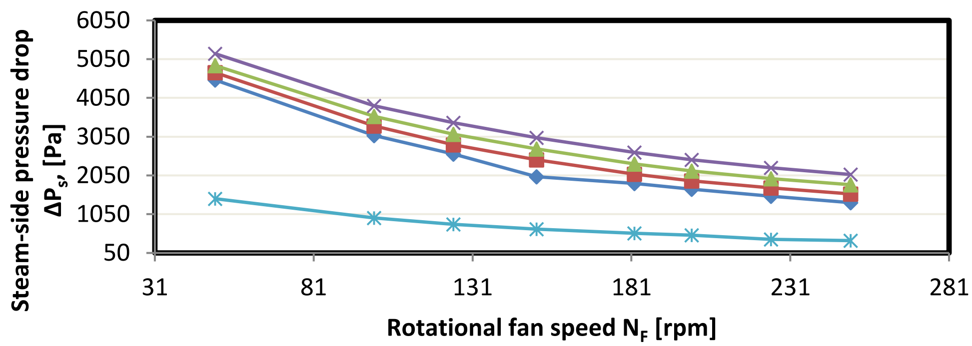

a) Primary condenser units

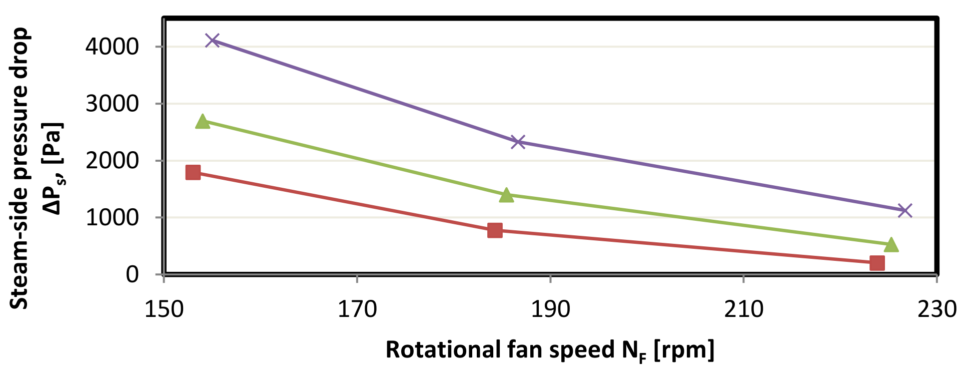

b) CD units

Figure 8. 26: Effects of rotational fan speed on the steam-side pressure drop at different ambient air temperatures

8.1.3. Interconnection between the ACC and steam turbine performance characteristics

The turbine performance mainly depends on the condenser performance, which heavily depends on the ambient air temperature. Therefore, the turbine exhaust pressure is governed by the condensing or operating pressure of ACC. To signify this, the interconnection between the heat transfer rate and the turbine exhaust pressure was investigated as depicted in Figure 8.27 at both constant rotational fan speed and ambient air temperature, respectively. For clear illustration purposes, only the cases corresponding to 182 rpm and 36 ℃ were shown. It is clear that as the heat transfer rate increased, the exhaust pressure decreased. This results in a greater pressure difference over the turbine, which leads to a huge amount of energy being extracted from the steam, and then a large turbine power output. Furthermore, the clear interrelationship between the exhaust pressure and turbine power output at ambient air temperature of 36℃ is presented in Figure 8.28.

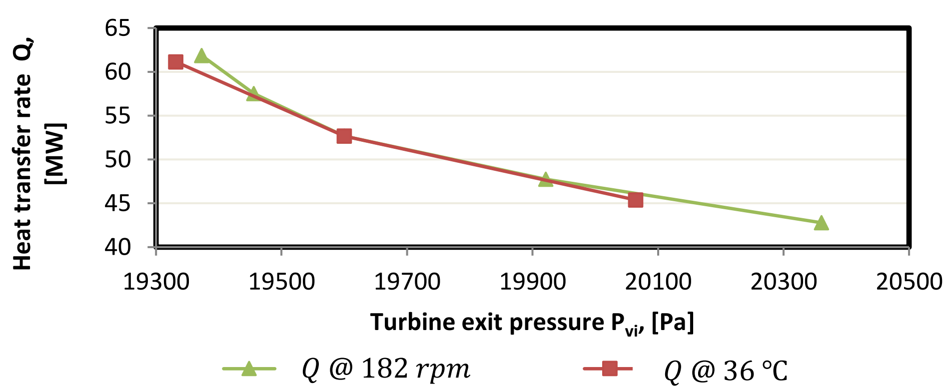

Figure 8. 27: Interconnection between the heat transfer rate and the turbine exhaust pressure

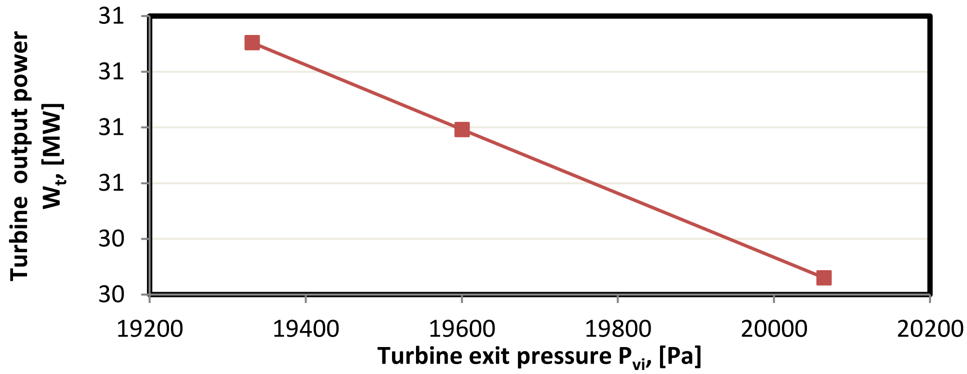

Figure 8. 28: Interconnection between the turbine output power and turbine exit pressure at constant ambient air temperature of 36 ℃

In addition to that, the effect of both ambient air temperature and fan speed on the turbine power output is illustrated in Figures 8.29 and 8.30, respectively. As discussed already, the increase of ambient air temperature and fan speed, decreases and increases the ACC performance (heat transfer rate), respectively. Thus, the turbine power output decreased when the ambient air temperature increased, and increased with fan speed. However, as stated early, increasing of fan speed resulted on higher air-side pressure drop, and as a consequence, the fan power consumption raised. Below the optimum operating conditions, increasing the fan speed has the effect of reducing the turbine back pressure, and hence, increasing the turbine power by a greater magnitude than the increase in fan power consumption. Above the optimum operating conditions, further increasing of a fan speed continues to reduce the turbine back pressure, however, the fan power consumption increased by greater magnitude than the corresponding increase in turbine power. Increasing ambient air temperature results in an increase in the optimum fan speed, and the fan speed should always be adjusted to the optimum speed. This badly affects the turbine net power, which decreased as both ambient air temperature and fan speed increased, as shown in Figures 8.31 and 8.32, respectively.

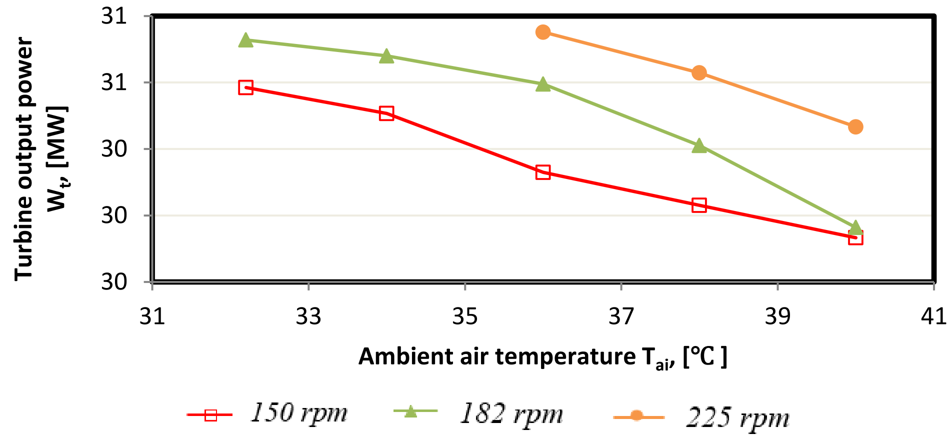

Figure 8. 29: Effect of ambient air temperature on the turbine output power at different rotational fan speeds

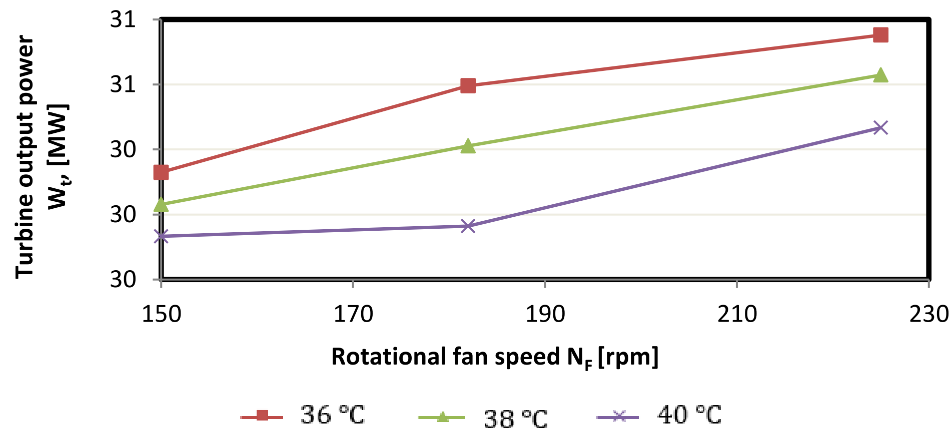

Figure 8. 30: Effect of rotational fan speed on the turbine output power at different ambient air temperatures

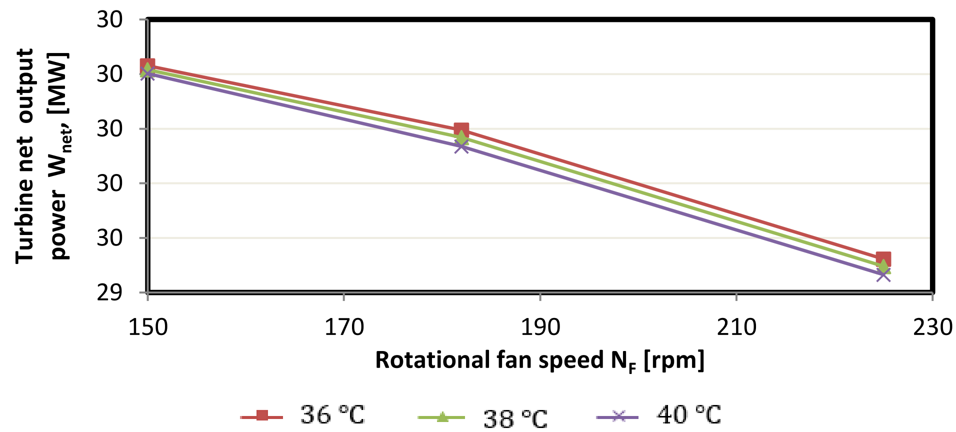

Figure 8. 31: Effect of rotational fan speed on the turbine net output power at different ambient air temperatures

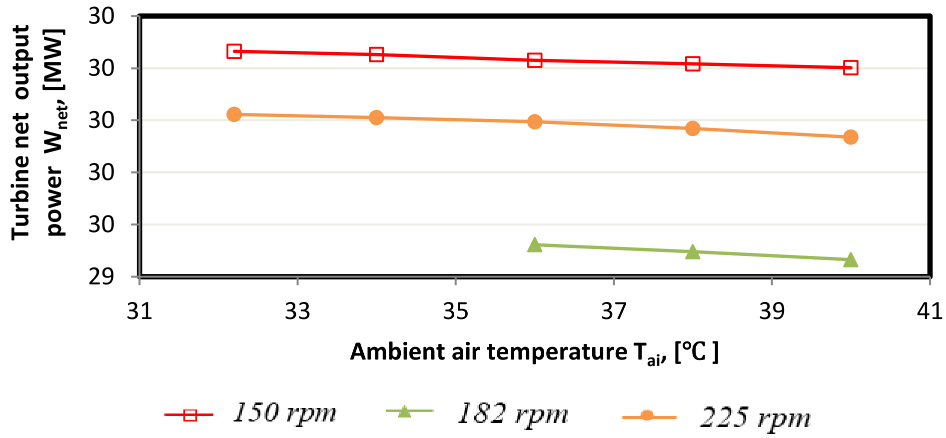

Figure 8. 32: Effect of ambient air temperature on the turbine net output power at different rotational fan speeds

For clarity purpose, only the efficiency loss due to condenser performance as defined by Eq. (5.66) at optimum fan speed was plotted in Figure 8.33, however, the efficiency loss due to condenser performance behaved the same way at all the considered fan speeds. It is clear that, the efficiency loss due to condenser performance decreased as the heat transfer rate increased. This is similar to what Moore *et al.* (2014) found when they plotted the condenser face area against the efficiency loss due to condenser performance. The efficiency loss due to condenser performance was found to decrease as the condenser face area increased. This is due to the fact that, increasing condenser face area increases the heat transfer rate.

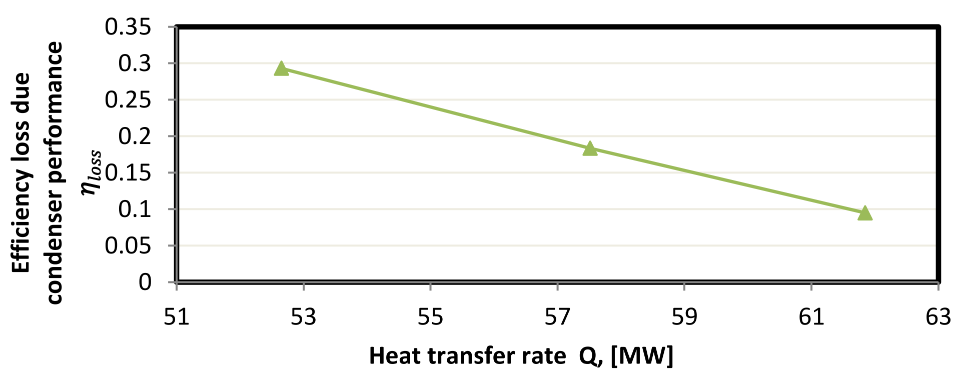

Figure 8. 33: Interconnection between the efficiency loss due to condenser performance and heat transfer rate at constant rotational fan speed of 182 rpm

8.2. Thermal Performance for HDWD Incorporated with Conventional Delugeable Tube Bundle

8.2.1. Air - side Performance Characteristics

On the air- side, the HDWD incorporated with CDTB performance data were presented in terms of the heat transfer rate, air-side pressure drop, fan power consumption, and outlet air temperature. As the ambient air temperature increased, the air density decreased, which results in slight decreasing of the air mass flow rate as indicated in Figure 8.34.

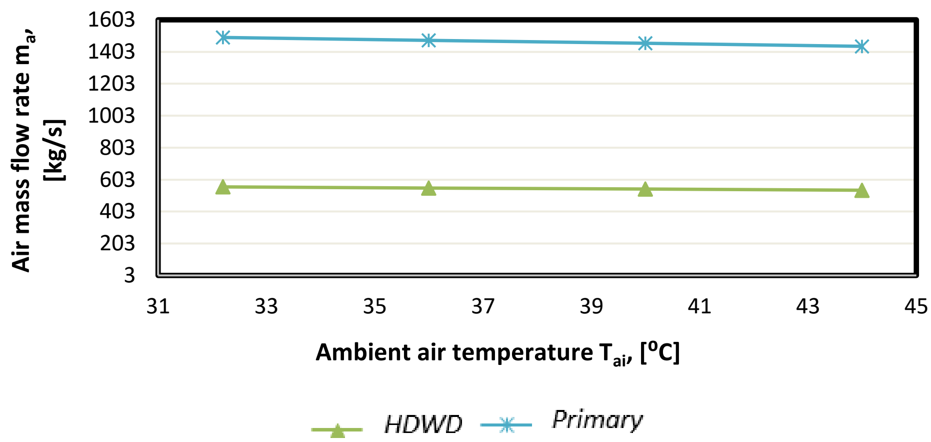

Figure 8. 34: Effect of the ambient air temperature on the air mass flow rate

a) Heat transfer rate

As it is indicated in Figure 8.35, for both HDWD stages, as well as for the ACC incorporated with HDWD, the heat transfer rate decreased as the ambient air temperature increased. This is signified by the increasing air temperature at the exit of the tube bundles, as well as by the large amount of steam exiting the tube bundles as depicted in Figures 8.36 and 8.37, respectively. The increase of the outlet air temperature with inlet air temperature, concurs with Jaafarian and Kazemian (2017) study, which reported a linear increase of outlet air temperature with inlet air temperature in their study of performance analysis of a two-stage evaporative cooler.

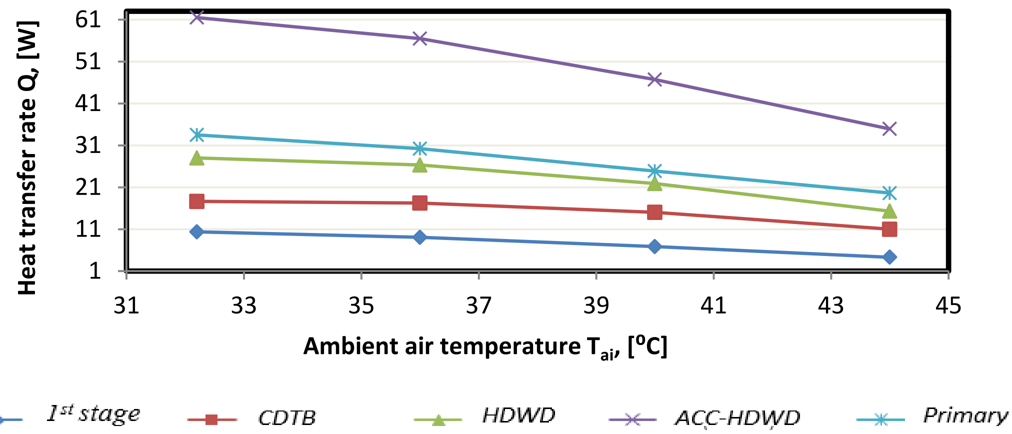

Figure 8. 35: Effect of the ambient air temperature on the heat transfer rate

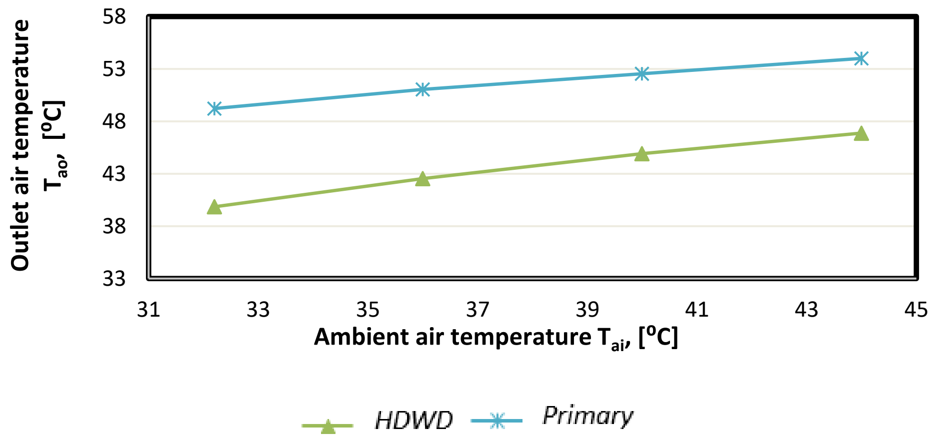

Figure 8. 36: Effect of the ambient air temperature on the outlet air temperature

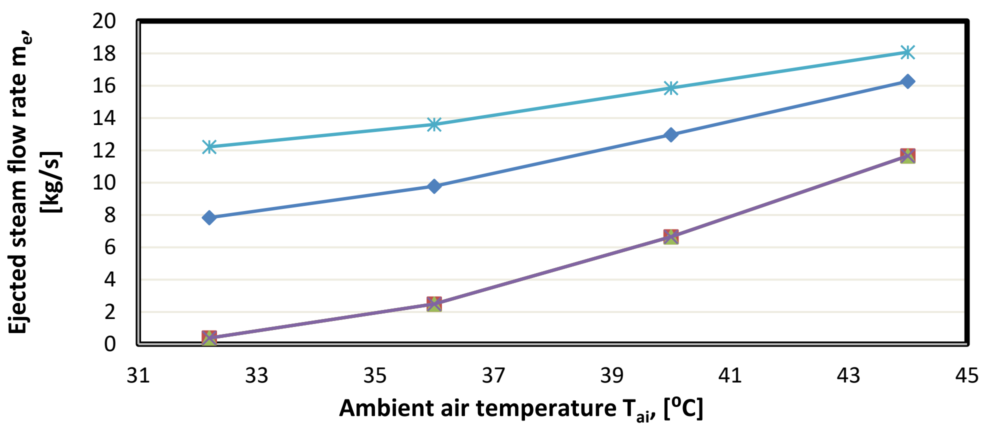

Figure 8. 37: Effect of the ambient air temperature on the ejected steam flow rate

b) Air-side pressure drop

Figure 8.38 shows that, as the ambient air temperature increased, the air-side pressure drop decreased. This is due to the decreasing of the air density as its temperature increases, which results in the dropping of static pressure. However, if the analysis was conducted at constant air mass flow rate, air-side pressure drop was found to increase as the ambient air temperature increases. Furthermore, the higher fan speed resulted on the higher air-side pressure drop through first stage tube bundle. Without considering the losses through collecting troughs and drift eliminators, air-side pressure drop through CDTB was found to be insignificant when compared to that of first stage tube bundle. Since, the air-side pressure drop is directly related to fan power consumption, the fan power consumption was found to decrease as the ambient air temperature increases as depicted in Figure 8.39.

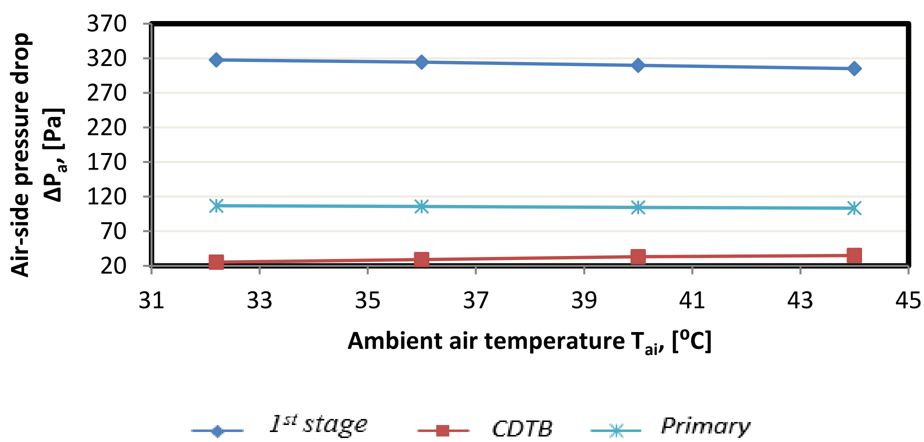

Figure 8. 38: Effect of the ambient air temperature on the air-side pressure drop

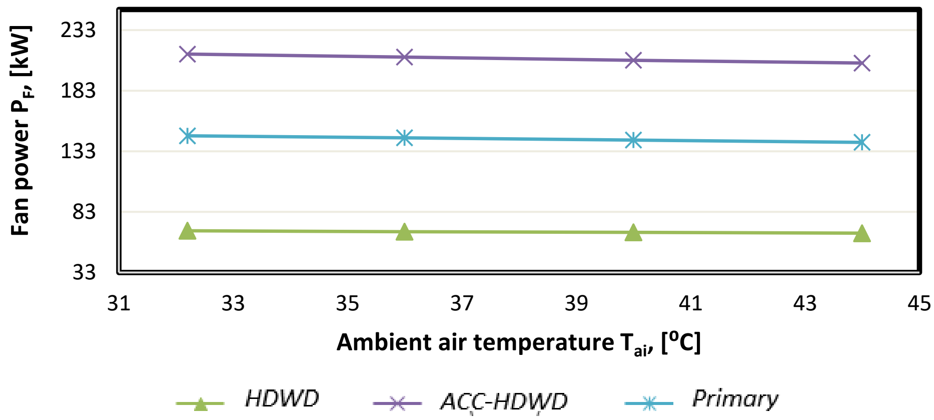

Figure 8. 39: Effect of the ambient air temperature on the fan power

8.2.2. Steam - side Performance Characteristics

On the steam-side, the HDWD performance data were presented in terms of the inlet steam flow rate, ejected steam flow rate, condensation rate, steam-side pressure drop, and condensing pressure. Both primary condenser units and first stage tube bundle operate as air-cooled condenser, therefore they are both severely affected by the raising of ambient air temperature. As shown in Figure 8.40, as the ambient air temperature increased, the inlet steam flow rate into the first stage tube bundle and CDTB increased. This was due to poor performance of primary condenser units and first stage tube bundle. The effect of the ambient air temperature is also indicated by the decreasing of condensation rate in the tube bundles as illustrated in Figure 8.41.

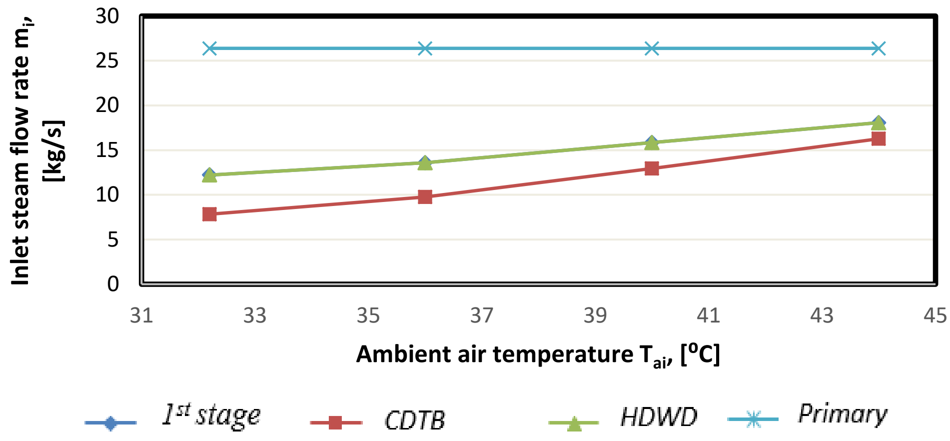

Figure 8. 40: Effect of the ambient air temperature on the inlet steam flow rate

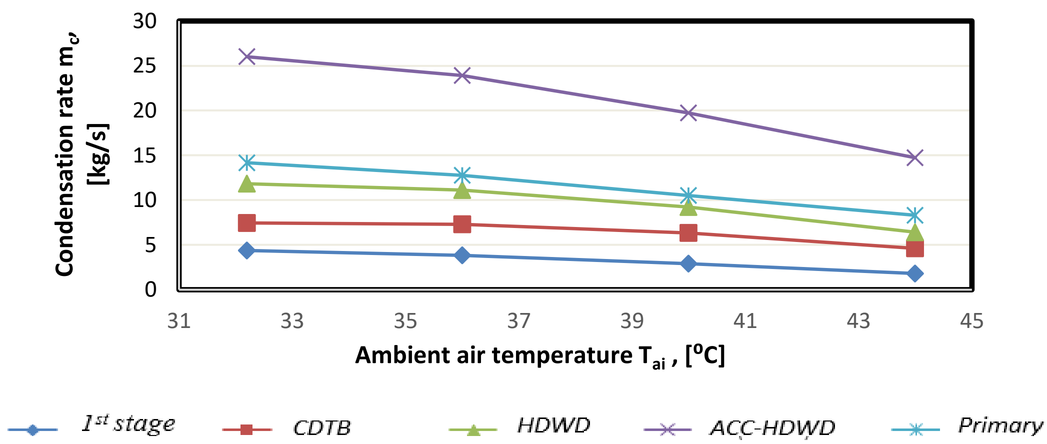

Figure 8. 41: Effect of the ambient air temperature on the condensation rate

Furthermore, as shown in Figure 8.42, the inlet steam velocity at the first stage tube bundle entrance was found to increase with ambient air temperature. Due to the pressure drop in primary condenser tubes, the steam entered the first stage tube bundle at low pressure and temperature. This resulted in a low steam/ vapor density, which in return resulted in the increasing of steam velocity at the first stage tube bundle entrance. Higher inlet steam velocity led to high frictional, momentum and inlet losses. Furthermore, the higher inlet steam flow rates were found to cause condensing pressure reduction (O'Donovan *et al.*, 2014). Thus, as shown in Figures 8.43 and 8.44, in the HDWD (first stage), the steam-side pressure drop, and condensing pressure were found to increase and decrease, respectively as the ambient air temperature increased. However, in the primary condenser units the condensing pressure was found to increase with ambient air temperature. This is because the inlet mass flow rate to the primary condenser units was constant as indicated in Figure 8.40.

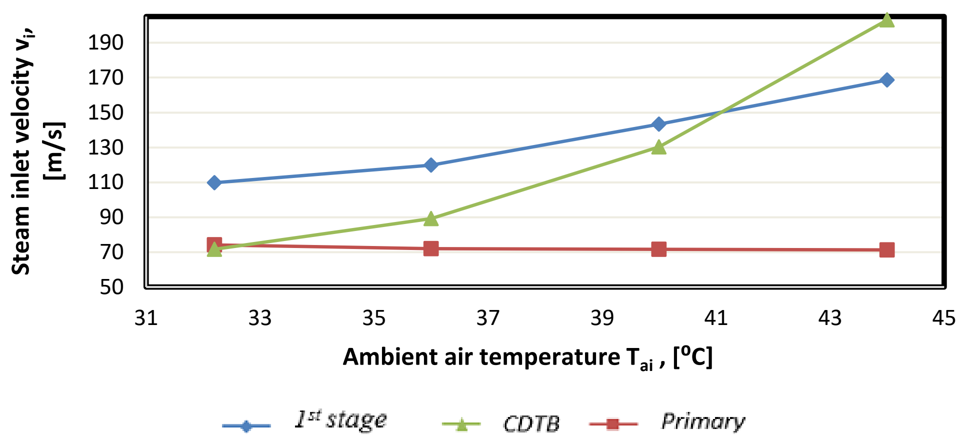

Figure 8. 42: Effect of the ambient air temperature on the steam inlet velocity

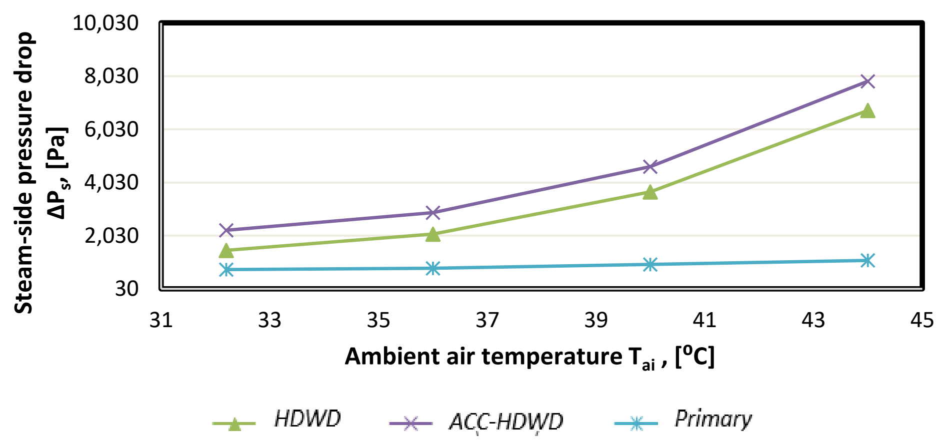

Figure 8. 43: Effect of the ambient air temperature on the steam-side pressure drop

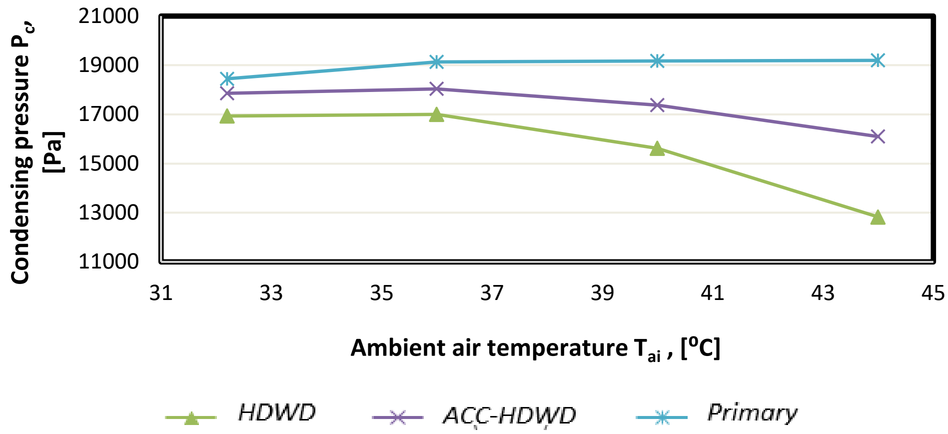

Figure 8. 44: Effect of the ambient air temperature on the condensing pressure

8.2.3. Steam Turbine Performance Characteristics

As emphasized in the previous sections, the steam turbine power output is highly depending on the ACC performance. The turbine exhaust pressure and the corresponding total heat to be rejected by the ACC was presented in Figure 8.45. From Figure 8.45 it is clear that, when the ACC performance is higher, less uncondensed steam will be ejected into the atmosphere together with uncondensable gases. Hence, less heat energy escapes with this uncondensed steam, and the turbine exit pressure is low.

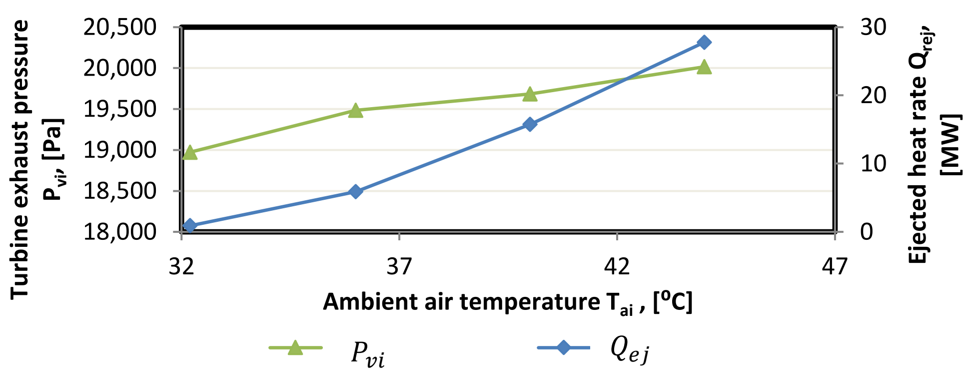

Figure 8. 45: Effect of the ambient air temperature on the turbine exhaust pressure and ejected heat rate

However, as the ambient air temperature increased, the ACC performance decreased, and the amount of heat to be rejected by ACC increased, and the steam exhaust pressure increased, which resulted in the reduction of turbine output power (Figure 8.46).

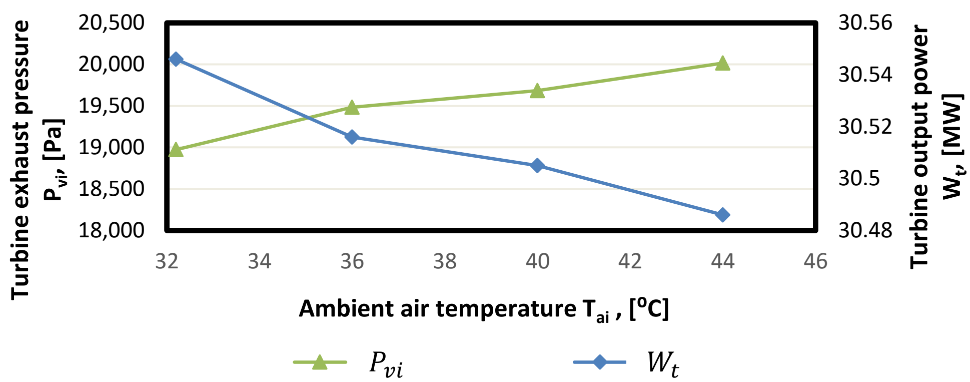

Figure 8. 46: Effect of the ambient air temperature on the turbine output power and exhaust pressure

By considering the fan power consumption as showed in Figure 8.39, the net generating unit output power was computed as illustrated in Figure 8.47. As expected, it also decreased as the ambient air temperature increased.

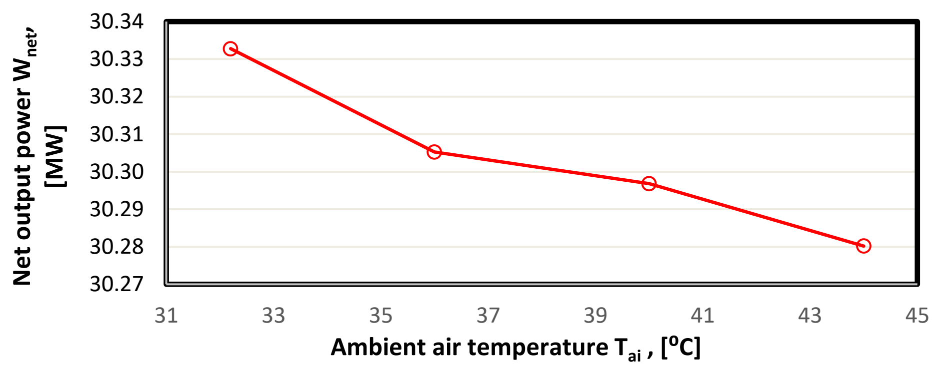

Figure 8. 47: Effect of the ambient air temperature on the generating unit net output power

8.2.4. Water Consumption

The ACC incorporated with a HDWD was found to consume water in the range of 12.6 kg/s to 19.5 kg/s, which is equivalent to evaporation rate of 4.20 kg/s to 6.45 kg/s per

HDWD. The water consumption was found to increase with the steam temperature at the CDTB's entrance as illustrated in Figure 8.48.

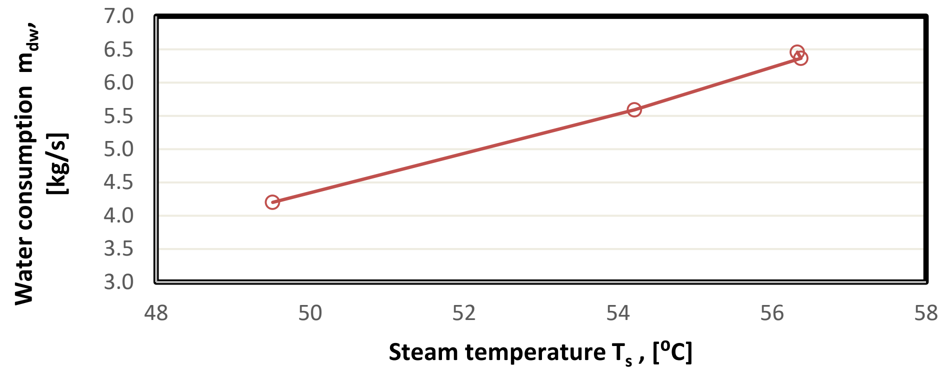

Figure 8. 48: Effect of steam temperature on the water consumption

Furthermore, as the ambient air temperature increased, the water consumption was found to decrease as illustrated in Figure 9.49. This is due to the fact that, at constant relative humidity of 30%, the humidity ratios of the inlet air, and that of air at exit of CDTB increased with ambient air temperature. This resulted in decreasing of the humidity ratio change.

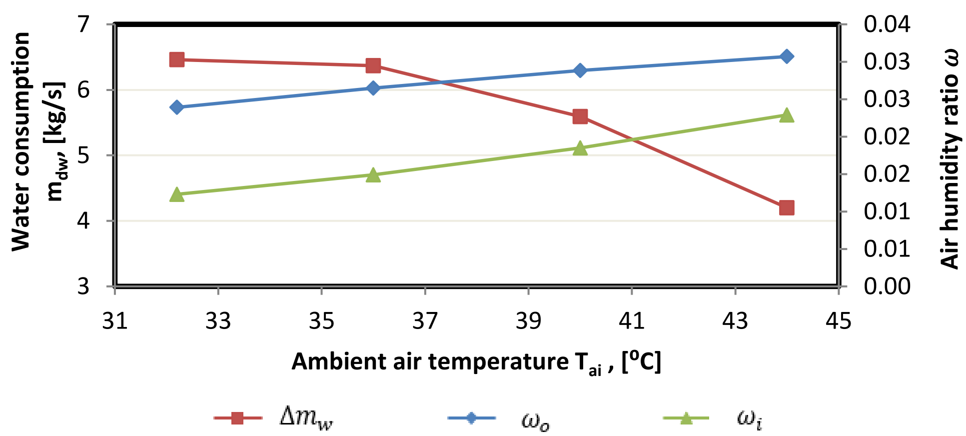

Figure 8. 49: Effect of the ambient air temperature on the water consumption and air humidity ratios

8.3. Performance Comparison of Conventional and Hybrid Dry/ Wet Dephlegmators

As shown in Figure 8.50, at component level, as the ambient air temperature increased, the heat transfer rate of HDWD incorporated with CDTB was found to be 2.5 to 3 times that of CD. This results are in line with Plessis and Owen (2021) finding, which reported heat transfer rate of HDWD's being approximately 4.7 times greater than for CD unit, in their comparative study in which the single-stage HDWD was incorporated into the ACC consisted of 4 streets of 6 units. At system level, an ACC incorporated with the HDWD provided 27 % to 31 % heat transfer rate greater than that of the ACC incorporated with CD. These findings concur with that of Owen (2013) study, in which the heat transfer rate of HDWD was found to be two to three times, and 15 % to 30 % greater than CD's heat transfer rate at the component and system levels, respectively. Owen (2013) investigated the performance of an ACC consisting of four streets with five primary condenser units and one dephlegmator unit equipped with or without a HDWD. However, the second stage tube bundle consists of round tubes.

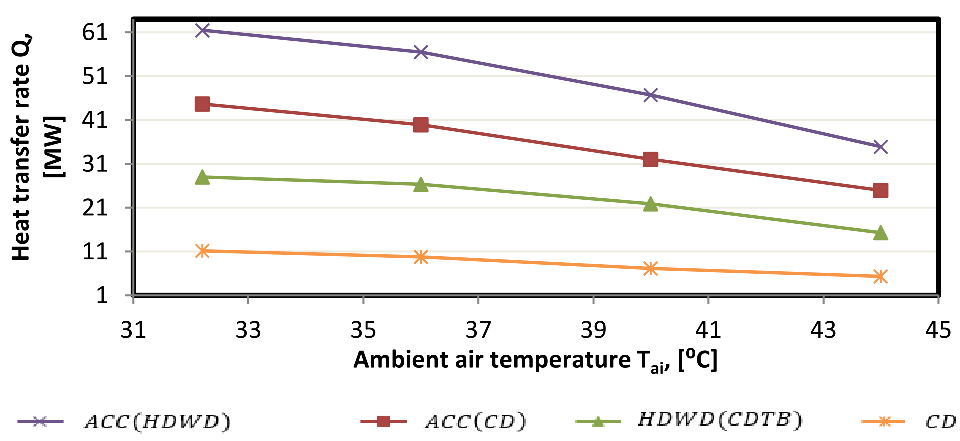

Figure 8. 50: Comparison of CD and HDWD heat transfer rates at component and system levels

When the CD heat transfer rate compared to that of first stage tube bundle of HDWD, it can be seen that the first stage tube bundle provides about 93 % of CD heat transfer rate as shown in Figure 8.51. This means, only 7 % will be needed to be offered by CDTB (second stage) for the heat transferred by HDWD to be equal to that of CD. This shows that, when the HDWD, operates on dry mode, it will still provide higher heat transfer rate than that of CD.

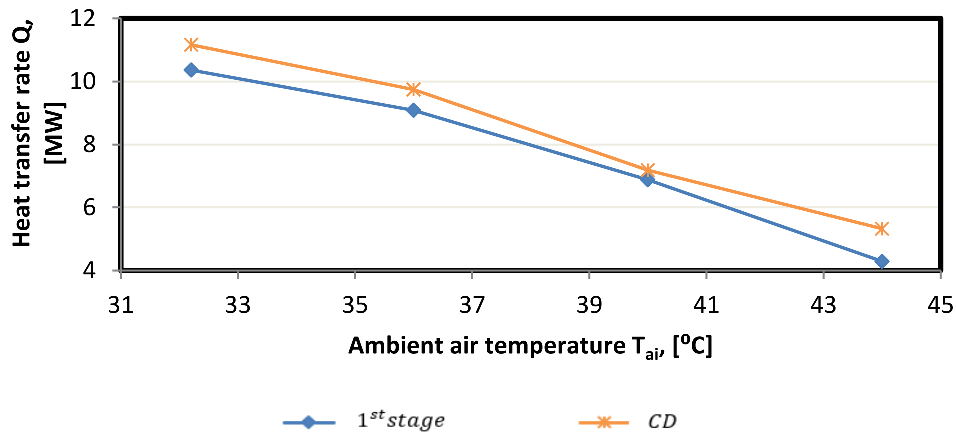

Figure 8. 51: Comparison of CD and HDWD first stage tube bundle heat transfer rates

The tubes of the first stage tube bundle of HDWD are shorter than that of CD. This was done in order to accommodate the second stage tube bundle (CDTB). The short length of HDWD first stage bundle tubes resulted in reduction of its frontal area, which resulted in higher mean air velocity through the bundle. As a consequence, the air-side pressure drop of first stage tube bundle is greater than that of CD, which also made the HDWD's air-side pressure drop to be higher than that of CD as depicted in Figure 8.52.

The steam turbine exit pressure increases with ambient air temperature, but at lower pace and closer to the optimum turbine exit pressure as indicated by dashed line, Figure 8.53, compare to that of the ACC with CD. For considered turbine, at ambient air temperature up to 38 ℃, the ACC with HDWD leads to turbine exit pressure below the optimum than the ACC with CD. This signifies that, the HDWD mainly needed to be operated on wet mode when the ambient temperatures are higher.

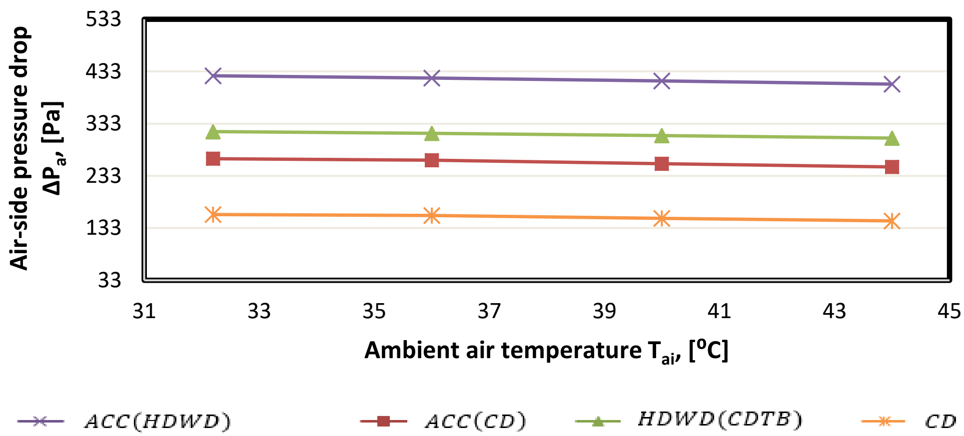

Figure 8. 52: Comparison of CD and HDWD air-side pressure drops at component and system levels

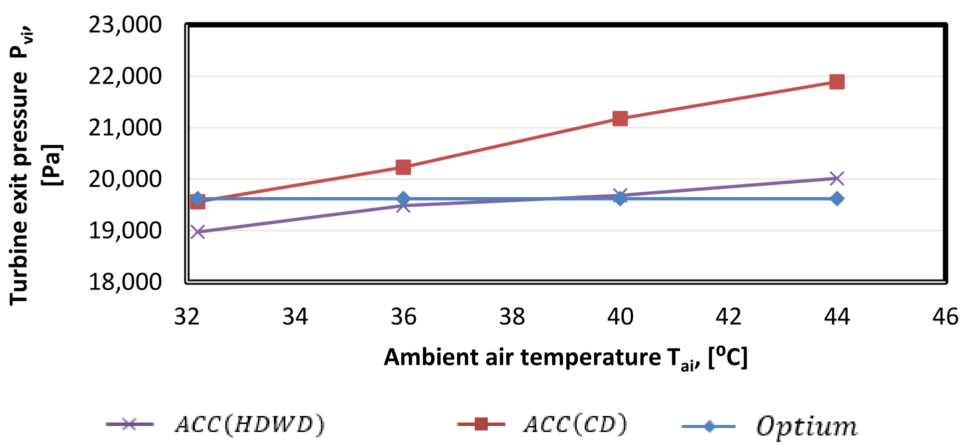

Figure 8. 53: Comparison of CD and HDWD turbine exit pressure at system level

As indicated in Figures 8.54 and 8.55, the ACC incorporated with HDWD has a quantifiable enhancement in the steam turbine power output, as well as in the net power output than its counterpart ACC incorporated with CD. The difference between the turbine output powers of the two systems was found to be smaller, due to the fact that, the steam flow rate at the turbine exit was considered constant. At lower turbine exit pressure, more steam extraction through the last turbine stage, which results in an increasing of last turbine stage output power. Thus, the difference in turbine output powers between the systems was only due to the enthalpy difference across the last turbine stage.

Furthermore, the make-up water to be added into the system to compensate the uncondensed steam loss was less for ACC system incorporated with HDWD, which is in the range of 1 % to 44 % compare to 28 % to 60 % for ACC system incorporated with CD, as the ambient air temperature varies from 32 ℃ to 44 ℃.

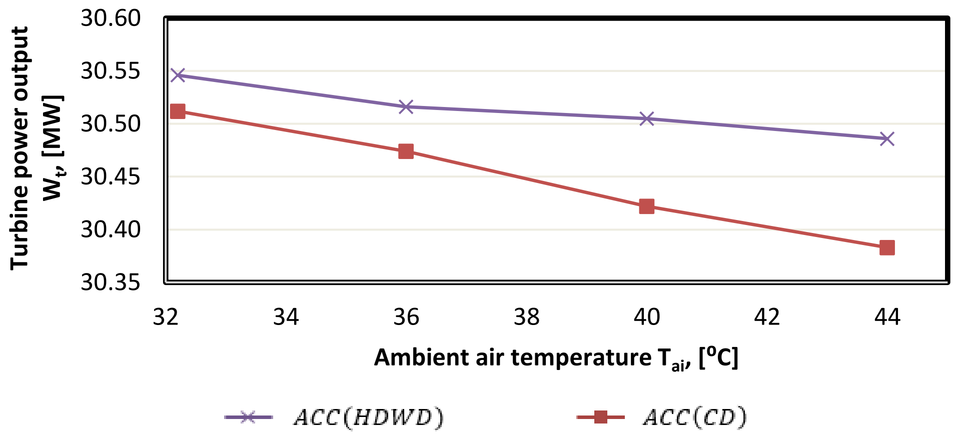

Figure 8. 54: Comparison of CD and HDWD turbine power output at system level

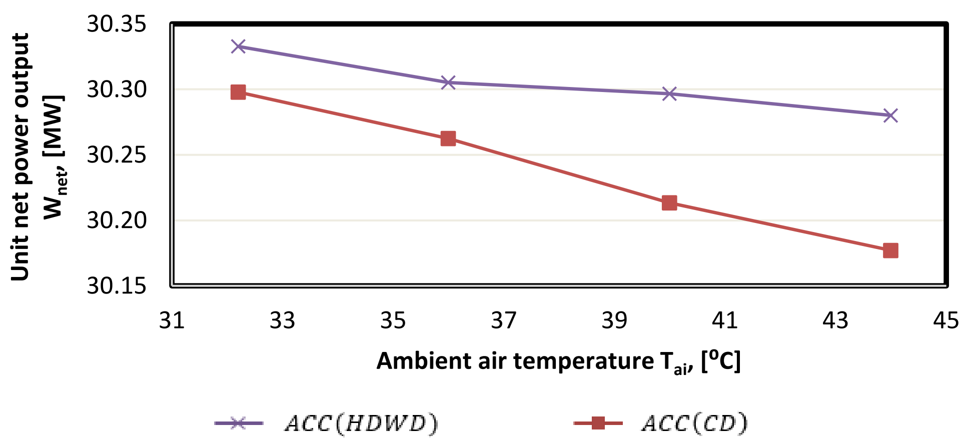

Figure 8. 55: Comparison of CD and HDWD net power output at system level

8.4. Microchannel Delugeable Tube Bundle Thermal Performance

The effects of the geometric parameters on the performance of microchannel tube bundles or heat exchangers have been extensively studied in the literatures. As presented in Figure 8.56, for the constant flat tube width, as the number of ports in one flat microchannel tube increased, the hydraulic diameter of microchannel ports decreased.

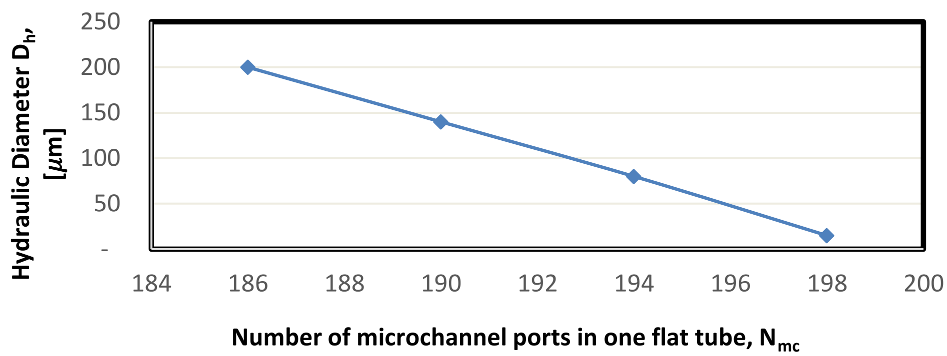

Figure 8. 56: Effect of number of channels in one flat microchannel tube on the hydraulic diameter of microchannel

8.4.1. Hydrodynamic Entry Length

The hydraulic diameter effect on the dimensionless hydrodynamic entry length (L_e/D_h) was assessed for the hydraulic diameter in the range of 10 to 200 μm, and corresponding aspect ratio in the range of 0.0180 and 0.02654. In this the study, the width for the considered microchannel tube was kept constant throughout the study. Therefore, the aspect ratios corresponding to all the considered scenarios were found to be out of range of aspect ratios for Galvis *et al.* (2012) proposed correlations. Hence, the hydrodynamic entry length was defined using Ahmad and Hassan (2010) correlation, (Eq. (2.1)) which was proposed and depends only on the Reynolds number.

From Figures 8.57 and 8.58, it is clearly indicated that the effect of the hydraulic diameter on the dimensionless hydrodynamic entry length was insignificant. This concurs with Sahar *et al.* (2017) numerical results, in the dimensionless entrance length was found to be independent of hydraulic diameter. Furthermore, Sahar *et al.* (2017) conclusion was in good agreement with Ahmad and Hassan (2010) findings, which state that for Re > 10, the effect of the hydraulic diameter on dimensionless hydrodynamic entry length was insignificant.

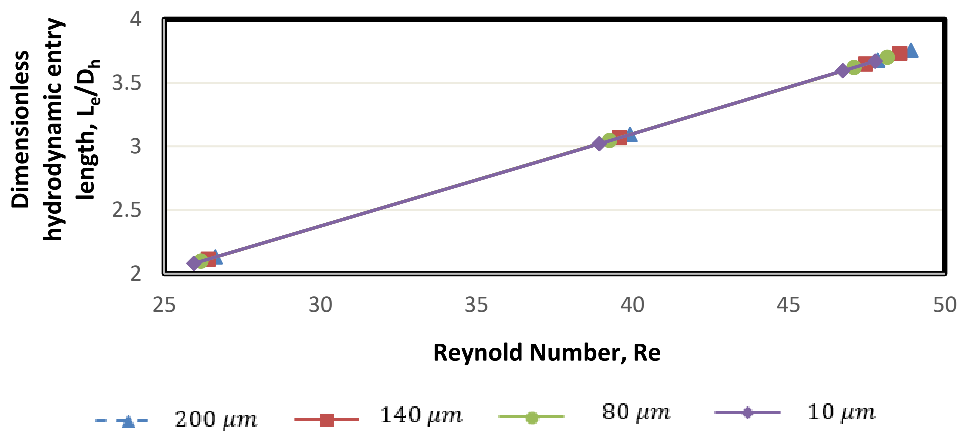

Figure 8. 57: Interconnection between the dimensionless hydrodynamic entry length and Reynolds number for different hydraulic diameters

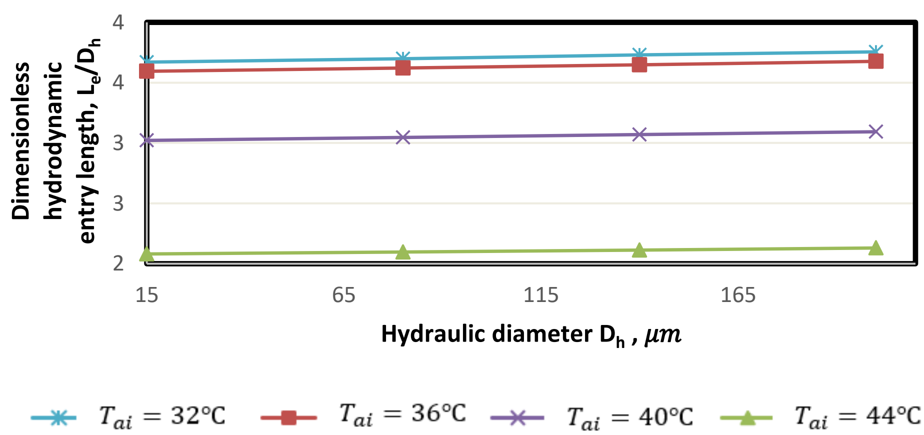

Figure 8. 58: Effect of hydraulic diameter on the dimensionless hydrodynamic entry length at different ambient air temperatures

8.4.2. Heat Transfer Rate

The impact of the hydraulic diameter on rate of heat transfer, from steam to the water, then to air, was assessed through Nusselt number and condensation heat transfer coefficient. Shah and London (1978) correlations for both friction factor and heat transfer coefficient have been used in most of recent studies, such as Zhang *et al.* (2014 b); Sahar *et al.* (2017); Al-Zaidi *et al*., (2018); Ren *et al.* (2020) and Hsieh *et al.*, (2021). Therefore, in this study, the same correlations were employed.

As shown in Figure 8.59, at constant steam flow rate, and for different hydraulic diameters, the Nusselt number was found to slightly increase with Reynolds number. The flow through the microchannels was found to be laminar, since the Re < 2300. The increase in Nusselt number shows that the flow was thermally developing. Furthermore, the hydrodynamic length was found to be smaller, compared to the tube length, and decreased as the hydraulic diameter of the microchannel decreased, as presented in Figure 8.60. Therefore, the flow through the entire channel can be considered as fully developed.

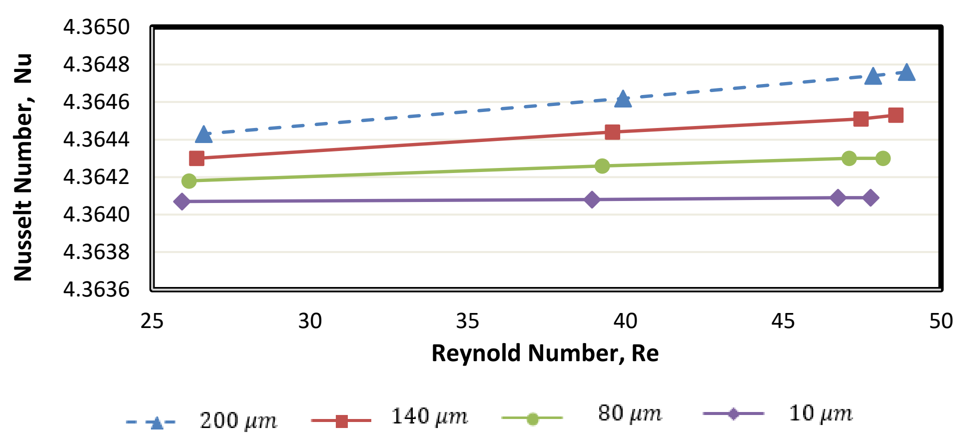

Figure 8. 59: Interconnection between the Nusselt number and Reynolds number for different hydraulic diameters

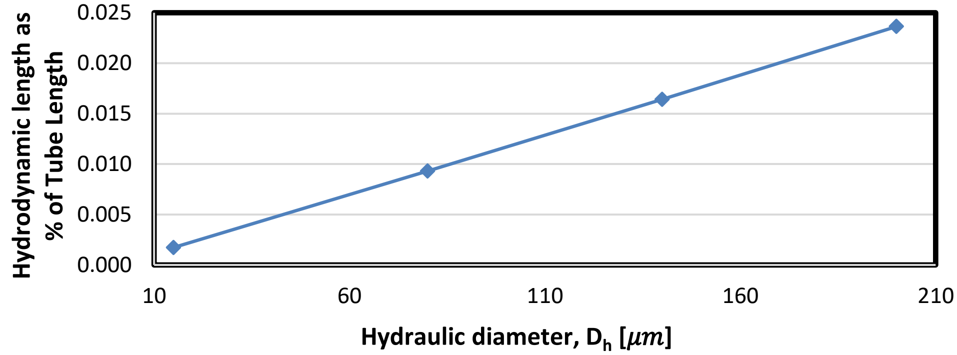

Figure 8. 60: Effect of hydraulic diameter on the hydrodynamic length as a % of tube length

The hydraulic diameter effect on Nusselt number is shown in Figure 8.61. From Figure 8.61, the Nusselt number increased with increasing of the hydraulic diameter, which may appear as a contradiction to the heat transfer coefficient (h_c), which decreased as the hydraulic diameter increased as shown in Figure 8.62. The Nusselt number is a function of both hydraulic diameter and heat transfer coefficient as expressed in Eq. (8.2), therefore, Nusselt number values depend on the effect of the more dominant variable.

$$Nu = h_c D_h / k \tag{8. 2}$$

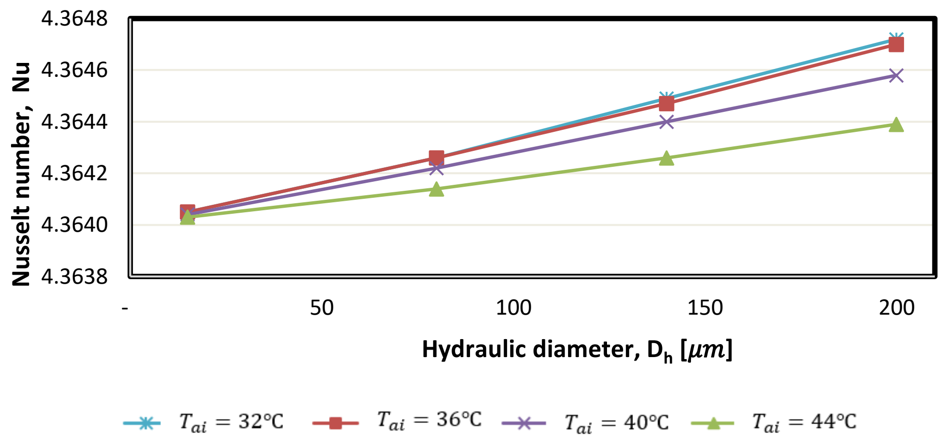

Figure 8. 61: Effect of hydraulic diameter on the Nusselt number at different ambient air temperatures

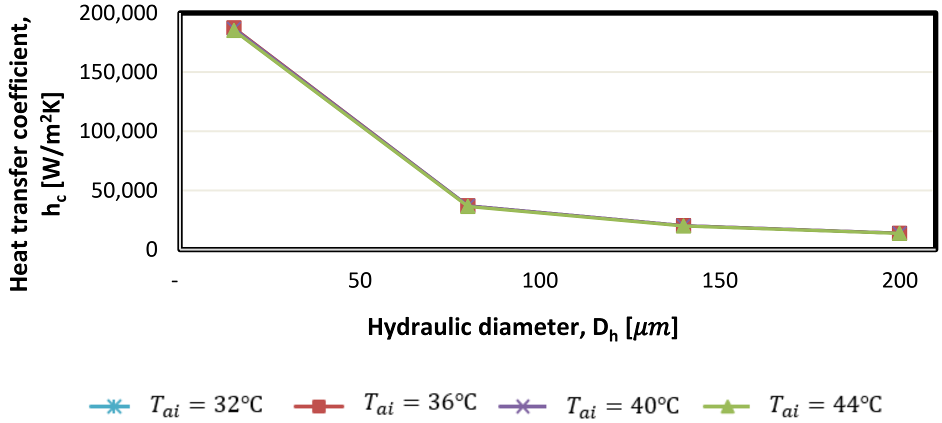

Figure 8. 62: Effect of hydraulic diameter on the heat transfer coefficient at different ambient air temperatures

Moreover, as it is indicated in Figures 8.63 and 8.64, it was found that at larger hydraulic diameters, the temperature difference between the tube wall and fluid (steam) was greater than at smaller hydraulic diameters, and as a result, heat transfer coefficient obtained at smaller hydraulic diameters is higher compare to the one obtained at larger hydraulic diameter. Sahar *et al.* (2017) also reported the similar scenario when it comes to the relationship between the Nusselt number and the heat transfer coefficient obtained for different hydraulic diameters.

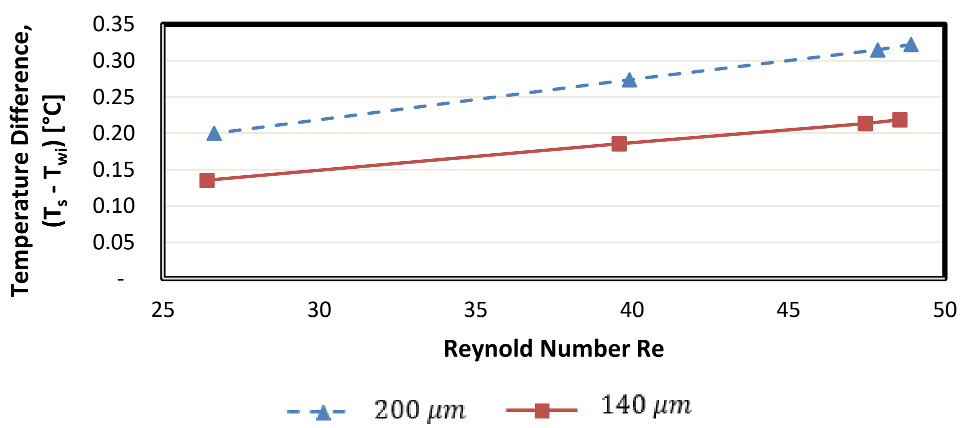

Figure 8. 63: Effect of Reynolds number on the temperature difference between the tube wall and fluid (steam) for different hydraulic diameters

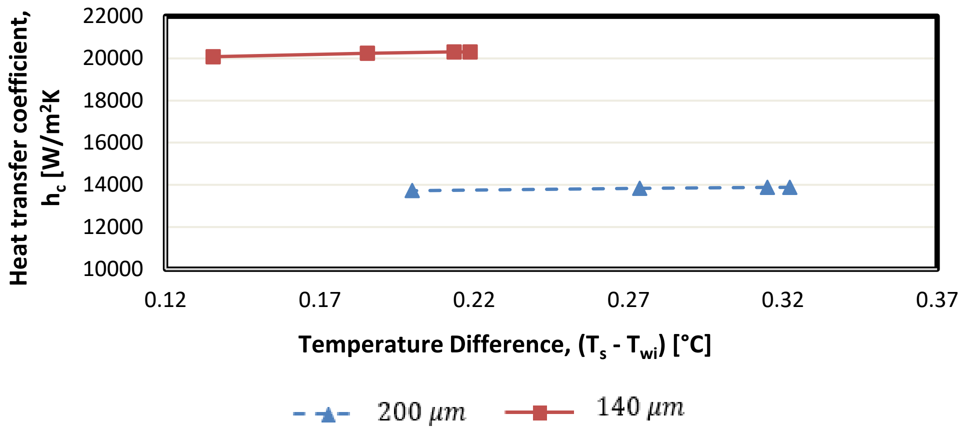

Figure 8. 64: Effect of the temperature difference between the tube wall and fluid (steam) on the heat transfer coefficient for different hydraulic diameters

Furthermore, as shown in Figure 8.62, for the same steam mass flow rate, as the hydraulic diameter decreased from 200 μm to 140 μm, the heat transfer coefficient increased by 32 %. This concurs with several studies results such as El Mghaira *et al.* (2014); Sahar *et al.* (2017); and Başaran and Yurddaş (2021). El Mghaira *et al.* (2014) investigated the steam condensation in a horizontal square section microchannels, and for the same mass flux, the Authors indicated a 20 % increase of the average heat transfer coefficient as the microchannel hydraulic diameter varied from 0.250 mm to 0.110 mm. Başaran and Yurddaş (2021) reported that, by decreasing the hydraulic diameter, the heat capacity coefficient of isobutane inside the microchannel can be increased by 12 % to 62 %.

As presented in Figures 8.65 and 8.66, the heat transfer rate decreased as the hydraulic diameter increased, and increased as the number of the channels in one flat microchannel tube increased. This is due the fact that, the steam flow area and velocity (Figure 8.67) decreased and increased, respectively, as the number of microchannel in one flat tube increased. As a result, the steam-side heat transfer coefficient increased, and subsequently, the heat transfer rate increased. This concurs with Ling *et al.* (2015) findings, which indicate an increase in the cooling rate from 3194 W to 3209 W with the increasing of number of microchannel in one flat tube.

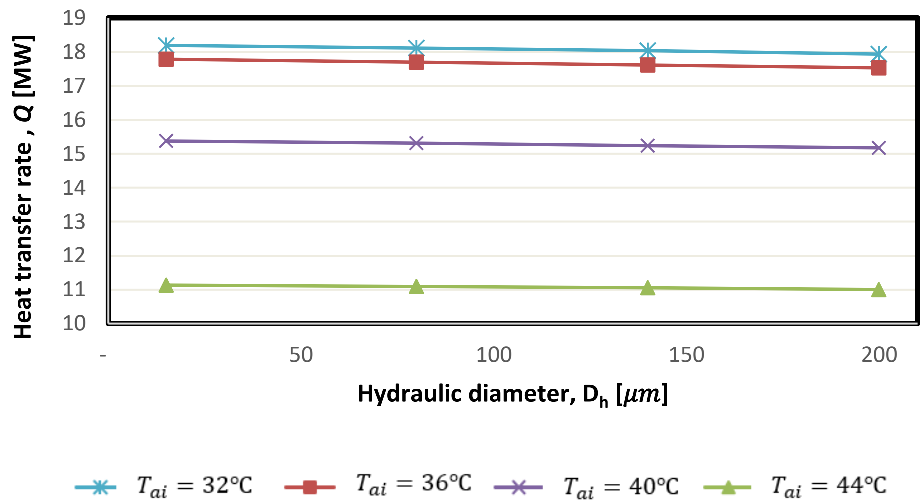

Figure 8. 65: Effect of hydraulic diameter on the heat transfer rate at different ambient air temperatures

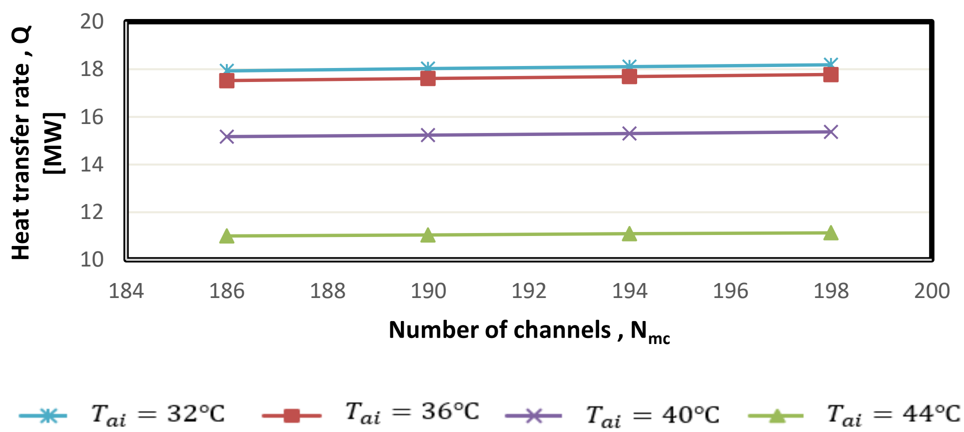

Figure 8. 66: Effect of the number of channels in one flat tube on the heat transfer rate at different ambient air temperatures

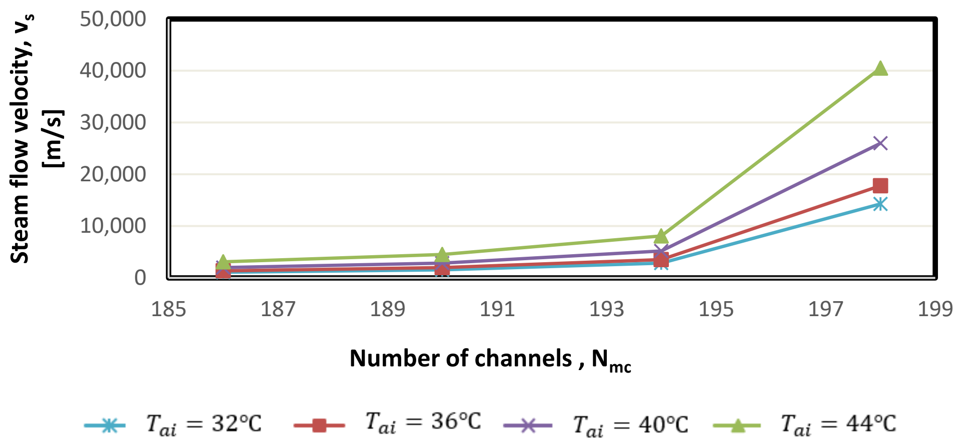

Figure 8. 67: The effect of number of channels in one flat tube on the steam flow velocity at different ambient air temperatures

8.4.3. Steam-side Frictional Pressure Drop

The impact of the hydraulic diameter on the friction factor was investigated for hydraulic diameter range of 10 to 200 μm. Aspect ratio effect on the friction factor was not considered, and since it was reported to be insignificant, especially for the AR < 2 (Sahar *et al.*, 2017). All the considered cases have the aspect ratio less than 0. The friction factor was determined using Shah and London (1978) correlation. Shah and London (1978) correlation was found to agree with findings for many experimental and numerical studies of single-phase flow and heat transfer including both developing and developed flows. Sahar *et al.* (2017) reported that the trend and magnitude of their results were very close to the Shah and London (1978) correlation prediction. Xing *et al.* (2013) indicated a good agreement for simplified friction factor correlation with the experimental data of mini/micro channels and Shah and London (1978) correlation.

When the friction factors obtained for different hydraulic diameters were plotted against Reynolds number (Figure 8.68), the effect of the hydraulic diameter on the friction factor was not clearly visible. This concurs with Sahar *et al.* (2017) work, which indicated insignificant impact of hydraulic diameter on the friction factor. However, when the friction factor was plotted against the hydraulic diameter (Figure 8.69), it was found to increase as the hydraulic diameter decreased.

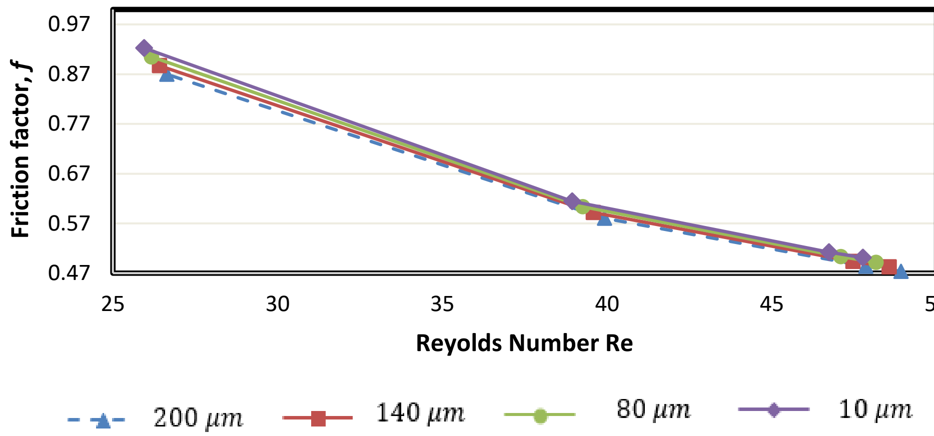

Figure 8. 68: Interconnection between Friction factor and Reynolds number for different hydraulic diameters

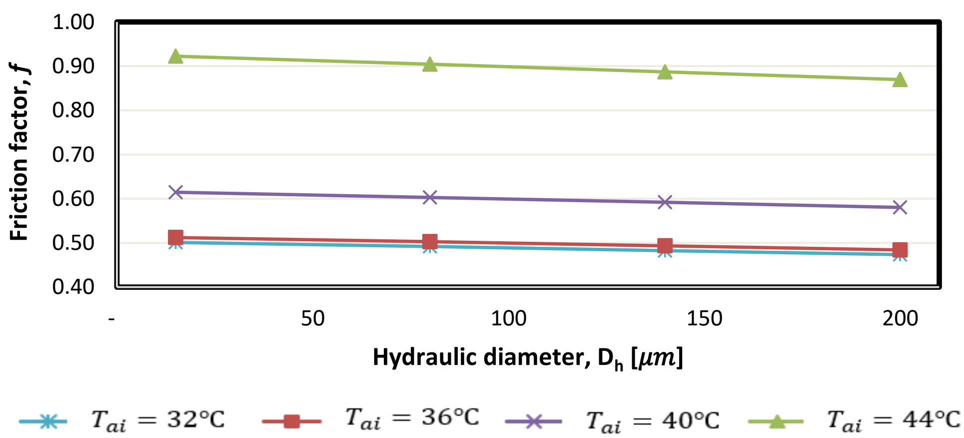

Figure 9. 69: Effect of hydraulic diameter on the friction factor at different ambient air temperatures

In Figure 8.70, the steam-side pressure drop (ΔP_s) increased as the hydraulic diameter decreased. This is due to the fact that, as the hydraulic diameter decreased, the steam flow velocity increased, and therefore, the steam-side pressure drop increased. Moreover, this concurs with Ling *et al.* (2015); Ali *et al.* (2019); and Başaran and Yurddaş (2021) findings. Ling *et al.* (2015) experimentally investigated the microchannel separate heat pipe and reported an increase of pressure drop from 0.05 to 0.7 kPa as the number of microchannels in one flat tube increased, therefore, the hydraulic diameter decreased.

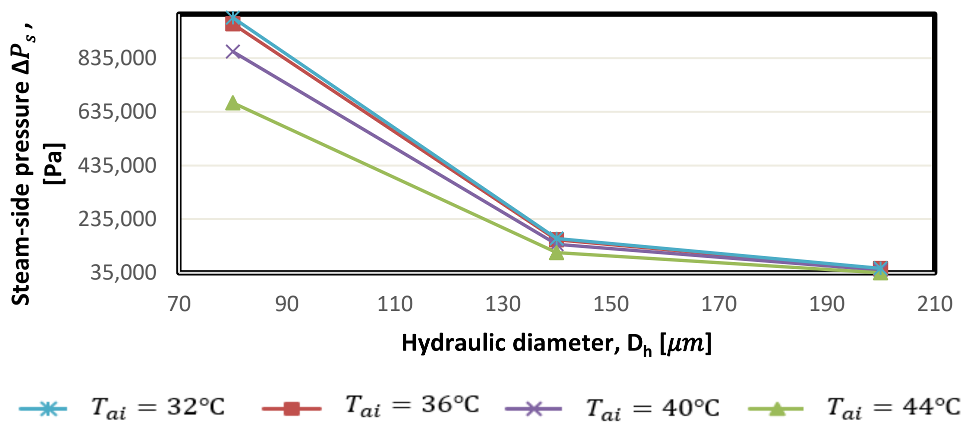

Figure 8. 70: Effect of hydraulic diameter on the steam-side pressure drop at different ambient air temperatures

8.4.4. Thermal performance index (TPI)

The Thermal Performance Index (TPI) was used to analyse the overall performance of the MDTB by taking into account both thermal and hydrodynamic performances. Sahar *et al.* (2017) concluded that, the performance index analysis was more reliable than friction factor analysis, hence, the inclusion of the TPI on the thermal-hydraulic performance analysis of the microchannel heat exchanger is crucial. In this study, the TPI was defined in the same way, Eq. (8.3), as it was determined in the work of Hasan *et al.* (2012), in which numerical investigations of the counter flow microchannel heat exchanger performance, with a nanofluid as a cooling medium, was conducted.

$$\eta = \varepsilon / \Delta P_s \tag{8. 3}$$

where, ε is bundle effectiveness and ΔP_s is steam-side pressure drop, which defined as:

$$\Delta P_s = \left(f_{Shah} \, {}^{D_h}\!/_{L_t} \, {}^{\rho V^2}\!/_{2} \right) \tag{8. 4}$$

As presented in Figure 8.71, the effectiveness for the MDTB at different ambient air temperatures was found slightly decreasing with the increasing hydraulic diameter. This agrees with Ali *et al.* (2019) who indicated that the effectiveness decreases with increasing hydraulic diameter because the heat transfer area increases with size.

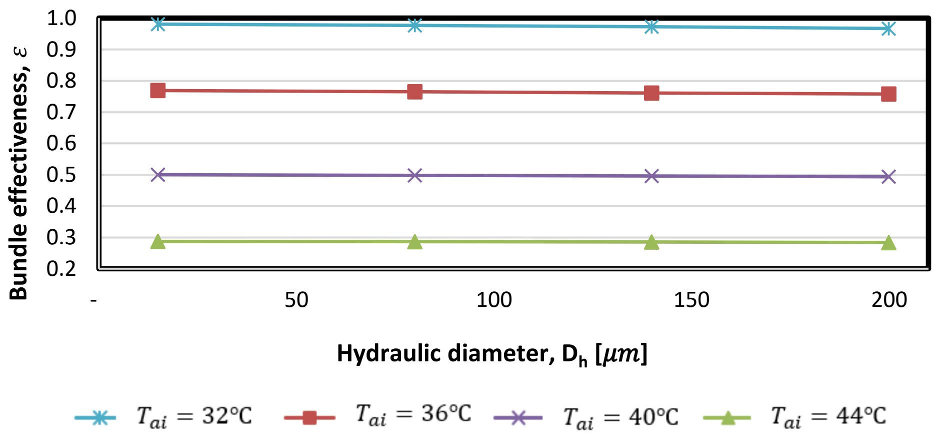

Figure 8. 71: Effect of hydraulic diameter on the bundle effectiveness at different ambient air temperatures

The TPI was found to be higher for larger hydraulic diameters as depicted in Figure 8.72. This is due to the fact that, for larger diameter the pressure drop is low and dominating, which results in higher *TPI*. This agrees with Sahar *et al.* (2017); and Ali *et al.* (2019) findings. Ali *et al.* (2019) reported a higher performance factor (a ratio of heat transfer rate to pumping power) for larger hydraulic diameters, due to higher pumping power in comparison with increasing in convective heat transfer.

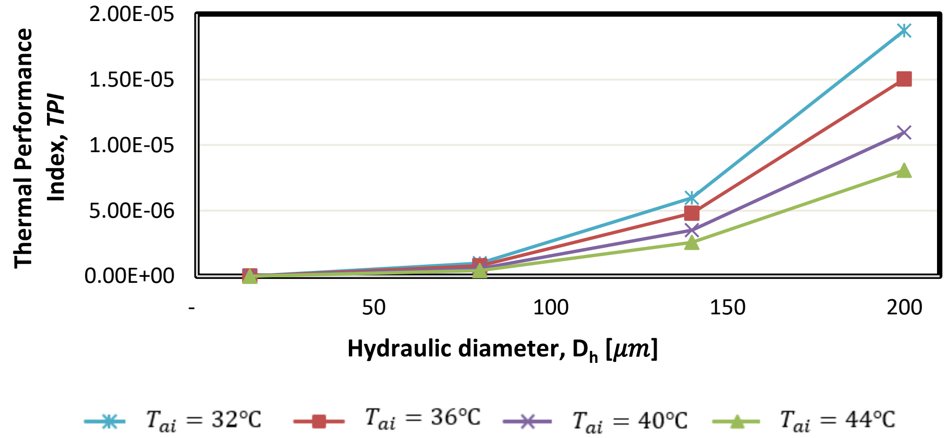

Figure 8. 72: Effect of hydraulic diameter on the Thermal Performance Index at different ambient air temperatures

8.5. Performance Comparison of CDTB and MDTB

8.5.1. Heat Transfer Rate

Since the MDTB on steam-side was divided into several microchannels, and the tube wall thickness between the channels was kept constant and equal to the tube wall thickness, the steam flow area reduces around 23 times compare to that of CDTB. The amount of steam flow through both bundles were kept constant, to ensure that same amount of steam was available for condensation in both bundles. Since the heat transfer from the channels were assumed to be transferred in all directions, as shown in Figure 8.73, surface heat transfer area on steam-side per channel, tube, bundle and for nine (9) bundles, respectively were expressed as:

$$A_{sc} = P_{mc} L_t \tag{8. 5}$$

$$A_{st} = P_{mc} N_{mc} L_t \tag{8. 6}$$

$$A_{sb} = P_{mc} N_{mc} n_{tr} L_t \tag{8. 7}$$

$$A_{sT} = P_{mc}N_{mc}n_{tr}n_bL_t \quad (8.\ 8)$$

Hence, in MDTB, the steam is in contact with larger surface heat transfer area compare to CDTB.

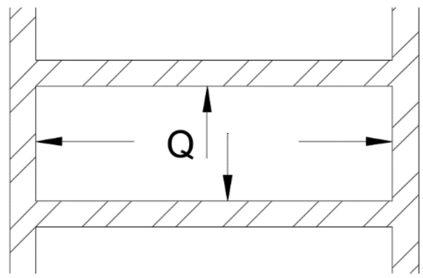

Figure 8. 73: Orientation of the heat transfer in the microchannels

The condensation heat transfer coefficient in MDTB is higher with 29 % to 19 % than that of CDTB, and it was found to decrease as the ambient air temperature increased from 32 ℃ to 44 ℃ as depicted in Figure 8.74. The high condensation heat transfer coefficient was due to small hydraulic diameter of the microchannels. This concurs with Pawar *et al.* (2017) as well as Abdel-Baky *et al.* (2020) findings, who conducted a comparison performance study of dry conventional/finned tube and microchannel condensers, for vapour compression refrigeration system and air-conditioning applications, respectively.

However, the condensation heat transfer coefficient in CDTB was found to increase with ambient air temperature, because, it was defined using Dobson and Chato (1998) correlation, Eq. (8.9) for the flow on the flat vertical plate. Whereas, in MDTB, the condensation heat transfer coefficient was computed using Shah and London (1978), Eq. (2.12).

$$h_c = 0.943\left[\frac{\rho_c(\rho_c - \rho_v)k_c^3 i_{fg}}{\mu_c(T_v - T_{wi})}\right]^{0.25} \tag{8. 9}$$

Dobson and Chato (1998) correlation is a function of temperature difference between steam and inside tube wall temperature, which was found to decrease as ambient air temperature increased as illustrated in Figure 8.75. Moreover, the temperature difference between steam and inside tube wall in MDTB was found to be 71 % to 68 % less than that in CDTB as the ambient air temperature increased from 32 ℃ to 44 ℃.

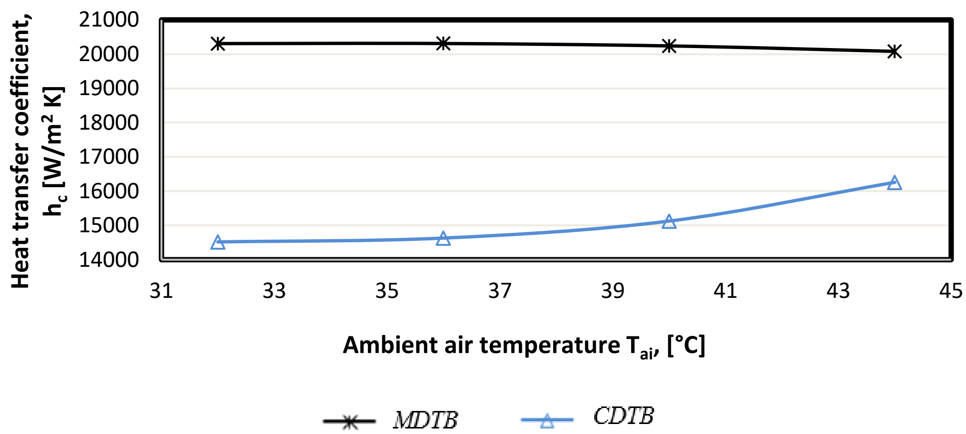

Figure 8. 74: Effect of the ambient air temperature on the heat transfer coefficient

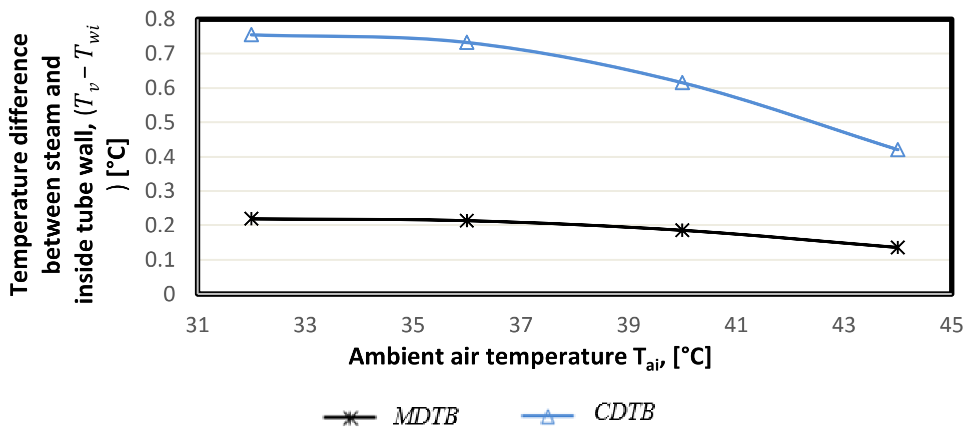

Figure 8. 75: Effect of the ambient air temperature on temperature difference between steam and inside tube wall

Although, the heat transfer coefficient in MDTB is higher, its heat transfer rate was only found to be 2.2 % to 0.44 % higher than that of CDTB, as the ambient air temperature increased from 32 °C to 44 °C. This smaller performance difference was a result of lower temperature difference between steam and inside tube wall in MDTB, since heat transfer rate was defined by Eq. (8.10). Moreover, from Figure 8.76, it is evident that, as the ambient air temperature increased from 32 °C to 44 °C, the performance of both bundles decreased.

$$Q = h_c A_{sT}(T_v - T_{wi}) \tag{8. 10}$$

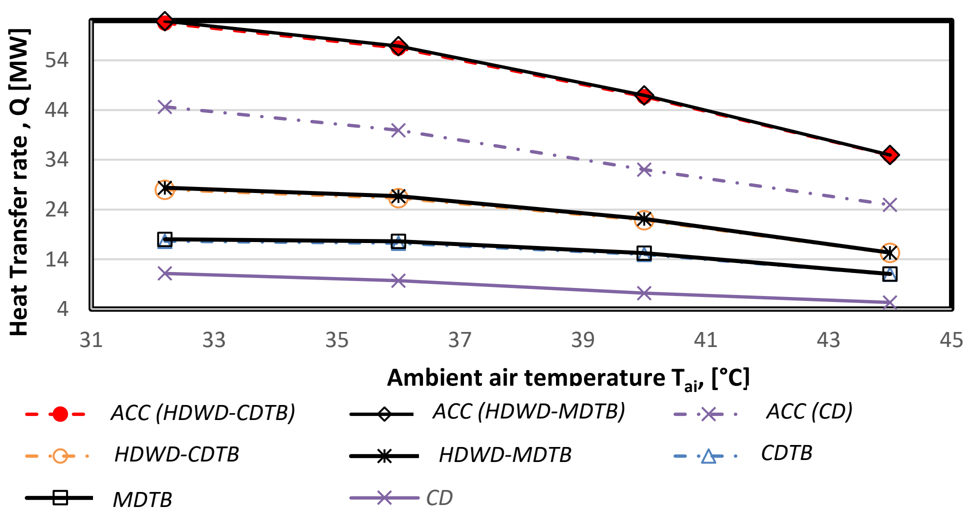

Figure 8. 76: Effect of the ambient air temperature on the heat transfer rate of tube bundles

Since the total heat transfer rate for HDWD incorporated with either CDTB or MDTB were sum of first and second stage, the performance of HDWD (MDTB) was found to be higher with the same percentage (%), as that of MDTB performance when it was compared to CDTB performance. While, on a system level, an ACC incorporated with the HDWD

(CDTB or MDTB) attained 27 % to 31 % heat transfer rate greater than that of ACC incorporated with CD.

8.5.2. Air-side Pressure Drop

The air-side flows for both tube bundles were treated as a flow over the flat tube, and both local and average friction coefficients were determined by the formulas, presented in Yunus and Afshin (2011). As indicated in Figure 8.77 (a), at bundle level, the air-side pressure drop was found to increase with ambient air temperature, and the variations in air-side pressure drop for the two tube bundles were insignificant. However, with a closer look, the air-side pressure drop for CDTB was less than that of MDTB. This was as a result of a slightly higher outlet air temperature at the exit of MDTB than at CDTB exit. A higher outlet air temperature led to a higher air mean temperature in the bundle, which consequently, resulted in a lower air mean density, and in turns in a slightly increased the air mean velocity.

At component and system level, Figure 8.77 (b, c), the air-side pressure drop comprises of pressure drop in first and second stages, and HDWD and primary condenser units. In first stage and primary condenser units, it was found that, as the ambient air temperature increased, the air-side pressure drop decreased. This was due to the decrease of the air density as its temperature increases, which was sequential resulted in air mass flow rate and fan static pressure dropping. However, if the study was conducted at constant air mass flow rate, air-side pressure drop was found to increase as the ambient air temperature increased. Hence, due to mentioned reasons, the air-side pressure drop at component level was found to increase as the ambient air temperature increased from 32 ℃ to 36 ℃, and beyond that, it started to decrease as the ambient air temperature increased. While at system level, it was found to decrease as the ambient air temperature increases.

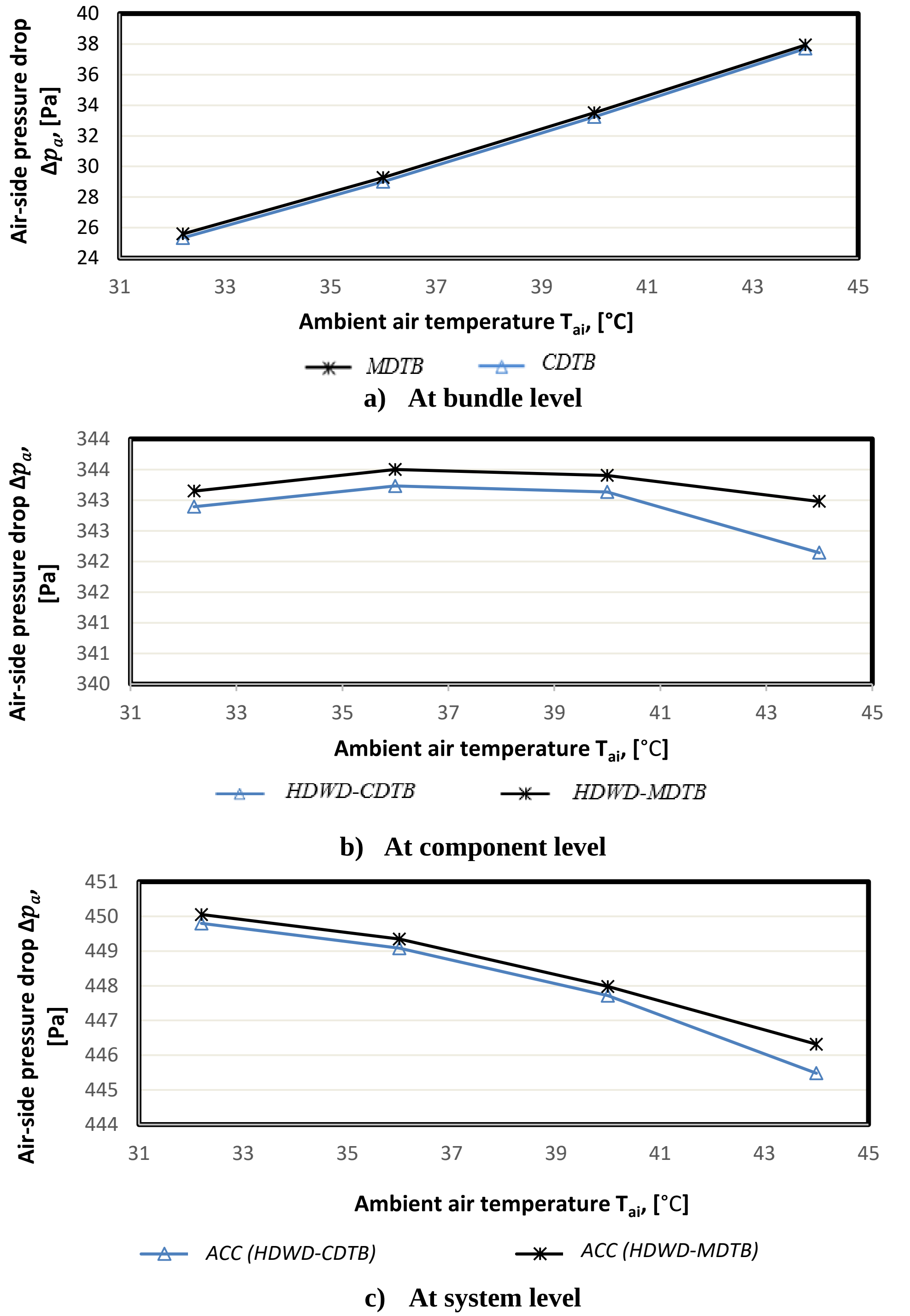

Figure 8. 77: Effect of the ambient air temperature on the air-side pressure drop

8.5.3. Steam-side Frictional Pressure Drop

The steam-side pressure changes mainly due to the effects of the friction, momentum and gravitation force through the bundle tubes. The tubes, in the considered bundles, were arranged horizontal. Therefore, only the frictional effect was taken into account as a main contributor to the steam-side pressure changes in the bundles.

As shown in Figure 8.78 (a), the frictional steam-side pressure drop was found to be higher in MDTB than in CDTB, and increased with ambient air temperature. This was due to the fact that, the hydraulic diameter for the tube's channels in MDTB was about 56 times smaller than that of CDTB tubes, hence its frictional steam-side pressure drop was significantly higher. Furthermore, the steam entering both bundles from first stage increased with ambient air temperature, and the steam velocity at the bundles entrance tends to increase, which leads to higher friction factor, and sequentially to greater frictional steam-pressure drop. The higher frictional steam-pressure drop at bundle level has a significant effect on the steam-pressure drop at both component and system level as indicated in Figure 8.78 (b).

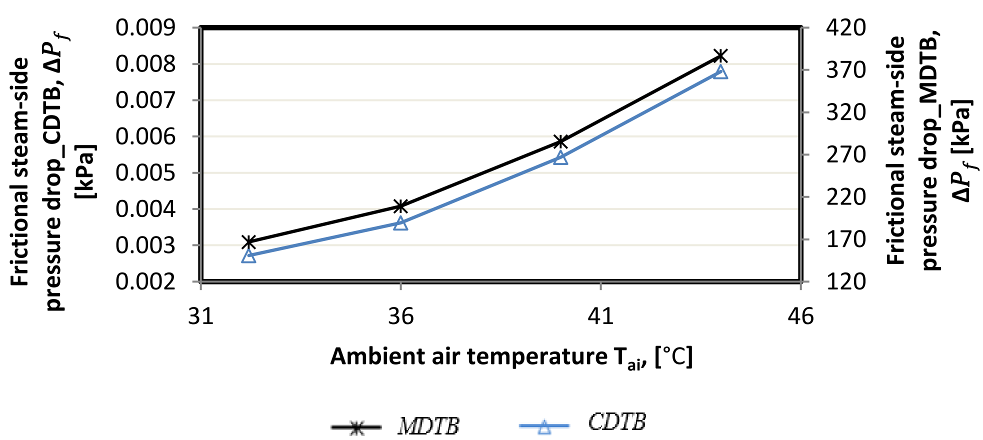

a) At bundle level

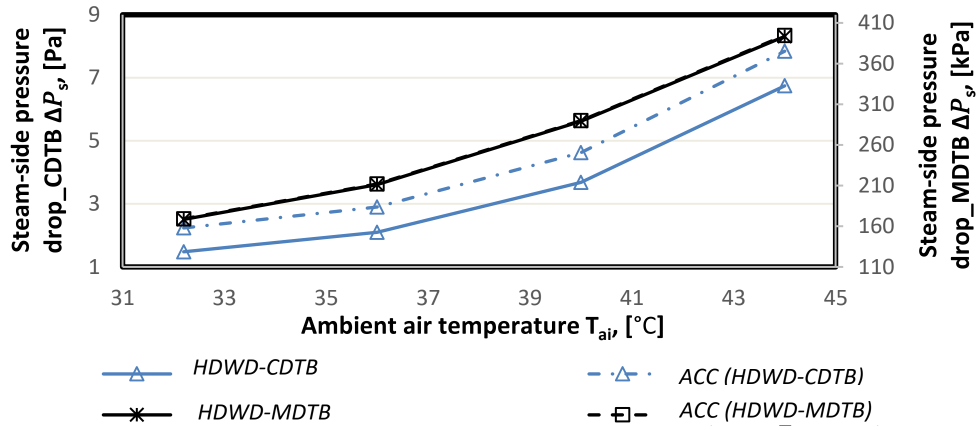

b) At component and system level

Figure 8. 78: Effect of the ambient air temperature on the steam-side pressure drop

8.5.4. Condensing Pressure

The condensation rate depends primarily on the vapor pressure. Therefore, higher concentration of water vapor in the tubes, results in an increasing vapor pressure. The rate at which the heat is released when condensing steam can be expressed as:

$$Q = m_c i_{fg} \tag{8. 11}$$

If the ambient air temperature of 32 °C is taken as a baseline, Figure 8.79 shows that, as the ambient air temperature increased from 32 °C to 44 °C, the rate of condensation and heat transfer decreased by 0 to 43.35 %. As a consequence, the steam pressure reduced by 0 to 9.85 % and the corresponding enthalpy of condensation increased by 0 to 0.23 %. Furthermore, the increasing of the enthalpy of condensation was due to the fact that the reduction of rate of condensation was slightly dominant compare to the decreased heat transfer rate. Moreover, as depicted in Figure 8.80, the condensing pressure of the systems incorporated with HDWD (CDTB or MDTB) were found to be closer to each other, and lower, when were compared to that of the system incorporated with CD. For both systems, the condensing pressure increased with the ambient temperature as it increased from 32 °C to 36 °C, and beyond 36 °C, it started to decrease as the ambient temperature increased.

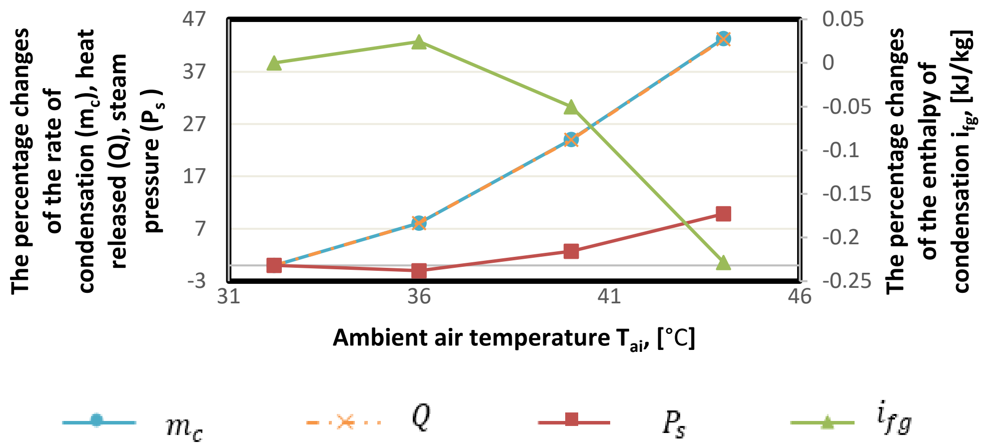

Figure 8. 79: The percentage changes of the rate of condensation, heat released, steam pressure and the corresponding enthalpy of condensation with ambient air temperature.

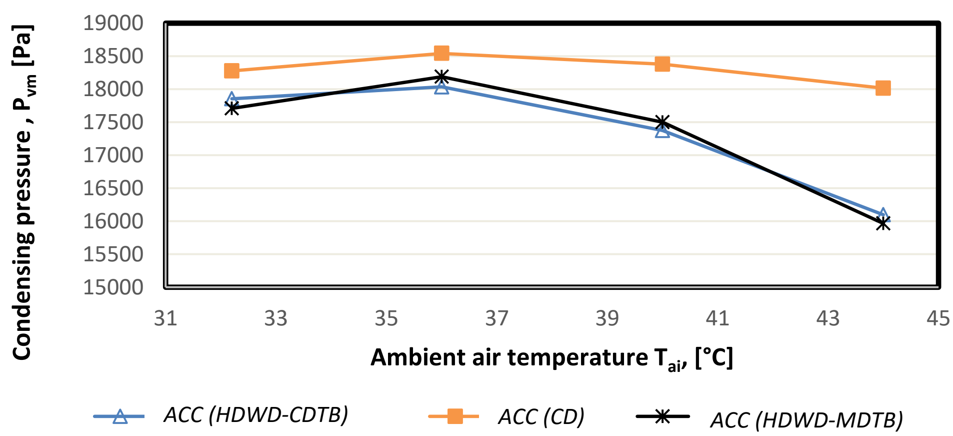

Figure 8. 80: Effect of the ambient air temperature on the condensing pressure

8.5.5. ACC Exit Pressure

The condenser creates a vacuum which extracts more steam from low pressure turbine exhaust, and thus create a suction natural phenomenon. For easier steam flow and more extraction of work from the steam in the turbine, a vacuum in the ACC is maintained. This means, the condenser should condense the steam to the temperature below the atmospheric pressure (Singh *et al.*, 2014). For the considered generating unit, the ACC vacuum pressure is in the range of 3 to 6 Inch Mercury (0.102 to 0.2032 bar). Beyond this vacuum pressure range (lower vacuum), the temperature and pressure at the turbine exit increase, and the turbine may vibrate, this may lead to the trips-off of the generating unit, and therefore, the running-up of unit could restart from the beginning. The unit running-up is an intensive fuel consumption process, hence operation cost increases. Lower vacuum pressure may be caused by high ACC load and ambient temperature. Therefore, it is advisably and beneficial to operate the condenser at the highest vacuum pressure (lowest pressure). However, too high vacuum pressure can lead to the higher leakage of the atmospheric gas (non-condensable gases) in the condenser. The non-condensable gases occur in the heat transfer area inside the tubes, which leads to the reduction of the heat transfer rate. Furthermore, high vacuum pressure may account for the vacuum level prevailing at turbine outlet, which can lead to plant output reduction (Donovan *et al.*, 2012).

Figure 8.81 shows that, all the considered systems, achieved high vacuum pressure, which as expected decreased as the ambient air temperature increased. However, the highest vacuum pressure was attained in the system incorporated with MDTB. This signified smaller pressure at the exit of systems incorporated with MDTB than that of the system incorporated with CDTB.

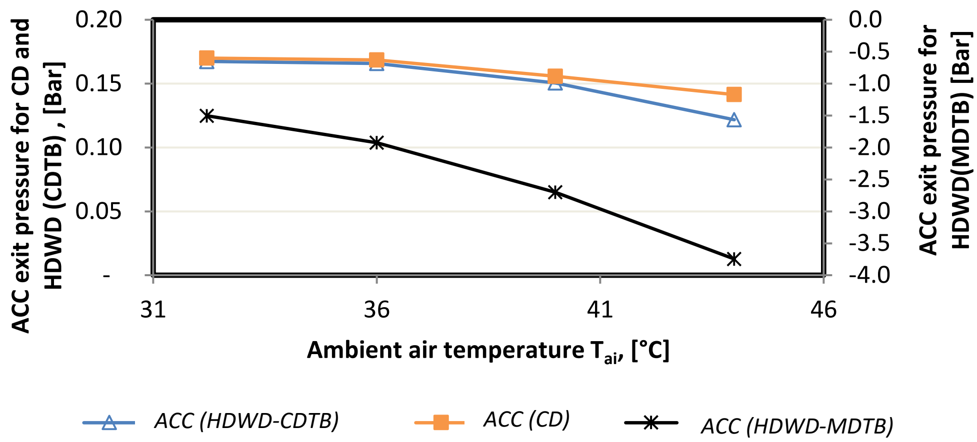

Figure 8. 81: Effect of the ambient air temperature on on ACC exit pressure

8.5.6. Steam Turbine Performance Characteristics

The steam turbine power output depends on ACC performance, since the ACC maintains the turbine exit pressure constant at optimum pressure or at lower pressure than designed. However, ACC performance is adversely affected by high ambient air temperature. The steam turbine exit pressure increased as the ambient air temperature increased (Figure 8.82). The increasing of the steam turbine exit pressure decreased the pressure difference across the last turbine stage, and as results, the enthalpy difference across the last turbine stage (Figure 8.83) reduced too. Hence, the turbine power output decreased (Figure 8.84). For the considered generating unit, the optimum turbine exit pressure was 19.62 kPa. Therefore, the ACC should maintain the turbine exit pressure at this value or lower.

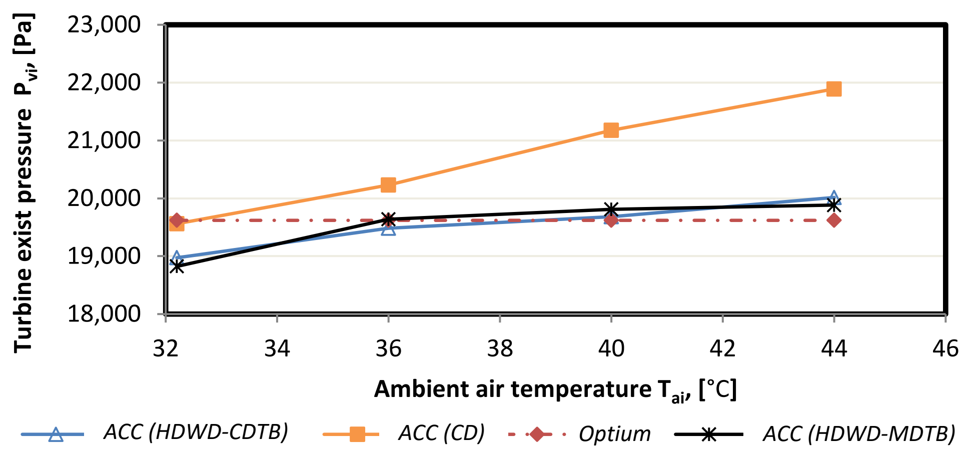

Figure 8. 82: Effect of the ambient air temperature on the turbine exit pressure

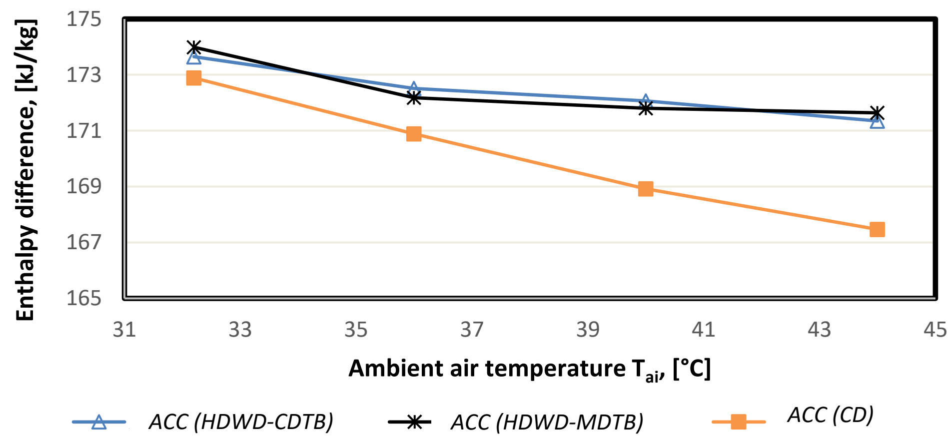

Figure 8. 83: Effect of the ambient air temperature on the enthalpy difference across the last turbine stage

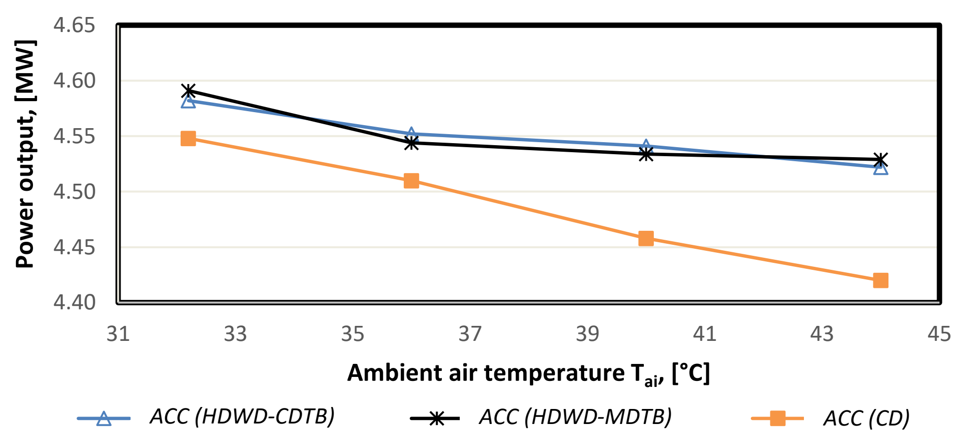

Figure 8. 84: Effect of the ambient air temperature on the last turbine stage power output

As depicted in Figure 8.82, for all systems, the steam turbine exit pressure increased with ambient air temperature. However, for systems with ACC incorporated with HDWD, the steam turbine exit pressure increased at lower pace and closer to the optimum turbine exit pressure as indicated by dashed line in Figure 8.82, when it is compared with the system that had ACC incorporated with CD.

At ambient temperatures up to 36 ℃, the systems with ACC incorporated with HDWD maintained the turbine exit pressure below the optimum. While the systems, with ACC incorporated with CD, maintained the turbine exit pressure at the optimum, only when the ambient temperature was equal to the design operating value (32.2 ℃). Above this value, the turbine exit pressure was beyond the optimum value. It can be seen that, the turbine exit pressure for the system, when MDTB was incorporated into HDWD, was lower and closer to the optimum value.

Similarly, as shown in Figure 8.85, for turbine output power at ambient temperatures up to 36 ℃, the systems with ACC incorporated with HDWD allows the turbine to produce output power which is greater than the maximum. As the ambient air temperature increased from 36 ℃ to 44 ℃, the turbine output power for the systems incorporated with CDTB and MDTB reduced by 0.013 % to 0.11 % and 0.043 % to 0.089 %, respectively. When the systems with ACC incorporated with CD was considered, the turbine output power reduced by 0.15 % to 0.45 %. The turbine net power, is shown in Figure 8.86, and the changes in net power for all the systems have same trends as those of turbine output power shown in Figure 8.85.

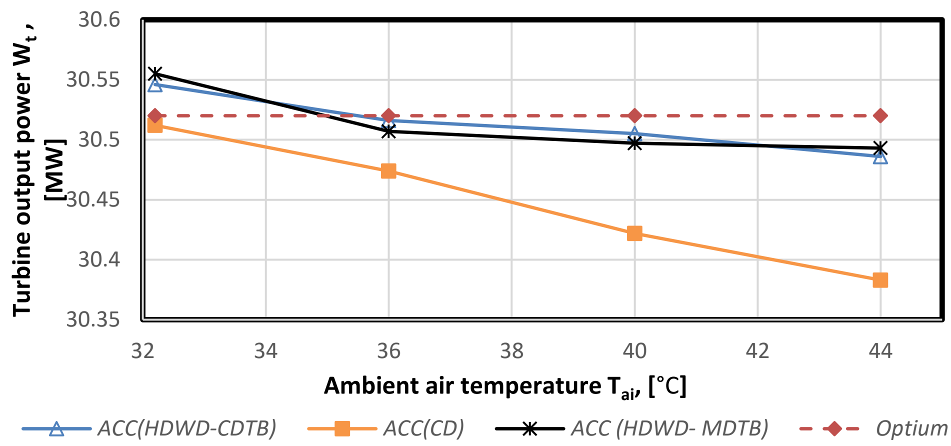

Figure 8. 85: Effect of the ambient air temperature on the turbine output power

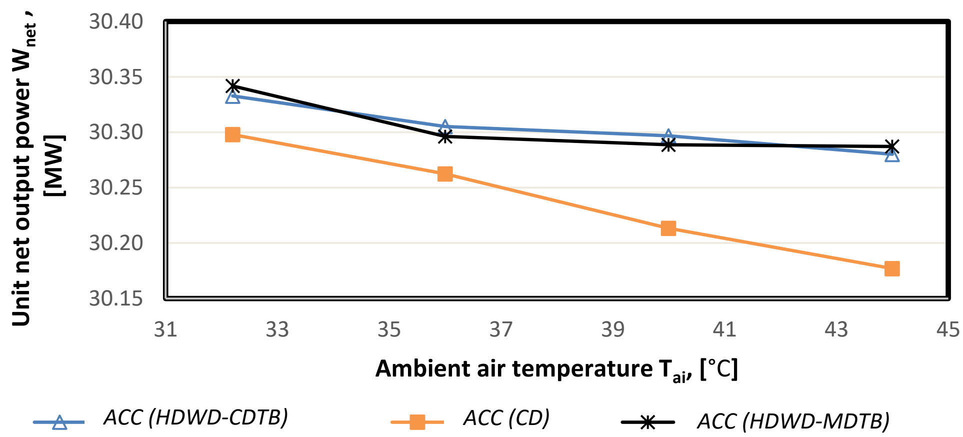

Figure 8. 86: Effect of the ambient air temperature on the plant net output power

Chapter 9: Statistical Analysis of Performance Data

The thermal performance data of CDTB and MDTB at both bundle, component, and system levels were subjected to statistical analysis to test the hypotheses, as well as to signify the differences in thermal performances of the two bundles at a significance level of 0.05. Since, the two samples were considered and compared, the two-sample, two tailed, paired T-Test for means was employed for statistical analysis. The compared data were obtained from two different bundles, therefore, the two-sample T-test was used. Furthermore, both one and two – tailed T-test were considered, since it is required to know whether the performance of the two bundles differ (two-tailed), as well as whether, the MDTB performs better than CDTB (one-tailed). Moreover, since the thermal performance data were obtained at certain air temperatures, the paired T-test was taken into account.

The T-test was carried out in Excel. The p-values were used to define whether the results of hypothesis test are statistically significant. The difference between the means is statistically significant if the p-value is smaller than level of significance (0.05). Therefore, when the obtained p-value is smaller than 0.05 (level of significance), the null hypothesis of the thermal performance was rejected. Since, the Two-tailed tests that can distinguish differences in either direction was considered, the results of the p-values for the two-tailed form ($P(T<=t)$) of the t-test were used.

9.1. At bundle level

The heat transfer rates of CDTB and MDTB, as depicted in Tables 6.4 and 7.5 respectively, were subjected to a T-test analysis, and the results are shown in Table 9.1.

Table 9. 1: T-Test: Performance data of CDTB and MDTB at bundle level

Bundle	CDTB	MDTB
Mean	15.22	15.48
Variance	9.28	10.25
Observations	4	4
Pearson Correlation	0.999	
Hypothesized Mean Difference	0	
df	3	
t Stat	-3.43	
P(T<=t) one-tail	0.021	
t Critical one-tail	2.35	
P(T<=t) two-tail	0.042	
t Critical two-tail	3.18	
SD	3.05	3.20

The difference in heat transfer rates of CDTB (Mean = 15.22; SD = 3.05) and MDTB (Mean = 15.48; SD = 3.12) was significant (t (3) = -3.43; p = 0.042). The obtained p-value was smaller than 0.05 level of significance, therefore, the null hypothesis (H_{02}) of the thermal performance (heat transfer rate) of MDTB being not higher than that of CDTB at bundle level was rejected.

9.2. At component level

The heat transfer rates of HDWD incorporated with CDTB and MDTB, as depicted in Tables 6.5 and 7.6 respectively, were subjected to a T-test analysis. Furthermore, CD heat transfer rate (Table 5.6) was compared to that of HDWD incorporated with CDTB. The results of tests are presented in Tables 9.2 and 9.3.

Table 9. 2: T-Test: Performance data of CDTB and MDTB at component level

Component	HDWD (CDTB)	HDWD (MDTB)
Mean	22.87	23.13
Variance	32.25	34.02
Observations	4.00	4.00
Pearson Correlation	1.00	
Hypothesized Mean Difference	0.00	
df	3.00	
t Stat	-3.43	
P(T<=t) one-tail	0.02	
t Critical one-tail	2.35	
P(T<=t) two-tail	0.04	
t Critical two-tail	3.18	
SD	5.68	5.83

The difference in heat transfer rates of HDWD (CDTB) (Mean = 22.87; SD = 5.68) and HDWD (MDTB) (Mean = 23.13; SD = 5.83) was significant (t (3) = -3.43; p = 0.004). The obtained p-value was smaller than 0.05 level of significance, therefore, the null hypothesis (H_{02}) of the thermal performance (heat transfer rate) of MDTB being not higher than that of CDTB at component level was rejected.

Table 9. 3: T-Test: Performance data of HDWD (CDTB) and CD at component level

Component	HDWD (CDTB)	CD
Mean	22.87	8.35
Variance	32.25	6.78
Observations	4.00	4.00
Pearson Correlation	0.98	
Hypothesized Mean Difference	0.00	
df	3.00	
t Stat	9.11	
P(T<=t) one-tail	0.0014	
t Critical one-tail	2.35	
P(T<=t) two-tail	0.0028	
t Critical two-tail	3.18	
SD	5.68	2.60

The difference in heat transfer rates of HDWD (CDTB) (Mean = 22.87; SD = 5.68) and CD (Mean = 8.35; SD = 2.60) was significant (t (3) = 9.11; p = 0.0028). The obtained p-value was smaller than 0.05 level of significance, therefore, the null hypothesis (H_{01}) of the thermal performance (heat transfer rate) of HDWD being not higher than that of CD at component level was rejected.

9.3. At system level

The heat transfer rates of ACC incorporated with HDWD (CDTB) and HDWD (MDTB), as depicted in Tables 6.6 and 7.7 respectively, were subjected to a T-test analysis. Furthermore, the ACC incorporated with CD heat transfer rate (Table 5.8) was compared to that of ACC incorporated with HDWD (CDTB). The results of tests are presented in Tables 9.4 and 9.5.

Table 9. 4: T-Test: Performance data of CDTB and MDTB at system level

System	ACC-HDWD (CDTB)	ACC-HDWD (MDTB)
Mean	49.90	50.17
Variance	137.54	141.13
Observations	4.00	4.00
Pearson Correlation	1.00	
Hypothesized Mean Difference	0.00	
df	3.00	
t Stat	-3.43	
P(T<=t) one-tail	0.02	
t Critical one-tail	2.35	
P(T<=t) two-tail	0.04	
t Critical two-tail	3.18	
SD	11.73	11.88

The difference in heat transfer rates of ACC incorporated with HDWD (CDTB) (Mean = 49.90; SD = 11.73) and ACC incorporated with HDWD (MDTB) (Mean = 50.17; SD = 11.88) was significant (t (3) = -3.43; p = 0.04). The obtained p-value was smaller than

0.05 level of significance, therefore, the null hypothesis (H_{02}) of the thermal performance (heat transfer rate) of ACC incorporated with HDWD (MDTB) being not higher than that of ACC incorporated with HDWD (CDTB) at system level was rejected.

Table 9. 5: T-Test: Performance data of HDWD-CDTB and CD at System level

System	ACC-HDWD (CDTB)	ACC-CD
Mean	49.90	35.39
Variance	137.54	75.48
Observations	4.00	4.00
Pearson Correlation	1.00	
Hypothesized Mean Difference	0.00	
df	3.00	
t Stat	9.11	
P(T<=t) one-tail	0.001	
t Critical one-tail	2.35	
P(T<=t) two-tail	0.003	
t Critical two-tail	3.18	
SD	11.73	8.69

The difference in heat transfer rates of ACC incorporated with HDWD (CDTB) (Mean = 49.90; SD = 11.73) and ACC incorporated with CD (Mean = 35.39; SD = 8.69) was significant (t (3) = 9.11; p = 0.003). The obtained p-value was smaller than 0.05 level of significance, therefore, the null hypothesis (H_{01}) of the thermal performance (heat transfer rate) of ACC incorporated with HDWD (CDTB) being not higher than that of ACC incorporated with CD at system level was rejected.

Chapter 10: Conclusions and Recommendations

In this study the models for CDTB, CD, MDTB thermal performance analysis were developed and validated. The thermal performance of an induced draft HDWD incorporated with CDTB into its second stage was compared to that of CD at both component and system levels. Furthermore, the CDTB thermal performance was compared to that of MDTB at bundle, component and system levels.

10.1. CDTB Models Development

The one-dimensional (1D) analytical and two-dimensional (2D) numerical models that were employed to analyse the thermal performance of the CDTB were developed. For both 1D and 2D models, the governing equations were derived by applying the mass and energy balance to the control volumes taken around the bundle's tubes. The 1D analytical model was developed and solved based on Poppe, Merkel as well as heat and mass transfer analogy methods of analysis, while 2D numerical model was developed and solved based on heat and mass transfer analogy method of analysis.

By comparing the Merkel solutions to Poppe solutions, the outlet air temperature and humidity ratio were found to be 0.24 % and 1.22 % higher and lower, respectively. While by comparing the heat and mass transfer analogy solutions to Poppe solutions, the outlet air temperature and humidity ratio were found to be 0.06 % and 3.2 % lower, respectively. Due to the fact that Merkel method assumes saturated air output, the outlet air humidity ratio supposed to be higher than that of Poppe method, however, this is not a case in this study. By comparing the Merkel and heat and mass transfer analogy solutions to Poppe solutions, 2.94 % and 8.99 % differences in heat transfer rate were achieved, respectively. This is due to the fact that, the deluge water evaporation rate is believed to be higher when Lewis factor is smaller, which results in higher latent heat transfer. The Lewis factor for Poppe method was found to be less than a unity, while the Merkel method assumes that the Lewis factor is equal to one. Hence, the slight inconsistencies between solutions were mainly due to the assumptions made in Merkel model.

The heat transfer rate and air-side pressure drop obtained from one-dimensional model were found to be 4.83 % and 1 % higher than that obtained from two-dimensional model. The differences between one- and two-dimensional solutions were primarily due to the variation of air and water properties in two-dimensional model. Hence, with these slight differences it can be concluded that, the two-dimensional model is valid for the analysis of the thermal performance of a CDTB. Furthermore, it was concluded that, using either model, did not affect the thermal performance of a CDTB that much. Furthermore, by comparing the current model results to that of Angula (2015), slight differences were found. Therefore, it can be also concluded that, considering the tube round-ends to be as flat ends, does not has much impact the thermal performance of the tube bundle.

10.2. Optimization and geometric parameter's adjustment

The best configuration for the HDWD second stages tube bundle (CDTB), as well as the overall size of HDWD that can replace the CD in an existing ACC system of the local considered generating unit were identified through design optimization and geometric parameters adjustment, using the validated 2D model. As the tube pitch varied from 25 mm to 38 mm, the TPI of CDTB decreased by 19 %. Furthermore, at smaller tube pitches (e.g. 25 mm), both heat transfer and air-side pressure drop were found to be around 1.4 times that of DRTB.

As the CDTB ‘1’ width changed from 2870 mm to 2320 mm, the heat transfer rate and air-side pressure drop decreased and increased by 15 % and 20 %, respectively. While, as the CDTB ‘2’ length changed from 2500 mm to 3178 mm, the heat transfer rate and air-side pressure drop increased and decreased by 21 % and 13 %, respectively. Moreover, as the CDTB ‘3’ steam flow area reduced from 0.368 m^2 to 0.142 m^2, the heat transfer rate and air-side pressure drop increased and decreased by 0.3 % and 11 %, respectively. However, the outside tube width decreased with steam flow area, which may lead to manufacturing complications. Hence the final tube height was adjusted to 300 mm.

10.3. HDWD incorporated with CDTB thermal performance

The HDWD thermal performance, at component and system level, was evaluated. As the ambient air temperature increased from 32,2 ℃ to 44 ℃, the heat transfer rate for HDWD 1st stage tube bundle, CDTB and ACC system incorporated with HDWD decreased by 59 %, 38 % and 43 %, respectively. While, the air-side pressure drop and fan power both were found to decrease as the ambient air temperature increased, however, this was due to the fact that, the analysis was not conducted at constant air mass flow rate, at which the opposite results were obtained. The steam-side pressure drop of HDWD and ACC system incorporated with HDWD were found to increase by 78 % and 75 %, respectively as the ambient air temperature increased from 32,2 ℃ to 44 ℃. The HDWD and ACC system incorporated with HDWD condensing pressures were found to decrease as the ambient air temperature increased. This is because the inlet mass flow rate to HDWD was not constant, but rather increasing with ambient air temperature. The turbine exhaust pressure for the considered generating unit, increased by 5.5 % as the ambient air temperature increased from 32,2 ℃ to 44 ℃. This resulted in reduction of the pressured difference across the turbine, and therefore leads to the reduction of turbine output power.

10.4. CD thermal performance

The CD unit's performance was outlined through the thermal performance evaluation of ACC system, which was achieved by modelling it's the cold-end system. It was found that the model accurate predicts the ACC and steam turbine end-stage performance. Furthermore, through sensitivity analysis, the ACC performance was found to be badly affected as the ambient air temperature increases beyond the design value. This can be corrected or offset by increasing the fan speed, however increasing the fan speed leads to higher fan power consumption which reduces the net power output of the generating unit.

The heat transfer rate of the CD was found to decrease by around 37 % as the ambient air temperature varied from 32,2 ℃ to 40 ℃, and as a result the outlet air temperature increased. Furthermore, both air-side pressure drop and fan power were found to increase with both ambient air temperature and fan speed. The total steam-side pressure drop was found to increase with ambient air temperature; and decreased as the fan speed increased. The turbine output power was found to decrease as the ambient air temperature increased, and increase as the fan speed increased. However, the net turbine output power was found to decrease as the ambient air temperature increased.

10.5. CD and HDWD Thermal Performance Comparison.

The CD performance data which were obtained at different ambient air temperatures when the CD was operating at design conditions were compared to that of HDWD incorporated with CDTB. The performances data comparison was performed at both component and system levels. At component level, as the ambient air temperature increased, the heat transfer rate of HDWD incorporated with CDTB was found to be 2.5 to 3 times that of CD. At system level, an ACC incorporated with the HDWD provided 27 % to 31 % heat transfer rate greater than that of the ACC incorporated with CD. At ambient temperatures up to 36 ℃, the system with ACC incorporated with HDWD maintained the turbine exit pressure below the optimum. While the system, with ACC incorporated with CD, maintained the turbine exit pressure at the optimum, only when the ambient temperature was equal to the design operating value (32.2 ℃).

10.6. MDTB thermal performance

The thermal performance of the MDTB was analysed. This was achieved by employing the semi-empirical model which make use of existing correlation of Shah and London

(1978) to define friction factor and heat transfer. Furthermore, the model was validated against the experimental data of Doan *et al,* (2020). Both steam-side pressure and heat transfer rate were found to increase as the hydraulic diameter decreased by 95 % and 1.5 %, respectively. It was also essential to determine the TPI in order assess the overall performance of the MDTB. The TPI was found to increase with the hydraulic diameter.

10.7. MDTB and CDTB Thermal Performance Comparison

The thermal performance comparison of the CDTB and MDTB at bundle, component and system levels was carried out. The condensation heat transfer coefficient in MDTB was found to be higher with 29 % to 19 % than that of CDTB, and it was found to decrease as the ambient air temperature increased. Although, the heat transfer coefficient in MDTB is higher, its heat transfer rate was only found to be 2.2 % to 0.44 % higher than that of CDTB, as the ambient air temperature increased from 32 ℃ to 44 ℃. This smaller performance difference was a result of lower temperature difference between steam and inside tube wall in MDTB, since heat transfer rate. The frictional steam-side pressure drop was found to be higher in MDTB than in CDTB, and increased with ambient air temperature. As the ambient air temperature increased from 36 ℃ to 44 ℃, the turbine output power for the systems incorporated with CDTB and MDTB reduced by 0.013 % to 0.11 % and 0.043 % to 0.089 %, respectively.

10.8. Statistical analysis on the tube bundles performance data

The hypotheses of the study were tested using a T-test statistical tool. For all the performance data considered and compared, the computed p-values were found to be smaller than the level of significance of 0.05. Hence, all the null hypotheses were rejected.

10.9. Recommendation for future work

Future works that can be conducted as an extension of this study are:

1. Computational Fluid Dynamics (CFD) simulation of CD, CDTB and MDTB thermal performances.
2. The consideration of scale effects such as surface roughness, surface tension gradients, axial conduction, slip condition, viscous dissipation on the MDTB performance evaluation.
3. The equipment selection and economic analysis of HDWD.

References

Abdel-Baky, M., Mousa, M. and Koraim, A.-F., 2020. An Investigation of Using Michrochannel Condenser to Improve the Performance of Air Conditioning Unit. *ERJ. Engineering Research Journal*, 43(4), pp. 293–304.

Adams, T. M., Abdel-Khalik, S. I., Jeter, S. M., Qureshi, Z. H., 1997. An experimental investigation of single-phase forced convection in microchannels. *International Journal of Heat and Mass Transfer*, 41(6–7), pp. 851–857.

Ahmad, T. and Hassan, I., 2010. Experimental Analysis of Microchannel Entrance Length Characteristics Using Microparticle Image Velocimetry. *Journal of Fluids Engineering*, 132(4), p. 041102.

Al-zaidi, A. H., Mahmoud, M. M. and Karayiannis, T. G., 2018. Condensation fl ow patterns and heat transfer in horizontal microchannels. *Experimental Thermal and Fluid Science*, pp. 153–173.

Ali, A. A., Hasan, M. I. and Adnan, G., 2019. Numerical Investigation of Rougness Effects on Hyderdynmic and Thermal Performance of Counter Flow Microchannel Heat Exchanger. *Al-Qadisiyah Journal for Engineering Sciences*, 11(4), pp. 426–445.

Anderson, N. R., 2014. Evaluation of the performance characteristics of a hybrid (dry / wet) induced draft dephlegmator. *Master Thesis*, University of Stellenbosch, RSA.

Angula, E., 2015. Numerical performance evaluation of a delugeable flat bare tube air-cooled steam condenser bundle. *Master Thesis, Stellenbosch University, RSA.*

Angula, E., 2018. Modelling of a delugeable flat bare tube bundle for an air-cooled steam condenser. *EPH - International Journal of Science And Engineering*, (5).

Bandhauer, T. M., A. Agarwal and S. Garimella, 2006. Measurement and Modeling of Condensation Heat Transfer Coefficients in Circular Microchannels. Journal of Heat Transfer. Vol. 128(10), pp. 1050-1059

Başaran, A. and Yurddaş, A., 2021. Thermal modeling and designing of microchannel condenser for refrigeration applications operating with isobutane (R600a). *Applied Thermal Engineering*, 198.

Bejan, A., 2004. *Convection Heat Transfer*. New Jersey: John Wiley & Son, Inc.

Bosjnakovic, F., 1965. Technical thermodynamics', in. New York: Holt, Reinhart and Winston, pp. 326–331.

Catton, I. 2010. *Optimization of Heat Exchangers*, *Optimization of Heat Exchangers*.

Charles, K. and David, C., 2002. Assessment of Evaporative Cooling Enhancement Methods for Air-Cooled Geothermal Power Plants. *National Renewable Energy Laboratory (NREL/CP-550-32394).*

Chen, S., Z. Yang, Y. Duan, Y. Chen and D. Wu, 2014. Simulation of Condensation Flow in a Rectangular Microchannel, Chemical Engineering and Processing: Process Intensification. (76), pp. 60-69

Chen, C.-W., Yang, C.-Y. and Hu, Y.-T., 2013. Heat Transfer Enhancement of Spray Cooling on Flat Aluminum Tube Heat Exchanger. *Heat Transfer Engineering*, 34(1), pp. 29–36.

Cheng, L. and Xia, G., 2017. Fundamental issues , mechanisms and models of flow boiling heat transfer in microscale channels. *International Journal of Heat and Mass Transfer*, 108, pp. 97–127.

Churchill, S. W., 1977. Friction-fact or equation spans all fluid flow regimes. *Chemical Engineering*, 84, pp. 91–92.

Corberán, José M, Fernández de Córdoba, P., Ortuno, S., Ferri, V., Montes, P., 2000. Detailed modelling of evaporators and condensers. *Proceedings of the 8th International Refrigeration and Air Conditioning Conference*, pp. 217–224.

Dang, T. T., Teng, J. T. and Chu, J. C., 2010. A study on the simulation and experiment of a microchannel counter-flow heat exchanger. *Appllied Thermal Engineering*, 30, pp. 2163–2172.

Derby, M., Lee, H. J., Peles, Y., Michael J. K., 2012. Condensation heat transfer in square, triangular, and semi-circular mini-channels. *International Journal of Heat and Mass Transfer*, 55(1–3), pp. 187–197.

Dittus, F. W. and Boelter, L. M. K., 1930. Heat Transfer in Automobile Radiators of Tubular Type. *In: Univ. California, Berkeley, Publ. Eng*, 2(13), pp. 443–461.

Doan, M., Le, T., Dang, T., Teng, J., 2017. A Numerical Simulation on Phase Change of Steam in a Microchannel Condenser. *International Journal of Power and Energy Research*, 1(2).

Doan, M., Dang, T. and Nguyen, X., 2020. The effects of gravity on the pressure drop and heat transfer characteristics of steam in microchannels: An experimental study. *Energies*, 13(14).

Dobson, M. K. and Chato, J. C., 1998. Condensation in smooth horizontal tubes. *ASME Journal Heat Transfer*, 120, pp. 193–213.

Donovan, O. A., Grimes, R., Walsh, E. J., Moore, J., Reams, N., 2012. Steam-side characterisation of a modular air-cooled condenser. *ASME International Mechanical Engineering Congress and Exposition*, *Proceedings (IMECE)*, (PARTS A AND B), pp. 1719–1730.

Ducoulombier, M., Colasson, S., Haberschill, P., Tingaud, F., 2011. Charge reduction experimental investigation of CO2 singlephase flow in a horizontal micro-channel with constant heatflux conditions. *International Journal of Refrigeration*, 36, pp. 827–833.

Fayyadh, E. M., Mahmoud, M. M. and Tassos G., K., 2015. Flow Boiling Heat Transfer of R134a in Multi Micro Channels. *Proceedings of the World Congress on Mechanical, Chemical, and Material Engineering (MCM)*, pp. 1–13.

Fesanghary, M., Damangir, E. and Soleimani, I., 2009. Design optimization of shell and tube heat exchangers using global sensitivity analysis and harmony search algorithm. *Applied Thermal Engineering*, 29(5–6), pp. 1026–1031.

Filonenko, G. K., 1954. Hydraulic resistance in pipes, Heat Exchanger Design Handbook. *Teploenergetica*, 1, pp. 40–44.

Fiorentino, M. and Starace, G., 2017a. Experimental Investigations on Evaporative

Condensers Performance. *Energy Procedia*, 140(May), pp. 458–466.

Fiorentino, M. and Starace, G., 2017b. The Design of Countercurrent Evaporative Condensers with the Hybrid Method. *Applied Thermal Engineering*, 130.

Fung, C. K. and Majnis, M. F., 2019. Computational fluid dynamic simulation analysis of effect of microchannel geometry on thermal and hydraulic performances of micro channel heat exchanger. *Journal of Advanced Research in Fluid Mechanics and Thermal Sciences*, 62(2), pp. 198–208.

Gadhamshetty, V., Nirmalakhandan, N., Myint, M. & Ricketts, C., 2006. Improving aircooled condenser performance in combined cycle power plants. *Journal of Energy Engineering*, 132 (2), p. 81 – 88.

Galvis, E., Yarusevych, S. and Culham, J. R., 2012. Incompressible Laminar Developing Flow in Microchannels. *Journal of Fluids Engineering*, 134(1), p. 014503.

Gao, P., Le Person, S. and Favre-Marinet, M., 2002. Scale effects on hydrodynamics and heat transfer in two-dimensional mini and microchannels. *International Journal of Thermal Sciences*, 41(11), pp. 1017–1027.

GEA, 1978. *Air-Cooled Steam Condensing Plant for Van Eck Power Station*.

Ghajar, M. and Darabi, J., 2014. Evaporative heat transfer analysis of a micro loop heat pipe with rectangular grooves. *International Journal of Thermal Sciences*, 79, pp. 51–59.

Gnielinski, V., 1976. New equations for heat and mass transfer in turbulent pipe and channel flow. *International Chemical Engineering*, 16, pp. 359–368.

Graaff, H., 2017. Performance Evaluation of a Hybrid (dry/wet) Cooling System. *Master of Engineering (Mechanical),* Stellenbosch University, RSA.

Groenewald, W., 1993. Heat Transfer and Pressure Change in an Inclined Air-cooled Flattened Tube During Condensation of Steam. *Master Thesis*, University of Stellenbosch, Stellenbosch, RSA.

Gunnasegaran, P., Mohammed, H. A., Shuaib, N. H., Rahman, S., 2010. The effect of geometrical parameters on heat transfer characteristics of microchannels heat sink with different shapes. *International Communications in Heat and Mass Transfer*, 37(8), pp. 1078–1086.

Hasan, M. I., Rageb, A. M. A. R. and Yaghoubi, M., 2012. Investigation of a Counter Flow Microchannel Heat Exchanger Performance with Using Nanofluid as a Coolant. *Journal of Electronics Cooling and Thermal Control*, 02(03), pp. 35–43.

Hassani, V., Dickens, J. and Bell, K. J., 2005. The Fin-on-Plate Heat Exchanger: A New Configuration for Air-Cooled Power Plants. *Heat Transfer Engineering*, 26(6).

Heyns, J. A., 2008. Performance characteristics of an air - cooled steam condenser incorporating a hybrid (dry / wet) dephlegmator. *Master Thesis*, University of Stellenbosch, RSA.

Heyns, J. A. and Kröger, D. G., 2012. Performance Characteristics of an Air-Cooled Steam Condenser with a Hybrid Dephlegmator. *R&D Journal of SAIMechE,* 28, pp. 31–36.

Honing, W., 2009. Steam Flow Distribution in Air-Cooled Condenser for Power Plant Application. *Master Thesis*, University of Stellenbosch, RSA.

Hsieh, S., Huang, C. and Pan, J., 2021. Low Reynolds numbers convective heat transfer in single / two-phase roughened microchannels. *Applied Thermal Engineering*, 198(April), p. 117468.

Huang, L., Bacellar, D., Aute, V., Radermacher, R., 2015. Variable geometry microchannel heat exchanger modeling under dry, wet, and partially wet surface conditions accounting for tube-to-tube heat conduction. *Science and Technology for the Built Environment*, 21(5), pp. 703–717.

Huang, W., Chen, L., Wang, W., Yang, L., Du, X., 2020. Cooling Performance Optimization of Direct Dry. *Energies*, 13, 3179.

Jaafarian, M. and Kazemian, M. E., 2017. Performance analysis of a two-stage evaporative cooler. *Mechanics and Industry*, 18(4), pp. 1–8.

Jahangeer, K. A., Tay, A. A. O. and Raisul Islam, M., 2011. Numerical investigation of transfer coefficients of an evaporatively-cooled condenser. *Applied Thermal Engineering*, 31(10), pp. 1655–1663.

Keniar, K., 2020. Analytical Modeling of Condensation in Microchannels With Experimental Validation. *Doctor Dissertation*, G. W. Woodruff School of Mechanical Engineering, Georgia.

Khan, W. A., Culham, J. R. and Yovanovich, M., 2004. Fluid Flow and Heat Transfer from a Cylinder Between Parallel Planes. *Journal of Thermophysics and Heat*

Transfer, 18(3).

Kim, M. and Bullard, C. W., 2000. Air-Side Thermal Performance of Micro-Channel Heat Exchangers Under Dehumidifying Conditions. *International Refrigeration and Air Conditioning Conference*, pp. 119–126.

Kim, S. and Mudawar, I., 2012. International Journal of Heat and Mass Transfer Theoretical model for annular flow condensation in rectangular micro-channels. *International Journal of Heat and Mass Transfer*, 55(4), pp. 958–970.

Korte, C. and Jacobi, A. M., 2001. Condensate Retention Effects on the Performance of Plain-Fin-and-Tube Heat Exchangers: Retention Data and Modeling. *Journal of Heat Transfer*, 123(5), p. 926.

Kröger, D. G., 2004. *Air-cooled Heat exchangers and Cooling Towers: Thermal-Flow Performance Evaluation and Design*. Oklahoma, USA: PennWell Corporation, Tulsa.

Kromhout, J., Goudappel, E. and Pechtl, P., 2001. Economic Optimization of a 540 MW Coal Fired Power Plant Using Thermodynamic Simulation. *VGB Powertech*, 81(11), pp. 43–46.

Laković, M. S., Stojiljkovic, M. M., Lakovic, S. V., Stefanovic, V. P., Mitrović, D. D., 2010. Impact of the cold end operating conditions on energy efficiency of the steam power plants. *Thermal Science*, 14(SUPPL.1).

Li, S., Zhao, Z., Zhang, Y., Zeng, H., Xu W., 2020. Experimental and Numerical Analysis of Condensation Heat Transfer and Pressure Drop of Refrigerant R22 in Minichannels of a Printed Circuit. *Energies*, 13, 6589.

Ling, L., Zhang, Q., Yu, Y., Wu, Y., Liao, S., 2015. Study on Thermal Performance of Micro-Channel Separate Heat Pipe for Telecommunication Stations : Experiment and Simulation. *International Journal of Refrigeration*, 59, pp.198–209.

Lockhart, R. W. and Martinelli, R. C., 1949. Proposed correlation of data for isothermal two-phase, two- component flow in pipes. *Chemical Engineering Progress*, 45(1), pp. 39–48.

Lui, C. W., Ko, H. S. and Gau, C., 2009. Microchannel heat transfer. *INTECH*.

Lydia, A. A. B., 2008. *Numerical Simulation on Microchannel Heat Exchager, Bachelor of Mechanical Engineering (Thermal-fluid), Universiti Teknikal Malaysia Melaka, Malaysia*.

Martı’nez-Ballester, S., Corbera’n, J.-M. and Gonza’lvez-Macia, J., 2013. Instituto de Ingenieria Energetica (Institute for Energy Engineering). *Research Publications* (34).

Masiwal, G., Kumar, P S., Chaudhary, S., 2017. Performance Analysis of Surface Condenser in 525 MW Thermal Power Plant. *International Journal of Engineering and Technology,* 9 (3)

McLellan, J., 2015. Modelling and Optimization Methods for a Microchannel Heat Exchanger. *Master Thesis,* Carleton University, Ottawa, Ontario, Canada.

El Mghaira, H., Asbik, M., Louahlia-gualous, H., Voicu, I., 2014. Condensation heat transfer enhancement in a horizontal non-circular microchannel. *Applied Thermal Engineering*, 64(1–2), pp. 358–370.

Mizushina, T., Ito, R. and Miyashita, H., 1967. Experimental study of an evaporative cooler. *International Chemical Engineering*, pp. 727–732.

Moharana, M. K. and Khandekar, S., 2015. Effect of aspect ratio of rectangular microchannels on the axial back conduction in its solid substrate. *Progress in Microscale and Nanoscale Thermal and Fluid Sciences*, 4(3), pp. 205–224.

Moore, J., Grimes, R., O'Donovan, A., Walsh, E., 2014. Design and testing of a novel air-cooled condenser for concentrated solar power plants. *Energy Procedia*, 49, pp. 1439–1449.

Moreno Quiben, J. and Thome, J. R., 2003. Two-phase pressure drops in horizontal tubes: new results for R-410A snd R- 134a compared to R-22. *International Congress of Refrigeration*, Washington.

Naphon, P. and Arisariyawong, T., 2018. Heat transfer analysis using artificial neural networks of the spirally fluted tubes. *Journal of Research and Applications in Mechanical Engineering*, 4(2), pp. 135–147.

Niitsu, Y., Naito, K. and Anzai, T., 1967. ‘Studies on characteristics and design procedure of evaporative coolers’, *Journal of SHASE, Japan*, 41(12).

O’Donovan, A. and Grimes, R., 2015. Pressure drop analysis of steam condensation in air-cooled circular tube bundles. *Applied Thermal Engineering*, 87, pp. 106–116.

O’Donovan, A., Grimes, R. and Moore, J., 2014. The influence of the steam-side characteristics of a modular air-cooled condenser on CSP plant performance. *Energy Procedia*, 49(June), pp. 1450–1459.

Orozaliev, J., Budig, C. and Vajen, K., 2010. Optimization of the Fin-and-Tube Heat Exchanger Design for Non-Standard Applications. *14th International Heat Transfer Conference, 8-13 August*.

Owen, M., 2013. Air-cooled condenser steam flow distribution and related dephlegmator design considerations. *Doctor Dissertation*, University of Stellenbosch, RSA.

Ozdemir, M. R., Mahmoud, M. M. and Karayiannis, T. G., 2015. Flow boiling heat transfer in rectangular copper microchannel. *International Conference on Advances in Mechanical Engineering Istanbul, Turkey*.

Ozdemir, O. E., 2006. Therrmal performance comparison between microchannel and round tube heat exchangers. *Master Thesis*, Middle East Technical University.

Palen, J. W., Kistler, R. S., and Yang, Z. F., 1993. What we still don't know about condensation in tubes. St. Augustine.

Pawar, T., Kulkarni, A., Kulkarni, G., Patil, S., Yadav, J., Shikalgar, V., 2017. Performance Comparison of Conventional and Microchannel Condenser in Vapour Compression refrigeration system. *International Journal of Innovative Research in Sience, Engineering and Technology*, 6(4), pp. 5441–5446.

Peng, X. F. and Peterson, G. P., 1996. Convective heat transfer and flow friction for water flow in microchannel structures. *Int. J. Heat Mass Transf.*, 39(12), pp. 2599–2608.

Pfund, D., Rector, D., Shekarriz, A., Popescu, A., Welty, J., 2000. Pressure drop measurements in a microchannel. AIChE J., 46(8), pp. 1496–1507.

Putman R, E., and Harpster J. W., 2000. The Economic Effects of Condenser Backpressure on Heat Rate, Condensate Subcooling and Feedwater Dissolved Oxygen. *Proceedings of International Joint Power Generation Conference*

Plessis, J. Du., 2021. *A single-stage dry/wet dephlegmator: development, performance evaluation and application in a hybrid ACC at CSP or NGCC scale*. Master Thesis, University of Stellenbosch, RSA.

Plessis, J. Du and Owen, M., 2020a. An Experimental Investigation of Pressure Drop During Partial Condensation of Low Pressure Steam. *Juornal of Thermal Sciences and Engineering Applications*, 12(15), p. 051018.

Plessis, J. Du and Owen, M., 2020b. An Experimental Investigation of the Air-Side Pressure Drop Through a Bare Tube Bundle. *Journal of Thermal Science and Engineering applications*, 12(1), p. 011012.

Plessis, J. Du and Owen, M., 2021. A single-stage hybrid (dry/wet) dephlegmator for application in air-cooled steam condensers: Performance analysis and implications. *Thermal Science and Engineering Progress*, 26(1), p. 101108.

Putman, R. E. and Harpster, J. W., 2000. The Economic Effects of Condenser Backpressure on Heat Rate , Condensate Subcooling and Feedwater Dissolved Oxygen. *Proceedings on CD, of 2000 International Joint Power Generation Conference.*

Qureshi, B. A. and Zubair, S. M., 2005. The impact of fouling on performance evaluation of evaporative coolers and condensers. *International Journal of Energy Research*, 29(14), pp. 1313–1330.

Ren, C., Weng, J. H., Yan, J. N., Wang, L., She, H. L., Cui, X. Y., 2020. Evaluation of a counter-flow microchannel heat exchanger performance with air-water vapor mixture to liquid water. *E3S Web of Conferences*, 194, pp. 1–5.

Resat Selbas, Onder Kızılkan, M. R., 2006. A new design approach for shell and tube heat exchanger using genetic algorithms from economic point of view. *Chemical Engineering and Processing 45*, 45, pp. 268–275.

Reuter, H. and Anderson, N., 2016. Performance evaluation of a bare tube air-cooled heat exchanger bundle in wet and dry mode. *Applied Thermal Engineering*, 105, pp. 1030–1040.

Reynoso-Jardón1 E., Tlatelpa-Becerro A., Rico-Martínez R., Calderón-Ramírez M., Urquiza G., 2019. Artificial Neural Networks (ANN) to Predict Overall Heat Transfer Coefficient and Pressure Drop on a Simulated Heat Exchanger. *International Journal of Applied Engineering Research*, 14(13), pp. 3097–3103.

Ribatski, G., 2013. A critical overview on the recent literature concerning flow boiling and twophase flows inside micro-scale channels. *Experimental Heat Transfer*, 26, pp. 198–246.

Ribatski, G. and Jaqueline, D. D. S., 2015. Condensation in Microchannels. *Microchannel Phase Change Transport Phenomena*, First Edition, pp. 287-324

Ritchie, H. and Roser, M., 2020. Fossil Fuels. *Our World in Data*, Accessed: Available at: available: https://ourworldindata.org/fossil-fuels.

Rodrigo F. A., Yuri H. B. R., Víctor L. de O. S., Luben C. G., Sérgio de M. H., 2013. The difference between merkel and poppe models and its influence on the prediction of wet-cooling towers. 22nd International Congress of Mechanical Engineering, November 3-7, Ribeirão Preto, SP, Brazil.

Sahar, A. M., Özdemir, M. R., Fayyadh, E. M., Wissink, J., Mahmoud, M. M., Karayiannis, T. G., 2016. Single phase flow pressure drop and heat transfer in rectangular metallic microchannels. *Applied Thermal Engineering*, 93, pp. 1324–1336.

Sahar, A.M., Wissink, J., Mahmoud, M.M., Karayiannis, T.G., Ashrul I. M.S., 2017. Effect of hydraulic diameter and aspect ratio on single phase flow and heat transfer in a rectangular microchannel. *Applied Thermal Engineering*, 115, pp. 793–814.

Shah, R. K. and London, A. L., 1978. *Laminar Flow Forced Convection in Ducts: A Source Book for Compact Heat Exchanger Analytical Data*. New York: Academic Press.

Singh, S. P., Phlip, G. and Singh, S. K., 2014. Effect of condenser vacuum on performance of a Reheat Regenerative 210 MW Fossil-Fuel based Power Plants. *International Journal of Emerging Technology and Advanced Engineering*, 4(1), pp. 190–195.

Smit, L., 2000. *Inlet manifold tests and performance evaluation dephlegmator in air-cooled steam condensers*. *Master Thesis,* University of Stellenbosch, RSA.

Srisomba, R., Asirvatham, L. G., Mahian, O., Dalkilic, A. S., Awad, M. M., Wongwises, S., 2017. Air-side performance of a micro-channel heat exchanger in wet surface conditions. *Thermal Science*, 21(1), pp. 375–385.

Suhas, V. P., 1980. *Numerical heat transfer and fluid flow, Series in computational methods in mechanics and thermal sciences. s.l.* Washington, D.C.: Hemisphere.

Walsh, E.J., Grimes, R., Griffin, G., 2011. Flow distribution measurements from an air cooled condenser in a 400 MW power plant. *ASME IMECE 2011*.

Wang, H., Chen, Z. and Gao, J., 2016. Influence of geometric parameters on flow and heat transfer performance of micro-channel heat sinks. *Applied Thermal Engineering*, 107, pp. 870–87.

Wang, J., Ming, J. and Hwang, Y., 2018. International Journal of Heat and Mass Transfer Modeling of film condensation flow in oval microchannels. *International Journal of Heat and Mass Transfer*, 126, pp. 1194–1205.

Xie, G.N., Wang, Q.W., Zeng, M., Luo, L.Q., 2007. Heat transfer analysis for shell and tube heat exchanger with experimental data by artificial neural networks approach. *Applied Thermal Engineering*, 27, pp. 1096–1104.

Xing, D., Yan, C., Wang, C., Sun, L., 2013. Progress in Nuclear Energy A theoretical analysis about the effect of aspect ratio on single-phase laminar fl ow in rectangular ducts. *Progress in Nuclear Energy*, 65, pp. 1–7.

Xu, B., Ooti, K., Wong, N., Choi, W., 2000. Experimental investigation of flow friction for liquid flow in microchannels. *Int. Commun. Heat Mass Transfer*, 27(8), pp. 1165–1176.

Xu, B., Zhang, C., Wang, Y., Chen, J., Xu, K., Li, F., Wang, N., 2015. Experimental investigation of the performance of microchannel heat exchangers with a new type of fin under wet and frosting conditions. *Applied Thermal Engineering*, 89, pp. 444–458.

Yan, S., Zhang, C., Li, Y., Cao, X., 2000. Steam-water distribution general matrix equation of thermal system for the coal-fired power unit. *Proc. CSEE*.

Yang, H., Rong, L., Liu, X., Liu, L., Fan, M., Pei, N., 2020. Experimental research on spray evaporative cooling system applied to air-cooled chiller condenser. *Energy Reports*, 6, pp. 906–913.

Yin, X., Wang, W., Patnaik, V., Zhou, J., Huang, X., 2015. Evaluation of microchannel condenser characteristics by numerical simulation. *International Journal of Refrigeration*, 54, pp. 126–141.

Yunus, A. C. and Afshin, J. G., 2011. *Heat and Mass transfer, Fundamentals and Applications. fourth ed.* New york: McGraw - Hill.

Zhang, F., Bock, J., Jacobi, A. M., Wu, H., 2014a. Simultaneous heat and mass transfer to air from a compact heat exchanger with water spray precooling and surface deluge cooling. *Applied Thermal Engineering*, 63, pp. 258–540.

Zhang, J., Diao, Y. H., Zhao, Y. H., Zhang, Y. N., 2014b. An experimental study of the characteristics of fl uid fl ow and heat transfer in the multiport microchannel fl at tube. *Applied Thermal Engineering*, 65, pp. 209–218.

Zhang, Y., Liu, J., Yang, T., Liu, J., Shen, J., Fang, F., 2021. Dynamic modeling and control of direct air-cooling condenser pressure considering couplings with adjacent systems. *Energy*, 236, p. 121487.

Zhang, Y., Zhang, F. and Shen, J., 2019. On the dynamic modeling and control of the cold-end system in a direct air-cooling generating unit. *Applied Thermal Engineering*, 151(January), pp. 373–384.

Zhou, J., Yan, Z. and Gao, Q., 2017. Development and Application of Micro Channel Heat Exchanger for Heat Pump. *12th IEA Heat Pump Conference*, p. 3.1.5.

Zou, Y., Li, H., Tang, K., Hrnjak, P., 2016. Round-Tube and Microchannel Heat Exchanger Modeling at Wet Air Condition. *International Refrigeration and Air Conditioning Conference*, p. 1774.

Appendix

A. Ethical Clearance Certificate

UNAM
UNIVERSITY OF NAMIBIA

ETHICAL CLEARANCE CERTIFICATE

Ethical Clearance Reference Number: EEREC/0001 **Date: 31st July 2019**

This Ethical Clearance Certificate is issued by the University of Namibia Research Ethics Committee (UREC) in accordance with the University of Namibia's Research Ethics Policy and Guidelines. Ethical approval is given in respect of undertakings contained in the Research Project outlined below. This Certificate is issued on the recommendations of the ethical evaluation done by the Environment and Engineering Research Ethics Committee (EEREC).

Title of Project: *Modelling of Conventional and Microchannel Delugeable tube bundle for a direct Air-cooled steam condenser*

Nature/Level of Project: *PhD*

Researcher: *Ester Angula*

Student Number: *2018178755*

Faculty: *Engineering & Information Technology*

Supervisors: *Prof. P. C. Chisale, (Main) NUST*
Dr Fillemon Nduvu Nangolo (Co-) UNAM

Take note of the following:

(a) Any significant changes in the conditions or undertakings outlined in the approved Proposal must be communicated to the EEREC. An application to make amendments may be necessary.
(b) Any breaches of ethical undertakings or practices that have an impact on ethical conduct of the research must be reported to the EEREC.
(c) The Principal Researcher must report issues of ethical compliance to the EEREC (through the Chairperson of the Faculty/Centre/Campus Research & Publications Committee) at the end of the Project or as may be requested by EEREC.
(d) The EEREC retains the right to:
  i. Withdraw or amend this Ethical Clearance if any unethical practices (as outlined in the Research Ethics Policy) have been detected or suspected,
  ii. Request for an ethical compliance report at any point during the course of the research.

REC wishes you the best in your research.

Prof. O. T. Johnson: EEREC Chairperson

Signature

B. Condensation Heat Transfer Coefficient

The correlations for determining the condensation heat transfer coefficient on a vertical flat plate and horizontal tube, respectively as presented in (Kröger, 2004) are:

$$h_{c,vert} = 0.943 \left[\frac{\rho_c g(\rho_c - \rho_s) i_{fg}{}^* k_c^3}{\mu_c (T_c - T_w) H_t}\right]^{0.25} \tag{B.1}$$

$$h_{c,hor} = 0.729 \left[\frac{\rho_c g(\rho_c - \rho_s) i_{fg}{}^* k_c^3}{\mu_c (T_c - T_w) D}\right]^{0.25} \tag{B.2}$$

where $i_{fg}{}^*$ is modified latent heat of vaporization, which determined as:

$$i_{fg}{}^* = i_{fg} + 0.68 c_{pc}(T_c - T_w) \tag{B.3}$$

For the heat transfer coefficient of turbulent flow in the duct, Gnielinski (1976) correlation can be used.

$$Nu = \frac{(f_D/8)(Re - 1000)Pr}{1 + 12.7(f_D/8)^{0.5}\left(Pr^{2/3} - 1\right)} \tag{B.4}$$

which valid for $3000 < Re < 5 \times 10^6$, $0.5 \leq Pr \leq 2000$. Petukhov (1970) correlation can be used to determine the friction factor in turbulent flow in smooth tubes:

$$f_D = (0.79\, lnRe - 1.64)^{-2} \tag{B.5}$$

which valid for $3000 < Re < 5 \times 10^6$

C. Deluge Water Heat Transfer Coefficients

The film heat transfer coefficient correlation as a function of the air mass velocity, deluge water mass velocity and deluge water temperature were developed in Heyns (2008) as:

$$h_w = 470 G_a^{0.1} G_w^{0.35} T_w^{0.3} \tag{C. 1}$$

which valid for:

$$0.7 < G_a < 3.6\ kg/m^2 s,\ 1.8 < G_w < 4.7\ kg/m^2 s\ and\ 35℃ < T_w < 53℃$$

The correlations for determining the heat transfer coefficient between the tubes and deluge water, as recommended Parker and Treybal (1961), Niitsu et al. (1969) and Mizushina et al (1967):

$$h_w = 704(1.3936 + 0.02214 T_{wm})(\Gamma_m/d_o)^{0.333} \tag{C. 2}$$

$$h_w = 990(\Gamma_m/d_o)^{0.46} \tag{C. 3}$$

$$h_w = 2102(\Gamma_m/d_o)^{0.333} \tag{C. 4}$$

Due to limited correlations for the deluged flat tube bundle, the heat transfer coefficient between the flat tubes and deluge water was determined from the relation between the heat convection and conduction through the deluge water film as:

$$h_w = \frac{k_{dw}}{\delta_{dw}} \tag{C. 5}$$

D. Air-side Heat and Mass Transfer Coefficients

D.1. Flow over the round tube

The average Nusselt number, for the flow over the cylinder was defined as (Yunus & Afshin , 2011):

$$Nu_{cyl} = \frac{h_a D}{k_a} = 0.3 + \frac{0.62 Re^{0.5} Pr^{1/3}}{\left[1+(0.4/Pr)^{\frac{2}{3}}\right]^{1/4}} \left[1 + \left(\frac{Re}{282000}\right)^{\frac{5}{8}}\right]^{4/5} \quad \text{(D. 1)}$$

which is valid for $Re,\ Pr > 0.2$

D.2. Flow over the flat tube

The local Nusselt number at any location z, along the tube height was determined using theories, as presented in (Yunus & Afshin , 2011):

$$Nu_z = \frac{h_a z}{k_a} = 0.332 {Re_z}^{0.5} Pr^{1/3} \quad \text{(D. 2)}$$

$$Nu_z = \frac{h_a z}{k_a} = 0.0296 \mathrm{Re}_z{}^{0.5} \mathrm{Pr}^{1/3} \quad \text{(D. 3)}$$

where Eq. (D.2) is valid for $Re_z < 5 \times 10^5, Pr > 0.6$, and Eq. (D.3) is valid for $5 \times 10^5 \leq \mathrm{Re}_z \leq 10^7,\ 0.6 \leq\ Pr \leq 60$. The average Nusselt number for the flow over the entire tube's height:

$$Nu = \frac{h_a H_t}{k_a} = 0.664 {Re_{H_t}}^{0.5} Pr^{1/3} \quad \text{(D. 4)}$$

$$\mathrm{Nu} = \frac{h_a H_t}{k_a} = 0.037 \mathrm{Re}_{H_t}{}^{0.5} \mathrm{Pr}^{1/3} \quad \text{(D. 5)}$$

where Eq. (D.4) is valid for $Re_{H_t} < 5 \times 10^5, Pr > 0.6$, and Eq. (D.5) is valid for $5 \times 10^5 \leq \mathrm{Re}_{H_t} \leq 10^7,\ 0.6 \leq\ Pr \leq 60$. The mass transfer convection coefficient is determined from the analogy between heat and mass transfer at the air-water interface. The local Sherwood number at any location z, along the tube height:

$$Sh_z = \frac{h_D z}{\mathrm{D_{AB}}} = 0.332 {Re_z}^{0.5} Sc^{1/3} \tag{D. 6}$$

$$Sh_z = \frac{h_D z}{\mathrm{D_{AB}}} = 0.0296 {Re_z}^{0.5} Sc^{1/3} \tag{D. 7}$$

where Eq. (D.6) is valid for $Re_z < 5 \times 10^5, Sc > 0.5$, and Eq. (D.7) is valid for $5 \times 10^5 \leq Re_z \leq 10^7,\ 0.5 \leq\ Sc \leq 60$. The average Sherwood number for the flow over the entire tube's height:

$$Sh = \frac{h_D H_t}{\mathrm{D_{AB}}} = 0.664 {Re_{H_t}}^{0.5} Sc^{1/3} \tag{D. 8}$$

$$Sh = \frac{h_D H_t}{\mathrm{D_{AB}}} = 0.037 {Re_{H_t}}^{0.5} Sc^{1/3} \tag{D. 9}$$

where Eq. (D.8) is valid for $Re_{H_t} < 5 \times 10^5, Sc > 0.5$, and Eq. (D.9) is valid for $5 \times 10^5 \leq Re_{H_t} \leq 10^7,\ 0.5 \leq\ Sc \leq 60$. Marrero and Mason (1972) recommended the following correlation for defining the mass diffusion of water vapour:

$$D_{H2O} = 1.87 \times 10^{-10} \frac{\left[\frac{T_{dws}+T_{am}}{2}+273.15\right]^{2.072}}{P_a} \tag{D. 10}$$

E. Mass Transfer Coefficients

The correlations for determining the mass transfer coefficients between the deluge water and air stream in the literatures for round tube bundles:

$$h_d = 0.04935[(1+\omega)(m_a/A_c)]^{0.905} \tag{E. 1}$$

which valid for $0.68\ kg/m^2 s\ < (m_a/A_c) < 5\ kg/m^2 s$

$$h_d = 5.5439 \times 10^{-8} Re_{avm}^{0.9} Re_{wm}^{0.15} d_o^{-1.6} \tag{E. 2}$$

which valid for $1.2 \times 10^3 < Re_{avm} < 1.4 \times 10^4$

$$h_d = 0.076(m_a/A_c)^{0.8} \tag{E. 3}$$

which valid for $1.5\, kg/m^2s < (m_a/A_c) < 5\ kg/m^2s$

The air-mass transfer coefficient as a function of the air mass velocity, deluge water mass velocity and deluge water temperature was derived by Heyns (2008):

$$h_d = 0.038 G_a^{0.73} G_w^{0.2} \tag{E. 4}$$

which valid for $0.7 < G_a < 3.6\ kg/m^2s,\ 1.8 < G_w < 4.7\ kg/m^2s$

F. Pressure Drop Correlations

F.1. Air-side pressure drop for the flow over the round tube

The correlation for determining the pressure drop over the tube bundle that was developed by (Heyns, 2008) as a function of the air mass velocity, deluge water mass velocity and deluge water temperature:

$$\Delta P = 10.28 G_a^{1.8} G_w^{0.22} \tag{F. 1}$$

which valid for $0.7 < G_a < 3.6\ kg/m^2s,\ 1.8 < G_w < 4.7\ kg/m^2s$

F.2. Air-side pressure drop for the flow over the flat tube

For the flow over the flat tube, both local and average friction coefficients were determined using correlations, as presented in (Yunus and Afshin, 2011). The local friction coefficients at any location z, along the tube's height:

$$C_{f,z} = 0.664Re_z^{-0.5} \tag{F. 2}$$

$$C_{f,z} = 0.059Re_z^{-0.2} \tag{F. 3}$$

where Eq. (F.2) is valid for $Re_z < 5 \times 10^5$, and Eq. (F.3) is valid for $5 \times 10^5 \leq \mathrm{Re}_z \leq 10^7$. The average friction coefficient for the flow over the entire tube's height:

$$C_f = 1.33Re_{H_t}^{-0.5} \tag{F. 4}$$

$$C_f = 0.074Re_{H_t}^{-0.2} \tag{F. 5}$$

where Eq. (F.4) is valid for $Re_{H_t} < 5 \times 10^5$, and Eq. (F.5) is valid for $5 \times 10^5 \leq \mathrm{Re}_{H_t} \leq 10^7$. The frictional pressure drop for external and internal flow can be expressed as:

$$\Delta P_f = C_f \left(\frac{A_a}{A_c}\right) \rho_a \frac{v_{am}^2}{2} \tag{F. 6}$$

$$\Delta P_f = f_D \left(\frac{H_t}{d_a}\right) \rho_a \frac{v_{am}^2}{2} \tag{F. 7}$$